DELINEATION OF AN INSULA-BNST CIRCUIT ENGAGED BY STRUGGLING BEHAVIOR THAT REGULATES AVOIDANCE

By

Joseph Richard Luchsinger

Dissertation

Submitted to the Faculty of the

Graduate School of Vanderbilt University

in partial fulfillment of the requirements

for the degree of

DOCTOR OF PHILOSOPHY

in

Neuroscience

May 31, 2021

Approved:

Sachin Patel, M.D., Ph.D.

Jenni Blackford, Ph.D.

Brad Grueter, Ph.D.

Tom Kash, Ph.D.

Danny Winder, Ph.D.

This work is dedicated to those struggling

with mental illness and their loved ones.

ACKNOWLEDGMENTS

This work and my training were made possible through collective contributions from the citizens of the United States. To each of you, I am grateful. A nation's long-term progress is directly tied to its investment in the arts and sciences, and there is no mechanism beyond national sponsorship to fund the scale of fundamental science that is required to better the world of tomorrow. This down payment on our future is often not realized for years or even decades. We patiently and methodically cultivate both our scientific understanding and human capital so that every so often, serendipity brings the right person, knowledge, and environment together to change our understanding of the universe. To the long lineage of forward-looking advocates and policymakers that put our collective future first, we owe you a great debt.

The National Institutes of Health sponsor the majority of basic biomedical research in the US. NIGMS(T32GM007347), NIDA (R01 DA042475), and NIAAA (R37 AA019455 and F30 AA027126) funded my training and the work in this dissertation specifically. For that support, I am very grateful. I am also thankful to the MSTP and VUSM leadership for their tireless effort on our behalf.

This project's completion is a significant milestone, and writing this dissertation provided me with time to consider my journey to this point. My life has been shaped by the hands of many, without whom I would not be in this position today. To each of you, I will be forever thankful.

I completed this work in Danny Winder's lab at Vanderbilt University. Danny, you created a culture of open science, collegiality, and collaboration. As a mentor, you help me grow as a scientist and as a team member. You provided a framework for quality science while allowing great latitude to pursue my interests (both scientific and otherwise). You set a tremendous example of lifting up those around you, a trait I hope to emulate in the future. Thank you for your ongoing support and mentorship (and the many holiday meals at Adele's). I sincerely hope we have a chance to work together in the future.

My Committee Members were Sachin Patel (Chair), Jenni Blackford, Brad Grueter, and Tom Kash. Each of you provided invaluable insight throughout my Ph.D. Thank you for your guidance and questions, which increased our work's rigor and my understanding of the scientific method. You pushed our research towards new and exciting avenues of inquiry.

We completed the light sheet analysis in collaboration with Richard Simerly. Rich, you have been a wonderful collaborator and mentor. I count myself lucky that our labs were in such proximity. Your advice, both scientific and not, was enormously valuable, and your generosity with your lab resources greatly enhanced my Ph.D. experience.

Bob Matthews, you are a patient teacher, eager to explore new questions, and have a passion for helping those around you do better science. Your stories and enthusiasm for life outside the lab always brightened my day. Thank you for being a friend and colleague.

To the current and past members of the Vanderbilt Center for Addiction Research, and particularly the Winder, Simerly, and Blackford labs, you have been terrific role models,

teammates, and friends. Much of the work in this document was made possible through your efforts, ideas, and feedback. I looked forward to coming to the lab each day to work with you and hope we have many opportunities to work together in the future. A special thanks to Elana Milano, Sam Centanni, Kellie Williford, Tracy Fetterly, Greg Salimando, Marie Doyle, and Jose Maldonado for directly contributing to this project.

On my path to Vanderbilt's M.D.-Ph.D. program, my academic career was shaped by many teachers who believed in and supported my efforts. My early education was inauspicious. I dreaded going to school each day. As a child with undiagnosed dyslexia, I did not understand why school was so hard. I wanted to quit. I was embarrassed. Fortunately, my fourth-grade teacher, Mrs. Lichty, changed the trajectory of my life. She taught her students, myself included, that it was not important to finish first, but instead placed the value on each child completing work at their own pace. I still remember her telling each of us, "I see your lightbulb going on," every time we finished a problem. Mrs. Lichty, from your class on, school started to become fun, and for that, I will be eternally grateful.

Dr. Mickley was my undergraduate PI at Baldwin Wallace University (BW). At the time, I did not appreciate the rarity of a productive lab staffed exclusively by undergraduates. Dr. Mickley, this was a formative experience in my scientific journey. The opportunity to design, carry out, and present our research set me on the path for a career in science. Thank you for your mentorship and showing me what it means to be a careful and meticulous scientist.

Dr. Meyer was my BW physics professor. Dr. Meyer, popping into your office to discuss a new puzzle or the workings of the universe were some of my favorite memories from BW. While I learned much from you during my time in Cleveland, perhaps the most lasting lesson was to sit back in a chair, stare at the ceiling, and just think about a problem. You taught me that only then, after completely understanding the question, should you dive in. For this and much more, thanks Doc.

To the members of Table 7, you are our family in Nashville. Ben, Brooke, Caleb, Cam, Elisabeth, Jack, Liz, and Virginia, this was true long before the pandemic, but your friendship and support after our son Axel's birth prevented us from feeling like we were drowning. Christelle and I share too many memories with each of you to list here. So, just know that our journey together has made the choice to move to Nashville one of the best decisions of our lives. Here is to many more years of friendship.

To my grandfather Richard E. Beck, you were a kind and loving teacher. Some of my earliest memories involve heading down to your basement to build things with you. For hours, we would work together, and you would patiently answer every query that I could produce. You nurtured my curiosity and encouraged me to continue to ask the question, "why?"

Wilbur Wright once said, "If I were giving a young man advice as to how he might succeed in life, I would say to him, pick out a good father and mother, and begin life in Ohio." I could not agree more. To my parents Beth and Frank, I will never know all of the sacrifices you made to make my life what it is today. I do know some, and I will always be thankful.

Dad, you lifted heaven and earth to make sure dyslexia did not prevent me from succeeding. Many a time, you stayed up to the wee hours of the morning, scanning my textbooks so that I could read them via text-to-speech. This quiet and often thankless act made school accessible to me. (My experience, of course, was quite an improvement from your marching in place so that you could stay away to trudge through your college books a few decades ago.) Your determination served as a continuous guiding light, and I hope to prove an equal exemplar of perseverance for Axel. Over the years, I grew up watching you shepherd our church and its members. Through your actions, you taught me the qualities of servant leadership, traits I hope to embody for the rest of my life.

Mom, you taught me to believe in all people. Your dedication to understanding those of a persuasion other than your own inspires me. Not only do you listen to other's perspectives, but you consistently seek them out. I believe this makes humanity stronger, and I hope to do the same. Along my academic road, no one has read more of my work than you. You have also acted as editor and proofreader for almost every document that I have produced from early education to this dissertation. Your ever-present feedback improved my writing and clarified my thoughts. Lastly, you moved into the hospital for months when I was ill. You held my hand for hours when I was too weak for anything else. Thank you.

Finally, thank you to my wife, Christelle. This accomplishment belongs as much to you as it does to me. Thank you for your endless love and steadfast support. Our journey was not always easy, and I am grateful that you were there to see me through my darkest days. During that time, I believed I would pass away without seeing you again. My only thought was that I wanted to hear your voice once more before I left. From that day on, I gained a renewed appreciation that every day with you is a rare gift. After I survived, you moved to the US to assist with everything from changing my ostomy to helping me recover - you made me feel whole again.

What does it mean to love like this? It means that I can be vulnerable yet still feel safe. It means I can take risks and know that that which is most important will remain constant. It means that every day begins and ends with the best part of my life. Our victories are sweeter, and losses are softer because we do them together. You believe in me when I do not. You push me to do more and be better. You give me strength when I have none. You are my everything.

TABLE OF CONTENTS

LIST OF TABLES

Table Page

LIST OF FIGURES

Figure Page

Chapter 1

Introduction

1.1 An overview of the stress response

"Stress" is a term refashioned from physics by the early stress research pioneer Hans Selye.[1] In physics, stress is a force applied over the cross-sectional area of a material body. The reaction to this force is strain, or the resultant deformation or displacement of the medium. These counterbalancing concepts resonated with Selye's goal of unifying the French physiologist, Claud Bernard's, work on the regulation of the "milieu intérieur" [2,3]; Walter Bradford Cannon's work on "homeostasis," which Cannon coined in 1926 [4,5], Frank Hartmann's corticoid theory [6–8], and A.P. Dustin's reflections regarding caryoclastic (or nuclear) poisons.[9] This, coupled with Selye's observations of non-specific therapeutic compounds and post-operative illness, informed his understanding of the body's homeostatic response to insult.

While attending medical school at the University of Prague, Selye noticed that his hospitalized patients reacted to their variety of maladies with a similar cadre of features. He later wrote, "stress is the interaction between damage and defense, just as in physics tension or pressure represents the interplay between a force and the resistance offered to it" [1]. As Selye's work, along with that of the rest of the stress field, progressed, investigators needed to avoid conflating the syndrome and the inducing cause; thus, these terms were delineated as "stress" and "stressor," respectively[10].

Today, we know organisms' survival depends on their ability to respond appropriately to an inevitable battery of varied stressors present throughout life. From the comparatively simple

single-celled organisms to the most complex known beings (i.e., humans), all must address noxious stimuli or risk harm. In fact, the word "stimulus" itself is derived from Latin with a similar context, in which case it means "a pointed stick used as a goad or weapon." [11] Roman soldiers would use a "stimulus," or buried steak, to impale inattentive enemy combatants with the technique that was used as recently as the Vietnam War. The word "stimulus" entered physiology in the 17th century after Jan Swammerdam used it to describe the retraction of a frog's leg after he pricked the nerve.

The trait of being able to flexibly adapt to a given "stimulus" or stressor is a quintessential competency for survival. Stress can generally be described as the organism's response to these noxious or dangerous stimuli[12]. Indeed, the importance of this allostasis, or 'stability through change,' was aptly outlined by Sterling and Eyer in 1988.[13]

The stress response is not uniformly adaptive, however. Stressors and the inability to engage or disengage the appropriate stress response increase the cumulative impact of the physiologic reaction to stress, termed allostatic load, and can damage the body and homeostatic systems[14]. This paradox, that the physiologic systems responsible for the stress reaction could both protect or harm the body, were described by Selye as far back as 1936[12]. This work substantiated that a variety of stressors, including cold exposure, surgical injury, excessive exercise, and various drug exposures induced a similar syndrome regardless of the noxious agent. Selye showed broad systemic dysfunction impacting systems ranging from immunologic to metabolic to neuroendocrine and noted that these changes appeared to happen in stages dependent upon the nature of the stress.

Stress can be divided into acute stress and chronic stress, both of which can have serious long-term effects. These stressful events occur throughout life and can have disparate impacts on

physical and mental health. Acute stress involves short events (e.g., fight-or-flight inducing, a term coined by Cannon in 1929), while chronic stress is engaged by ongoing exposure to smaller stressors. In higher-level organisms, the brain is the central mediator of acclimation to physical and social stress[15]. Thus, events with high salience or emotional engagement can have a long-lasting impression on the brain. As early as 1890, William James noted the potential for this, stating, "an impression may be so exciting emotionally as almost to leave a scar upon the cerebral tissues[16]." While visible macroscopic scaring is not present, he was ahead of his time given micro- and submicroscopic changes that we now know stressors can cause.

Shortly thereafter, in 1899, Colegrove noted similar phenomena, pointing out that individuals could describe in detail the day that occurred three decades prior, on which they learned that John Wilkes Booth assassinated President Abraham Lincoln[17]. Unfortunately, this observation has been tested, and the results repeated as each passing generation has a unique set of permanent scars seared into their memories by the catastrophic events of the day. Just as those alive in 1865 remembered Lincoln's assassination, those alive today have hypermnesia[18], or flashbulb memories[19] for Martin Luther King's and John F. Kennedy's assassinations, the Challenger explosion, and the attack on September 11th 2001[20–22]. This seems to be part of the very nature of being human, engraved in the genetic blueprint that orchestrates the function of our central nervous system. It will most certainly hold true for those who endured and observed the insurrection incited by Donald J. Trump on January 6th, 2021[23]. Hopefully, the lasting memory will serve as a reminder that democracy is fragile.

Clearly, acute stress has the ability to increase memory consolidation in certain circumstances. It has also been shown to enhance performance and thus augment survival. However, the relationship of greater stress increasing performance is not uniformly linear. This

paradox of stress can be seen when the intensity of a stressor increases beyond some point. After passing that threshold, which is distinct for each individual, performance decreases in a phenomenon known as the Yerkes-Dodson Law[24].

Interestingly, the Yerkes-Dodson Law states that simple task performance improves as stressor intensity, and thus presumably arousal, increases. However, for more challenging tasks, the relationship between stress intensity and performance is curvilinear (as an inverted U). Increasing stressor intensity, in this case, improves performance to a threshold, but anything further begins to decrease performance[25]. Therefore, it is plausible for an acute stressor to increase or decrease the organism's propensity to successfully adapt depending on the nature and severity of that stressor coupled with the complexity of the action required. Note: while some have proposed a linear relationship between stress and simple tasks, others hypothesize that there is likely some threshold where performance decreases again – e.g., panic-induced or if the stressor itself impedes the organism's function (Fig. 1).

Regardless of the acute stressor's nature, an organism will work to alleviate the pressure or potentially damaging stimulus. This survival mechanism of adaption is termed "allostasis" and attempts to address some of the ambiguities associated with Cannon's classical use of "homeostasis" [5,13,26–28]. These stress biology mechanisms provide flexibility for the variety of situational and environmental differences encountered throughout life, thus are generally positive. If, however, the organism is unable to adapt or reach an allostatic state by addressing a given stressor, the acute stressor may become chronic.

Contrary to acute stress, chronic stress tends to be unidirectional and induces maladaptive changes. These maladaptive changes are indicative of an imbalance in allostatic load and the

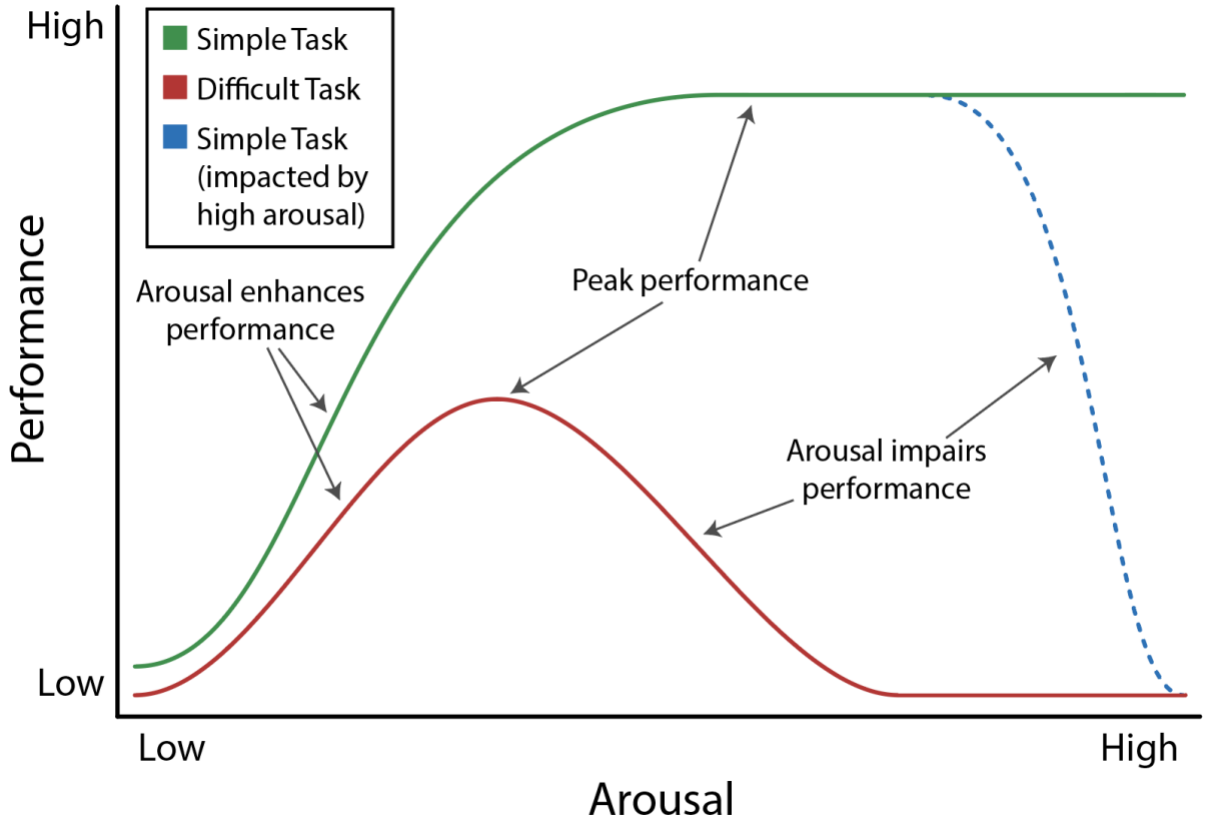

Figure 1: Diagram of arousal level vs. performance by task complexity.

Task complexity is separated by color. Green = simple task, Red = difficult task, Blue = simple task that has performance impacted at highest arousal levels.

allostatic systems meant to combat those stressors. In this context, chronic stress causes damage in a number of ways[14].

1. Most apparently, the repeated or frequent exposure to a stressor can cause damage to the organism.
2. If the adaptive mechanisms normally employed by an organism to address or adapt to a stressor are dysfunctional, it can lead to a lengthened exposure to the stress and increase the allostatic load.
3. The inability to shut down the stress response after the cessation of the stress exposure increases the exposure to stress signaling and stress hormones.
4. An inadequate response by one component of the stress system can lead to a harmful compensatory overactivation of the other parts of the system.

The maladaptive changes induced by these insults can alter brain networks, decreasing judgment and impulse control[29,30]. Depending on when these insults take place, during sensitive periods in children, for example, detrimental effects can cause problems well into adulthood[31–33]. During development, the ongoing exposure to glucocorticoids and excitatory amino acid neurotransmitters that accompany adverse childhood experiences (ACEs) can induce alterations in neuronal architecture that can persist for years[31]. The associated maladaptive behaviors coupled with the changes in neural architecture increase the probability of neuropsychiatric (and other) diseases[31,33]. A chronically overactive stress reaction can dysregulate the neurologic, cardiovascular, immunologic, and metabolic systems, and cause sustained depletion of energy. Moreover, stress responses continually directed at nonexistent threats can lead to long-lasting negative changes in behavior[14]. In humans, exposure to stress and the inability to cope with

stress are associated with posttraumatic stress disorder (PTSD), chronic depression, anxiety disorder, and substance use disorder[34–36].

1.2 Physiology of the stress response and an abbreviated history

Though there are no practical limits to the number of potential stressors that an organism might face, there are many typical components of the response to a stressor. Canonically, this is mediated through the hypothalamic-pituitary-adrenal (HPA) axis. Over the past have century, our understanding of stress, the stress axis, and the biologic response to stress has grown tremendously. The systems recruited by stress are engaged continuously in surveilling environmental pressures, coping with stressors, and predicting and addressing future events.

In brief, the HPA axis is a feedback system that regulates systemic glucocorticoid signaling (Fig. 1.2). The paraventricular nucleus of the hypothalamus (PVN) releases corticotrophin-releasing factor (CRF) and arginine vasopressin (AVP) in response to circadian rhythms. This circadian CRF cycle is merged with information about environmental stressors signaled by other brain regions, including the amygdala, bed nucleus of the stria terminalis (BNST), and hippocampus. The hypophyseal portal system transports CRF to the anterior pituitary, where CRF stimulates the local corticotropic cells. These corticotropic cells produce ACTH and release it into the systemic circulation. When ACTH reaches the adrenal cortex, it causes the adrenal cortex to release glucocorticoids systemically.

The work to flesh out the molecular players in this pathway began in the early 21st century and took decades. Prior to the late 1920s, many attempts to isolate the hormone in the adrenal cortex were unsuccessful. A 1928 report out of the University of Buffalo changed that. Adrenalectomized cats were kept alive by administering the compound extracted from the

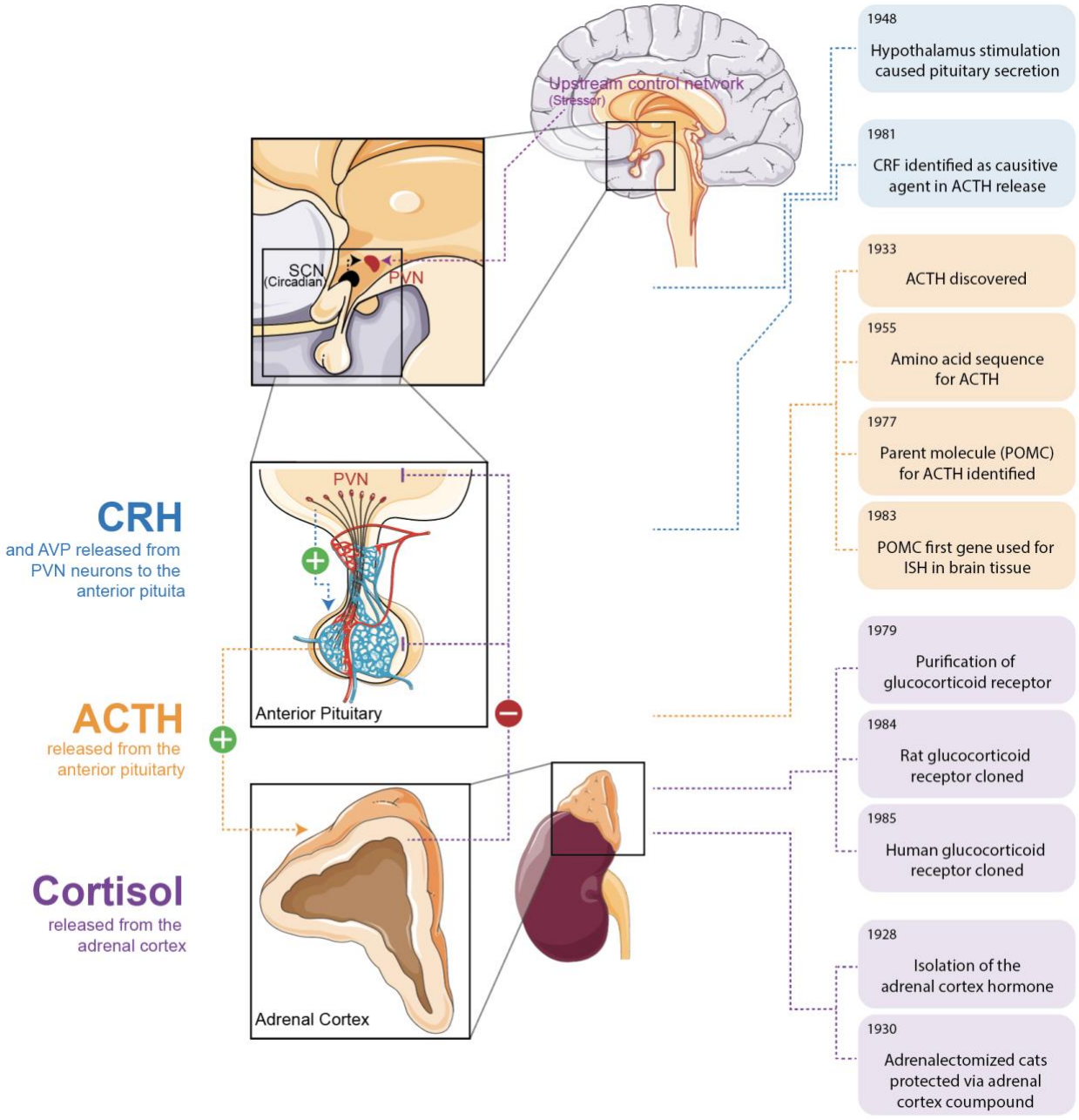

Figure 1.2: Schematic of HPA axis with historical discoveries.

adrenal cortex for between 5 and 16 days[7,8]. Interestingly, the name originally proposed for the hormone from the adrenal cortex was *cortin*, "in preference to *corticin* because the latter is the name of an alkaloid obtained from the bark of Populus tremula[8]." (We now know the main glucocorticoid in humans as cortisol, while in rodents, it is corticosterone.)

In 1933, Evelyn M. Anderson, James Bertram Collip, and David Landsborough Thomson published their pioneering work first reporting adrenocorticotropic hormone (ACTH), discovered while Anderson was working on her thesis at McGill University[37,38]. Subsequently, early studies of the HPA axis were in the field of neuroendocrinology and focused on nailing down the molecular components involved in stress signaling that were downstream of the hypothalamus.

Li et al. isolated ACTH from sheep pituitaries in 1942 and sequenced it 13 years later[39–41]. It was not until the late 1970s that detailed biochemical work by teams from the University of Colorado Medical Center and the University of Oregon demonstrated that ACTH was derived from a parent molecule that also encoded α- and β-melanocyte-stimulating hormone (MSH) and the opioid β-endorphin[42,43]. Two years later, Nakanishi et al. cloned the full parent molecule for ACTH, α- and β-MSH, and β-endorphin[44]. This parent molecule was named proopiomelanocortin or POMC. POMC was shown to be post-translationally cleaved in an ordered fashion[45,46] in the anterior pituitary such that ACTH could be released into the bloodstream. Yet, at the time, a major question for the field was if POMC was produced in the central nervous system or produced peripherally and then taken up by the pituitary from plasma in a retrograde fashion[47,48]. In effort to answer this question, POMC was the first gene to have its expression shown with in situ hybridization in brain tissue[49]. The finding of mRNA in pituitary cells helped concretely establish that pituitary (and hypothalamic) neurons produced POMC.

Investigators searched for decades to understand how ACTH was released from the anterior pituitary. Evidence attained shortly after world war II at Cambridge, through the electrical stimulation of the rabbit hypothalamus, suggested that the hypothalamus could modulate pituitary secretory functions[50]. The hunt for the responsible agent was well underway by 1960 when a collaboration between laboratories at Baylor University College of Medicine and College de France in Paris described "two distinct peptides with corticotrophin-releasing factor activity[51]." However, it took until 1981 for Vale et al. to isolate what we now call corticotrophin-releasing factor or CRF from "490,000 fragments" of sheep hypothalamus[52]. Once isolated, they were also able to successfully demonstrate that it could stimulate ACTH secretion.

While this ACTH secretion was known to induce glucocorticoid release from the adrenal cortex, the receptor for glucocorticoids was not known. By the early 1970s, evidence existed that it was a cytoplasmic receptor that translocated to the nucleus to alter gene expression[53]. The late '70s and early '80s saw the purification of the receptor, where researchers found it to have a mass of ~ 94,000KD[54,55], as well as the generation of antibodies targeting the receptor. Nevertheless, it was not until 1984 that a team from UCSF first cloned the rat glucocorticoid receptor[56]. This was followed shortly by a group from southern California cloning the human glucocorticoid receptor in 1985, rounding out the fundamental components of the HPA axis[57].

1.3 Impact of stress on the body

In common parlance, "stress" is often used as a broad scope of feelings of being overwhelmed or having difficulty addressing a potential threat. This could theoretically range from experiencing a life-threatening situation to waiting for a friend who is late for dinner. Consequently, the psychologist Jerome Kegan pushed back against this expansive

conceptualization of stress, for which he said Hans Selye deserved responsibility, stating it was too broad to be useful[58]. When discussing how stress can impact the body, it is indeed useful to adopt a definition that is more specific than "any demand that requires an adjustment or an adaption by an organism." For this subsection, we will focus on stress with the potential to induce persistent changes[59].

As mentioned above, the stress response (i.e., engagement of the HPA axis) can be, and is ordinarily adaptive. This functional reaction, or "good stress," acutely engages the physiological stress response then rapidly turns it off after successfully addressing the stressor, for example, presenting one's thesis work to his or her committee. In contrast, "tolerable stress" is more chronic but can be adapted to over time through resiliency, allowing the stress response to cease. Finally, "toxic stress" is also chronic, but adaption is insufficient or fails; thus, the stress reaction remains, leading to prolonged exposure to stress signaling. This last type of stress can be maladaptive and cause health problems with the potential to dysregulate metabolic, immunologic, cardiovascular, and neurologic systems.

1.4 Immunologic impact of stress

Some of the earliest evidence that stress could alter immune function came in 1936, when Selye, using over 1500 rats, observed that chronic stress-induced thymic atrophy[60]. Importantly, the immune response to HPA axis activation has high individual variability and is dependent on the duration of the stress (acute, subacute, or chronic), glucocorticoid levels (basal, physiologic, or supraphysiologic), the timing of HPA activation related to immune activation, and which glucocorticoid is deployed[61]. Evidence also exists for humans[62–64], non-human primates[65], and rodents[66,67], that blood leucocyte numbers track diurnal glucocorticoid levels, a finding that

appears to be driven by preferential migration into different body compartments[68–71]. Hyporesponsiveness of HPA axis signaling, due to a genetic mutation in CRF synthesis in experimental model animals, predisposed animals to an autoimmune inflammatory response[72]. This is consistent with human data that demonstrates a relationship between those with HPA axis dysfunction and fibromyalgia[73,74], chronic fatigue syndrome[75,76], and atopic dermatitis[77]. Childhood maltreatment also predicts inflammation later in life[78].

Under acute stress, activation of the sympathetic nervous system and the release of catecholamines enhances immune activation[79]. It is well understood that the autonomic nervous system innervates much of the lymphoid tissue throughout the body and is vital for immune cell development and deployment[80–83]. During this acute window, the basal levels of glucocorticoids are needed to permit immune activation in part because glucocorticoids are required for epinephrine synthesis by the adrenals[84]. Interestingly, when glucocorticoid levels rise acutely, blood leukocyte numbers drop. This counter-intuitive result is explained by leukocytes migrating from the blood into the tissues where they might be needed, similar to the diurnal cell redistribution[61,85].

Chronic stress generally has different effects. The thymic involution that Selye observed in his 1936 study of chronic stress was later demonstrated to be due to glucocorticoid-induced apoptosis of immature T cells[86]. Additionally, extended exposure to glucocorticoids decreases circulating leukocytes[81,87–89] and pro-inflammatory cytokines (e.g., IL-1, IL-6, and TNF-alpha)[87,90,91], a trait that is particularly true of supraphysiologic glucocorticoids and has made these synthetic variants useful therapeutically. Nuclear factor (NF)-κB and activator protein-1 (ACP-1) are critical pro-inflammatory transcription factors whose action is decreased by glucocorticoids through a variety of processes. For example, chronic glucocorticoid exposure

upregulates the expression of an inhibitor of NF-κB, namely IκB[92]. While early evidence suggested chronic glucocorticoid action was predominantly anti-inflamatory[93], more recent work paints a more nuanced picture[94]. Bowers et al. showed that varying acute and chronic stressors differentially alter immune function[94]. How this variable stress response is shaped based on stressor type and duration is still under investigation. It may include differential glucocorticoid receptor activation, changes in glucocorticoid receptor expression, changes in their inhibitors, changes in their downstream messengers, and alterations in metabolic function. Additionally, cytokine negative feedback to the central nervous system may be blunted through similar mechanisms after long-term stress exposure.

1.5 Impact of stress on HPA axis function

Chronic stress can lead to dysregulation of the HPA axis across species. In rodents placed in the psychosocial stress model, the visible burrow system, hierarchical relationships are created, and subordinate animals enter a chronically stressed state. In this environment, the subordinate rats experienced significant HPA hyporesponsiveness and showed decreased mRNA in the hypothalamus [95–97].

In humans, notable HPA axis alterations occur after early-life stressors. Childhood trauma blunted cortisol awakening response (CAR) in an exposure duration-dependent mannor[98]. Another study demonstrated heterogeneous HPA axis changes based on the trauma subtype[99]. Specifically, the group found that non-intentional stress increase bedtime cortisol, physical abuse quickened reactivity to an acute stressor, and emotional abuse delayed HPA axis recovery after an acute stressor. Stress-related affective disorders can lead to HPA axis dysfunction as well.

Depression, and to a lesser degree, anxiety disorders, have increased cortisol or morning cortisol levels that dexamethasone did not suppress[100,101].

1.6 Cardiovascular impact of stress

The cardiovascular system may be the most well-characterized system concerning the influence of stress. Indeed, almost 400 years ago, Sir William Harvey noticed a connection between psychological state and heart function. The eminent physician noted in 1626, "every affection of the mind that is attended with either pain or pleasure, hope or fear, is the cause of an agitation whose influence extends to the heart[102]." Not much systematic scientific progress was made regarding a psychological relationship to the heart before the 1930's when two longitudinal studies demonstrated a potential association between depression and cardiovascular disease.

For instance, in humans, the Whitehall II study found that followed participants for an average of 11 years found that the psychological stress of low job control was associated with increased coronary artery atherosclerosis[103]. Chronic stress was also related to elevated activation of fibrinogen and platelet function, a potential avenue for thrombus exacerbation[104]. This, coupled with the dysregulated inflammatory milieu mentioned in the previous section, create an environment predisposing to cardiac events[105].

In related work, job strain (the combination of lacking control over time and skill allocation, organizational decisions, and needing to work hard and quickly) was associated with coronary heart disease, elevated left ventricular mass index, atherosclerotic progression, and long-term sickness-related absences[103,106–110]. High job demands were particularly predictive of coronary heart disease. The researchers also found that factors that could alleviate stressors (e.g., social support, social network, and income) protected the cardiovascular system[111,112]. Thus,

decreased stress-buffering may provide one path by which socioeconomic status impacts cardiac health.

When stress buffering is dysfunctional, in PTSD or ACE cases, for example, individuals are at greater risk for cardiac illness, even when controlling for traditional cardiac, inflammatory, and behavior-related risk factors[113–117]. Other psychiatric conditions that alter HPA axis function, such as depression, general anxiety disorder, and panic disorder, are also associated with adverse cardiac outcomes[118–121] and risk factors[122]. Panic disorder, which often presents with chest pain, increases the likelihood of MI by as much as three- to four-fold compared to the general population[121], and phobic anxiety, identified by self-report, was associated with sudden cardiac death[123,124].

These results are mirrored by animal studies. In non-human primates, non-dominant males and socially subordinate females have elevated atherosclerotic burden[125,126]. The exact mechanism by which stress modulates cardiac event risk is still under investigation, but it is hypothesized that a combination of behavioral and biological processes are involved. As discussed above, stress can negatively influence impulse control and judgment, predisposing affected individuals to behavioral risk factors. Treatment of stress-related disorders also appears to decrease cardiac-related morbidity and mortality, possibly by ameliorating some of the aforementioned issues.

1.7 Neurobiological impact of stress

The brain perceives, interprets, and responds to social and environmental stressors. It stands at the nexus of a vast, interconnected system that allows higher-level organisms to orchestrate complex behaviors in the face of uncertain, constantly changing, and potentially

threatening situations. The brain is also the principal regulator of the HPA axis. Rather than remaining undisturbed and controlling the system from above, it is actively shaped by stress and the resultant stress response. In the CNS, glucocorticoids released during the stress response act through both genomic and nongenomic means, and like elsewhere in the body, have a U-shaped response that depends on the timing and nature of the stressors[127,128]. Glucocorticoids change gene expression through glucocorticoid receptor elements and interactions with other transcription factors[129]. They also can change excitatory and inhibitory amino acids and endocannabinoid levels through interaction with membrane-bound receptors[130–137]. Blocking either the stress-induced rise N-methyl-D-aspartate or the stress-induced rise in corticoids inhibits remodeling of dendrites[138,139]. The associated neuronal remodeling provides a flexible and resilient system that can adapt to new stressors and then recover once those stressors are alleviated. However, if the recovery is incomplete or fails, it may leave the organism vulnerable.

The brain is particularly crucial to the stress response because, in addition to controlling physiological and behavioral reactions, it resolves the difference between benign vs. threatening stimuli. It also stores and recalls that information for future decision-making.

As mentioned elsewhere in this document, glucocorticoids are critical downstream effector molecules of the stress response and have broad impact across the brain. In the dentate gyrus, a region of the hippocampus, acute stress, and glucocorticoid release seems to enhance synaptogenesis and hippocampal processing. Chronic exposure to glucocorticoids tends to hinder hippocampal synaptic plasticity, decrease spine density, diminish neurogenesis, and induce dendritic atrophy[140].

Regional sensitivity to glucocorticoids is driven by glucocorticoid receptors which are expressed highly in the cortex, extended amygdala, and hippocampus[141]. Regional differences

are also present in other neurotransmitters, and these combined differences appear to contribute to the divergent impact of chronic stress axis symptoms, e.g., heightened emotionality and impaired cognitive function[142]. Thus, the hippocampus, the amygdala, and the prefrontal cortex provide useful examples of regional differences in the stress response across brain structures.

After glucocorticoid receptors were identified in the hippocampus, the region became a focus for studying how systemic hormones could alter brain structure and function[143,144]. It became particularly relevant as evidence mounted that the hippocampus helped regulate the HPA axis[145–148]. At moderate physiologic levels, glucocorticoids and excitatory amino acids enhance hippocampal LTP and memory, while greater glucocorticoid and excitatory amino acids inhibit LTP[149,150]. Stress and glucocorticoids also enhanced LTD[151–153]. Repeated stress exposures reduced the dendritic arbor and collapsed synaptic spines through greater glucocorticoid and excitatory amino acids[139] and were also associated with decreases in the neurotrophin, brain-derived neurotrophic factor (BDNF)[154,155].

Conversely, chronic or significant stress causes expansion of the dendrites and increased spine density in the basolateral amygdala (BLA)[156], changes also demonstrated in models of PTSD and social defeate[156,157]. Chronic stress also induces c-Fos and dendritic arborization in the BNST, a finding that was reduced with the standard depression treatment, fluoxetine[158,159]. Chronic stress also increased the volume of the BNST, due at least in part to the increased arborization, both findings that could be recapitulated by chronic glucocorticoid administration[160,161]. Notably, even within the amygdala, the effects of stress can vary by region, demonstrated by the opposite effect of chronic stress on the medial amygdala[162].

Similar to the amygdala, the prefrontal cortex (PFC) shows regional specificity regarding stress and neuronal structural changes. After chronic stress, the medial PFC (mPFC) shows

decreased dendritic branching and spine density[163–166]. The orbitofrontal cortex instead shows dendritic expansion in the face of chronic stress[167].

Just as the changes above are seen in models of stress disorders, human stress-related conditions also demonstrate significant structural changes in the nervous system. Cushing's syndrome is a classic example of HPA axis dysfunction. Excess glucocorticoids, from either exogenous or endogenous sources, drive systemic changes that include hypertension, weight gain, buffalo hump, moon faces, and immunosuppression. Individuals with Cushing's disease often have exposure to the associated hypercortisolemia for months to years, providing useful insight into the impact of prolonged stress hormone exposure in humans. Starkman et al. observed a decrease in hippocampal volume in people with Cushing's disease[168], and found this decrease to be at least partially reversible with treatment[169–171]. Associated memory impairments also improved with treatment of the underlying illness[172–174].

Stress-related neuropsychiatric disorders are also associated with changes in brain structure and function. With respect to PTSD, for example, a reduced hippocampal volume may result from and be a risk factor for the illness[175,176]. Subjects with PTSD also have exaggerated amygdalar response to trauma-related cues and fear facial expressions, a response that is correlated with PTSD severity[177–180]. The opposite pattern is seen in the PFC[181,182]. Additionally, army recruits with higher amygdalar activation, who had yet to see combat, had a higher probability of stress symptoms after a traumatic encounter[183]. Combat stress was also shown to increase amygdalar and insular stress reactivity[184].

Human studies of depression demonstrate similar findings to those of PTSD[142]. Specifically, depression appeared to decrease hippocampal and PFC volumes[185,186]. Depression was also associated with changes in amygdalar activity during memory encoding[187]. Moreover,

evidence has existed since the 1970s that patients with depression have dysregulated autonomic nervous systems. Participants with depression were found to have increased levels of circulating catecholamines in plasma and urine as well as higher resting heart rates[188–191], and Veith et al. later demonstrated that these patients also displayed an increase in sympathetic nervous system activity[192].

1.8 Psychological impact of chronic stress

As noted above, many stress-related pathologies are associated with changes in brain structure and function. Stress can also alter the likelihood and prognosis for those stress-related pathologies. Posttraumatic stress disorder, for example, is by definition due to exposure to a stressful stimulus or set of stimuli. Children exposed to a stressor who also meet the criteria for acute stress disorder (ASD) are more likely to be diagnosed with PTSD later than children who are not[193]. Note that this does not necessitate a causal relationship as those who experience ASD symptoms could be less resilient, rather than the stress response making them more vulnerable. Additional research will be useful in determining causality this relationship.

However, various studies have linked childhood stressors (e.g., witnessing domestic violence, abuse, or neglect) to behaviors including depression, substance use, and suicide attempts[194–201]. A 2006 study found a relationship between the number of adverse childhood events and numerous health domains (i.e., affective, somatic, substance abuse, memory, sexual, and aggression). In each domain, a higher ACE score was correlated with an increased risk of a negative outcome[202]. Other studies, including prospective work with children who experienced abuse, also found increased psychiatric disorders in adulthood[203–205]. Further, patients with a documented history of depression were found to have significantly higher levels of C-reactive

protein, a cardiovascular risk factor, than patients with depression that did not have a history of abuse and healthy controls, indicating stress may also exacerbate mental health disorders in addition to predisposing to them[206]. This increased risk is evident for stress that occurs even as early as birth; the stress of low birth has been associated with increased risk of psychiatric illness[207].

While early forms of stress can lead to lasting negative outcomes, other more temporally proximal forms of stress are also linked with neuropsychiatric symptoms[208]. Much work has focused on employment environment, job security, and job status, and the relationship to mental health standing[209–211]. Job strain has been linked to adverse mental health outcomes[211–213]. High strain work and inadequate employment dramatically decrease mental wellbeing and increase the incidence of depression[214,215]. Similarly, job loss increased biomarkers of stress[216] and degraded mental health[217]. Notably, the decline in mental and physical health appears to be true even if job insecurity does not worsen health behaviors[218,219]. In one example from the 1980s, shipyard workers in Malmö, Sweden were evaluated during a time of economic stability and again at the shipyard's closure. Compared to stable times, the closure saw the increased participant sleep disturbances, anxiety, depression, and serum cortisol[220].

If we again turn to Cushing's disease to examine chronic HPA axis dysregulations, we find that afflicted individuals have also been described as experiencing melancholia and depressive sympotms[221]. Indeed, the literature bears out some of the neuropsychiatric symptoms initially noted by Harvey Cushing when he initially described the syndrome in 1932[222]. 54%-81% of patients with Cushing's have been found to meet the DSM criteria for major depression[223–225]. General anxiety disorder is a significant comorbidity (66% - 79%) in these patients as well[225,226].

1.9 Strategies of stress coping

The brain is the central arbiter of the stress response for reasons outlined above and critical here because it dictates the coping mechanism employed to address the stress. For any given stress, there are multiple coping strategies, and the method selected can impact the vulnerability to the stressor[227]. One animal model of stress that can induce multiple responses is fear conditioning. In fear conditioning, an aversive stimulus (e.g., shock) is paired with a cue (e.g., tone). After the cue, animals often either freeze or dart around the cage[228]. Another example is the looming disk threat. In this model, a disk above a rodent's cage expands in size and simulates a swooping predator[229]. Generally, two strategies predominate; freeze or bolt to hide in a hut. Each of these provide a good example of how the same stimulus with the same environmental stimuli can drive very different behaviors, even within the same animal.

Stress coping strategies can be categorized in several ways, one of which is active vs. passive coping[230–233]. Generally, active coping involves taking action to either 1) address the stressor directly by attacking or removing it, or 2) moving to a safer location, away from the immediate danger. In the repeated social defeat stress paradigm, one animal (the intruder) is placed in the home cage of another (resident). After a brief exploratory period, the resident attacks the intruder. When the intruder is defeated (supine position for two to three seconds), the animals are separated by a wire mesh to 30 min[234,235]. After these repeated exposures, rats segregated into subpopulations, one active coping and the other passive coping[233,236–238]. This segregation also correlated with other measures of resilience and vulnerability respectively[239,240]. In related work, preventing rats from engaging the innate active coping strategy of burying leads to increased active HPA axis activation[241]. Clinical work has demonstrated similar results, that is,

people who engage in passive coping mechanisms are more likely to develop depression than people who use active strategies[242,243].

1.10 Stress-related tests in animal models

Animal models have been critical to our ability to understand the neurobiology of stress and the stress response. Systems that analyze stress in animal models often use an approach-avoidance system to examine the conflict between opposing motivational drivers. Many of these use the natural tendency for rodents to explore and the competing preference of avoiding exposed environments. A classic example of this particular scenario is the elevated plus maze (EPM). The EPM evolved from a raised Y-shaped maze[244] into its current form (with two open arms and two closed arms), first described by Handley and Mithani[245]. Instead of using a noxious stimulus (e.g., shock, predator odor, food or water restriction, etc.), the EPM uses the conflict between the natural proclivity for enclosed dark spaces and the drive to explore. Pellow and File pharmacologically validated that higher anxiety states decrease the time spent in open arms and vice versa[246]. Like many tests of anxiety or stress, it can also be used to induce a stress reaction. In this case, restriction to the open arms, which are elevated and brightly lit, leads to an increase in both defecation and corticosterone levels[246]. Slight alterations have been implemented to try to address some of the shortcomings of the EPM. The elevated zero maze (EZM) eliminates the ambiguous center section of the EPM by forming a ring with all segments (divided into alternating quadrants) either open or closed[247]. The elevated T-maze switched to a "T" confirmation to provide a binary choice between open and closed arms while adding the capacity to investigate memory[248].

A different model capitalizes on the discovery that a state of increased stress decreases food intake[249]. In 1988, Bondoff et al. published a study validating the novelty-suppressed feeding test (NSFT)[250]. NSFT involves food restricting an animal for 24 hours and then placing them in a brightly lit open field with chow at the center. The competing hunger and aversion to open spaces drive the conflict between food approach and avoidance. Latency to the first bite is measured as a measure of anxiety. One potential caveat to be aware of with this model is the possibility of an interaction between changes in food-seeking behavior and pharmacological intervention.

The above models place the animals in a scenario which the environmental stressors tend to be relatively benign. Another option is to expose the animals to more extreme psychological or physical stressors. One behavioral paradigm that has been of recent controversy is the forced swim test[251]. Introduced by Porsolt et al. in 1977, the forced swim test places the rodents in inescapable danger[252,253]. In the forced swim test, rodents are placed in a container of water that has walls too high for them to climb. In this case, the inescapable threat of drowning and the resultant propensity to swim or float to avoid drowning are used as behavioral readouts.

Long used as a model of "depression-like behavior" [254–256], due to antidepressants' ability to shift coping strategies towards active vs. passive, it has come under scrutiny for lacking face and construct validity for depression[257]. Regardless, it does appear to be a useful screened for candidate antidipressants[258,259]. Further, little doubt exists that this is useful as a stressor and to test stress coping. Repeated exposure to the forced swim test increased HPA axis activation and other markers of stress. The test is also sensitive to early life stress, chronic stress in adulthood, and glucocorticoid administration[254–256,260,261].

Another stress paradigm that can be used both as a stressor and to evaluate the animal's state is exposure to a predator[262]. This can be accomplished in many ways, the most common of which is predator odor, often in the form of the urine of a predator[263,264]. When experimenters expose a rodent to predator odor, the animal reacts defensively and exhibits avoidance behaviors. Even stronger reactions can be induced if the exposure is to the live predator. When exposed to predator odor, non-defensive actions like grooming decrease, and other vigilance behaviors increase[265]. The endocrine system also responds strongly to predator odors. After exposure, testosterone levels decrease and stress hormones (ACTH and corticosteroid) increase, a result that is especially strong with 2,5-dihydro-2,4,5-trimethylthiazoline (TMT)[266–270]. This exposure can also induce lasting changes in other behavioral tests of anxiety[271–273].

Immobilization stress, or restraint stress, is another commonly employed stressor that has been used for over half a century[274]. Animals are placed in an inescapable chamber (with holes for air exchange) in which their movement is restricted for a set amount of time, often between 30 and 60 min[275–277]. Restraint stress can be applied either acutely or chronically. It has even been repeated for 300 exposures[274]. Restraint stress shows activation in a variety of stress-relevant brain areas[276]. Further, struggling or escape behavior during restraint can be used as a readout of stress status and can be pharmacologically modulated[276]. Like other stressors, restraint stress exposure leads to stress phenotypes on other tests[278]. Chronic exposure has also been shown to induce synaptic remodeling and region-specific dendritic arborization ordebranching[156,164,166,279–283].

Many other stress paradigms not mentioned here exist. Additionally, scientists are likely to create new variants, refine those discussed above. These animal models of stress have allowed us to begin to untangle the neurocircuitry governing stress and the stress response.

1.11 The BNST structure, function, and the stress response

Before the 1900s, there was no name for the region that sits at the anterior end of the stria terminalis. The white matter structure, the stria terminalis, derives its name from Latin. Stria means “a grove” in Latin and referred explicitly to the flutes of a column[11]. In both cases, the columns and the white matter tract, a series of grooves create a striped or striated appearance.

Cajal first described the grey matter that surrounds the stria terminalis as the “interstitial nucleus”[284]. The term “bed nucleus of the stria terminalis” was not used until Johnston coined it in 1923[285]. These were more broad definitions than today’s, which is located in the rostromedial portion of Johnston’s BNST[286]. Today’s BNST has between 12 and 18 subnuclei, sits ventral to the lateral ventricles, and surrounds the anterior commissure (Fig. 1.3)[287–292]. It is positioned medial to the striatum, dorsal to the hypothalamus, and rostral to the thalamus.

The BNST is often described as part of the macrostructure known as the extended amygdala. The importance of the extended amygdalar components in fear, anxiety, affect, the stress response, and neuropsychopathologies have been discussed in detail[160,161,287,293,294]. The term “extended amygdala” originated in Alheid and Heimer's work and is used to describe the centromedial amygdala, the bed nucleus of the stria terminalis, the nucleus accumbens shell, and sublenticular substantia innominata as combined a macrostructure[295,296]. This terminology was driven mainly by the substantial innervation of these structures by the amygdala and their similarity to amygdalar descending projections. While the term “extended amygdala” is useful with respect to general connectivity and related functionality, it is worth noting that the BNST is not truly an extension of the amygdala as the name might imply[297]. Instead, the BNST appears to

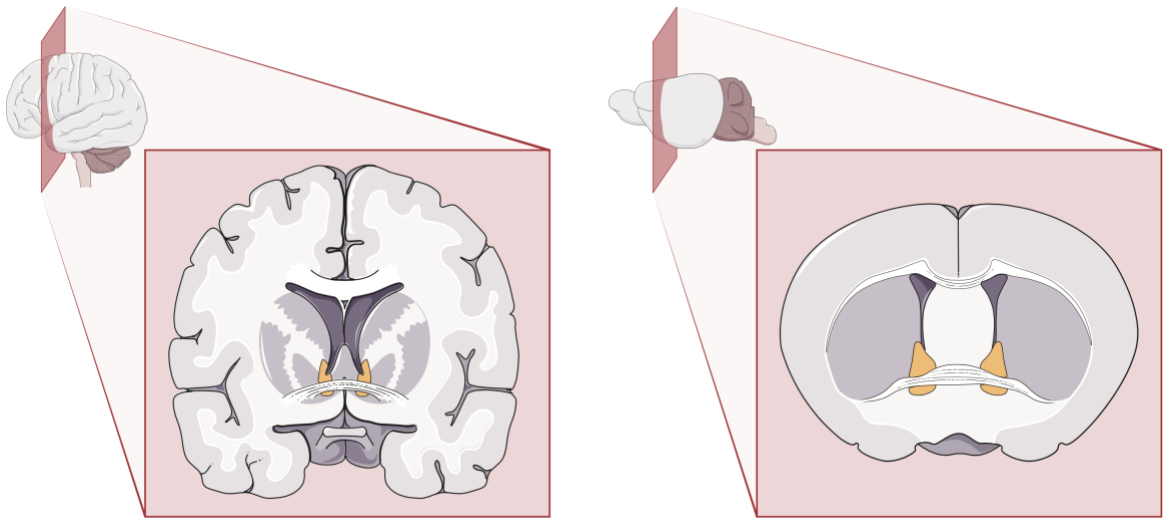

Figure 1.3: Illustration of the BNST in human and mouse brains.

Brains are cut in coronal view at the location of the red plane. The human brain is on the left, and the mouse brain is on the right. The bed nucleus of the stria terminalis in each brain is highlighted in yellow. (Adapted from Servier Medical Art).

arise from the pallidal ridge[298]. Nor do the downstream projections from the BNST completely overlap with those of other amygdalar structures[299,300].

That being said, the function of the BNST and its connectivity does overlap with other regions involved in stress and reward. Further, while limbic and cortical areas modulate HPA axis activity, many do not directly project to the paraventricular nucleus of the hypothalamus. However, these structures do project to various parts of the BNST, regions that directly communicate with the PVN. Given this key location in the network, it plays an essential role in integrating cortical and subcortical information used to inform and shape affective state and the response to stressors. The structure's heterogeneity and diverse subregions are critical for its ability to differentially modulate stress neurocircuitry. (The current nomenclature for the various divisions and subregions of the rodent BNST are found in Table 1.1.) The BNST's role in regulating the HPA axis is a good example of this diversity. The dorsomedial nucleus (BNSTdm) of the anterior division BNST (aBNST) activates the HPA axis while the posterior BNST (pBNST) inhibits it[301,302]. Evidence suggests that the different actions of these regions may be driven by intra-BNST circuitry[288,301,303,304].

1.11.1 Anterior division of the BNST

Beyond activation of the HPA axis, the anterior division of the BNST also plays a role in a variety of social stress functions and stress-induced reward-seeking [305–310]. As we focus on the subregions of the anterior BNST, we find further separation of duties. A variety of studies implicate the anterolateral BNST in processing sensory stimuli, potential threats, social and mating behavior, and noxious stimuli or pain, while the more medial BNSTam, controls fluid homeostasis through projections to Barrington's nucleus and the HPA axis through a high

Abbreviation	Region name
aBNST	Anterior BNST
dBNST	Dorsal BNST
BNSTov	Oval nucleus of the BNST
BNSTjx	Juxtacapsular nucleus of the BNST
BNSTal	Anterolateral nucleus of the BNST
BNSTam	Anteromedial nucleus of the BNST
vBNST	Ventral BNST
BNSTfu	Fusiform nucleus of the BNST
BNSTmg	Magnocellular nucleus of the BNST
BNSTrh	Rhomboid nucleus of the BNST
BNSTdm	Dorsomedial nucleus of the BNST
BNSTv	Ventral nucleus of the BNST

Abbreviation	Region name
pBNST	Posterior BNST
BNSTpr	Principle nucleus of the BNST
BNSTif	Interfascicular nucleus of the BNST
BNSTtr	Transverse nucleus

Table 1.1: Overview of rodent BNST divisions and subregion organization.

Major divisions are denoted with letters preceding "BNST" well subregions have letters following "BNST." Structures are nested by increasingly light colors. Blue indicates anterior division structures, and yellow indicates posterior division structure. Note: the BNSTov, BNSTjx, and BNSTal are collectively known as the dorsolateral (dlBNST).

density of efferents to the PVN[309,311–316]. The oval nucleus, one of the most dorsal segments of the aBNST and located immediately dorsal to the BNSTal, appears to process negative valence and engages anxiety-like states[317]. The fusiform, juxtacapsular, and rhomboid nuclei await in-depth functional study[287].

Noradrenergic afferents densely innervate the vBNST, more than any other region in the CNS, implicating it as a player in arousal[310,318,319]. Stimulation of the fusiform nucleus (BNSTfu) specifically has been shown to control cardiovascular output through projections to the nucleus of the solitary tract (NTS)[320]. Norepinephrine is released in response to various stressors (e.g., TMT, restraint stress, and foot-shock) and reward anticipaiotn[303,320,321]. Evidence also exists that the vBNST coordinates the inhibitory signals to the HPA axis and alters passive coping strategies via GABAergic input to the periaqueductal gray (PAG) during inescapable stressors[322]. The BNSTdm, a component of the vBNST, has the most extensive projections to the hypothalamus and extensively innervates PVN parvocellular and magnocellular neurons[314]. BNSTdm lesions also attenuate the HPA axis's activation, and chronic unpredictable stress increases fos expression in the region[301,323].

1.11.2 Posterior division of the BNST

The posterior BNST (pBNST) is highly sexually dimorphic and expresses alpha and beta estrogen receptors and androgen[324,325]. Projections for the principle BNST (BNSTp), a subregion of the pBNST, are concentrated in regions of the hypothalamus and lateral septum shown to play a role in defensive behaviors and reproduction[288,326]. The BNSTp has also been hypothesized to inhibit other BNST regions (e.g., BNSTdm and magnocellular BNST (BNSTmg)) that are upstream to the HPA axis, and BNSTp stimulation inhibits ACTH release and the corticosterone

response[287,301]. Other pBNST regions, e.g., the transverse nucleus, also innervates stress-regulating cells in the hypothalamus[288]. Ultimately the intra- and extra-BNST signaling from pBNST nuclei place this portion of the BNST at the center of regulating many components of the stress response.

1.11.3 The heterogeneous makeup of the BNST

The BNST contains roughly 90% GABAergic neurons and 10% glutamatergic neurons, and thus at first blush, it may seem like a homogeneous region. Rest assured, it is not. The BNST is extraordinarily heterogeneous and is composed of a vast array of different cell types and varied projections. Many of the functions of the BNST are associated with varying populations of neuropeptides and proteins. Some of the most commonly examined cell types (defined by their expression of a protein or neuropeptide) in the BNST are arginine vasopressin, corticotropin-releasing factor, cholecystokinin, dynorphin, enkephalin, nociception, neuropeptide Y, neurotensin, oxytocin, protein kinase C delta, somatostatin (Fig. 1.4)[159,287,291,327–332].

Many of these markers are neuropeptides. Rather than only being a method for dividing cells into functional groups, neuropeptides themselves perform necessary signaling. Therefore, we will begin with a brief discussion of what neuropeptides are and how they function. This family of peptides and their respective receptors are broadly and differentially distributed throughout the nervous system. Many if not most CNS neurons contain neuropeptides, molecules made of roughly 9-40+ amino acids[328]. In the BNST, more than one neuropeptide is often co-expressed in the same cell[159,331,333]. With respect to fast amino acid neurotransmission (e.g., GABA and Glutamate), which occurs on the order of milliseconds, neuropeptide communication is comparatively slower and can be on the order of seconds, minutes, or even hours[334]. Another major difference between fast neurotransmitters and neuropeptides is their release locations. The

fast neurotransmitters are released at the synapse while neuropeptide release bears no such restriction[335,336].

In many cases, the neuronal processes that contain a given peptide and those that express the homologous receptor are in relatively close proximity to one another. However, some significant mismatches exist between receptor population location and the location of the neuropeptide release sites, indicating some neuropeptide signaling can extend great distances to modulate remote brain regions[336,337]. For many neuropeptides, though, it seems likely that much of their signaling occurs via relatively local diffusion[338]. Once released, the neuropeptides diffuse and bind to their respective receptors, often a seven-transmembrane G-protein coupled receptor[328].

Arginine vasopressin (AVP) tends to be expressed basally at higher levels in males than female[339,340]. It is primarily expressed in the pBNST with some expression in the BNSTam[341–344]. The specific function of AVP appears to be both stress exposure and sex-dependent. Infusion of AVP into the BNST of aggressive male mice or female mice during maternal care decreased aggression[345,346], but the opposite effect, an increase in aggression, was found with AVP release elsewhere in the brain[340]. During the resident intruder test, aggression was positively correlated with the number of AVP positive cells in males, but this relationship collapsed if the mice were previously stressed[347].

Corticotropin-releasing factor (CRF) expressing cells have been found throughout the BNST with a preference towards the lateral BNST, are diffusely distributed in both sexes of mice, and have some sex-specific increases in BNSTal and BNSTov of females[291,348–352]. Numerous stressors have been shown to increase CRF expression in the BNST, including novel

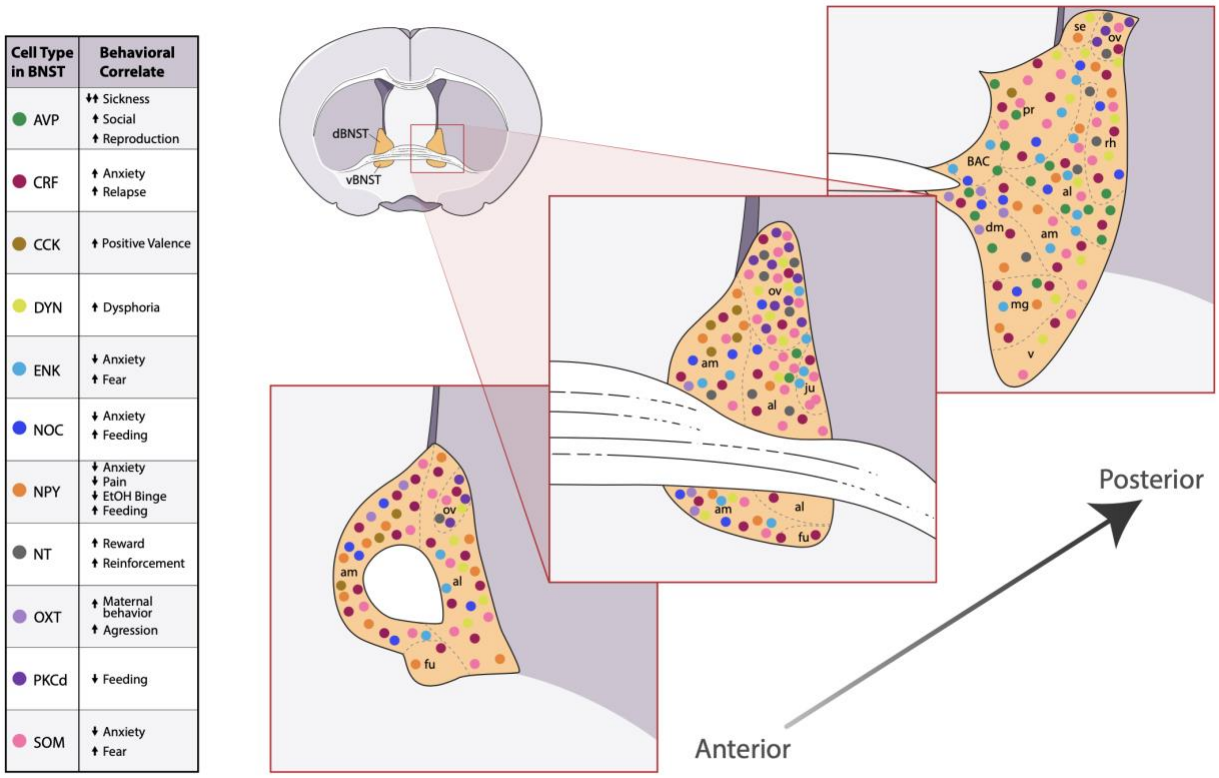

Figure 1.4: Diagram of cell-type distribution in the BNST.

Three planes of the BNST are shown. Planes progress from anterior to posterior when moving from left to right. Cell types included: AVP = arginine vasopressin, CRF = corticotropin releasing factor, CCK = cholecystokinin, DYN = dynorphin, ENK = enkephalin, NOC = nociception, NPY = neuropeptide Y, NT = neurotensin, OXT = oxytocin, PKCδ = protein kinase C delta, SOM = somatostatin.

environments[353] and social defeat stress[354]. Likewise, restraint stress increases BNST CRF cell c-Fos[159]. Global administration of CRF enhances the response to a stressor, as demonstrated by intraventricular CRF infusion[355]. HPA axis signaling can increase CRF mRNA in the BNST[356]. CRF signaling in the BNST specifically also plays a role in stress and anxiety[357–360]. This is true for various stress paradigms, including novel environments, social anxiety, stress, and drug withdrawal[359,361–365]. Depending on the CRF receptor that is activated, different outcomes can occur. CRF receptor 1 (CRFR1) appears to elevate stress, anxiety, and pain, while the opposite is true for CRF receptor 2 (CRFR2)[363]. Stimulation of CRF-producing cells in the BNST with optogenetics or chemogenetics appears to be aversive[366]. (For further reading, see: [320,367])

Cholecystokinin (CCK) cells are primarily located in the BNSTam with more robust expression dorsally and less ventrally[366]. Some expression is also present in the BNSTal. Desai et al. showed that intraventricular administration of CCK reduced social interaction and increased immobile time during the FST, leading the authors to conclude brain-wide CCK exposure to be anxiogenic[368]. Giardino et al. found different results when manipulating the BNST. Specifically they found that activation of BNST CCK neurons with either optogenetics or Gq-designer receptors activated exclusively by designer drugs (DREADs) was positively valanced[366].

Dynorphin and enkephalin, members of the opioid peptide family, are expressed throughout the anterior or posterior BNST. Work using in situ hybridization demonstrated pre-prodynorphin mRNA to be particularly abundant in the BNSTov, BNSTfu, BNSTal, and BNSTrh with less expression in BNSTif and BNSTam[369]. Cre driver mice also exhibit numerous cells in the dlBNST that express dynorphin[370]. Dynorphin has been hypothesized to play a

crucial role in stress and anxiety[371]. After the FST, animals showed an increase in prodynorphin mRNA[372]. Work also suggests that local BNST dynorphin release can modulate anxiety-related inputs afferents[370]. When examining enkephalin, in situ hybridization showed the expression in the BNSTal, BNSTov, BNSTjx, BNSTam, and broadly throughout the pBNST[369,373]. Enkephalin cells in the BNST were robustly activated by interleukin-1B, a pro-inflammatory cytokine[373].

Neuropeptide Y (NPY) is an excellent example of the regional specificity of neuropeptide expression in the BNST. As shown above, many neuropeptides are expressed in the BNSTov. For NPY, it appears to be largely excluded from the BNSTov, even though some cell bodies and many fibers are present throughout much of the BNST[374,375]. The densest NPY labeling is in the vBNST with less in the dBNST and particular sparsity in the BNSTjx. NPY is generally stress-protective[376–378]. In the BNST, NPY has been shown to have opposing modulatory effects on GABAergic transmission compared to CRF [334]. This signaling through the NPY receptor 2 (NPYR2) is degraded by restraint stress in susceptible mice[374].

Oxytocin is a small neuropeptide of only nine amino acids. Its name, oxytocin, means "quick birth" in Greek, a function of Dale's initial discovery in1906 that it caused uterine contractions[379]. The BNST cells that produce oxytocin can be found in the vBNST, BNSTdm, BNSTam, and BNSTmg[308,380]. Much of the work researching oxytocin has focused on social behavior and parenting functions. Research on oxytocin in the BNST remains relatively open as many questions are yet unanswered. In one study, oxytocin infused into the BNST decreased maternal aggression towards an intruder. Other work has shown that oxytocin infusion into the BNST improves male social recognition[305], but reduces social approach and increases social vigilance in both sexes[308]. This may indicate a role for these extra-hypothalamic oxytocin-producing cells in increasing the salience of positive and negative social contexts.

Protein kinase C delta (PKCδ) is an outlier in this group as it is not a neuropeptide. It is, however, often used to demarcate a specific subset of cells in the BNST[159,330,331]. PKCδ is expressed in the BNSTov[331,381]. BNST PKCδ cells have been shown to be activated during food approach in the NSFT[382]. They can also bidirectionally control feeding[304].

Somatostatin cells, like PKCδ neurons, are most concentrated in the BNSTov[350,383]. Other regions (i.e., dBNST, vBNST, and pBNST) have neurons that express somatostatin, but at levels far less than the oval. Recently it was shown that optogenetic stimulation of BNST somatostatin neurons that project to the nucleus accumbens shell is anxiolytic and chronic stress attenuates signaling through this pathway[384]. However, it does appear that this is a complex system with potentially divergent behavioral outcomes as chemogenetic stimulation of BNST somatostatin cells also enhance fear memory consolidation[350].

1.11.4 BNST circuitry

As seen in the previous section, the BNST is a highly nuanced region with many cell types, a pattern that also holds true for its afferent and efferent networks. Understanding this connectivity is necessary when working to understand the BNST function. In rodents, the dorsal bundle (stria terminalis) and the ventral bundle (ansa peduncularis) are avenues by which the BNST is connected to other regions. First, I will discuss components of the afferent network and follow that with a discussion of efferent network targets (for an overview, see Fig. 1.5).

Glutamatergic afferents arise in cortical and subcortical regions across the brain. Cortical glutamatergic inputs can be found in the PFC (i.e., orbital, infralimbic, and prelimbic cortices), insula, entorhinal cortex, and basolateral amygdala[300,385–388]. Non-cortical regions also send

glutamatergic afferents to the BNST and include the ventral subiculum of the hippocampus, paraventricular thalamus, lateral hypothalamus, and the parabrachial nucleus[289,386,389–391].

The densest GABAergic input to the BNST is the central nucleus of the amygdala (CeA)[391,392]. Other regions that also contribute to the GABAergic afferent network are the medial amygdala (MeA), lateral septum, NAcc shell, medial preoptic area, anterior hypothalamus, PVN, substantia innominata, and zona inserta[391].

As previously noted, the neuropeptides in the BNST are critical for its diverse functionality. This also appears to be the case for external inputs of neuropeptides. One of the most studied neuropeptides in the BNST is CRF, and the predominant external CRF input is cells in the CeA[392,393]. Dynorphin neurons from the CeA also project to the BNST from the CeA[394]. NPY is released via an afferent from the arcuate nucleus of the hypothalamus[395,396].

Multiple midbrain nuclei send monoamines to the BNST. Dopamine and norepinephrine fiber distributions are inverted from one another, with dopamine most dense dorsally and norepinephrine most dense ventrally. Dopamine is sent from the PAG and the ventral tegmental area (VTA)[397,398] and diffusely innervates the dlBNST with a more substantial presence in the BNSTjx and BNSTov[319,397–399]. Noradrenergic fibers blanket the vBNST in one of the highest concentrations in the brain[319,397,400,401]. Stimulation of the dorsal and ventral bundles cause norepinephrine to be released in the BNST, a phenomena demonstrated through fast-scan cyclic voltamitry[402]. The cell bodies giving rise to these fibers appear to be located in the noradrenergic cell group A1[403–406], A2 (nucleus tractus solitarius (NTS))[406], and only very lightly present in the locus coeruleus[403]. Serotonergic neurons that terminate in the BNST are found in the caudal portion of the dorsal raphe[319,407].

Mapping the BNST efferents has been ongoing for decades and as technology has evolved, so too has our understanding of the outflowing networks from the BNST[287]. The BNST projects broadly to downstream regions that include the CeA, lateral hypothalamus, paraventricular, PBN, VTA, PAG, and substantia nigra.

The hypothalamus receives significant input from BNST, and the connection with the PVN is essential to the stress response[408]. These connections are mostly GABAergic (with sparse glutamatergic and CRF populations also identified)[288,314,390,409,410]. The BNST also sends two distinct pathways, CRF and CCK, to the lateral hypothalamus that each responds differently to stress[366,411]. Both the dBNST and vBNST project to the VTA, but the vBNST is stronger[289,412]. The projections to the VTA, a significant collection of dopamine neurons, from the BNST are mostly GABAergic, but some glutamatergic cells are present[413]. These two cell types seem to be activated by different stimuli and have opposing stress-related functions[413,414]. Some of the projections to the VTA are also CRF positive[415]. The BNST also sends a reciprocal projection to the PAG[300]. This output is largely from the BNSTov CRF cells. Parabrachial-directed projections come from cells found throughout the BNST, particularly cells containing somatostatin, neurotensin, or CRF the dlBNST[292].

1.12 The insular cortex

As noted above, the insula is one of the key brain structures that sends projections to the BNST[385,416]. The German psychiatrist Johann Christian Reil first described the region now known as the insula ("island" in Latin) in 1796[417]. More than half a century later, in 1858, the structure was dubbed the "Island of Reil" in the first edition of *Anatomy: Descriptive and Surgical*, a publication that would become renowned Gray's Anatomy[418].

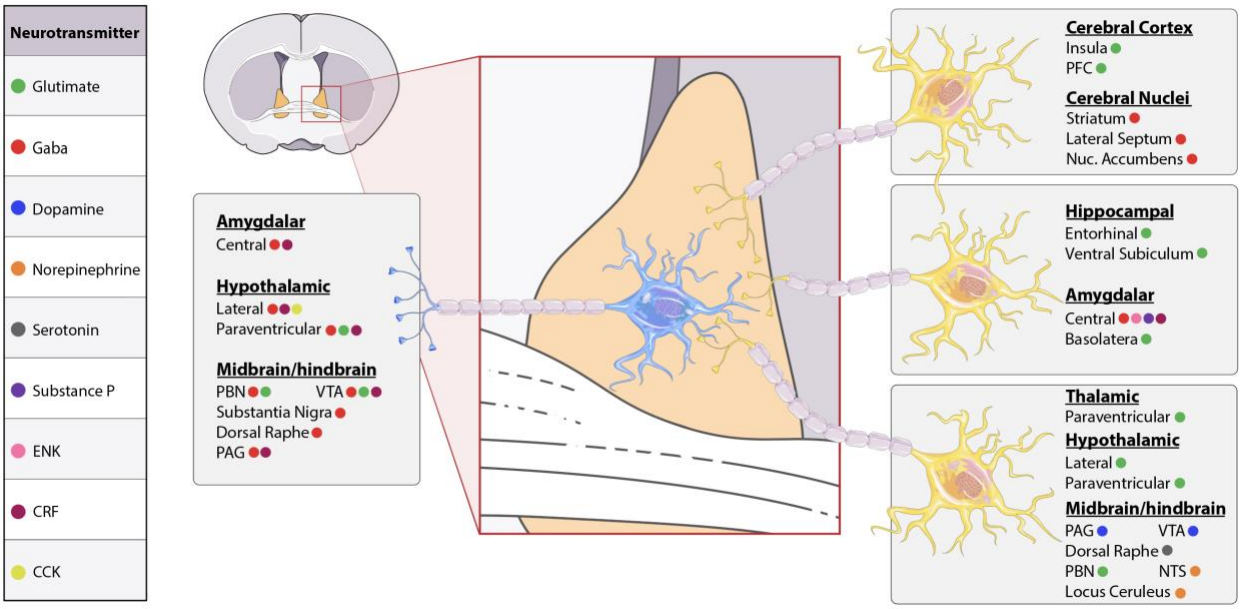

Figure 1.5: Diagram of inputs and outputs from the BNST.

Yellow neurons represent regions projecting to the BNST (BNST afferents) with specific regions identified in boxes on the right. Blue neuron represents regions receiving projections from the BNST (BNST efferents). Associated neurotransmitters are demarcated by colored dots next to each regional input. (Adapted from Servier Medical Art)

Compared to other primates, the human insula is structurally distinct but not significantly larger than what would be predicted by our size[419,420]. In lissencephalic species (e.g., mice and rats), the insula is located laterally on the brain's surface. In gyrencephalic species like humans, the insula is also located laterally, but rather than being located on the surface, it is found within the Sylvian fissure, deep to the temporal and frontal lobes (Fig. 1.6).

The insula can be divided in several ways. Commonly, it is divided into three regions, (anterior, middle, and posterior) based on the cytoarchitecture (agranular, dysgranular, and granular) of layers II and IV[421]. This cytoarchitectural change is smooth, thus drawing exact lines can be challenging. The distribution of granular, disgranular, and agranular varies by species, but usually, the posterodorsal insula is dominated by granular tissue that transitions to dysgranular followed by agranular when moving towards the anteroventral insula[422]. It can also be separated into anterior and posterior divisions via a ventral to dorsal line (along the middle cerebral artery in mice and the central insular sulcus in humans). The insula is hypothesized to process information in a posterior to anterior flow that travels from granular to agranular insula[423,424]. Through this process, the complexity of integration is believed to increase as the signal travels forward.

The insular cortex integrates multimodal sensory information. It forms a broad array of connections with both cortical and subcortical structures[423,425–429]. It also has topographically specialized regions for different sensory modalities (e.g., auditory, visceral, gustatory, and somatosensory)[422]. Unlike primary sensory cortical areas, these substructures not only process their respective sensory inputs but are also heavily innervated by cross-modal fibers. Thus, these regions are thought to be important contributors to multimodal integration.

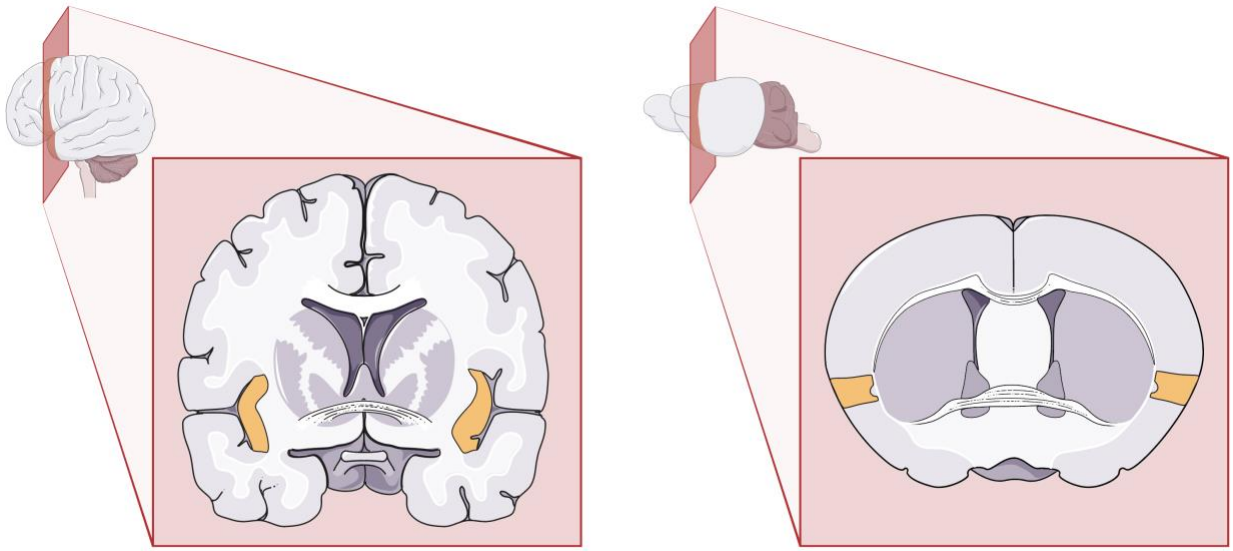

Figure 1.6: Illustration of the insula in human and mouse brains.

Brains are cut in coronal view at the location of the red plane. Human brain is on the left, and mouse brain is on the right. Insula in each brain is highlighted in yellow. (Adapted from Servier Medical Art).

The insula's most widely cited role may be integrating external sensory information with internal bodily sensory or state information[422,430]. Studies have also demonstrated insular participation in emotional regulation[431], empathy, and physical and emotional awareness[432,433]. Work in animal models has implicated insular participation in learning and memory[434,435], social behavior[436], malaise[437], drug craving[437], aversive state[438,439], and valence[440].

Anatomical dissection of the insula demonstrates broad efferent and afferent connectivity to stress-related brain regions in addition to extensive intra-insular connectivity. Cortical areas connect to the insula bidirectionally, but many pathways to or from subcortical regions are unidirectional[429]. Reciprocal connections to frontal brain structures include the mPFC, anterior cingulate, and orbitofrontal cortices. Beyond frontal and sensory regions, the insula is heavily interconnected with the limbic system. For example, afferents from the BLA project to the granular and dysgranular parts of the insula, and one of the densest insular efferents returns to the BLA, central, and lateral amygdalar nuclei[438]. Significant outputs also include the entorhinal cortices, nucleus accumbens, and the mediodorsal nucleus of the thalamus. Recent work by Gerhlach et al. demonstrated that the anterior insula has a distinct projection pattern when compared to the posterior and mid insula (which have similar inputs and outputs to one another)[429]. Notably, this work confirms a unidirectional pathway from the insula to the BNST. This innervation is preferential to the lateral BNST, and this pathway can modulate negative affect phenotypes in mice[385].

Gerhlach et al. also demonstrated connectivity between the insula and motor cortices, a relevant connection for the remainder of this thesis[429]. While other collateralized motor outputs, particularly to sensory areas, have been studied, what this insular afferent from motor cortex

does, and the information it carries have yet to be determined. We will propose one potential role, that of "motor efference copy," in the succeeding sections.

1.13 Motor Efference Copy – why we can't tickle ourselves

How does the central nervous system predict and account for the sensory stimuli generated by our actions? One theory, termed "efference copy," states that our brains predict the sensory feedback that a given action will cause[441,442]. This prediction can then inform relevant brain regions of upcoming self-generated signals, changing the neuronal response properties. Using audio stimuli as an example, participants have suppressed neuronal response to their own self-generated speech compared to a recording of the same speech[443–446]. It is hypothesized that incoming sensory signals are matched to motor signals, and those motor signals can partially cancel the self-generated sensory stimuli[447–449]. This suppression goes away if the motor and auditory signals are perturbed so that they no longer match[450–452]. Suppression via motor efference copy has been demonstrated in a variety of sensory systems and species[453–455].

Intended motor action does not always equate to a congruent motor outcome, thus a question of which of these, predicted motor action or actual motor action, motor efference copy response represents remained. In work published in 2013, Niziolek et al. provided evidence that at least in some cases, it is the intended or predicted motor action that is encoded as motor efference copy. In this case, if the actual outcome varied from the expected result, there was a signal mismatch that prevented the efference copy from fully canceling the self-generated stimuli. Thus, as the action outcome separated further from the intended result, sensory stimuli also increased. The group hypothesized that this could be a mechanism by which the CNS can identify a discrepancy between intent vs. outcome and perform error correction.

How does this prevent self-tickling? The CNS suppresses reafferent stimuli, or sensory stimuli generated by movement commands, in order to increase more relevant signals. In self-tickling, the stimuli that would normally tickle aligns with the motor efference copy, and therefore, cancelation occurs. This is true even if a system (e.g., a robotic interface) is used to physically distance the participant from the tickling action. However, the participant-controlled robot introduces a time delay between motor command and tickling, the sensation of being ticklish returns. As the time delay is increased, so too does the tickling sensation[456].

1.14 A pathway for regulation of affective circuitry by motor efference copy

As noted, organisms must respond to stress to adapt and survive. How this stress engages circuits in the brain and how it can change subsequent behavior and affect is an active research area. In many instances, the same context or threat can have a very different behavioral response. We also know that the strategy employed to combat a stressor can lead to lasting changes in affective state; consequently, understanding the circuitry involved at this behavioral divergence could provide valuable insight into how stress impacts the brain and may open new avenues for inquiry and intervention.

This thesis's remainder will investigate the relationship between stress and the BNST, insula, and motor cortex. While the insula and BNST have been explored in various stress paradigms, to our knowledge, their activity has not been thoroughly dissected at the onset of an active behavioral response to a stressor. The BNST's role in avoidance behavior[366], coupled with evidence of afferent pathways modulating passive coping[457], makes for an attractive candidate node in stress response signaling. As stated above, the BNST shares a dense connection with the insula, and this projection has been implicated in negative affect[385]. That, paired with the insula's

role in integrating internal and external stimuli with affective information, led us to hypothesize that it could also be engaged at this time. Finally, an active physical response to a stressor necessarily engages the motor system. Therefore, we aimed to explore the potential of motor contributions to this circuit and to evaluate if they were recruited by the response to a stressor.

Chapter 2

Delineation of an Insula-BNST Circuit Engaged by Struggling Behavior that Regulates Avoidance

2.1 Introduction

The response to stress is critical to every organism's capacity to adapt and survive. An appropriate stress response shifts metabolic resources towards critical systems involved in threat perception and the subsequent fight-or-flight response. *Active stress coping* relies on an individual's resources to escape a stressor, while *passive stress coping* relies on external factors to end the stressor[458]. In humans, active coping is thought to be a crucial component of resilience[458]. Evidence also exists in animals that active coping can change the behavioral and physiological response to a stressor[233]. The antecedent effects of stress on neuronal activity in many brain regions and the real-time effects of stress in the paraventricular nucleus have been examined[15,459,460]; however, the circuits that participate in the real-time reporting of selected active stress coping strategies have not been determined.

Integration of active stress coping activity into a maintained stress response necessarily entails coordination of interoceptive and stress-axis circuitry. The insula is an ideal candidate, given its role in both interoception and affect[422]. Moreover, the insula shares dense interconnections with stress-related regions such as the bed nucleus of the stria terminalis (BST, BNST), which plays a major role in modulating the hypothalamic-pituitary-adrenal (HPA) axis and has been implicated in passive stress-coping behavior[457]. In addition, recent studies have indicated that optogenetic stimulation of the posterior insula produces avoidance-related

behaviors[438], and given the BNST's role in avoidance behavior[366], an insula-BNST circuit could also play an integral role in active escape behavior during a stressor.

In many stress models, animals actively cope through physical motor activity. Physical activity can regulate multiple aspects of central nervous system (CNS) function[461]. Despite posited relationships between physical activity and affective state, functional paths between executive motor regions and forebrain structures encoding this relationship have not been clearly defined. Moreover, how, or if, these functional motor pathways mediate stress responses and coordinate affective state remains unclear.

In this study, we elucidated a mid-insula:BNST^{CRF} neuronal circuit (insula$^{\rightarrow BNST}$) that reports struggling behavior during restraint stress, a potential active coping response, and show this circuit regulates subsequent affective behavior. Further, we demonstrate that the size of the calcium transient in this pathway correlates with the duration of physical struggle, and that this correlation degrades with habituation to a homotypic stressor. While the fidelity between insula$^{\rightarrow BNST}$ calcium transient and physical struggles decayed during stress habituation, insular glutamate transient-physical activity fidelity did not, suggesting that habituation may occur downstream of insular afferents. We performed unbiased retrograde and anterograde whole-brain mapping of neuronal connections to determine the afferent network for insula$^{\rightarrow BNST}$ neurons. In doing so, we uncovered a surprisingly large input from executive motor cortical regions and demonstrated that activity in these insula-projecting motor cortex neurons is time-locked to- and precedes- the onset of the restraint stress struggle events and insula$^{\rightarrow BNST}$ activity.

2.2 Results

2.2.1 BNST neurons are activated at the onset of struggling bouts during restraint stress.

We investigated BNST neuronal activity during acute restraint stress. Restraint stress is a widely used stressor in rodents and a pharmacologically-validated model for inducing negative affect[276] and engaging BNST signaling[462]. During restraint stress, rodents engage in periodic physical struggle events (i.e., escape behavior) that are thought to underlie active stress coping[276,463]. Compounds known to increase anxiogenic behavior in rodents, such as the anxiogenic cannabinoid 1 (CB_1) receptor antagonist rimonabant, significantly increase this struggling behavior and also elevate the expression of the immediate-early gene *fos* in the BNST[276], suggesting a link between struggling behavior and increased BNST activity. We engineered a custom restraint stress apparatus (RESTRAINT, **RE**cording **S**ignal **TR**ansients **A**ccessible **IN** a **T**ube) to enable concurrent behavior and fiber photometry recordings (Fig. 2.1a, Fig. 2.2a-e). This simultaneous recording permitted the direct comparison of time-locked active struggling behavior to calcium transients measured in the BNST (Fig. 2.1b-d). Consistent with previous *fos* data, BNST calcium transients tightly aligned with struggling bout onset (Fig. 2.1e,f), while offsetting the behavioral alignment by +10 sec eliminated this association (Fig. 2.2f,g). Next, to increase the throughput and reproducibility of struggling bout analysis, we implemented computer vision-based behavioral scoring using DeepLabCut (DLC)[464,465] (Fig. 2.1g,h). We recorded behavior during restraint stress from 136 trials of 36 mice used in this study, analyzed 60,456 total movement bouts, and categorized struggle types into either head only, tail only, or a combination of head and tail movements (full body movements). Head only movements were more frequent than tail only and full body (Fig. 2.1i). However, the cumulative time spent

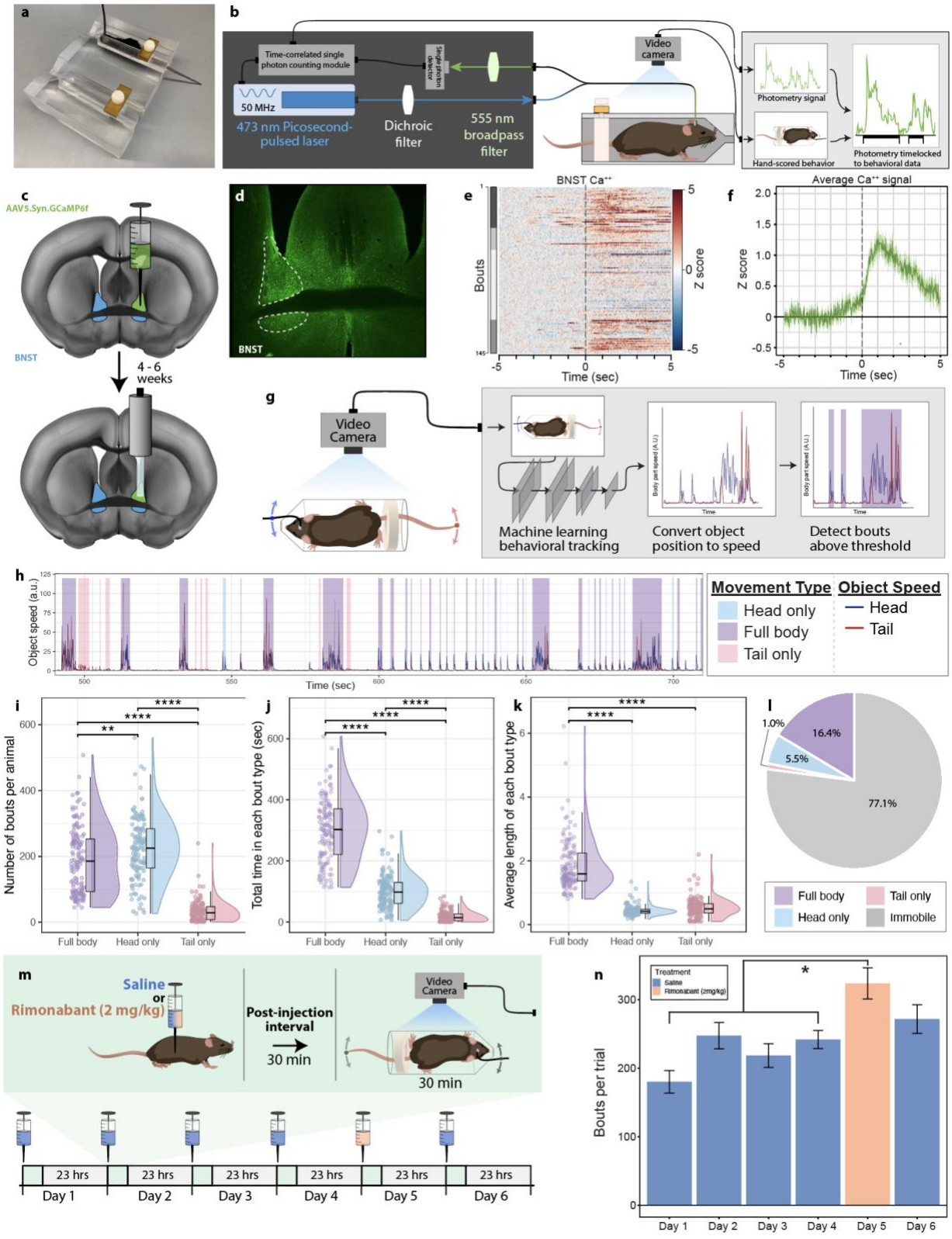
a
b
Time-correlated single photon counting module
Single-photon detector
50 MHz
473 nm Picosecond-pulsed laser
Dichroic filter
555 nm broadpass filter
Video camera
Photometry signal
Hand-scored behavior
Photometry timelocked to behavioral data
c
AAV5.Syn.GCaMP6f
BNST
4 - 6 weeks
d
BNST
e
BNST Ca++
Bouts
Z score
Time (sec)
f
Average Ca++ signal
Z score
Time (sec)
g
Video Camera
Machine learning behavioral tracking
Convert object position to speed
Detect bouts above threshold
h
Object speed (a.u.)
Time (sec)
Movement Type
Head only
Full body
Tail only
Object Speed
Head
Tail
i
Number of bouts per animal
Full body
Head only
Tail only
j
Total time in each bout type (sec)
k
Average length of each bout type
l
1.0%
16.4%
5.5%
77.1%
Full body
Tail only
Head only
Immobile
m
Saline
or
Rimonabant (2 mg/kg)
Post-injection interval
30 min
Video Camera
30 min
23 hrs
Day 1
Day 2
Day 3
Day 4
Day 5
Day 6
n
Treatment
Saline
Rimonabant (2mg/kg)
Bouts per trial

Figure 2.1: Struggling bouts during restraint stress increase with rimonabant and are associated with calcium transients in the BNST.

a, Image of RESTRAINT (**RE**cording **S**ignal **TR**ansients **A**ccessible **IN** a **T**ube) device for simultaneous fiber photometry and behavior recordings. **b**, Schematic of fiber photometry with RESTRAINT device and behavioral scoring pipeline. **c**, Diagram of AAV5.hSyn.GCaMP6f injection and fiberoptic implant into the BNST. Animals were tested 4-6 weeks after fiber implantation. (In collaboration with Sam Centanni.) **d**, Representative image of GCaMP expression in the BNST. **e**, Heatmap of bout associated GCaMP transients in the BNST. For all heatmaps, photometry signals run horizontally. Signals were time-locked to bout onset and were aligned such that bout onset began at zero seconds on the x-axis. Red indicates an intensity increase, and blue indicates a decrease relative to baseline. Values beyond the max/min values noted on the color legend are displayed with the color at the legend's respective ends. The total number of traces for each heatmap is displayed at the graph's far left (i.e., 1 through the total trace number). Data from individual animals are grouped in this plot, as indicated by distinct gray shaded bars along the left axis (n=4 mice, 145 total bouts). **f**, Average time-locked GCaMP signal from all bouts. Lighter shading: s.e.m. across all bouts. **g**, Schematic of automated behavior capture, tracking, and analysis pipeline using DeepLabCut. Fiber attached to the head (blue dot) and the tail tip (red dot) were tracked. Position data were then converted to speed. Speed above a set threshold indicated object movement. **h**, Zoomed in example output of a movement trace from the 30-minute restraint test. Struggling was classified by head (via the fiberoptic cable) and tail movements. Dark blue line indicates head (fiber) speed in arbitrary units (a.u.) Dark red line indicates tail speed in a.u. Movement category is indicated by background shading. Light blue: head only. Light red: tail only. Purple: time of overlapping head

and tail movements (i.e., full body). **i-l,** Combined data from 136 restraint stress trials (30-min each) with a total of 60,456 bouts. Each point represents the average from one 30-min trial. Points indicate the number of bouts for a 30 min restraint period. The distribution is indicated with a split violin normalized to width. Median, quartiles, and 1.5 * the interquartile range are indicated with the associated box plot. Purple: full body movements. Light blue: head only movements. Light red: tail only movements. **i,** Number of movement bouts by bout type. One-way ANOVA $F_{(2, 397)} = 200.3$, $P < 0.0001$; Bonferroni post hoc analysis: **P = 0.0014 for full body vs. head only; ****P < 0.0001 for full body vs. tail only; ****P < 0.0001 for head only vs. tail only. **j**, Total time spent in each bout type. One-way ANOVA $F_{(2, 397)} = 587.2$, $P < 0.0001$; Bonferroni post hoc analysis: ****P < 0.0001 for full body vs. head only; ****P < 0.0001 for full body vs. tail only; ****P < 0.0001 for head only vs. tail only. **k**, Average length of each bout type. One-way ANOVA $F_{(2, 397)} = 335.6$, $P < 0.0001$; Bonferroni post hoc analysis: ****P < 0.0001 for full body vs. head only; ****P < 0.0001 for full body vs. tail only; P = 0.47 for head only vs. tail only. **l**, Average percent of restraint stress trial time spent on each bout type. Light grey: immobile time. **m,** Schematic of repeated restraint exposures with either i.p. saline or rimonabant administered 30 minutes prior to the 30-minute restraint session. **n**, Mean number of detected full body, overlapping head and tail movement bouts, (purple bars from Fig. 1h) by day. (n =14 mice). Mixed-effects model Dunnett's multiple comparisons test ***P = 0.0002 for Day 1 vs. Day 5; *P = 0.0288 for Day 2 vs. Day 5; **P = 0.0025 for Day 3 vs. Day 5; **P = 0.0048 for Day 4 vs. Day 5; P = 0.1138 for Day 6 vs. Day 5. Bar color: i.p. saline or rimonabant. Error bars: s.e.m. across animals.

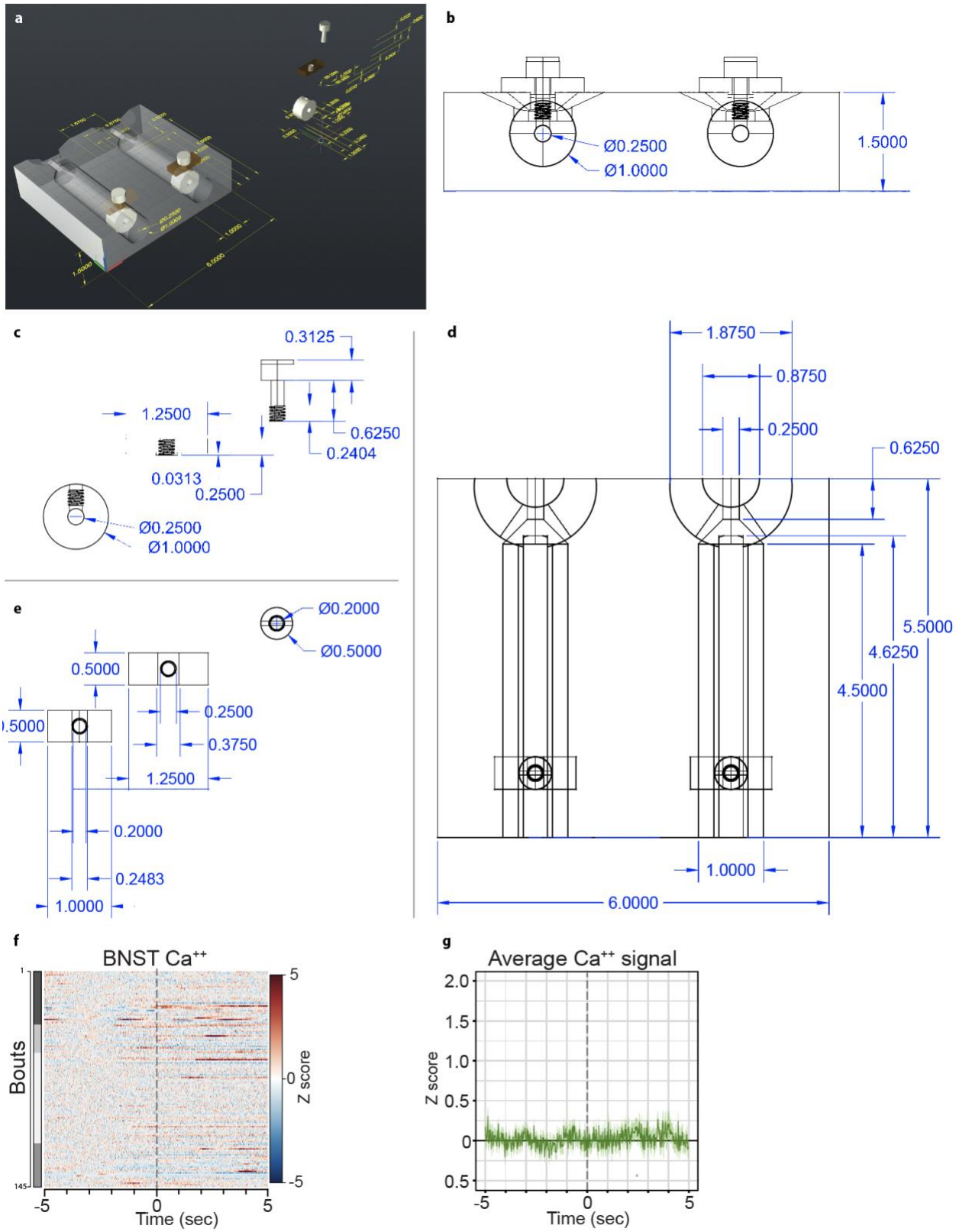
a
b
Ø0.2500
Ø1.0000
1.5000
c
0.3125
1.2500
0.6250
0.2404
0.0313
0.2500
Ø0.2500
Ø1.0000
d
1.8750
0.8750
0.2500
0.6250
5.5000
4.6250
4.5000
1.0000
6.0000
e
Ø0.2000
Ø0.5000
0.5000
0.2500
0.3750
1.2500
0.2000
0.2483
1.0000
f
BNST Ca++
Bouts
Z score
Time (sec)
g
Average Ca++ signal
Z score
Time (sec)

Figure 2.2: RESTRAINT device design and initial BNST-GCaMP control signal.

a, Overview of computer-aided design (CAD) of RESTRAINT (**RE**cording **S**ignal **TR**ansients **A**ccessible **IN** a **T**ube) device for concurrent *in vivo* recordings. All indicated measurements are in inches. (In collaboration with Kellie Williford) **b**, Front view of the CAD diagram of the RESTRAINT device. Black lines indicate edges of the device. Blue lines and text are measurements. **c**, Front view of the bung for the RESTRAINT. **d**, Top view of the RESTRAINT device. **e**, Top view of the bung for the RESTRAINT. **f**, Control heatmap for GCaMP signals in the BNST. Instead of GCaMP signal being time-locked to bout onset, the GCaMP signals were offset from bouts by +10 seconds. **g**, Average of the control GCaMP signals that were offset from bout initiation by +10 seconds.

engaging in these behaviors, and the average length (duration) of the bouts were highest for the full body struggles (Fig. 2.1j,k).

Thus, analyses here focused on full body struggles as these produced the most robust behavioral response, requiring coordinated head and tail movement. Of note, all struggling behavior is rare relative to the duration of the entire restraint stress assay (Fig. 2.1l), suggesting this behavior marks unique timepoints during restraint stress where mice initiate and sustain stress-responsive behavior. To determine if DLC-based scoring could accurately detect changes in anxiogenic behavior, we subjected mice to 30 minutes of restraint stress on six consecutive days. On each of the first four days, we injected mice with saline prior to restraint stress. On the fifth day, we injected the mice with the CB_1 receptor antagonist, rimonabant[276,466,467] (i.p. 2 mg/kg, a dose that does not alter locomotor activity[468])(Fig. 2.1m). Rimonabant increased the number of algorithm-detected struggling bouts compared to previous saline injection days. Moreover, when saline was administered prior to restraint stress on day six, struggling bouts were no longer elevated, indicating that our DLC-based system could accurately measure salient anxiogenic behaviors during restraint stress (Fig. 2.1n).

The BNST is composed of many subtypes of neurons, including a dense population of cells expressing the neuropeptide corticotropin-releasing factor (CRF). $BNST^{CRF}$ neurons have been identified as stress-responsive cells that drive affective behaviors[364,469,470], and acute stress models such as restraint stress reliably induce increases in *fos* activity in CRF cells that persist after the stress has ended[159,471]. $BNST^{CRF}$ activity *during* a stressor has not been assessed to date. To explore signaling specifically within $BNST^{CRF}$ cells, we unilaterally injected the BNST of CRF-Cre mice with a Cre-dependent GCaMP7f adeno-associated virus (AAV). We then simultaneously recorded behavior and *in vivo* calcium signaling during restraint stress (Fig. 2.3a,b). Struggling bouts were associated with increased calcium transients in $BNST^{CRF}$ cells (Fig. 2.3f-h). Struggling bout duration was positively correlated with calcium transient area

under the curve (AUC) and maximum peak amplitude (Fig. 2.4p,q). Further, there were significantly more struggle bouts with positive calcium transients (**P = 0.002511 for AUC) than there were without (Fig. 2.4r,s), suggesting that while $BNST^{CRF}$ calcium transients are not exclusive to struggle bouts, as a whole, the transients are positively correlated with the duration of the bouts. To assess the specificity of the $BNST^{CRF}$ response, we compared it to signals associated with struggling behavior from a distinct population of $BNST^{PKC\delta}$ cells (Fig. 2.4a-e), and found that the $BNST^{CRF}$ response was significantly larger (Fig. 2.4f,g). Because stress can increase glutamatergic signaling in the $BNST^{349}$, we incorporated a direct measurement of extracellular glutamate by utilizing the fluorescence intensity-based glutamate sensor, SF-iGluSnFR[472]. This extracellular glutamate sensor revealed an increase in extracellular glutamate at BNST neurons at the onset of struggling bouts (Fig. 2.3i-k).

Because struggling bouts are movement-dependent, the observed signals could involve movement artifacts. Therefore, we tested this possibility with a number of experiments. 1) As an internal control, we used a photometry system that measures calcium-independent isosbestic GCaMP signal, allowing for the subtraction of movement artifacts from the calcium-dependent GCaMP signal (Fig. 2.3b). 2) We injected a stable, activity-independent fluorophore (eGFP) in lieu of a sensor (Fig. 2.3a-e). Minimal time-locked signals were seen across eGFP animals, suggesting movement had only a very small contribution to the overall signal we observed. $BNST^{CRF}$ and SF-iGluSnFR sensors generated much higher average peak transient amplitudes and AUC from 0-5 seconds compared to the eGFP control (Fig. 2.3l,m). 3) We also identified calcium signaling in

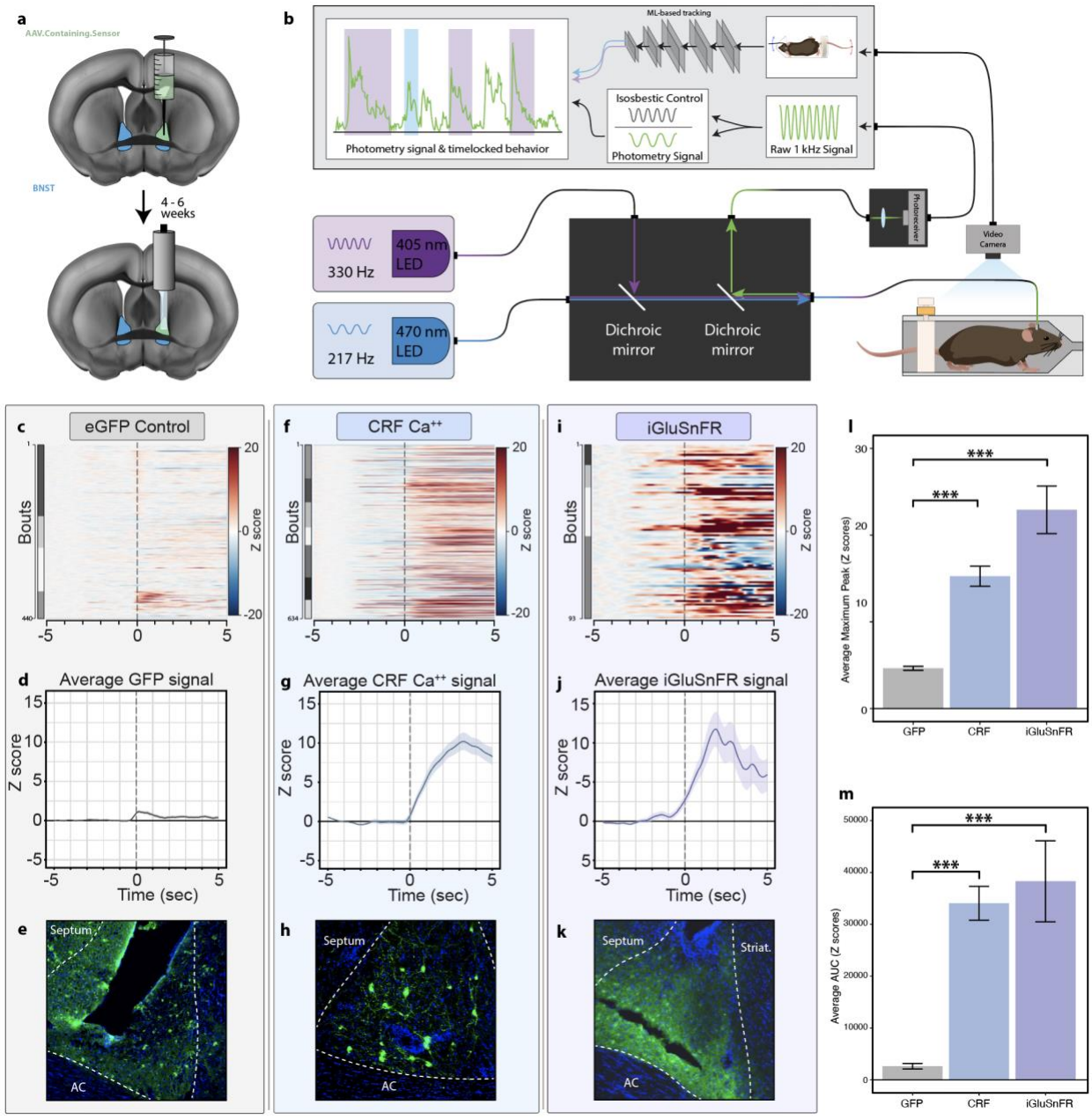

Figure 2.3: Calcium signals from BNST^{CRF} neurons and BNST glutamate transients are associated with struggling bouts.

a, Diagram of sensor-containing virus injection and fiber photometry implant into the BNST. Viral constructs coded for either eGFP control, Cre-dependent GCaMP, or SF-iGluSnFR. (In collaboration with Sam Centanni.) **b**, Schematic of two-channel fiber photometry system with

the ability to implement an isosbestic control. Signal is time-locked to machine learning-based scoring of RESTRAINT device behavior. **c-e,** Photometry recording from mice that received an injection of AAV5.eGFP in the BNST. **c**, eGFP control heatmap of time-locked bouts. **d**, Average eGFP signal. Lighter shading: s.e.m. across all bouts. **e**, Example image of eGFP expression in the BNST. **f-h,** Photometry recording from CRF-Cre mice that received an injection of Cre-dependent GCaMP in the BNST. (In collaboration with Greg Salimando) **f**, Heatmap of Cre-dependent GCaMP signal in CRF-Cre mice that was time-locked to bouts. **g**, Average Cre-dependent GCaMP signal in CRF-Cre mice. Lighter shading: s.e.m. across all bouts. **h**, Example image of Cre-dependent GCaMP expression in CRF-Cre mice. **i-k,** Photometry recording from mice that received an injection of AAV1.SF-iGluSnfR in the BNST. **i**, Heatmap of SF-iGluSnFR signal time-locked to bouts. **j**, Average SF-iGluSnFR signal. Lighter shading: s.e.m. across all bouts. **k**, Example image of SF-iGluSnFR expression in the BNST. **l**, Average maximum peak Z score of CRF GCaMP (n = 634 bouts from nine mice) and SF-iGluSnFR (n = 93 bouts from four mice) were higher than eGFP (n = 440 bouts from four mice) controls. One-way ANOVA $F_{(3,1744)} = 40.23$, $P < 0.0001$; Bonferroni post hoc analysis: ***$P < 0.0001$ for eGFP vs. CRF-GCaMP; ***$P < 0.0001$ for eGFP vs. SF-iGluSnFR. **m**, Average AUC Z score of CRF GCaMP and SF-iGluSnFR were higher than eGFP controls. One-way ANOVA $F_{(3,1744)} = 31.98$, $P < 0.0001$; Bonferroni post hoc analysis: ***$P < 0.0001$ for eGFP vs. CRF-GCaMP; ***$P < 0.0001$ for eGFP vs. SF-iGluSnFR.

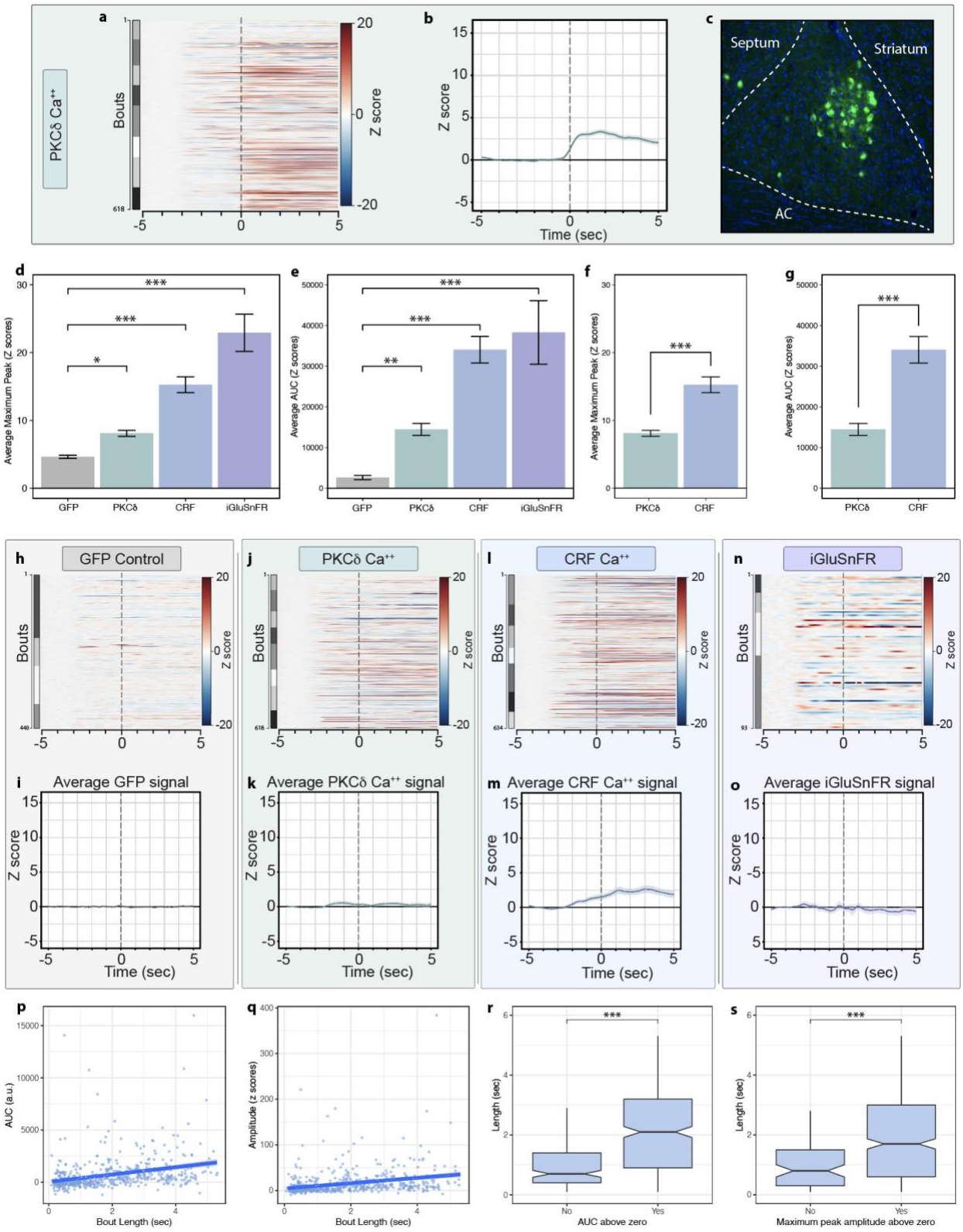
a
PKCδ Ca++
Bouts
Z score
b
Z score
Time (sec)
c
Septum
Striatum
AC
d
Average Maximum Peak (Z scores)
GFP
PKCδ
CRF
iGluSnFR
e
Average AUC (Z scores)
f
Average Maximum Peak (Z scores)
g
Average AUC (Z scores)
h
GFP Control
j
PKCδ Ca++
l
CRF Ca++
n
iGluSnFR
i
Average GFP signal
k
Average PKCδ Ca++ signal
m
Average CRF Ca++ signal
o
Average iGluSnFR signal
p
AUC (a.u.)
Bout Length (sec)
q
Amplitude (z scores)
Bout Length (sec)
r
Length (sec)
No
Yes
AUC above zero
s
Length (sec)
No
Yes
Maximum peak amplitude above zero

Figure 2.4: Fiber photometry controls for Cre-dependent sensors and SF-iGluSnFR.

a-c, Photometry recording from PKCd-Cre mice that received an injection of Cre-dependent GCaMP in the BNST. (In collaboration with Kellie Williford) **a**, Heatmap of Cre-dependent GCaMP signal in PKCd-Cre mice that was time-locked bouts. **b**, Average Cre-dependent GCaMP signal PKCd -Cre mice. Lighter shading: s.e.m. across all bouts. **c**, Example image of Cre-dependent GCaMP expression in PKCd-Cre mice. **d**, Average maximum peak Z score of PKCd GCaMP (n = 618 from eight mice), CRF GCaMP (n = 634 from nine mice), and SF-iGluSnFR (n = 93 from four mice) were higher than eGFP (n = 440 from four mice) controls. One-way ANOVA $F_{(3,1744)} = 40.23$, P < .0001; Bonferroni post hoc analysis: *P = 0.034 for eGFP vs. PKCd -GCaMP; ***P < .0001 for eGFP vs. CRF-GCaMP; ***P < .0001 for eGFP vs. SF-iGluSnFR. **e**, Average AUC Z score of PKCd GCaMP, CRF GCaMP, and SF-iGluSnFR were higher than eGFP controls. One-way ANOVA $F_{(3,1744)} = 31.98$, P < .0001; Bonferroni post hoc analysis: **P = 0. 0056 for eGFP vs. PKCd-GCaMP; ***P < .0001 for eGFP vs. CRF-GCaMP; ***P < .0001 for eGFP vs. SF-iGluSnFR. **f**, Average maximum peak Z score of CRF-GCaMP signal was higher than PKCd-GCaMP signal. Welch two-sample t-test, $t_{(811.98)} = 5.7621$, ***P < .0001. **g**, Average AUC Z score of CRF-GCaMP signal was higher than PKCd-GCaMP signal. Welch two-sample t-test, $t_{(874.12)} = 5.4682$, ***P < .0001. (note: * = p< 0.05, ** = p< 0.01, *** = p< 0.001). **h-o,** For all traces, instead of signals being time-locked to the beginning of each bout, they were offset from the bout onset by +10 seconds. **h**, Time-shifted control heatmap for GFP signals in the BNST. **i**, Average ± s.e.m of the time-shifted GFP signals that were offset from bout initiation by +10 seconds. **j**, Time-shifted heatmap for signals from GCaMP expressed in PKCd cells in the BNST. **k**, Average ± s.e.m of the offset GCaMP-PKCd signals. **l**, Time-shifted heatmap for signals from GCaMP expressed in CRF cells in the BNST. **m**, Average ±

s.e.m of the offset CRF-GCaMP signals. Slight increase in CRF-GCaMP signal likely reflects CRF cell activity occurring outside of bouts. **n**, Time-shifted heatmap for signals from SF-iGluSnFR expressed in the BNST. **o**, Average ± s.e.m of the offset SF-iGluSnFR signals. **p-s,** Analysis of CRF-GCaMP during the window from 0 to 5 seconds following bout onset. **p,** AUC vs. bout length (sec). Blue line: the slope of AUC vs. bout length with 95% confidence interval. $r_{(571)}$ = 0. 311, P < 0.0001. **q,** Bout length of bouts with an AUC above zero ('yes'= above zero) vs. those with an AUC not above zero ('no'= not above zero). Welch two-sample t-test, $t_{(572)}$ = -10.324, P < 0.0001. **r**, Maximum peak z-score amplitude vs. bout length (sec). Blue line slope of maximum peak vs. bout length with 95% confidence interval. $r_{(571)}$ = 0.2784, P < 0.0001. **s,** Bout length of bouts with a maximum peak above zero vs. those with a maximum peak not above zero. Welch two-sample t-test, Welch two-sample t-test, $t_{(574.64)}$ = -11.001, P < 0.0001.

the insula that was negatively correlated with movement. We trained mice expressing GCaMP in the insula to run on a running wheel while simultaneous photometry signals were measured. While the initiation of running induced a time-locked increase in calcium transient amplitude, transient frequency was significantly lower overall when the mice were running than when they were not (Fig. 2.5). 4) We reliably observed transients for multiple fluorescent sensors that occurred outside of struggle bouts (data not shown) as well as struggle bouts that failed to initiate an increase in sensor photometry signal (Fig. 2.19, Figs. 15-16), collectively negating the possibility of fiber movement in the brain as a driver of the signal.

To test for uncorrelated activity, we offset the behavior-photometry time-lock by +10 seconds for all eGFP, GCaMP, and SF-iGluSnFR experiments. In each case, transient signal decreased or was eliminated altogether (Fig. 2.4h-o). In total, these findings demonstrate that $BNST^{CRF}$ neurons are recruited in tight association with struggling events, and that increased glutamatergic drive onto BNST cells could be responsible for the changes in calcium transients that we observed in select stress-sensitive neuronal populations.

2.2.2 The insula is engaged by acute restraint stress and modulates stress-related BNST activity.

Given the large glutamatergic transients observed in the BNST associated with struggling bouts, coupled with our previous work indicating that insular afferents release glutamate at synapses on $BNST^{CRF}$ neurons[159,385], we explored the influence of this projection on BNST activity during stress. We first used retrograde and anterograde viral tracing strategies in combination with light sheet-based whole-brain mapping to better characterize the distribution of these BNST afferents (Fig. 2.6a-c). We identified the middle insula as the densest

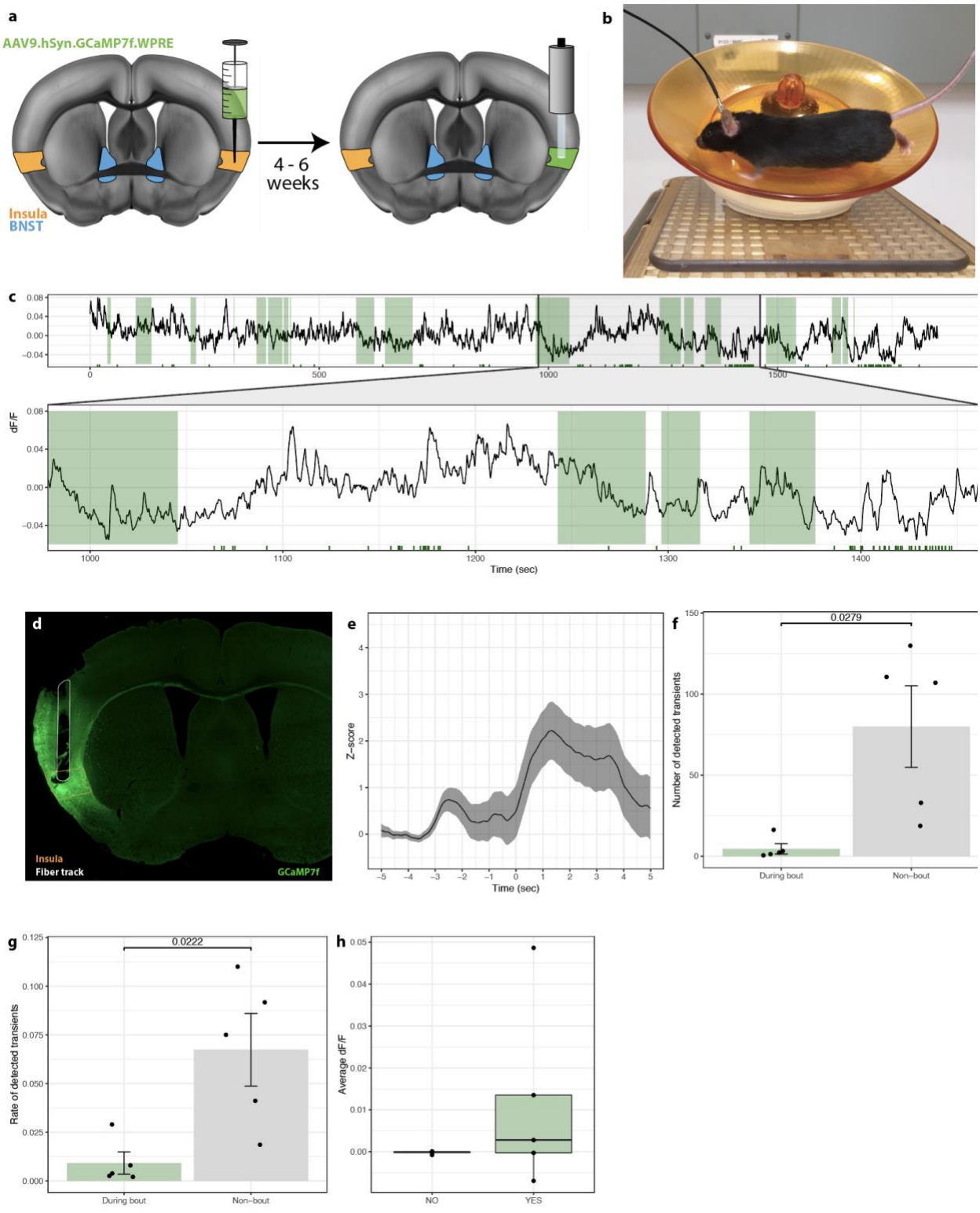
a
AAV9.hSyn.GCaMP7f.WPRE
4 - 6 weeks
Insula
BNST
b
c
dF/F
Time (sec)
d
Insula
Fiber track
GCaMP7f
e
Z-score
Time (sec)
f
0.0279
Number of detected transients
During bout
Non-bout
g
0.0222
Rate of detected transients
During bout
Non-bout
h
Average dF/F
NO
YES

Figure 2.5: Running motion does not increase insular GCaMP signal.

a, Diagram of AAV9.jGCaMP7f injected into the insula and fiberoptic implant into the insular cortex. **b,** Image of a mouse on a saucer-style running wheel with fiber photometry implant and cable. **c,** Representative fiber photometry trace (dF/F) while mouse had access to a running wheel. Top trace: whole 30 minutes. Bottom trace: expansion of the highlighted section of the top trace. Running status is indicated by background shading. Light green: running on wheel. White: not running on wheel. Detected transients are indicated with dark green tick marks at the bottom of the graph. **d,** Representative histological coronal slice. Fluorescent channel: GCaMP7f (green). Outlines: Insula (orange), Fiber track (white). **e,** Average GCaMP signal in mouse insula. Lighter shading: s.e.m. across all bouts. **f,** Aggregate number of detected transients during running vs. non-running portions of the trial. **g,** Rate of detected transients (Hz) during running vs. non-running portions of the trial. **h**, Average dF/F signal during running vs. non-running. Each point is the average for one animal.

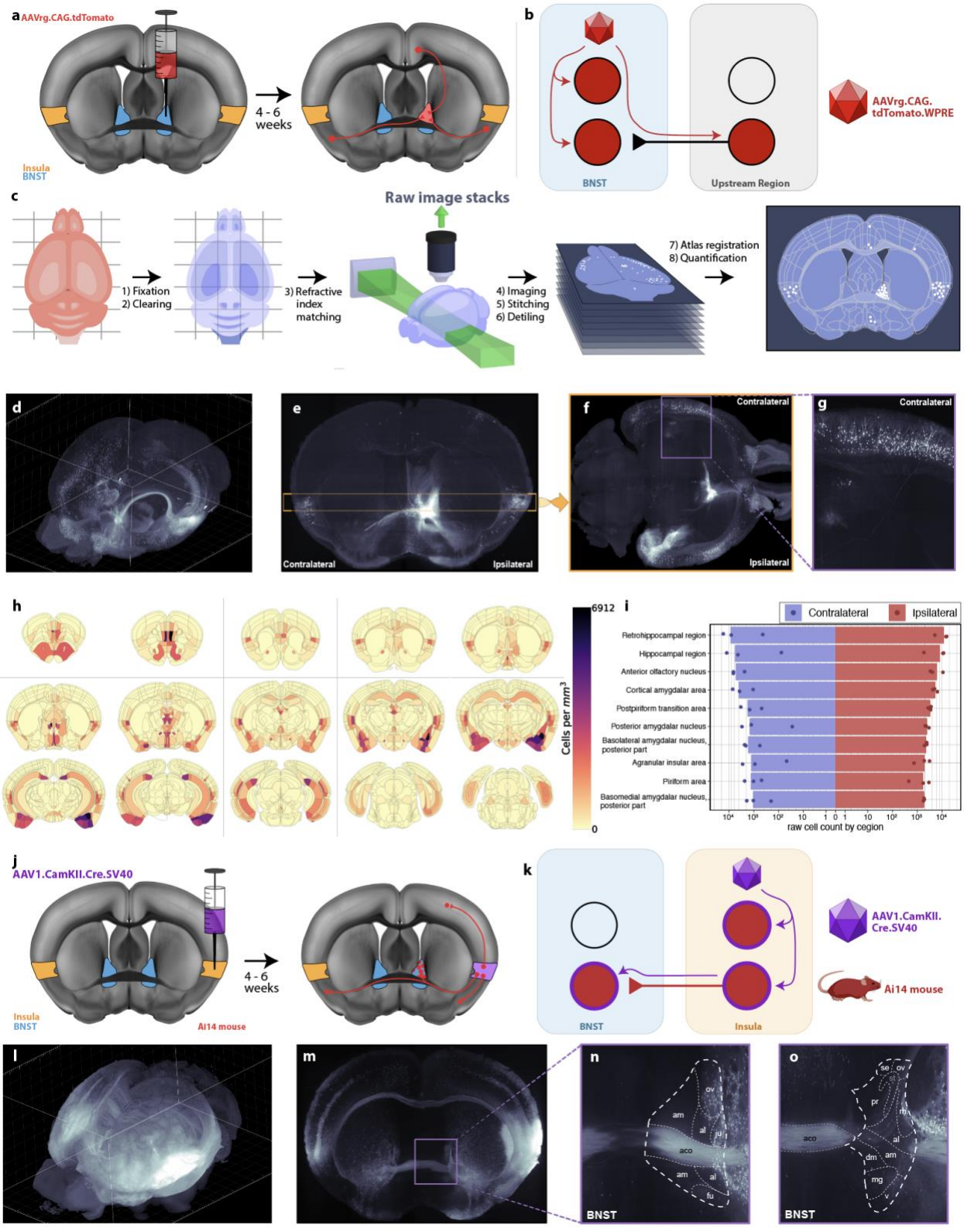
a
AAVrg.CAG.tdTomato
4 - 6 weeks
Insula
BNST
b
BNST
Upstream Region
AAVrg.CAG.
tdTomato.WPRE
c
Raw image stacks
1) Fixation
2) Clearing
3) Refractive index matching
4) Imaging
5) Stitching
6) Detiling
7) Atlas registration
8) Quantification
d
e
Contralateral
Ipsilateral
f
Contralateral
Ipsilateral
g
Contralateral
h
6912
Cells per mm³
0
i
Contralateral
Ipsilateral
Retrohippocampal region
Hippocampal region
Anterior olfactory nucleus
Cortical amygdalar area
Postpiriform transition area
Posterior amygdalar nucleus
Basolateral amygdalar nucleus, posterior part
Agranular insular area
Piriform area
Basomedial amygdalar nucleus, posterior part
raw cell count by cegion
j
AAV1.CamKII.Cre.SV40
4 - 6 weeks
Insula
BNST
Ai14 mouse
k
AAV1.CamKII.
Cre.SV40
Ai14 mouse
BNST
Insula
l
m
n
ov
am
al
pu
aco
am
al
fu
BNST
o
se
ov
pr
fu
aco
al
dm
am
mg
v
BNST

Figure 2.6: Inputs to the BNST originate from many stress-implicated regions across the brain, including broad insular inputs that appear to preferentially innervate the dorsal lateral BNST. **a**, Diagram of AAVrg coding for tdTomato injection into the BNST. Infected neuron cell bodies, axons, and dendrites are filled with tdTomato. **b**, Schematic of local and upstream viral infection. Cells that do not send projections to the injection site should not be infected. **c**, Overview of light sheet pipeline. **d**, Whole mouse brain after AAVrg-tdTomato injection into the BNST and subsequent light sheet imaging. Olfactory bulbs are in the bottom left corner, and the cerebellum is in the top right corner. **e**, Resampled image in the coronal plane, derived from 3D data set, at the level of the injection site in the BNST. Yellow outline illustrates the transverse plane sliced through for the next image. **f**, Transverse plane through the brain at the level of the insula. **g**, Magnified image of cells in the contralateral insula. Note the readily distinguishable cell bodies to be used for automated cell detection. **h**, Representation of cell density (mm^3) on a composite whole-brain heatmap (averaged from three mice). Cells were semiautonomously quantified using NUGGT[51]. **i**, Top ten labeled upstream regions (based on density of labeled cells) from unilateral AAVrg.tdTomato injection into the BNST in each of 3 mice. Bars: Mean from all three counts per region. Points: Counts from individual animals. Ipsilateral counts on the right in red. Contralateral counts are on the left in blue. The x-axis is an inverse hyperbolic sine transformation. **j**, Diagram of AAV1.Cre anterograde tracing with the injection in the insula of Ai14 mice (n=3). **k**, Overview of AAV1.Cre viral approach in the insula of Ai14 mice. **l**, 3D projection image of whole brain derived from an Ai14 mouse injected in the insula with AAV1.Cre. **m**, Resampled slice in coronal plane at the level of the BNST. tdTomato positive cells are visible bilaterally in both BNSTs. **n**, Magnified view of tdTomato positive cells in the

anterior region of the BNST. Note: For n-o, the morphological borders of subnuclei were charted from the Allen Brain Atlas. **o**, tdTomato positive cells in the posterior region of the BNST.

insular input to the mouse BNST (Fig. 2.6d-i, Supplementary Videos 1-4)[287], and the oval, juxtacapsular, rhomboid, and anterolateral subnuclei of the BNST (Fig. 2.6l-o) as major sites of insular afferent targeting in the region.

To test the role of insular inputs in modulating $BNST^{CRF}$ neuron stress responses, we injected the mid-insula of one hemisphere with a virus containing the G_i-Designer Receptor Exclusively Activated by Designer Drug (DREADD) hM4Di, and an eGFP control virus contralaterally. We administered Clozapine-*N*-oxide (CNO, i.p. 3 mg/kg) or saline 30 minutes prior to 60 minutes of restraint stress. We then quantified *fos* expression as a proxy for neuronal activity in $BNST^{CRF}$ cells using fluorescent *in situ* hybridization (Fig. 2.7a,b). Consistent with our hypothesis, the percent of $BNST^{CRF}$ cells that expressed *fos* after stress was significantly lower in the G_i-DREADD-injected hemisphere relative to the GFP injected hemisphere in CNO-treated mice (Fig. 2.7c).

Because of the effect of restraint on the BNST and the insula-BNST pathway, we next determined how restraint stress impacted the signaling within the insula by virally transducing GCaMP into the mid-insula (Fig. 2.7d). Average struggle bout-associated insular GCaMP signal increased at bout initiation. We used two fluorescent intensity-based neurotransmitter sensors, SF-iGluSnFR and iGABASnFR[473], to examine the contribution of insular microcircuitry to struggle behavior. SF-iGluSnFR showed increased glutamate release onto insula neurons at the onset of a struggling bout. Conversely, iGABASnFR recordings demonstrated bout-associated signals deflected in the negative direction at bout onset (Fig. 2.7e-f), suggesting transiently decreased extracellular GABA. This pattern was consistent across mice (Fig. 2.7f). Additionally, the duration of struggle bouts was positively correlated with AUC for insula GCaMP and SF-iGluSnFR signal and negatively correlated with insula iGABASnFR (Fig. 2.7g Day 1,

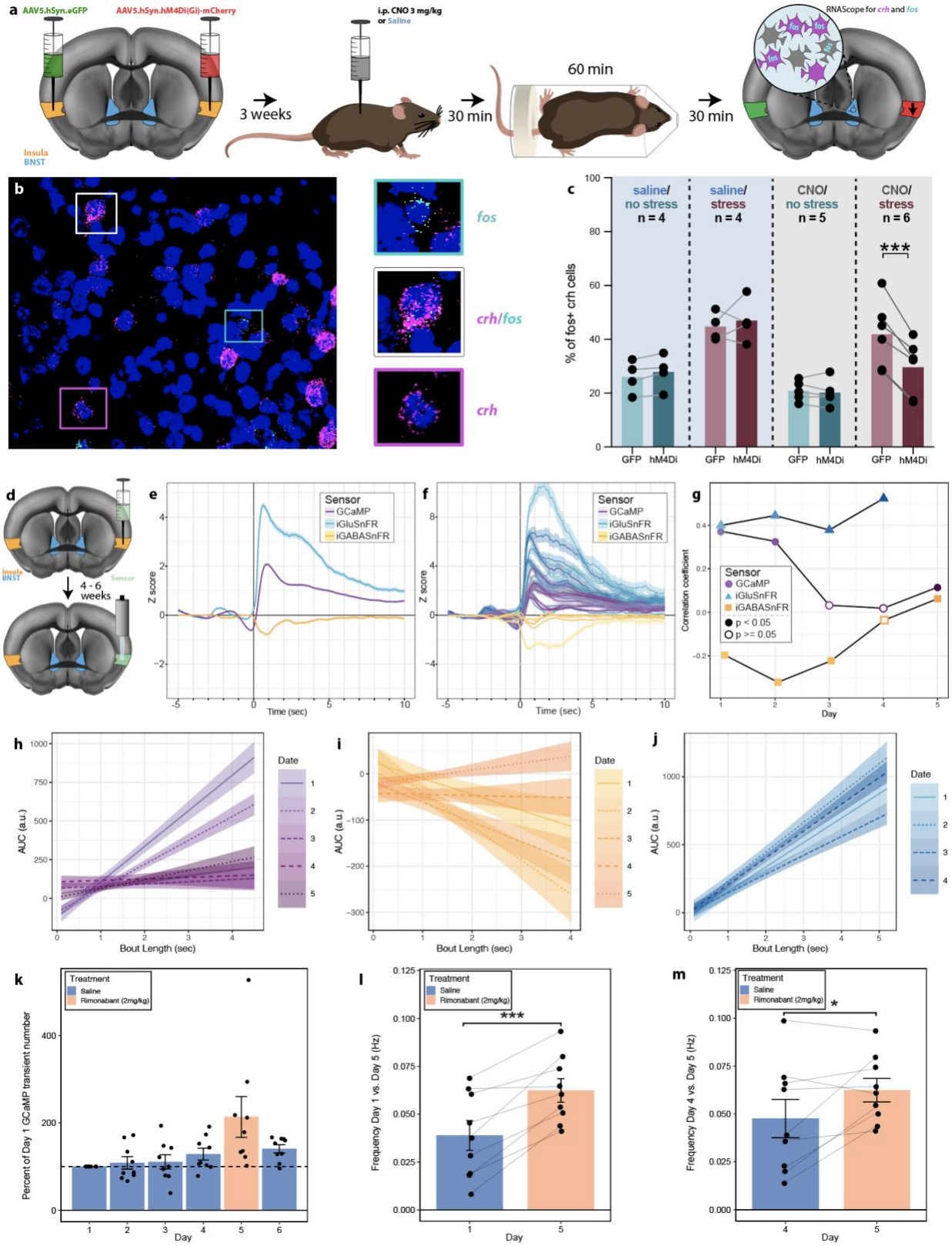
a
AAV5.hSyn.eGFP
AAV5.hSyn.hM4Di(Gi)-mCherry
Insula
BNST
3 weeks
i.p. CNO 3 mg/kg
or Saline
30 min
60 min
30 min
RNAScope for crh and fos
b
fos
crh/fos
crh
c
saline/
no stress
n = 4
saline/
stress
n = 4
CNO/
no stress
n = 5
CNO/
stress
n = 6
***
% of fos+ crh cells
GFP
hM4Di
d
Insula
BNST
Sensor
4 - 6
weeks
e
Sensor
GCaMP
iGluSnFR
iGABASnFR
Z score
Time (sec)
f
Sensor
GCaMP
iGluSnFR
iGABASnFR
Z score
Time (sec)
g
Sensor
GCaMP
iGluSnFR
iGABASnFR
p < 0.05
p >= 0.05
Correlation coefficient
Day
h
AUC (a.u.)
Bout Length (sec)
Date
i
AUC (a.u.)
Bout Length (sec)
Date
j
AUC (a.u.)
Bout Length (sec)
Date
k
Treatment
Saline
Rimonabant (2mg/kg)
Percent of Day 1 GCaMP transient number
Day
l
Treatment
Saline
Rimonabant (2mg/kg)
***
Frequency Day 1 vs. Day 5 (Hz)
Day
m
Treatment
Saline
Rimonabant (2mg/kg)
*
Frequency Day 4 vs. Day 5 (Hz)
Day

Figure 2.7: Insular G_i-DREADD activation decreases BNST fos expression after restraint stress, and insular transients are associated with struggling bouts.

a, Diagram of experimental timeline. Mice were injected with a G_i-DREADD (hM4Di) coding virus in one hemisphere and an eGFP control in the other. Three weeks later, mice were injected with CNO (i.p.) at 3 mg/kg. After 30 minutes, they were restrained for one hour. Thirty minutes after restraint, animals were sacrificed and processed for fluorescent *in situ* hybridization analysis of the BNST. (Work by Tracy Fetterly) **b**, Example fluorescent *in situ* hybridization from the BNST. Color-coordinated boxes show zoomed-in examples of *crh* only (magenta box), *fos* only (cyan box), and *crh/fos* doubly-labeled (white box) cells. **c**, Comparison of the effect of restraint stress and/or CNO exposure on percent of *fos*-positive *crh* cells in the BNST ipsilateral to the G_i-DREADD injection vs. the BNST ipsilateral to the eGFP control. Paired t-test, $t_{(5)}$ = 7.122, ***P = 0.0008. **d**, Schematic of viral strategy for insular fiber photometry experiment. Virus coding for either GCaMP7f (n = 9), SF-iGluSnFR (n =10), iGABASnFR (n = 5) was injected into the insula, followed by fiber placement. **e**, Average of all bout-associated signals from GCaMP (purple), SF-iGluSnFR (blue), or iGABASnFR (yellow) across six 30-minute restraint exposures (see Fig. 1i). Lighter shading: s.e.m. across bouts. **f**, Average bout-associated signals separated by animal.

g, Correlation coefficient of the relationship between AUC from 0 - 5 sec and bout length over days. GCaMP (purple circle), SF-iGluSnFR (blue triangle), and iGABASnFR (yellow square). Correlation coefficient shape is solid if $P < 0.05$ and open if $P \geq 0.05$. Rimonabant was administered to GCaMP and iGABASnFR on day 5. SF-iGluSnFR experiment finished on day 4. **h – j,** Slope of AUC vs. bout length by day with 95% confidence interval. **h,** GCaMP (purple). **i,** SF-iGluSnFR (blue). **j,** iGABASnFR (yellow). **k,** Percent of GCaMP transient number

normalized to day 1 (set at 100%). (n = 9) Error bars: s.e.m. across animals. **l**, Frequency of GCaMP transients during restraint on day 1 (30 minutes after i.p. saline injection) vs. day 5 (30 minutes after i.p. rimonabant injection). Paired t-test, $t_{(8)} = -5.4881$, ***P = 0.0006. **m**, Frequency of GCaMP transients during restraint on day 4 (30 minutes after i.p. saline injection) vs. day 5 (30 minutes after i.p. rimonabant injection). Paired t-test, $t_{(8)} = -2.3889$, *P = 0

Fig. 2.9a,c,e). The maximum peak amplitude for GCaMP, SF-iGluSnFR, and iGABASnFR followed a similar pattern (Fig. 2.10a,e,i). Further analysis revealed that a significantly higher number of bouts corresponded to increased calcium (*P = 0.01673 for GCaMP AUC) and glutamate signaling (****P < 0.0001 for SF-iGluSnFR AUC) than bouts that did not correspond with a change in signal. This suggests that while bouts with an associated increase in calcium/glutamate occur more frequently than bouts without an increase, insular calcium/glutamate changes are not uniformly dictated by struggling bouts (and vice versa) and are likely modulated by interdependent nodes of a larger related network. Insula neurons expressing iGABASnFR did not follow this pattern, as bouts were slightly more likely to occur with a transient AUC below zero (P = 0.0607 for iGABASnFR AUC). The greater likelihood of bouts being associated with an iGABASnFR AUC below zero is consistent with the negative deflection observed when the signal is time-locked to the onset of struggle bouts.

2.2.3 Homotypic stress habituation is associated with decreased fidelity of insula$^{\rightarrow BNST}$ struggle response.

A hallmark of stress biology is that repeated homotypic stressor exposure leads to response habituation[474]. Thus, we examined the signals with each sensor across multiple stress days to test if there was a change in the relationship between photometry signal and behavior (Fig. 2.7g-j, Figs. 15-16). We found that the GCaMP and iGABASnFR correlations between signal size and struggle duration collapsed across repeated days of exposure. Interestingly, however, insular SF-iGluSnFR signals remained elevated after repeated days of stress, suggesting habituation occurs postsynaptic to insular afferents (Fig. 2.7g, Fig. 2.9e-f, Fig. 2.10i-l).

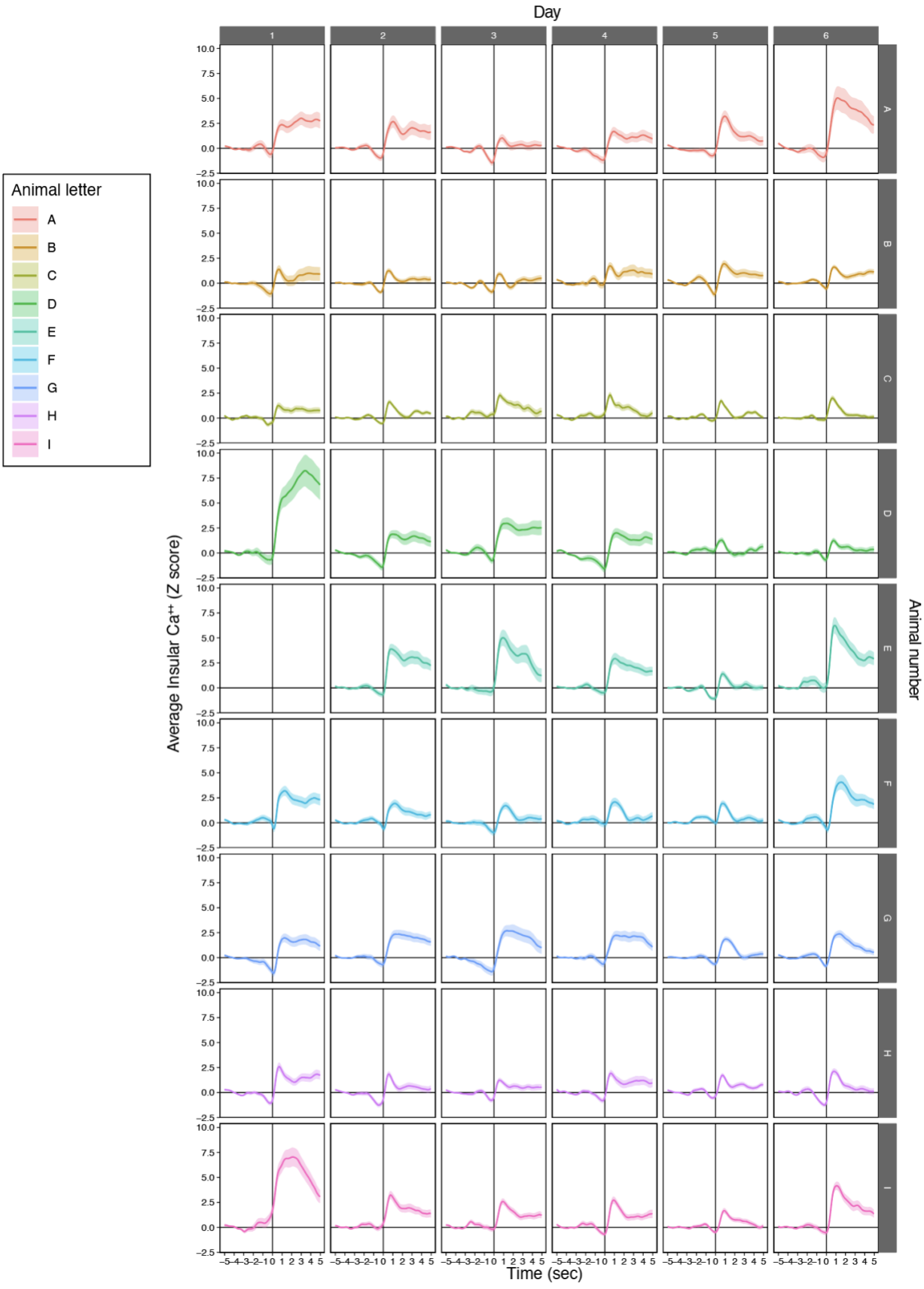
Day
1
2
3
4
5
6
Animal letter
A
B
C
D
E
F
G
H
I
Average Insular Ca++ (Z score)
Animal number
Time (sec)

Figure 2.8: Average time-locked insular GCaMP signal separated by day and animal. Average signal from individual animals separated by day of experiment. Days 1-6 are separated horizontally. Animals A-I are colored by subject number and are separated vertically. The x-axis is time from -5 seconds preceding to 5 seconds after bout onset. The y-axis is the average GCaMP signal Z score across all bouts for each animal on the indicated day. Lighter shading: s.e.m. across all bouts for that session.

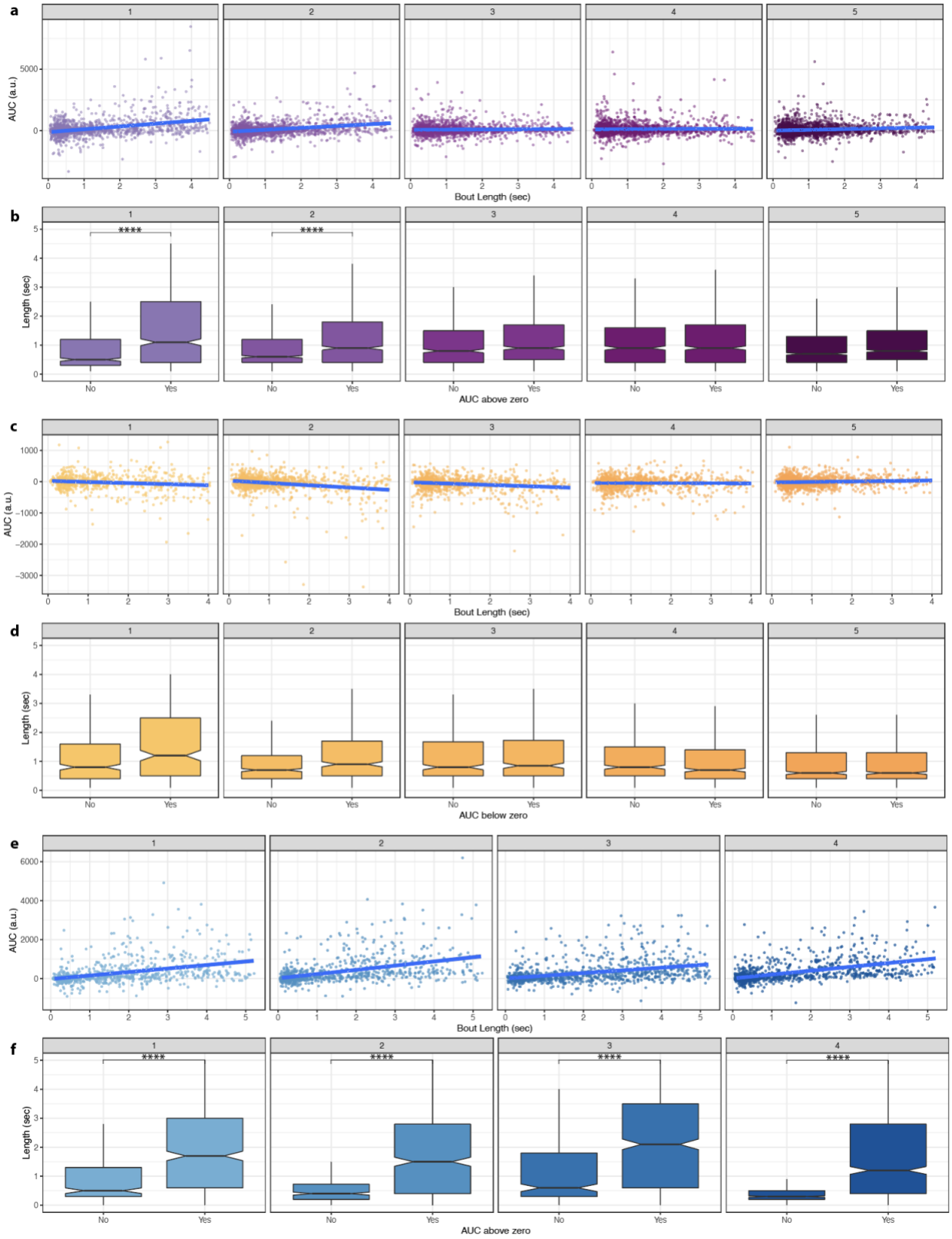
a
1
2
3
4
5
AUC (a.u.)
5000
0
0
1
2
3
4
Bout Length (sec)
b
****
Length (sec)
No
Yes
AUC above zero
c
1000
−1000
−2000
−3000
d
AUC below zero
e
6000
4000
2000
f

Figure 2.9: Analysis of AUC vs. bout length for insular GCaMP7f, iGABASnFR, and SF-iGluSnFR after bout onset.

Colors: GCaMP (purple), iGABASnFR (yellow), SF-iGluSnFR (blue). Dots on scatterplots represent the bout length vs. the AUC of the photometry signal for individual bouts on the given day. Blue line: slope of AUC vs. bout length with 95% confidence interval. Note: correlation coefficients are indicated in Fig. 3g. Boxplots compare bouts with an AUC above zero vs. those with an AUC not above zero. Notch indicates confidence interval around the median. ****P < 0.0001. **a,** GCaMP: AUC vs. bout length (sec) from days one to five. Rimonabant given on day five. **b,** GCaMP: Bout length of bouts with an AUC above zero ('yes'= above zero) vs. those with an AUC not above zero ('no'= not above zero). Rimonabant given on day five. **c,** iGABASnFR: AUC vs. bout length (sec) from days one to five. Rimonabant given on day five. Blue line slope of AUC vs. bout length with 95% confidence interval. **d,** iGABASnFR: Bout length of bouts with an AUC below zero ('yes'= below zero) vs. those with an AUC not below zero ('no'= not below zero). Rimonabant given on day five. **e,** SF-iGluSnFR: AUC vs. bout length (sec) from days one to four. Blue line slope of AUC vs. bout length with 95% confidence interval. **f,** SF-iGluSnFR: Bout length of bouts with an AUC above zero ('yes'= above zero) vs. those with an AUC not above zero ('no'= not above zero).

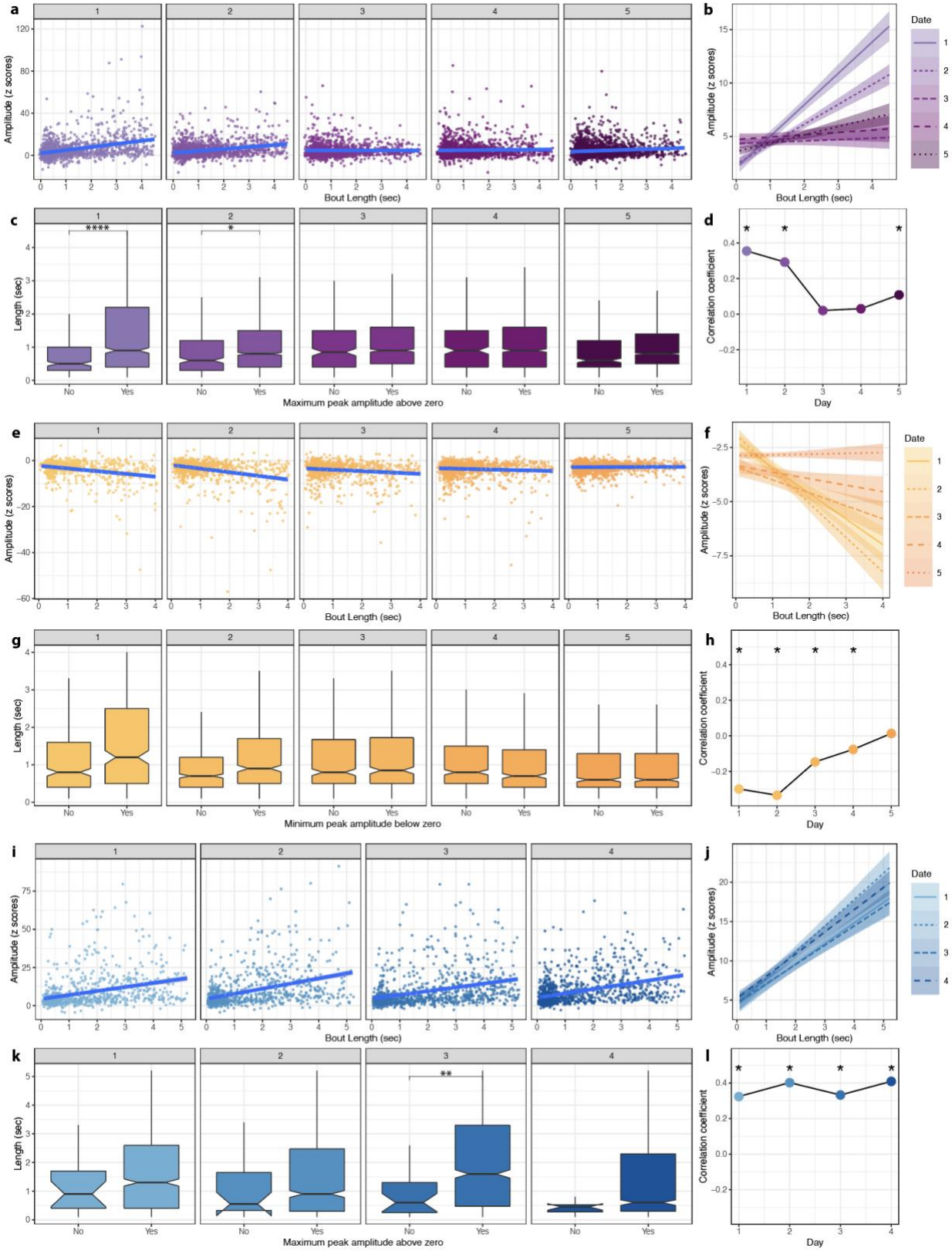
a
b
c
d
e
f
g
h
i
j
k
l
Amplitude (z scores)
Bout Length (sec)
Date
Length (sec)
Maximum peak amplitude above zero
Correlation coefficient
Day
Minimum peak amplitude below zero
No
Yes

Figure 2.10: Analysis of maximum peak photometry amplitude vs. bout length for insular GCaMP7f, iGABASnFR, and SF-iGluSnFR following bout onset.

Colors: **a-d,** GCaMP (purple). **e-h,** iGABASnFR (yellow). **i-l,** SF-iGluSnFR (blue). Dots on scatterplots represent the bout length vs. the photometry signal's peak amplitude for individual bouts on the given day. Blue line: slope of peak amplitude vs. bout length with 95% confidence interval. Slopes for each sensor are overlayed for comparison across days. Boxplots compare bouts with a peak amplitude above zero vs. those with a peak amplitude not above zero. Notch indicates confidence interval around the median. Correlation coefficients are shown across days. *P < 0.05, **P < 0.01, ****P < 0.0001. **a,** GCaMP: maximum peak amplitude vs. bout length (sec) from days one to five. Rimonabant given on day five. **b,** GCaMP: overlayed slopes of maximum peak amplitude vs. bout across days length from Fig. S7a. **c,** GCaMP: Bout length of bouts with a maximum peak amplitude above zero ('yes'= above zero) vs. those with a maximum peak amplitude not above zero ('no'= not above zero). Rimonabant given on day five. **d,** GCaMP: correlation coefficients for maximum peak amplitude vs. bout length across days from Fig. S7a. **e,** iGABASnFR: minimum peak amplitude vs. bout length (sec) from days one to five. Rimonabant given on day five. **f,** iGABASnFR: overlayed slopes of minimum peak amplitude vs. bout across days length from Fig. S7e. **g,** iGABASnFR: Bout length of bouts with a minimum peak amplitude above zero ('yes'= below zero) vs. those with n maximum peak amplitude not above zero ('no'= not below zero). **h,** iGABASnFR: correlation coefficients for minimum peak amplitude vs. bout length across days from Fig. S7e. **i,** SF-iGluSnFR: maximum peak amplitude vs. bout length (sec) from days one to five. Rimonabant given on day five. **j,** SF-iGluSnFR: overlayed slopes of maximum peak amplitude vs. bout across days length from Fig. S7i. **k,** SF-iGluSnFR: bout length of bouts with maximum peak amplitude above zero ('yes'=

above zero) vs. those with a maximum peak amplitude not above zero ('no'= not above zero). **l,** SF-iGluSnFR: correlation coefficients for maximum peak amplitude vs. bout length across days from Fig. S7i.

Given that rimonabant increased struggling bouts, we next tested whether the drug acts in part through increasing insular activity. SF-iGluSnFR signal did not habituate; therefore, we examined rimonabant's effect on insular iGABASnFR and GCaMP signal. Rimonabant re-established a positive correlation between AUC and bout length for GCaMP but did not restore the correlation between iGABASnFR and bout length (Fig. 2.7g-i, Fig. 2.9-16). We then normalized insular calcium transient frequency over days 2-6 to each subject's number of transients on day 1 (Fig. 2.7k). We compared GCaMP transient frequencies from the first restraint exposure (day 1) and the exposure immediately preceding rimonabant (day 4) to the frequencies observed following rimonabant administration (day 5). Rimonabant significantly increased insular GCaMP transient frequency (Fig. 2.7l-m) suggesting the anxiogenic actions of rimonabant act in part through insular cortex signaling.

2.2.4 Chemogenetically activating insula$^{\rightarrow BNST}$ neurons increases behaviorally time-locked BNST calcium signal during restraint stress and subsequent anxiety-like behavior.

After demonstrating that insula G_i-DREADD activation decreased BNST *fos* following restraint, we tested the hypothesis that specifically activating insula$^{\rightarrow BNST}$ neurons could change BNST activity during restraint. We injected AAVrg-Cre (retrograde AAV expressing Cre) into the BNST and Cre-dependent G_q-DREADD (hM3Dq) into the insula. CNO (i.p. 3 mg/kg) injection then selectively activated the G_q-DREADD in insula$^{\rightarrow BNST}$ neurons while calcium transients from the BNST were recorded during restraint (Fig. 2.11a-e). Averaged time-locked bout-associated transients can be seen in Fig. 2.11f. CNO-treated animals exhibited higher average BNST peak transient amplitudes and AUCs from 0-5 seconds after bout onset (Fig. 2.11g,h).

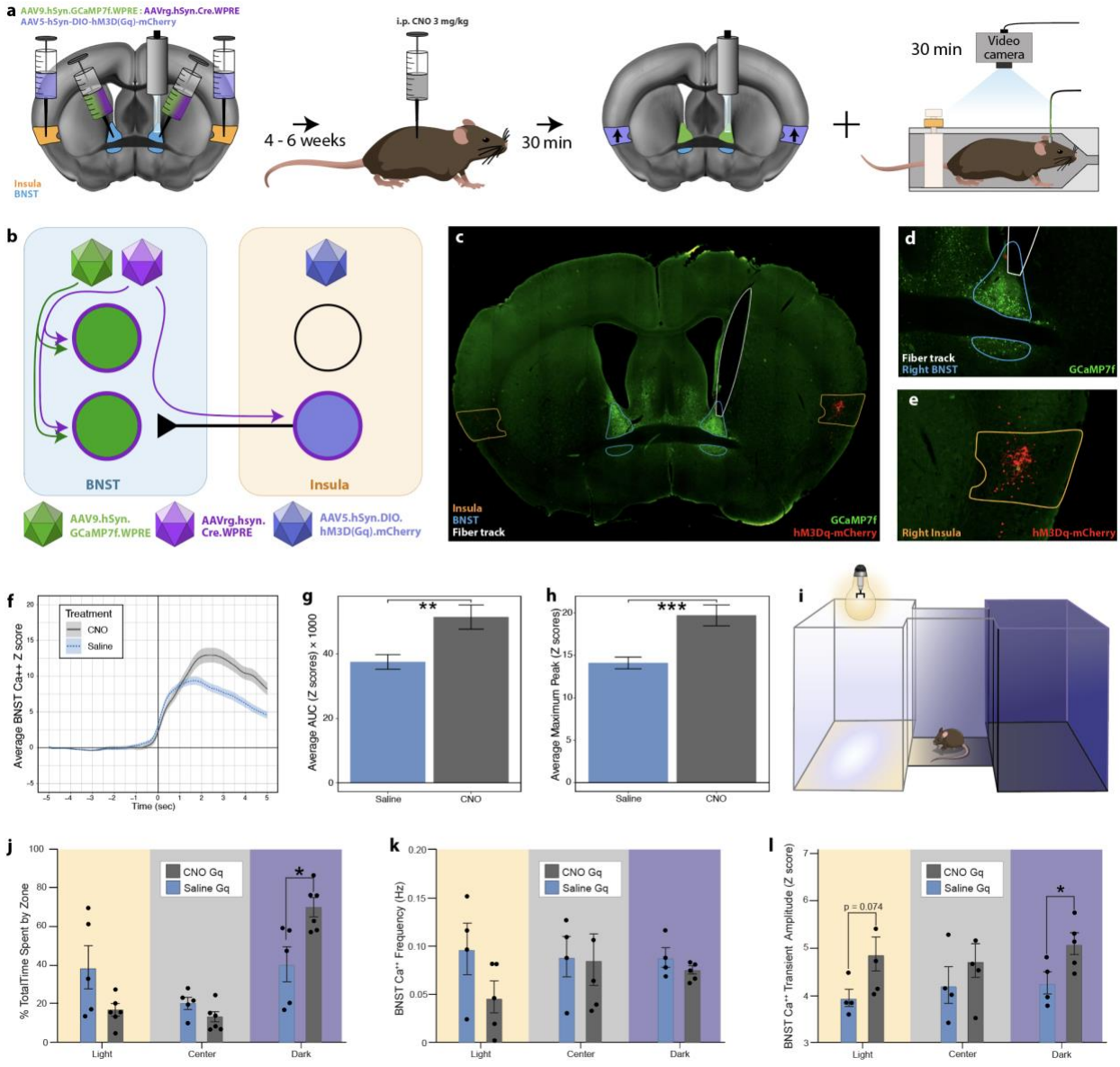

Figure 2.11: Chemogenetically activating insula$^{\rightarrow BNST}$ cells increases struggling bout-associated BNST calcium transients and anxiety-like behavior after restraint.

a, Schematic of viral and behavioral experimental design. A 1:1 ratio of virus coding for GCaMP and a retrograde AAV coding for Cre were injected into the BNST. A virus coding for Cre-dependent G_q-DREADD (hM3Dq) was injected into the insula, thus restricting G_q-DREADD

expression to the cells in the insula that project to the BNST. A fiber photometry implant was also placed in the BNST. Four to six weeks after fiber implantation, animals were injected with CNO (i.p. 3 mg/kg). Thirty minutes later, animals were placed in a restraint stress device and recorded for automated behavioral analysis. (In collaboration with Sam Centanni.) **b**, Diagram of GCaMP and G_q-DREADD viral expression. GCaMP was expressed in BNST neurons, while G_q-DREADD was only expressed in insula$^{\rightarrow BNST}$ cells. **c**, Representative histological coronal slice. Fluorescent channels: GCaMP7f (green), hM3Dq-mCherry (red); Outlines: BNST (blue), Insula (orange), Fiber track (white). **d-e,** Expanded views of the respective injection sites. Colors and outlines match Fig 4c. **d,** Right BNST. **e,** Right insula. **f**, Average BNST calcium transient time-locked to struggling onset. (CNO = grey, saline = blue). **g**, Average area under the curve (AUC) of Z scores from all bouts of CNO (grey) and saline (blue) treated animals. Welch two-sample t-test, $t_{(494.56)} = 3.1668$, **P = 0.0016. **h**, Average Maximum Peak Z score from all bouts of CNO (grey) and saline (blue) treated animals. Welch two-sample t-test, $t_{(467.1)} = 3.9858$, ***P = 0.0008. **i**, Diagram of light-dark box with three zones (light, center, and dark). Mice were placed in the center chamber of the light-dark box for 10 minutes immediately after restraint testing. **j**, Percent of total time spent in each zone (light, center, and dark) by CNO (n = 5) and saline (n = 5) treated animals. CNO treated animals spent more time than saline controls in the dark zone and trended towards less time in the light zone. Multiple unpaired t-tests with the false discovery rate (FSD) approach of two-stage step-up method of Benjamini, Krieger, and Yekutieli. FSD = 1%. light zone: $t_{(8)} = 1.833$, P = 0.104; center zone: $t_{(8)} = 1.463$, P = 0.1814; dark zone: $t_{(8)} = 2.636$, *P = 0.0299. **k,** BNST calcium transient frequency in each zone (light, center, and dark) by CNO (n = 5) and saline (n = 4) treated animals. CNO-treated mice had similar frequencies in any of the three zones. Multiple unpaired t-tests with the FSD approach of two-stage step-up

method of Benjamini, Krieger, and Yekutieli. FSD = 1%. light zone: $t_{(7)}$ = 1.660, P = 0.1410; center zone: $t_{(7)}$ = 0.0965, P = 0.9258; dark zone: $t_{(7)}$ = 1.255, P = 0.2499. **l,** Average BNST calcium transient amplitude in each zone (light, center, and dark) by CNO (n = 5) and saline (n = 4) treated animals. CNO-treated animals had great averaged transient amplitude in the dark zone and trended towards greater amplitude in the light zone. Multiple unpaired t-tests with the FSD approach of two-stage step-up method of Benjamini, Krieger, and Yekutieli. FSD = 1%. light zone: $t_{(7)}$ = 2.096, P = 0.0743; center zone: $t_{(7)}$ = 0.9764, P = 0.3614; dark zone: $t_{(7)}$ = 2.527, *P = 0.0394.

Interestingly, G_q-DREADD activation did not significantly change the characteristics of the bouts themselves, including the number and duration of bouts and total struggle time (Fig. 2.12). We hypothesized that G_q-DREADD activation of insular input to the BNST would exacerbate post-stress avoidance of the light side in the light-dark box, a test validated for assessing negative affective state in mice[475], immediately after restraint (Fig 4i). Indeed, CNO-treated mice spent significantly more time in the dark side than saline-treated mice (Fig. 2.11j), suggesting a DREADD-induced increase in negative affective behavior. BNST signaling also changed with CNO, such that treated animals exhibited higher average GCaMP transient amplitude (but not frequency) in the dark zone and a trend toward higher amplitude in the light zone (Fig. 2.11k,l). We next performed the same experiment in mice using a pan-neuronal G_i-DREADD in bilateral mid-insular neurons. Inactivating mid-insular neurons decreased BNST GCaMP transient amplitude at the onset of struggling bout behavior during restraint stress (Fig. 2.13), but unlike activating insula$^{\rightarrow BNST}$ neurons, inactivating mid-insula neurons did not change subsequent behavior in the light-dark box ($F_{(1,13)} = 0.114$, $P = 0.741$).

2.2.5 The afferent network for the insula$^{\rightarrow BNST}$ pathway is broadly distributed and includes significant somatomotor input.

Struggling bouts are tightly coupled with insular-BNST signaling, yet it is unclear how motor information reaches this pathway. In an effort to understand the control network for the insula$^{\rightarrow BNST}$ pathway, we turned to a rabies-based tracing method, TRIO (Tracing the Relationships between Inputs and Outputs)[476], to selectively label the inputs directly synapsing onto insula$^{\rightarrow BNST}$ neurons (Fig. 2.14a-f, Supplementary Videos 5). Five brains were registered

with the Allen Brain Atlas Coordinate Reference Framework[477]. The densities of labeled neurons in

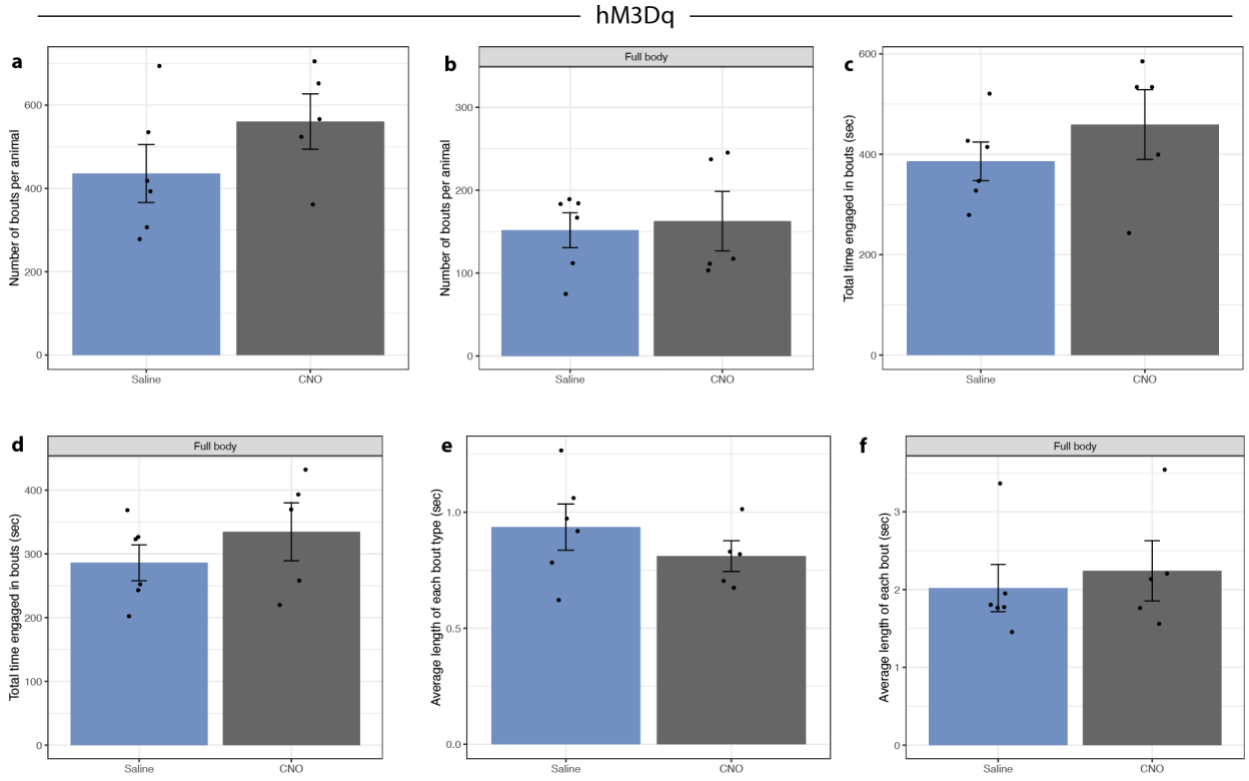

Figure 2.12: Restraint bout data when chemogenetically activating insula$^{\rightarrow BNST}$ cells.

a, Average number of bouts (all types) during the 30-minute restraint with CNO (grey) and saline (blue) treated animals. Welch two-sample t-test, $t_{(8.98)} = -1.4359$, $P = 0.1849$. **b,** Average number of full body bouts during the 30-minute restraint of CNO (grey) and saline (blue) treated animals. Welch two-sample t-test, $t_{(6.70)} = -0.292$, $P = 0.779$. **c**, Average time engaged in bouts (all types) during the 30-minute restraint of CNO (grey) and saline (blue) treated animals. Welch two-sample t-test, $t_{(6.45)} = -1.024$, $P = 0.3428$. **d,** Average time engaged in full body bouts during the 30-minute restraint of CNO (grey) and saline (blue) treated animals. Welch two-sample t-test, $t_{(6.94)} = -1.0097$, $P = 0.3465$. **c**, Average time engaged in bouts (all types) during the 30-

minute restraint of CNO (grey) and saline (blue) treated animals. Welch two-sample t-test, $t_{(6.45)}$ = -1.024, P = 0.3428. **d,** Average number of full body bouts during the 30-minute restraint of CNO (grey) and saline (blue) treated animals. Welch two-sample t-test, $t_{(6.94)}$ = -1.0097, P = 0.3465. **e**, Average time length of each bout (all types) during the 30-minute restraint of CNO (grey) and saline (blue) treated animals. Welch two-sample t-test, $t_{(8.29)}$ = 1.1504, P = 0.2821. **f,** Average number of full body bouts during the 30-minute restraint of CNO (grey) and saline (blue) treated animals. Welch two-sample t-test, $t_{(8.11)}$ = -0.50056, P = 0.63.

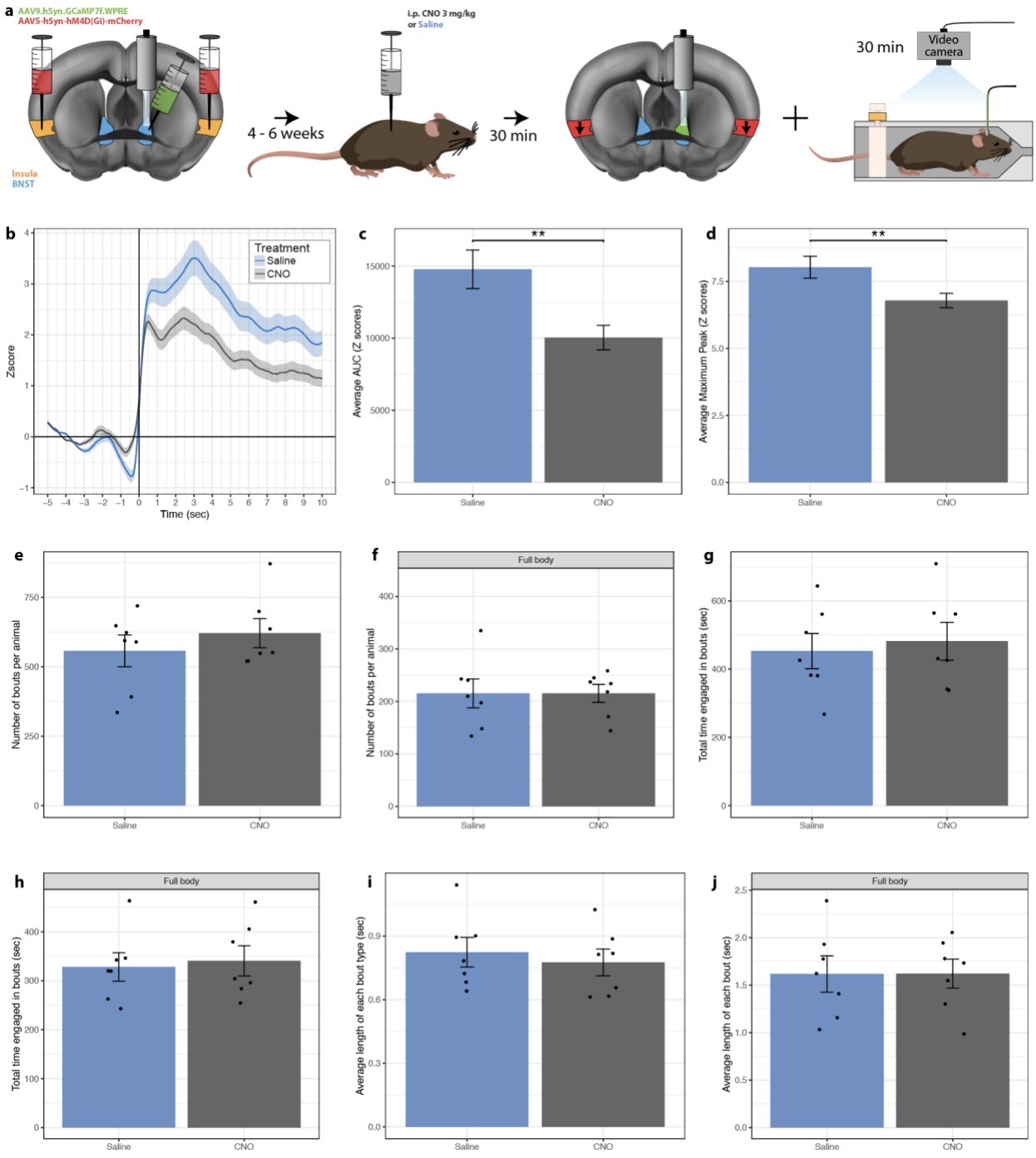
a
AAV9.hSyn.GCaMP7f.WPRE
AAV5-hSyn-hM4D(Gi)-mCherry
Insula
BNST
4 - 6 weeks
i.p. CNO 3 mg/kg
or Saline
30 min
30 min
Video camera
b
Treatment
Saline
CNO
Zscore
Time (sec)
c
Average AUC (Z scores)
Saline
CNO
d
Average Maximum Peak (Z scores)
Saline
CNO
e
Number of bouts per animal
Saline
CNO
f
Full body
Number of bouts per animal
Saline
CNO
g
Total time engaged in bouts (sec)
Saline
CNO
h
Full body
Total time engaged in bouts (sec)
Saline
CNO
i
Average length of each bout type (sec)
Saline
CNO
j
Full body
Average length of each bout (sec)
Saline
CNO

Figure 2.13: Insular G_i-DREADD activation decreases BNST transient size but does not change struggling bouts.

a, Diagram of experimental timeline. Mice received bilateral insula injections with a G_i-DREADD (hM4Di) coding virus and unilateral BNST injections coding for GCaMP7f. A fiber photometry implant was also placed in the same BNST. Four to six weeks after fiber implantation, animals were injected with CNO (i.p. 3 mg/kg). Thirty minutes later, animals were placed in a restraint stress device and recorded for automated behavioral analysis. (In collaboration with Sam Centanni.) **b**, Average of all full body bout-associated signals from GCaMP signal in CNO (grey) and saline (blue) treated animals. Lighter shading: s.e.m. across bouts. **c,** Average area under the curve (AUC) of Z scores from all bouts of CNO (grey) and saline (blue) treated animals. Welch two-sample t-test, $t_{(2220.6)} = 2.9892$, **P = 0.0028 **d,** Average Maximum Peak Z score from all bouts of CNO (grey) and saline (blue) treated animals. Welch two-sample t-test, $t_{(2265.9)} = 2.5376$, *P = 0.0112. **e**, Average number of bouts (all types) during the 30-minute restraint of CNO (grey) and saline (blue) treated animals. Welch two-sample t-test, $t_{(11.913)} = -0.88636$, P = 0.393. **f,** Average number of full body bouts during the 30-minute restraint of CNO (grey) and saline (blue) treated animals. Welch two-sample t-test, $t_{(10.053)} = 0$, P = 1. **g**, Average time engaged in bouts (all types) during the 30-minute restraint of CNO (grey) and saline (blue) treated animals. Welch two-sample t-test, $t_{(11.942)} = -0.41159$, P = 0.6879. **h,** Average time engaged in full body bouts during the 30-minute restraint of CNO (grey) and saline (blue) treated animals. Welch two-sample t-test, $t_{(11.96)} = -0.3151$, P = 0.7581. **i**, Average time length of each bout (all types) during the 30-minute restraint of CNO (grey) and

saline (blue) treated animals. Welch two-sample t-test, $t_{(11.874)} = 0.55116$, P = 0.5917. **j,** Average number of full body bouts during the 30-minute restraint of CNO (grey) and saline (blue) treated animals. Welch two-sample t-test, $t_{(11.446)} = -0.01907$, P = 0.9851.

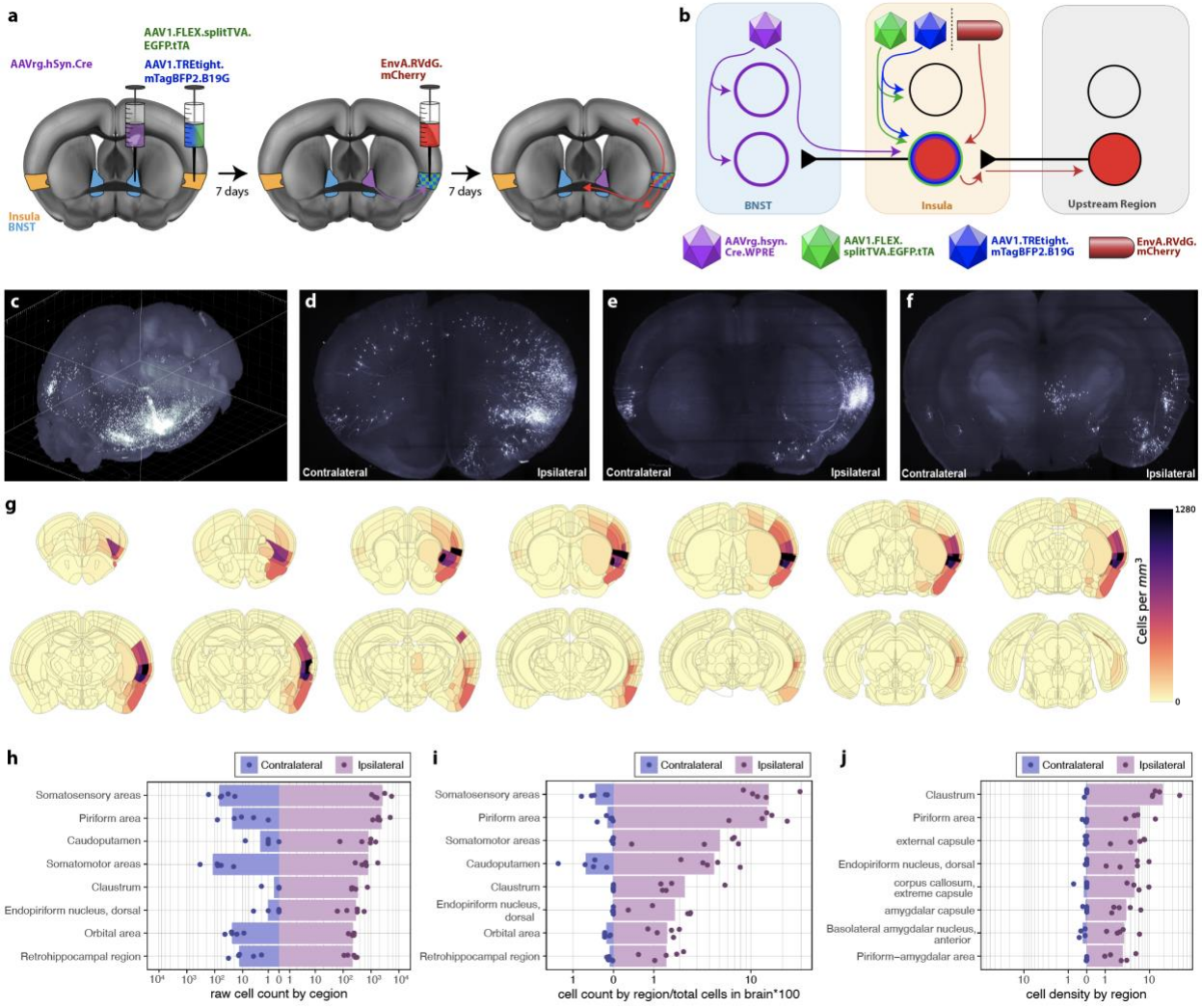

Figure 2.14: The control network for the insula$^{\rightarrow BNST}$ pathway includes piriform, somatosensory, somatomotor, and amygdalar nuclei.

a, Diagram of the viral strategy for tracing the control network for insula$^{\rightarrow BNST}$ cells. AAVrg.Cre was injected into the BNST. Viruses carrying the Cre-dependent helper proteins TVA and B19G were injected into the insula. After seven days, rabies virus (EnvA.RVdG.mCherry) was injected

into the same region of the insula. Seven days later, the brains were collected and started on the light sheet microscopy pipeline. **b**, Schematic of rabies tracing strategy. AAVrg.Cre infects cells locally in the BNST and afferents. The TVA and B19G viruses infect many neurons near the injection site, but only express their proteins in insula$^{\rightarrow BNST}$ neurons that also express Cre. Entry of the modified rabies is restricted to TVA expressing cells, and transsynaptic retrograde infection is limited to cells expressing B19G. Therefore, labeled neurons outside of the injection region are monosynaptically connected to the insula$^{\rightarrow BNST}$ neurons. **c**, Maximum projection image of 3D reconstruction of light sheet data set to illustrate insula$^{\rightarrow BNST}$ control network. Olfactory bulbs are in the bottom left corner, and the cerebellum is in the top right corner. **d**, Resampled images in the coronal plane at the level of the anterior insula. **e**, at the level of the BNST **f**, and at the level of thalamic and amygdalar structures. **g**, Distribution of labeled neurons represented as a composite whole-brain density heatmap (averaged from five mice) of semiautonomously quantified insula$^{\rightarrow BNST}$ control network cells as density in mm^3. **h**, Graphical representation of cell densities in top eight regions (by raw cell count) labeled as part of the labeled insula$^{\rightarrow BNST}$ control network of five mice. Bars: Mean from all three counts per region. Points: Counts from individual animals. Ipsilateral counts are on the right in purple. Contralateral counts are on the left in blue. The x-axis is an inverse hyperbolic sine transformation. **i**, Top eight regions (by cell count per region / total cells in each respective brain * 100) of the labeled insula$^{\rightarrow BNST}$ control network. **j**, Top eight regions (by cell density) of the labeled insula$^{\rightarrow BNST}$ control network.

each region were quantified, averaged across the five samples and the results overlayed on the Allen Brain Atlas (Fig. 2.14g, Fig. 2.15a,b). Raw cell counts and normalized cell counts (normalized to the total number of neurons in respective brains) revealed high densities of afferent neurons in somatosensory, piriform, and somatomotor regions (Fig. 2.14h,i, Fig. 2.16a, Supplementary Videos 6,7). Relative to the overall volume of certain structures, high densities of labeled cells were found in smaller regions such as the claustrum and basolateral amygdala. (Fig. 2.14j, Fig. 2.16b). Because the TRIO findings detailed a motor component that had yet to be explored, we evaluated this pathway's fidelity using other convergent viral techniques. Indeed, the TRIO data was compatible with retrogradely labeled motor input to the mid-insula (Fig. 2.17a-h; Supplementary Videos 8-10) and the distribution of anterogradely labeled cells receiving input from the motor cortex (Fig. 2.17i-n; Supplementary Video 11).

We next aimed to isolate the specific insula$^{\rightarrow BNST}$ neurons that receive motor input. We injected an anterograde transneuronal Cre virus (AAV1.Cre) into the motor cortex of Ai14 (Cre-dependent tdTomato expressing) mice and retrograde eGFP virus (AAVrg.eGFP) into the BNST (Fig. 2.18a). This strategy labeled neurons that send projections to the BNST with eGFP, while labeling cells that receive inputs from the motor cortex with tdTomato (Fig. 2.18b). We observed largely discrete populations of neurons labeled with either eGFP or tdTomato (Fig. 2.18c-f; Supplementary Videos 12). However, in the insula, eGFP (+) cells occupied space that overlapped with the tdTomato (+) cell distribution. The tdTomato cells dominated rostrally, becoming fewer in number relative to those labeled with eGFP at more caudal levels. Doubly-labeled cells (Fig. 2.18g-m) were sparse but reproducibly found throughout the insula. This also

held true contralaterally (Fig. 2.18n-q). Doubly-labeled cells were readily distinguished from singly-

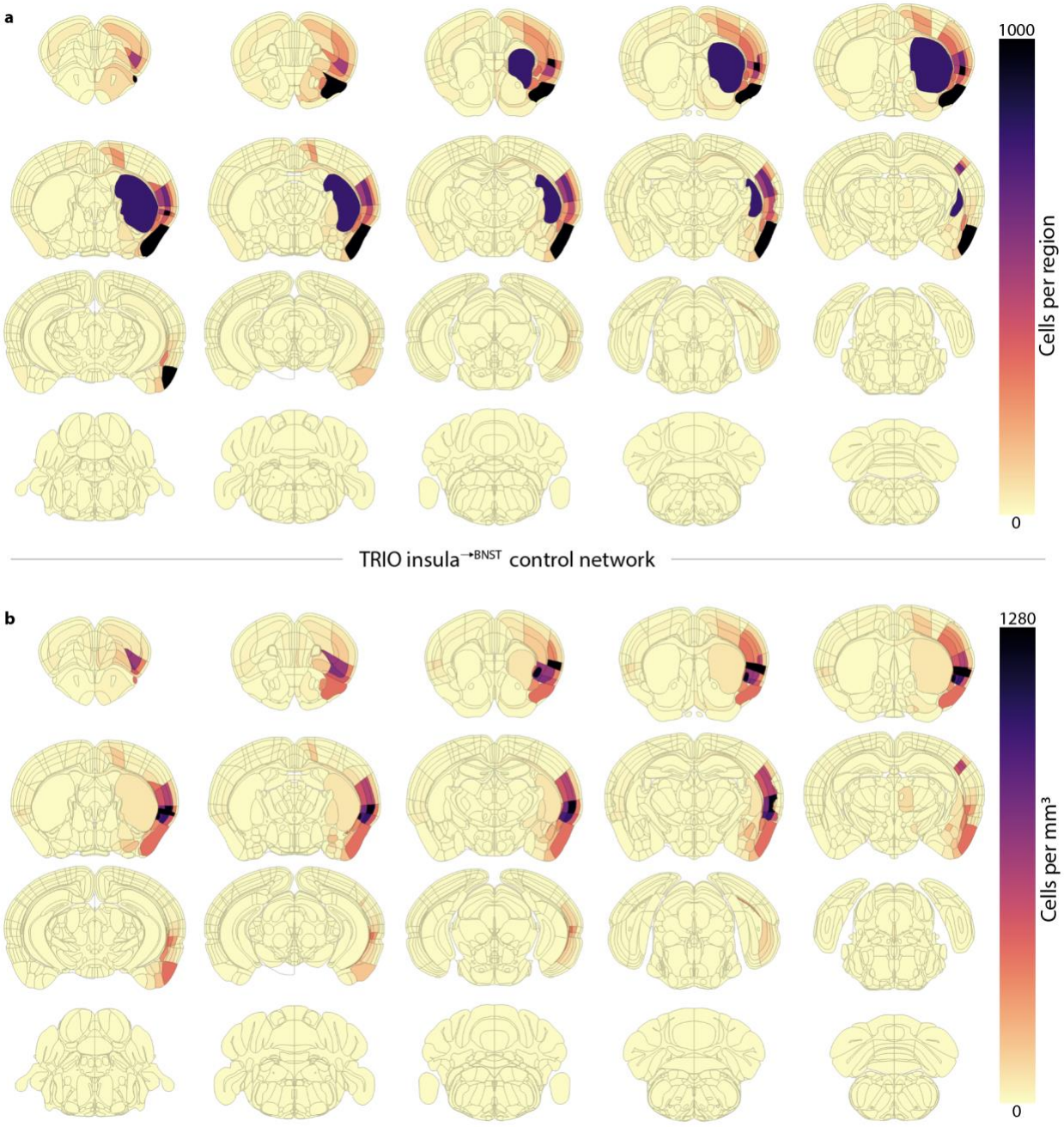

Figure 2.15: Expanded maps of the control network for the insula$^{\rightarrow BNST}$ pathway.

a, Raw cell counts of labeled cells represented as composite whole-brain heatmap showing relative number of cells that project to insula$^{\rightarrow BNST}$ neurons (averaged from five mice). **b**, Complete set of levels from composite whole-brain heatmap showing regional cell density in mm^3 of cell per region that project to insula$^{\rightarrow BNST}$ neurons (averaged from five mice).

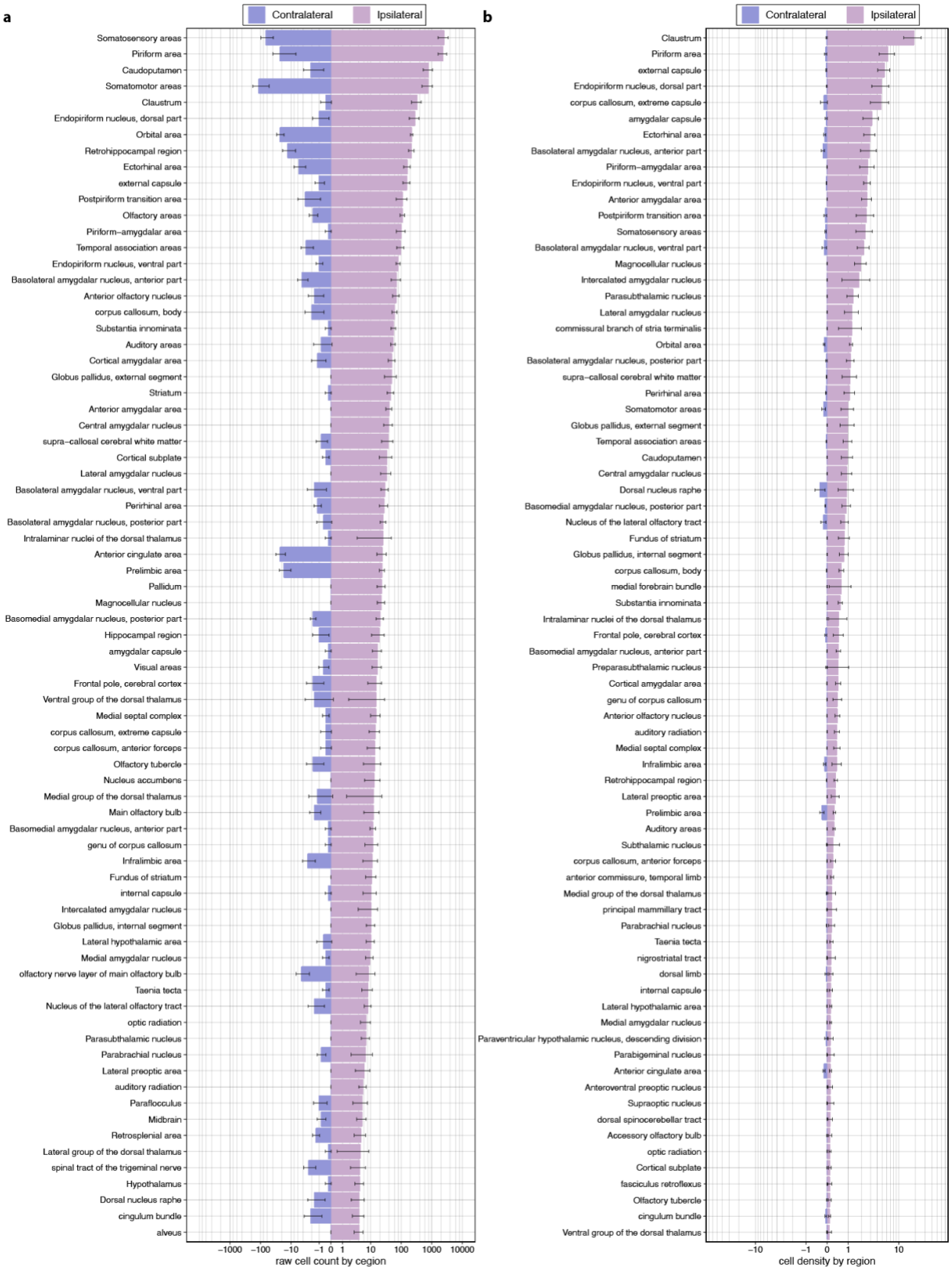
a
Contralateral
Ipsilateral
Somatosensory areas
Piriform area
Caudoputamen
Somatomotor areas
Claustrum
Endopiriform nucleus, dorsal part
Orbital area
Retrohippocampal region
Ectorhinal area
external capsule
Postpiriform transition area
Olfactory areas
Piriform–amygdalar area
Temporal association areas
Endopiriform nucleus, ventral part
Basolateral amygdalar nucleus, anterior part
Anterior olfactory nucleus
corpus callosum, body
Substantia innominata
Auditory areas
Cortical amygdalar area
Globus pallidus, external segment
Striatum
Anterior amygdalar area
Central amygdalar nucleus
supra–callosal cerebral white matter
Cortical subplate
Lateral amygdalar nucleus
Basolateral amygdalar nucleus, ventral part
Perirhinal area
Basolateral amygdalar nucleus, posterior part
Intralaminar nuclei of the dorsal thalamus
Anterior cingulate area
Prelimbic area
Pallidum
Magnocellular nucleus
Basomedial amygdalar nucleus, posterior part
Hippocampal region
amygdalar capsule
Visual areas
Frontal pole, cerebral cortex
Ventral group of the dorsal thalamus
Medial septal complex
corpus callosum, extreme capsule
corpus callosum, anterior forceps
Olfactory tubercle
Nucleus accumbens
Medial group of the dorsal thalamus
Main olfactory bulb
Basomedial amygdalar nucleus, anterior part
genu of corpus callosum
Infralimbic area
Fundus of striatum
internal capsule
Intercalated amygdalar nucleus
Globus pallidus, internal segment
Lateral hypothalamic area
Medial amygdalar nucleus
olfactory nerve layer of main olfactory bulb
Taenia tecta
Nucleus of the lateral olfactory tract
optic radiation
Parasubthalamic nucleus
Parabrachial nucleus
Lateral preoptic area
auditory radiation
Paraflocculus
Midbrain
Retrosplenial area
Lateral group of the dorsal thalamus
spinal tract of the trigeminal nerve
Hypothalamus
Dorsal nucleus raphe
cingulum bundle
alveus
−1000 −100 −10 −1 0 1 10 100 1000 10000
raw cell count by cegion
b
Contralateral
Ipsilateral
Claustrum
Piriform area
external capsule
Endopiriform nucleus, dorsal part
corpus callosum, extreme capsule
amygdalar capsule
Ectorhinal area
Basolateral amygdalar nucleus, anterior part
Piriform–amygdalar area
Endopiriform nucleus, ventral part
Anterior amygdalar area
Postpiriform transition area
Somatosensory areas
Basolateral amygdalar nucleus, ventral part
Magnocellular nucleus
Intercalated amygdalar nucleus
Parasubthalamic nucleus
Lateral amygdalar nucleus
commissural branch of stria terminalis
Orbital area
Basolateral amygdalar nucleus, posterior part
supra–callosal cerebral white matter
Perirhinal area
Somatomotor areas
Globus pallidus, external segment
Temporal association areas
Caudoputamen
Central amygdalar nucleus
Dorsal nucleus raphe
Basomedial amygdalar nucleus, posterior part
Nucleus of the lateral olfactory tract
Fundus of striatum
Globus pallidus, internal segment
corpus callosum, body
medial forebrain bundle
Substantia innominata
Intralaminar nuclei of the dorsal thalamus
Frontal pole, cerebral cortex
Basomedial amygdalar nucleus, anterior part
Preparasubthalamic nucleus
Cortical amygdalar area
genu of corpus callosum
Anterior olfactory nucleus
auditory radiation
Medial septal complex
Infralimbic area
Retrohippocampal region
Lateral preoptic area
Prelimbic area
Auditory areas
Subthalamic nucleus
corpus callosum, anterior forceps
anterior commissure, temporal limb
Medial group of the dorsal thalamus
principal mammillary tract
Parabrachial nucleus
Taenia tecta
nigrostriatal tract
dorsal limb
internal capsule
Lateral hypothalamic area
Medial amygdalar nucleus
Paraventricular hypothalamic nucleus, descending division
Parabigeminal nucleus
Anterior cingulate area
Anteroventral preoptic nucleus
Supraoptic nucleus
dorsal spinocerebellar tract
Accessory olfactory bulb
optic radiation
Cortical subplate
fasciculus retroflexus
Olfactory tubercle
cingulum bundle
Ventral group of the dorsal thalamus
−10 −1 0 1 10
cell density by region

Figure 2.16: Expanded data of the control network for the insula$^{\rightarrow BNST}$ pathway using light sheet imaging.

a, Raw cell counts from top 75 labeled upstream regions from unilateral insula$^{\rightarrow BNST}$ cells in five mice. Bars: Mean from all three counts per region. Error bars: s.e.m. across animals. Ipsilateral counts on the right in purple. Contralateral counts are on the left in blue. The x-axis is an inverse hyperbolic sine transformation. **b**, Density (in mm^3) of top 75 labeled upstream regions from unilateral insula$^{\rightarrow BNST}$ cells in each of five mice.

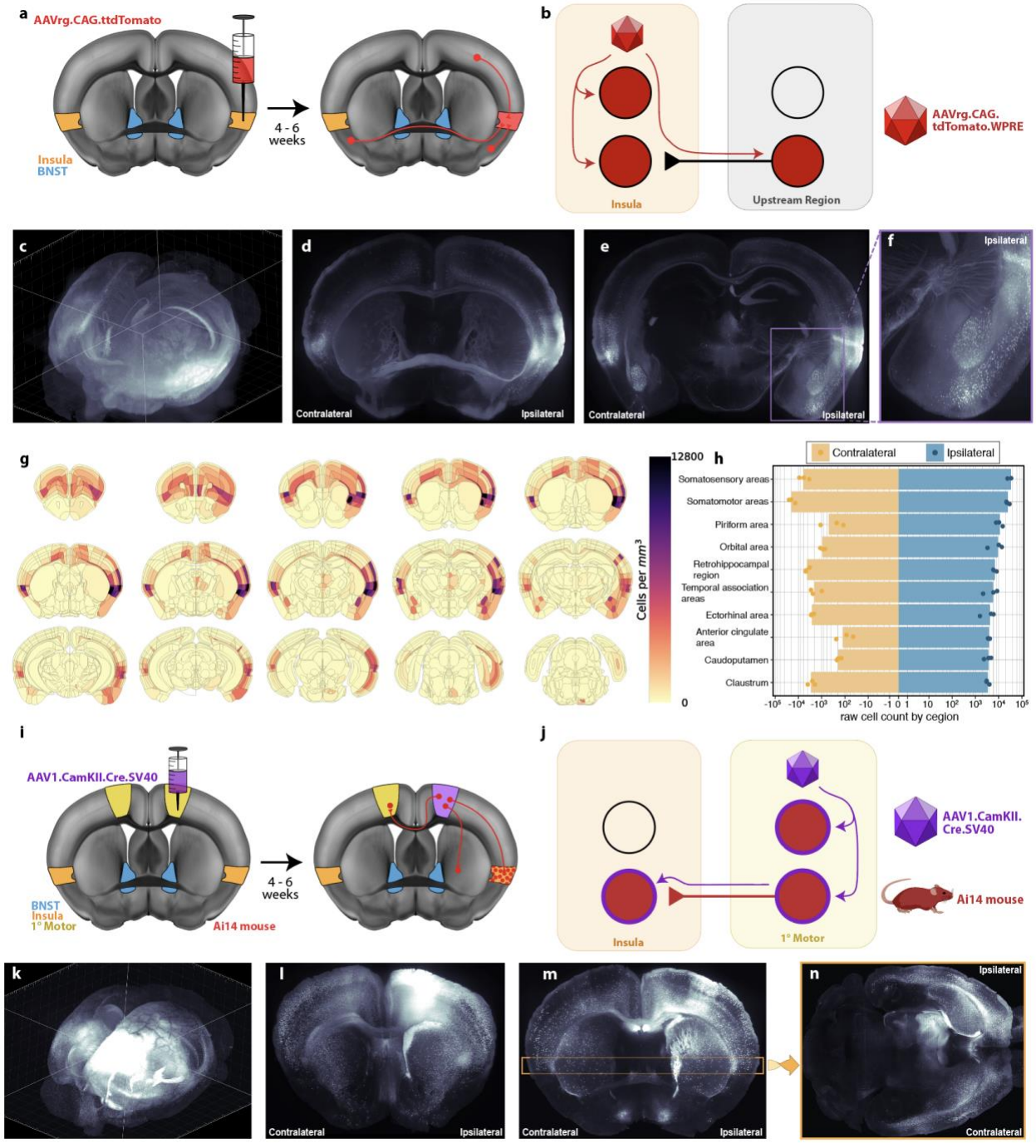
a
AAVrg.CAG.ttdTomato
Insula
BNST
4 - 6
weeks
b
Insula
Upstream Region
AAVrg.CAG.
tdTomato.WPRE
c
d
Contralateral
Ipsilateral
e
Contralateral
Ipsilateral
f
Ipsilateral
g
Cells per mm³
12800
0
h
Contralateral
Ipsilateral
Somatosensory areas
Somatomotor areas
Piriform area
Orbital area
Retrohippocampal region
Temporal association areas
Ectorhinal area
Anterior cingulate area
Caudoputamen
Claustrum
raw cell count by cegion
i
AAV1.CamKII.Cre.SV40
BNST
Insula
1° Motor
Ai14 mouse
4 - 6
weeks
j
Insula
1° Motor
AAV1.CamKII.
Cre.SV40
Ai14 mouse
k
l
Contralateral
Ipsilateral
m
Contralateral
Ipsilateral
n
Ipsilateral
Contralateral

Figure 2.17: The insular region that projects densely to the BNST receives input from motor cortex.

a, Diagram of AAVrg coding for tdTomato injection into the insula. Transduced neuron cell bodies, axons, and dendrites are labeled with tdTomato. **b**, Schematic of local insular and upstream viral infection. Cells that do not send projections to the injection site should not be labeled. **c**, 3D projection image of cellular labeling in whole mouse brain after AAVrg-tdTomato injection into the insula and subsequent light sheet imaging. Olfactory bulbs are in the bottom left corner, and the cerebellum is in the top right corner. **d**, Resampled image in coronal plane through the anterior BNST. The lack of labeled cells in the BNST indicates minimal direct BNST projections to the insula. **e**, Resampled image in coronal plane through the amygdala. The purple box illustrates the zoomed-in region in the following image. **f**, Magnified image of cells in the ipsilateral amygdala. **g**, Coronal sections from composite whole-brain heatmap (averaged from three mice with AAVrg.tdTomato injected into the insula) of cell density in mm^3. Cells were semiautonomously quantified using NUGGT[51]. **h**, Top ten labeled upstream regions from AAVrg.tdTomato injection into unilateral insula of 3 mice. Bars: Mean from all three counts per region. Points: Counts from individual animals. Ipsilateral counts on the right in teal. Contralateral counts are on the left in goldenrod. The x-axis is an inverse hyperbolic sine transformation. **i**, Diagram of AAV1.Cre injected into the motor cortex of an Ai14 mouse with downstream cells expressing tdTomato. **j**, Schematic of AAV1.Cre labeling downstream neurons. **k**, 3D projection image of a whole AAV1.Cre mouse (Ai14) brain injected in the motor cortex. Olfactory bulbs are in the bottom left corner, and the cerebellum is in the top right corner. **l**, Coronal view showing the injection site in motor cortex. **m**, Coronal view at the level of the BNST. The yellow outline indicates the transverse section through the insula shown in the

following image. **n**, Resampled image in the horizonal plane at the level of the insula (cerebellum = left, olfactory bulbs = right).

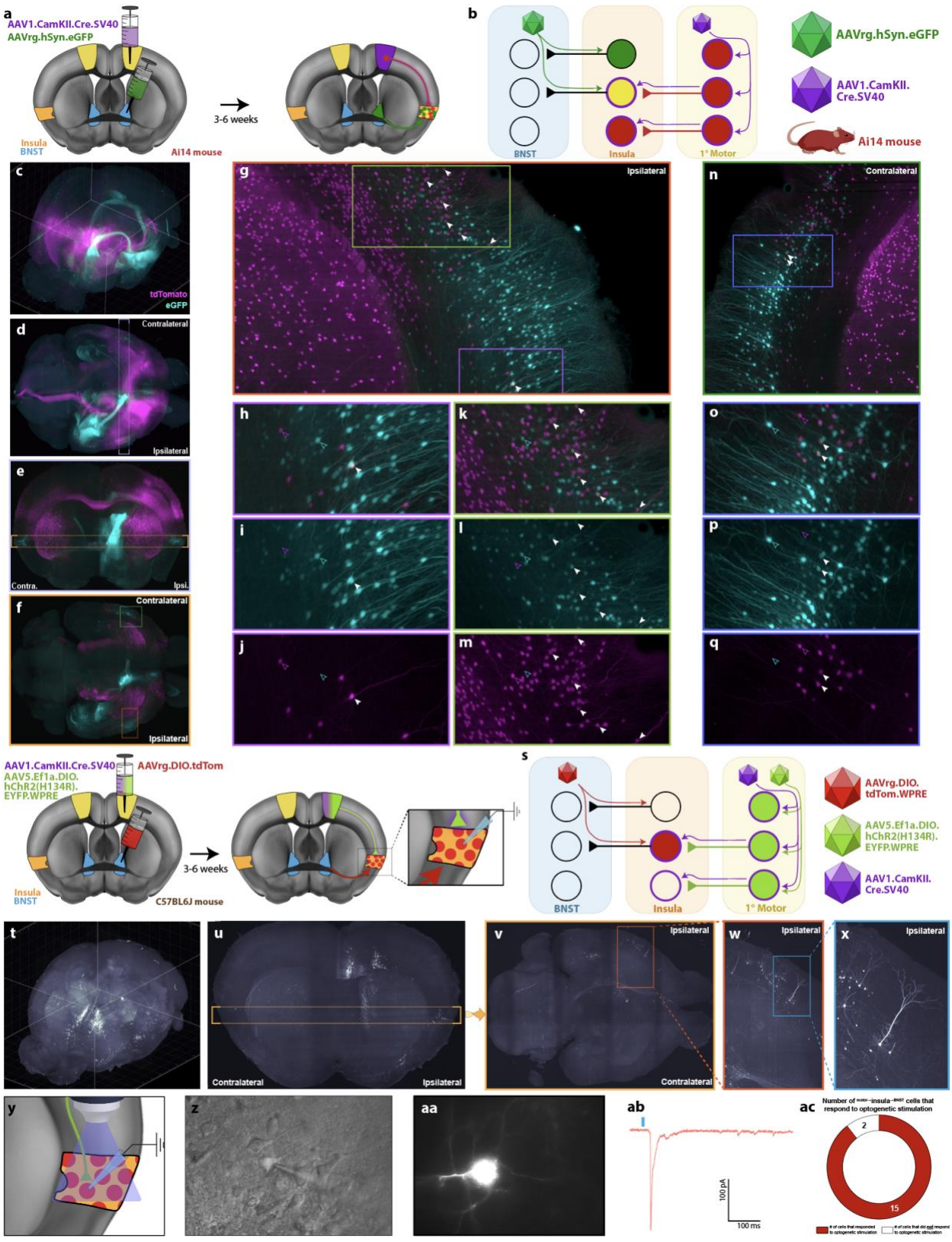
a
AAV1.CamKII.Cre.SV40
AAVrg.hSyn.eGFP
Insula
BNST
Ai14 mouse
3-6 weeks
b
BNST
Insula
1° Motor
AAVrg.hSyn.eGFP
AAV1.CamKII.
Cre.SV40
Ai14 mouse
c
tdTomato
eGFP
d
Contralateral
Ipsilateral
e
Contra.
Ipsi.
f
Contralateral
Ipsilateral
g
Ipsilateral
n
Contralateral
h
k
o
i
l
p
j
m
q
AAV1.CamKII.Cre.SV40
AAV5.Ef1a.DIO.
hChR2(H134R).
EYFP.WPRE
AAVrg.DIO.tdTom
Insula
BNST
C57BL6J mouse
3-6 weeks
s
BNST
Insula
1° Motor
AAVrg.DIO.
tdTom.WPRE
AAV5.Ef1a.DIO.
hChR2(H134R).
EYFP.WPRE
AAV1.CamKII.
Cre.SV40
t
u
Contralateral
Ipsilateral
v
Ipsilateral
Contralateral
w
Ipsilateral
x
Ipsilateral
y
z
aa
ab
100 pA
100 ms
ac
Number of motor–insula–BNST cells that
respond to optogenetic stimulation
2
15
# of cells that responded to optogenetic stimulation
# of cells that did not respond to optogenetic stimulation

Figure 2.18: Motor efferents directly synapse onto and activate insula$^{\rightarrow BNST}$ cells.

a, Diagram of AAVrg.eGFP injected into the BNST and AAV1.Cre injected into motor cortex of Ai.14 mice. **b**, Schematic of the viral strategy. AAVrg.eGFP retrogradely labeled insula$^{\rightarrow BNST}$ cells. AAV1.Cre labeled neurons that are downstream from the motor cortex. Neurons that were downstream from motor cortex and projected to the BNST were doubly-labeled. **c**, Maximum projection image for 3D reconstruction of whole-brain labeling; eGFP shown in cyan and tdTomato shown in magenta. Olfactory bulbs are in the bottom left corner, and the cerebellum is in the top right corner. **d**, Top-down view of whole-brain. Light purple outline indicates the slice taken for the next image. Olfactory bulbs are to the right. Cerebellum is to the left. **e**, Coronal slice taken at the level of the BNST. Yellow line indicates the transverse slice taken for the following image. **f**, Maximum intensity projection of a transverse slice taken at the level of the insula. Dark green and orange boxes indicate regions of the insula that project to the BNST. They are expanded later in the figure. **g**, Magnification of orange box from Fig. 2.2f. Image is ipsilateral to the injection site. Light green and purple boxes are expanded and split by channel in later images. White arrowheads indicate doubly-labeled neurons. **h**, Magnified image of purple box from Fig. 2.2g. Solid white arrowheads indicate doubly-labeled neurons. Cyan open arrowheads indicate eGFP-only labeling. Magenta open arrowheads indicate tdTomato-only labeling. **i**, eGFP-only channel from Fig. 2.2h. tdTomato signal does not bleed through (see open magenta arrowhead). **j**, tdTomato-only channel from Fig. 2.2h. eGFP signal does not bleed through (see open cyan arrowhead). **k**, Magnified image of light green box from Fig. 2.2g. **l**, eGFP-only channel from Fig. 2.2k. **m**, tdTomato-only channel from Fig. 2.2k. **n**, Magnification of dark green box from Fig. 2.2f. Image is contralateral to the injection site. Blue box is expanded and split by channel in later images. **o**, Magnified image of blue box from Fig. 2.2n. **p**,

eGFP-only channel from Fig. 2.2o. **q,** tdTomato-only channel from Fig. 2.2o. **r**, Diagram of the viral injections to isolate the $^{1°Motor}$→insula$^{→BNST}$ cells. A 1:1 ratio of AAV1.Cre and AAV5.DIO.ChR2.EYFP were injected into the motor cortex. AAVrg.DIO.tdTomato was injected into the BNST. We then performed whole-cell patch-clamp recordings on the labeled cells. **s**, Schematic of viral labeling. AAVrg.DIO.tdTomato infects cells that project to the BNST, but will only cause the expression of tdTomato in the presence of Cre. AAV1.Cre will infect neurons that are downstream from the motor cortex. Thus, only neurons that are both downstream of the motor cortex and send projections to the BNST are labeled. ChR2 is expressed in neurons in the motor cortex and their efferents. **t**, Maximum projection image for 3D reconstruction of whole-brain labeling to illustrate $^{1°Motor}$→insula$^{→BNST}$ cells. **u**, Resampled image in coronal plan at the level of the BNST. Yellow box indicates the transverse slice taken for the following image. **v**, Resampled image in transverse plane through the insula. Orange box is magnified in the next image. **w**, Magnified view of orange box (ipsilateral to the injection site) in Fig. 2.2v. Light blue box is magnified in next image. **x**, Magnified view of light blue box in Fig. 2.2x. Examples of $^{1°Motor}$→insula$^{→BNST}$ cells. **y**, Diagram of whole-cell patch-clamp experiment to verify motor input onto presumptive $^{1°Motor}$→insula$^{→BNST}$ cells. **z**, DIC image with pipet next to insula neuron. **aa**, Example of fluorescently labeled $^{1°Motor}$→insula$^{→BNST}$ cells visible on the electrophysiology rig. **ab**, Example of optically evoked postsynaptic current after blue light stimulation (blue bar). **ac**, Number of patched tdTomato-positive cells that responded to light.

labeled cells, providing further distributional information about the location of the diffuse insular neurons involved in the ^{motor}→insula$^{→BNST}$ pathway.

Next, we aimed to determine if motor cortex afferents could drive insula$^{→BNST}$ neurons (i.e., if the ^{motor}→insula$^{→BNST}$ represents a functional synapse). We used alternative viral strategies to confirm the doubly-labeled cells' identity and then provide efficient visual identification for whole-cell patch-clamp. We injected AAV1.Cre into the motor cortex and a Cre-dependent AAVrg.DIO.tdTomato into the BNST before processing the tissue for whole-brain imaging (Fig 6r,s). Consistent with our findings above, light sheet microscopy revealed specific insular distributions most densely distributed in the mid and posterior insula, demarcating a circuit from $^{1°Motor}$→insula$^{→BNST}$ (Fig. 2.18t-x). Finally, to verify monosynaptic connectivity and functionality of this synapse, we performed channelrhodopsin-assisted circuit mapping (CRACM)[478] with whole-cell patch-clamp in similarly tagged insula cells while stimulating motor terminals (Fig. 2.18y-z). We injected channelrhodopsin into the primary motor cortex and recorded whole-cell currents from insula$^{→BNST}$ cells (tdTomato-positive cells). Blue light stimulation resulted in a reliable optically-evoked excitatory post synaptic current (oEPSC) in 15 of the 17 (or ~88%) labeled cells we patched (Fig. 2.18ab-ac). This suggests that the labeled cells, which project from the insula to the BNST, receive functional input from cortical motor neurons.

2.2.6 Primary motor cortex neurons projecting to the mid-insula (motor$^{→insula}$) increase signaling prior to the initiation of a struggle bout.

Our findings suggest somatomotor projections to the insula can functionally impact insula neuron signaling. However, the contribution of insula-projecting motor cortex neurons to struggling behavior is unknown. To investigate this further, we isolated motor$^{\rightarrow insula}$ neurons by virally transducing mid-insula neurons with retrograde AAVrg.Cre and injecting Cre-dependent GCaMP7f into the primary motor cortex (1°Motor). We then placed a fiberoptic implant in the motor cortex (Fig. 2.19a-c). After 4-6 weeks, mice were subjected to restraint stress while simultaneous GCaMP measurements were collected. We detected a distinct signaling pattern from those observed in the insula and BNST, as an increase in calcium signaling in motor$^{\rightarrow insula}$ cells preceded the bout onset (Fig. 2.19d-e). The signal then returned to baseline before significantly increasing again shortly after the bout onset. As opposed to the insula signals, the maximum peak occurred several seconds after the struggle bout onset (Fig. 2.19d-e). Further, there was no correlation between bout length and AUC or maximum peak amplitude (Fig. 2.19f-m). Thus, motor$^{\rightarrow insula}$ cells represent a distinct population of neurons recruited both prior to and during motor action.

2.3 Discussion

Effective stress coping strategies are critical for survival, yet how coping strategy participation is encoded across neuronal circuits is not well understood. Here we delineated a circuit involved in affective behavior that encodes active struggling during restraint stress, a potential correlate to active stress coping in mice. In this study, we delineate a mid-insula→BNST^{CRF} neuron circuit that is recruited in tight association with struggling events. Even though this circuit's activity closely followed struggling behavior, chemogenetically manipulating this circuit did not alter

struggling during restraint. It did, however, change post-stress avoidance after the stressor, indicating this pathway encodes aspects of stress coping or its resultant outcome.

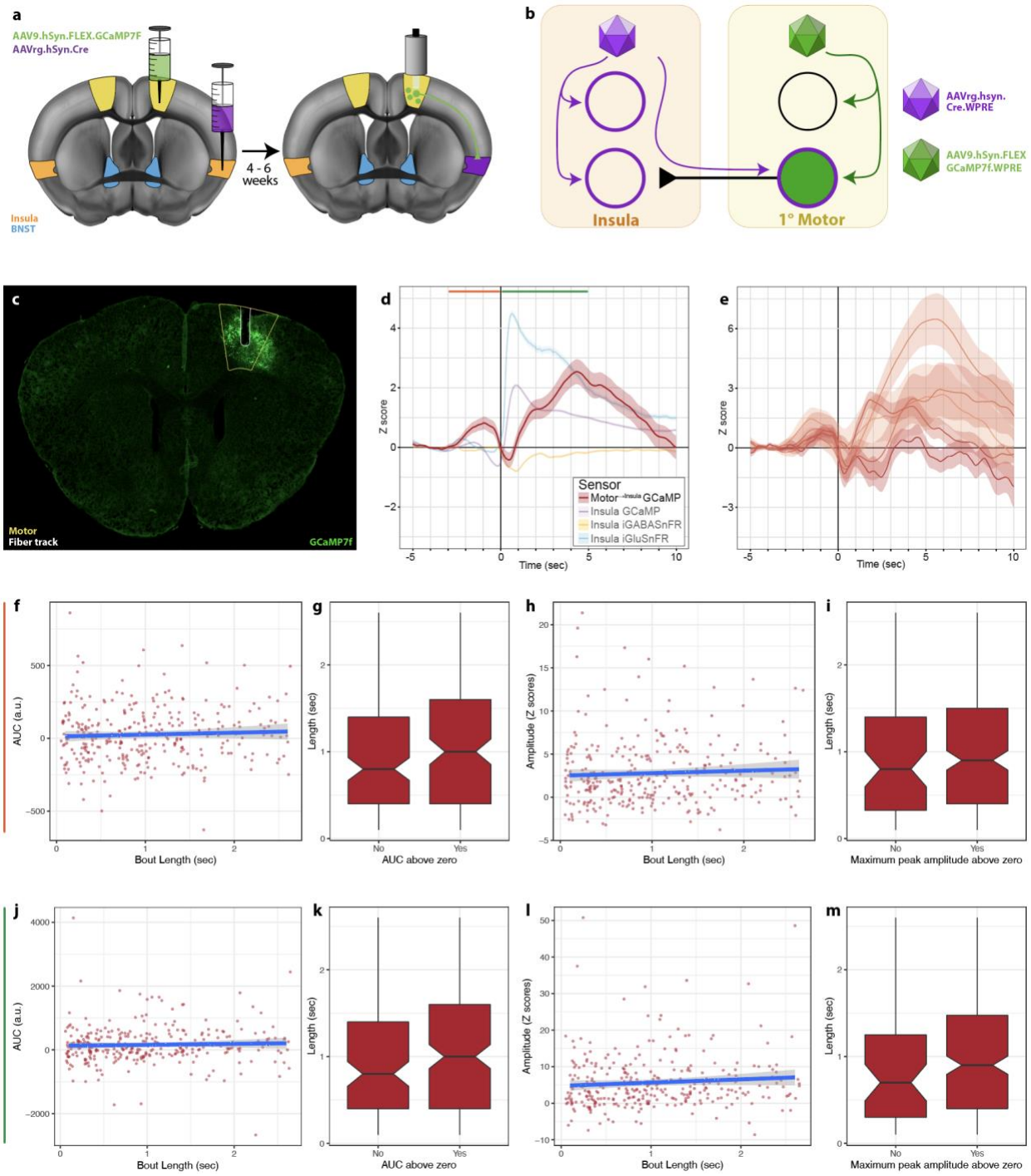

Figure 2.19: 1°Motor$^{\rightarrow insula}$ cells are engaged during struggling.

a, Diagram of AAVrg.Cre injected into the insula, AAV9.FLEX.jGCaMP7f injected into motor cortex and fiberoptic implant into the motor cortex. (In collaboration with Sam Centanni.) **b**, Schematic of the viral strategy. AAVrg.Cre retrogradely expressed in 1°Motor$^{\rightarrow insula}$ cells. GCaMP7f is then cre-dependently expressed exclusively in neurons that send direct projections to the insula. **c,** Representative histological coronal slice. Fluorescent channel: GCaMP7f (green); lines: 1°Motor cortex (yellow), Fiber track (white). **d**, Average of all bout-associated signals from GCaMP in 1°Motor$^{\rightarrow insula}$ cells (red). Insular recordings from Fig. 3e are included as faded colors for comparison. Insular GCaMP (purple), SF-iGluSnFR (blue), or iGABASnFR (yellow). See Fig. 3e for details. Lighter shading: s.e.m. across bouts. Green and orange lines at the top of graph indicate the corresponding windows for AUC and maximum peak amplitude analysis. From -3 to 0 seconds preceding bout onset (orange) corresponds to Figs. f-i. From 0 to 5 seconds following bout onset (green) corresponds to Figs. j-m. **e**, Average bout-associated signals separated by animal. **f-i,** Analysis of 1°Motor$^{\rightarrow insula}$ GCaMP during window from -3 to 0 seconds preceding bout onset. **f**, AUC vs. bout length (sec). Blue line slope of AUC vs. bout length with 95% confidence interval. $r_{(307)} = 0.047$, p = 0.412. **g,** Bout length of bouts with an AUC above zero (‘yes’= above zero) vs. those with an AUC not above zero (‘no’= not above zero). Welch two-sample t-test, $t_{(307)} = -1.6177$, P = 0.1068. **h**, Maximum peak Z score amplitude vs. bout length (sec). Blue line slope of maximum peak vs. bout length with 95% confidence interval. $r_{(307)} = 0.0515$, p = 0.366. **i,** Bout length of bouts with a maximum peak above zero vs.

those with a maximum peak not above zero. Welch two-sample t-test, $t_{(119.69)} = -1.6229$, P = 0.1072. **j-m,** Analysis of 1°Motor$^{\rightarrow insula}$ GCaMP during window from 0 to 5 seconds following bout onset. **j**, AUC vs. bout length (sec). Blue line slope of AUC vs. bout length with 95% confidence interval. $r_{(307)} = 0.036$, P = 0.5285. **k,** Bout length of bouts with an AUC above zero vs. those with an AUC not above zero. Welch two-sample t-test, $t_{(266.15)} = -1.5977$, P = 0.1113. **l**, Maximum peak Z score amplitude vs. bout length (sec). Blue line slope of maximum peak vs. bout length with 95% confidence interval. $r_{(307)} = 0.086$, P = 0.157. **m,** Bout length of bouts with a maximum peak above zero vs. those with a maximum peak not above zero. Welch two-sample t-test, $t_{(72.93)} = -1.5534$, P = 0.1247.

We also explored the relationship between insular signaling and struggling duration during repeated restraint stress. While a correlation between extracellular glutamate signal size and bout length remained stable over time, this relationship collapsed with repeated homotypic stress for both inhibitory and local calcium signals. This divergence may indicate that plasticity during homotypic stress occurs downstream of the glutamate afferents into the insula.

To begin to assess plausible neuronal paths for incoming information to reach this circuit, we generated extensive input maps for the insula$^{\rightarrow BNST}$ control network and identified prominent afferent regions. These findings show, for the first time, tightly correlated struggling-related activity in the cortical insula and subcortical BNST, along with an upstream network that includes significant motor, somatosensory, and amygdalar components. Given that the struggling bout is a motoric program, we chose to investigate the large motor input, characterizing the motor$^{\rightarrow insula}$ pathway's activity at struggling onset. We discovered that its calcium activity slightly preceded behavior initiation. Thus, we hypothesize this input may be a mechanism by which executive motor control circuits can inform interoceptive and affective circuits.

2.3.1 BNST ^{CRF} neurons encode active struggling behavior during an inescapable stressor.

Distinct subnuclei of the BNST process sustained fear states and the capacity to respond to threats via a network of topographically organized connections that extend throughout the brain[287,479]. CRF neurons in the BNST have been implicated in reinforcement/consumptive behaviors, and appear to play a role in regulating negative affective state[303,358,480]. Our findings

demonstrate that these cells monitor struggling responses. Consistent with previous work implicating $BNST^{CRF}$ cells in stress responses[159], we show that increased $BNST^{CRF}$ cell calcium transient signals are robustly time-locked to the onset of struggling bouts (Fig. 2.3f-h). Struggle bout-associated glutamate transients in the BNST suggest a circuit dependence to these signals (Fig. 2.3i-k). Together, these findings are consistent with Lebow et al.'s proposed "valence surveillance" role for the BNST in which this region integrates internal mood and arousal with external contexts to coordinate fight or flight via the HPA axis[287]. Our work expands this view to incorporate monitoring the impact of motor action on a subject's state. While the direct correlation of struggling behavior to stress coping in mice remains to be explored, the relationship between the struggling bouts and activity in BNST and BNST-connected circuits suggests this behavior is at least partly related to larger coping mechanisms. Consequently, we propose that the BNST may be involved in a larger network surveilling struggling actions when exposed to an inescapable stressor.

2.3.2 The insula sends a dense, unidirectional input to the lateral BNST ($insula^{\rightarrow BNST}$) that serves as a conduit for encoding struggling behavior information and alters BNST function and affective behavior.

Gogolla[422] proposed that the variety of afferents (e.g., sensory, limbic, autonomic, and frontal) converging in the insula may be a setting for cross-functional association. The distribution of inputs that we found to be retrogradely labeled from our injection site in the insula (Fig. 2.6a-i) bolsters the idea that the insula may indeed link internal state with external cues. There is also evidence that in rodents, the mid-insula is involved in valence computation[481]. Thus, the insula could be a critical node for the coalescing of state information, assigning it a

valence, and passing it on to relevant network structures to engage the most appropriate response.

Recent human studies suggest insular-BNST interactions may be important across species[482]. Here, we identified the region of the mouse insula with the densest projection to the BNST (near AP = 0.0) and chemogenetically inhibited this area to determine its role in modulating the stress-responsive $BNST^{CRF}$ cells. Indeed, decreasing insular activity with inhibitory G_i-DREADD decreased restraint-induced *fos* in $BNST^{CRF}$ neurons, indicating insular inputs can modulate the engagement of these cells during a stressor (Fig. 2.7a-c). This is in agreement with our previous work, demonstrating that insular G_i-DREADD activation can decrease excitatory drive onto BNST cells[159]. To interrogate the insular signaling responsible for this change, we used *in vivo* fiber photometry to record insular signaling during restraint. As in the BNST, insular calcium signals were tightly associated with struggling behavior in the RESTRAINT device (Fig. 2.7d-f). This insular calcium transient was paralleled by a tightly coupled decrease in GABA release and increased glutamate release (Fig. 2.7d-f), suggesting that altered excitatory-inhibitory balance leads to insular recruitment of BNST. Interestingly, bout duration was positively correlated with insula GCaMP and SF-iGluSnFR signal and negatively correlated with iGABASnFR signal. Repeated exposure to the homotypic stressor resulted in decreased correlation with GCaMP and iGABASnFR, but not SF-iGluSnFR signal providing intriguing mechanistic insight into the relationship between stress habituation and insular microcircuitry. Further, rimonabant restored the correlation for GCaMP but not iGABASnFR, suggesting rimonabant-induced anxiogenesis is not mediated through inhibition of insular GABA signaling.

We additionally assessed real-time changes in struggle event-associated calcium transients in the BNST by manipulating the insular input. G_q-DREADD, specifically targeted to insula$^{\rightarrow BNST}$ cells, increased the mean peak amplitude of BNST active struggle event-associated calcium signals following CNO administration (Fig. 2.11a-h). Activating this subset of cells also increased subsequent anxiety-like behavior and BNST calcium transient frequency during behavioral testing (Fig. 2.11i-l). Taken together, we propose that these findings indicate that the struggle response engages the insula$^{\rightarrow BNST}$ pathway.

2.3.3 The insula$^{\rightarrow BNST}$ control network reveals significant motor and premotor cortical input.

Our initial brain-wide retrograde AAV tracing experiment demonstrated a dense insular projection to the BNST (Fig. 2.6a-i). Later, in order to determine paths by which motor regions might transmit information to the insula, we used a retrograde viral tracing strategy to label cells across the brain from the insular region that projected most densely to the BNST (Fig. 2.17a-h). This strategy was not specific to the inputs of insula$^{\rightarrow BNST}$ neurons. Next, using a whole-brain imaging approach and monosynaptic rabies tracing, we created a global map of the upstream control network for the insula$^{\rightarrow BNST}$ pathway specifically. The rabies virus labeled cells in multiple brain regions, including many regions anticipated from previous traditional tracer studies, such as somatosensory cortex and parafascicular nucleus of the thalamus[483]. Moreover, neurons in the premotor and motor cortex were heavily represented.

As a convergent anatomical strategy, we combined retrograde (from the BNST) and anterograde (from the 1°Motor) viruses and identified insula$^{\rightarrow BNST}$ neurons that receive inputs from 1°Motor cortex. We later confirmed functional connectivity of this synapse using

channelrhodopsin-assisted mapping and whole-cell patch-clamp electrophysiology (Fig. 2.18). Doubly-labeled cells were sparse yet consistently found bilaterally in the insula, providing evidence of direct motor input onto affective state control circuitry (Fig. 2.18g-q). A far greater proportion of cells were infected with only one virus, yet, when compared with other regions, these two populations of singly infected cells appeared to be intermixed in the insula to a greater degree. This could be evidence of an avenue for polysynaptic modulation of an affective circuit by the motor cortex. Of note, while we focused on insular cells that project to the BNST, our results do not imply that insula$^{\rightarrow BNST}$ cells are the sole subpopulation receiving the identified inputs. Instead, we suspect it is more likely that the regional weights of the upstream distribution would differ based on the selected insular output or subpopulation. Previous insular mapping studies demonstrate distinct distributions of inputs to insular neurons, and moreover, the various outputs of insular neurons are largely discrete[416,429]. This suggests that monosynaptic tracing studies with different insula starter populations could yield unique upstream circuit maps involved in varying insula-related behaviors.

It bears noting that AAV1.Cre viral labeling is known to have retrograde properties, which can complicate interpretation when used in a bidirectional circuit[484,485]. The insula$^{\rightarrow BNST}$ pathway appears unidirectional (Fig. 2.18d)[429], thus greatly limiting spurious labeling. However, we cannot rule out this possibility for insula$^{\rightarrow 1°Motor}$ cells. We used numerous convergent techniques to mitigate that potential ambiguity. In addition, AAV1.Cre labeling may be activity dependent[485]. If this is indeed the case, low-activity or silent synapses could be falsely omitted. However, it is unlikely that this dependency would lead to false-positive cells; rather, under-sampling the cells that receive input is a more likely scenario.

2.3.4 Motor pathways to BNST-projecting insular neurons reveal a path for motor planning information to potentially influence affective circuitry.

This study provides the first evidence for a novel functional pathway by which affective circuitry can be directly informed of motor activity by structures involved in motor planning. While the BNST, central to longitudinal threat evaluation, receives no detectable direct motor input based on our tracing studies, the insula receives strong, broadly somatotopically distributed input from cortical motor regions. While a number of studies have outlined the role of physical activity in the regulation of affective behavior, they have focused on feedback mechanisms by which peripheral metabolites and other peripheral signals may convey information to the CNS to alter mood[486–489]. The present work identifies a unique feedforward pathway by which information relevant to physical activity can regulate affective circuitry directly, and we hypothesize that this may be consistent with the concept of efference copy that has been applied in other fields.

Efference copy is defined as collateralized information that works in parallel to the signals directly involved in motor action. This is a mechanism by which the brain can compare predicted actions to resultant outcomes and sensations[490]. The ability to maintain an undisturbed visual field during saccades and the inability to tickle one's self are functional examples of motor efference copy[491–493]. Thus, we propose that the motor$^{\rightarrow insula}$ pathway may represent an efference copy through which the insula$^{\rightarrow BNST}$ pathway acts as a motor surveillance system. The motor projections to the insula$^{\rightarrow BNST}$ may relay predicted motor action outcomes. In our restraint model, the discrepancy between the anticipated outcome from struggling and the reality of remaining restrained may generate and maintain the negative affective state associated with an inescapable stressor, driving increased activity in the insula and BNST.

Consistent with an efference copy model, G_q-DREADD activation of insula$^{\rightarrow BNST}$ neurons did not alter the number of struggle bouts (but did alter BNST activity), nor did the inactivation of mid-insula with a Gi-coupled DREADD (Fig. 2.13a-j). These results could suggest a model through which struggling behavior and affective state are basally correlated as a result of efference copy. In this theory, chemogenetically altering insula$^{\rightarrow BNST}$ activity could dissociate struggling behavior from affective state, resulting in altered affect without impacting struggling behavior. To our knowledge, this is the first model to incorporate an affective/interoceptive circuit into the efference copy theory. While further studies are needed to directly test this idea, this foundational work may help pave the way for future convergent studies exploring the involvement of feedforward motor pathways contributing to situational affective state.

Notably, increased activity in motor$^{\rightarrow insula}$ neurons appeared to be left-shifted compared to struggling behavior onset and average insular glutamate and calcium transients. Because we hypothesize the motor input communicates movement planning/initiation, this signal preceding movement would be predicted. The motor$^{\rightarrow insula}$ signals were recorded in motor cortex while the other recordings were conducted in the insula or BNST, thus confounding true temporal comparisons between these transients. It should be noted that motor innervation is not the only glutamatergic afferent for this circuit, and that other inputs may also play important roles in driving this activity. Indeed, we found that the amygdala sends a strong input to insula$^{\rightarrow BNST}$ cells, and moreover, the density of somatosensory input onto these neurons was greater than that of the motor input. We suspect it is likely that these and other regions participate in regulating the insula$^{\rightarrow BNST}$ pathway by passing other relevant data. For example, it is conceivable that sensory and affective information feed into the insula$^{\rightarrow BNST}$ pathway via the somatosensory

cortex and amygdala, respectively. In contrast to the BNST however, our AAV1-Cre data indicate that the motor cortex connects densely with both of these regions, thus information shaped by motor commands may also reach the insula$^{\rightarrow BNST}$ circuitry through polysynaptic connections in other brain areas. More studies will be needed to fully elucidate the breadth of functions held by the insula$^{\rightarrow BNST}$ pathway and its afferent and efferent networks. In all, this work provides foundational evidence that the insula$^{\rightarrow BNST}$ pathway is part of a large and diverse system governing affect following a stressor, and we anticipate ensuing work will determine the distinct roles of relevant inputs to this pathway.

2.4 Methods and Materials

2.4.1 Animals

The mice used in this study were female and at least 8 weeks old. C57BL/6J mice (RRID:IMSR_JAX:000664; The Jackson Laboratory) were delivered at 6 weeks of age and acclimated for 2 weeks prior to intervention. Crh-IRES-Cre (RRID:IMSR_JAX: 012704; The Jackson Laboratory) and PKCδ -Cre mice (RRID:MMRRC_011559-UCD; Mutant Mouse Resource & Research Centers) were bred in-house to be heterozygotes[494]. Homozygous Ai14 (RRID:IMSR_JAX: 007908; The Jackson Laboratory) mice were used[495]. Transgenic lines were maintained on a C57BL/6J background. All mice were housed with two to five mice per cage and provided food and water *ad libitum*. Light/dark cycle was 12 hours (lights on = 0600 h) with controlled humidity (30%-50%) and temperature (20-25°C). Behavioral testing and surgeries were conducted during the light phase. The Vanderbilt Animal Care and Use Committee approved procedures and interventions.

2.4.2 Reagents

Clozapine-*N*-oxide (CNO) (Sigma-Aldrich #C0832, >98%;) was diluted in sterile saline (3 mg/10 ml = 875 µM) and delivered intraperitoneally at a dose of 3 mg/kg.

Adeno-associated viruses (AAVs) were used as received unless otherwise specified. TREtight-mTagBFP2-B19G and syn-FLEX-splitTVA-EGFP-tTA were diluted 1:20 and 1:200 in sterile, filtered PBS and subsequently mixed 50/50 by volume.

2.4.3 Stereotaxic surgeries

Mice (>8 weeks) were anesthetized with isoflurane (3% initial dose, 1.5% maintenance dose) for intracranial recombinant AAV injection and fiberoptic cannula implant surgeries using a Leica Angle Two Small Animal Stereotaxic Instrument. Mice were injected with 300 nL of the indicated AAV at a rate of 50 nL/min driven by a Micro4 MicroSyringe pump (World Precision Instruments) into the specified region. The needle (World Precision Instruments Nanofil syringe fitted with a Nanofil 33G Blunt Needle) remained in place for an additional five minutes. All mice recovered for at least three weeks before further experimentation. Injection and implantation sites included insular cortex (from Bregma: AP=0.02, ML±3.66, DV=-4.30, 0° angle), dorsal BNST (from Bregma: AP=0.14, ML±0.88, DV=-4.24, 15.03° angle), and primary motor cortex (from Bregma: AP=1.60, ML±1.10, DV=-1.80, 15.03° angle). All mice received 5 mg/kg injections of meloxicam for once a day for 2 days following surgery.

2.4.3.1 Chronic optical fiber implantation specific procedures

Once the skull was exposed, it was etched with a gel etchant (Kerr Dental). One stainless steel mounting screw (PlasticsOne) was installed in the ipsilateral parietal plate posterior to the implant hole. The implant was bonded by applying Optibond Primer followed by Optibond Adhesive, which was then cured with UV light. Herculite Enamel was molded around the screw, implant, and skull. The enamel was then cured with UV light.

Fiberoptic implants for the ChiSquared Bioimaging system were constructed in house using a 0.22 NA, 300 μm core multimode fiber (Thorlabs). Fibers were cut to length using a DualScribe Wedge Tip Carbide Scribe (Ideal Industries) and secured inside a mounting ferrule with Epo-Tek general room temperature cure epoxy (Fiber Optic Center) and cured at 45°C overnight. The end to remain exposed was then cut to be flush with the implant and polished using a ferrule polishing disk (Thorlabs) and progressively finer (5, 3, 1, 0.1 μm) aluminum oxide lapping sheets (Thorlabs). Fibers were tested prior to implantation to ensure >90% power output. Mono fiber-optic cannulas (Doric Lenses) for the TDT system were purchased at the appropriate lengths for each brain region.

2.4.4 Restraint Stress

RESTRAINT (**RE**cording **S**ignal **TR**ansients **A**ccessible **IN** a **T**ube) device: The base was made from clear acrylic (McMaster-Carr). The screw and rear-guard components were made from extra plastic from our machine shop (Vanderbilt Kennedy Center Scientific Instrumentation Core). See diagram for detailed dimensions (Supplementary Fig. 1a-e).

Fibers were attached to each animal's implant with a stainless-steel sleeve (inner diameter = 400 µm) before the animal was placed inside the restraint device. Restraint exposure lasted 30 or 60 minutes. Video was captured with a webcam (Logitech), and movements were tracked using DeepLabCut.

Drug delivery: CNO was administered i.p. 30 minutes prior to restraint at a dose of 3 mg/kg. Equal volume saline was administered to the vehicle groups.

2.4.5 Behavioral scoring

All videos were acquired at ten fps using a Logitech C920 camera. For experiments detailed in Figures 1d-e, 2l-n, behavioral scoring was done manually using Anvil 6.0 video annotation software. Behavioral bouts were counted if the tail head and tail movement were visible on the recording. Bouts were considered contiguous if they were separated by less than 0.7 seconds. Automated video scoring was performed using DeepLabCut to track points across time and was based on the methods used for manual scoring[464,465]. The fiberoptic cable and the tip of the tail were manually located in each image of a training set made up of >15 images per video. A small green piece of tape was placed on the fiberoptic cable to ensure a consistent location during training and testing. DeepLabCut was trained for at least 200,000 iterations. We used R statistical software with the "tidyverse" package to convert X/Y position into speed of movement for the fiber and the tail during each frame[496,497]. To identify bouts, we first identified frames in which the fiber and tail were moving. We determined if the tracked objects were moving by setting speed thresholds (selected via trial and error) that were independently set for both the fiber and the tail tip. For the fiber, any frame with a speed greater than one standard deviation

above the bottom 95% of frame speeds was considered mobile. For the tail tip, the threshold was set at three standard deviations above the bottom 99% of tail tip frame speeds. The use of a normalized speed, rather than a raw pixel-based speed threshold, provided better consistency across trials because it accommodated slight changes in camera distance and restraint device position. When a tracked point transitioned from an immobile to a mobile state, that frame became time "0.0" for a bout. The bout continued until all tracked points were in an immobile state for greater than 0.7 seconds (to limit significant bout overlap). We observed three bout types: 1) movements of the head only, 2) movements of the tail only, 3) movements that included both head and tail movements, termed full body. Unless otherwise noted, we specifically focused our analysis on full body movements. To make the analysis uniform across bouts, AUC and maximum peak amplitude were calculated for the 5 seconds following bout onset independent of bout length. We used R with the "pheatmap" package to create the time-locked photometry heatmaps[498]. Figures were generated in R with the "ggplot2" package[499].

2.4.6 Wheel running

Training: One week prior to testing, we placed a low-profile running wheel (Med Associates) in the home cages of the mice to be tested, for 48 hours. These wheels use the Fast Track 100% PETE plastic wheel surface from Bio-Serve (K3250). The wheel was removed for the 5 days preceding testing.

Testing: Animals with fiberoptic implants had free access to the same style of low-profile running wheel for 30 minutes in their home cage. Running behavioral scoring was done manually using Anvil 6.0 video annotation software. Running was defined as being both on the

wheel and running (i.e., not standing on the wheel nor swinging back and forth on the wheel were counted).

2.4.7 *In vivo* fiber photometry

The ChiSquare χ^2-202 System (ChiSquare Biomaging) was one fiber photometry system used in this study. Briefly, blue light from a 473-nm picosecond-pulsed laser (50 MHz; Becker & Hickl) was directed onto a GFP dichroic filter (MD498, Thorlabs) and coupled using a FC/PC fiber coupler (Lasos) into a multimode fiber patch cord (FG105UCA, 0.22 N.A., 105/125 µm diameter core/cladding, Thorlabs) terminating in the ferrule described above. Fluorescence emission from the tissue was collected through the same fiber transmitting the blue light using a fiber coupler (Thorlabs) into a 200 µm diameter core, anti-reflection-coated multimode fiber (M200L02S-A, Thorlabs), filtered through a 550/49 nm single bandpass filter (Semrock) and dispersed into spectra by a polychromator (Becker and Hickl). Individual photons were detected and recorded by a time-correlated single-photon counting (TCSPC) module (Becker and Hickl) at a frequency of 50 Hz. The shape, location, and amplitude of the TCSPC-derived fluorescence spectrum were used to confirm *in vivo* GCaMP expression.

A Tucker-Davis Technologies (TDT) RZ5P fiber photometry system and Synapse software were also used in this study. Briefly, light from the 470 nm, 17.2 mW (Min) fiber-coupled LED (Thorlabs) and light from the 405 nm, 19.3 mW (Min) fiber-coupled LED (Thorlabs) was directed into a fluorescence mini cube with six ports and a built-in detector head (Doric Lenses)

with spectral bandwidths of 405 nm and 460 – 490 nm. 405 nm light was modulated at 217 Hz, while 470 nm light was modulated at 330 Hz. Power output was maintained at 20 mA with a DC offset of 3 mA for both wavelengths. The light was then directed through a low-autofluorescence mono fiber-optic patch cord with a 400 µm core (Precision Fiber Products). This fiber was connected to the mono fiber-optic cannulas that were implanted into the region of interest. The power output at the fiber tip was 25 - 30 µW. Fluorescent emission from the tissue was collected through the same fiber and was detected using a femtowatt photoreceiver. Signal acquisition was 1 kHz and lowpass filtered at 6 Hz. The 405 nm excitation channel served as an isosbestic, calcium-independent control wavelength for GCaMP, allowing for bleaching and movement artifact corrections when directly fit to the calcium-dependent 470 nm channel. MATLAB scripts from TDT (https://www.tdt.com/support/matlab-sdk/) were used to fit the 405 nm signal to the 470 nm signal using linear regression. Change in GCaMP-mediated signal was calculated as:

$$\Delta F/F = \frac{\text{change in 470 nm induced signal } / \text{change in 405 nm induced signal}}{\text{change in 405 nm induced signal}}$$

Time-locked Z scores were then calculated from GCaMP-mediate signal as:

$$Z = \frac{\text{instantaneous } \frac{\Delta F}{F} \ / \ \text{mean } \frac{\Delta F}{F} \ (\text{from } -5 \text{ sec to } -3 \text{ sec})}{\text{standard deviation of } \frac{\Delta F}{F} \ (\text{from } -5 \text{ sec to } -3 \text{ sec})}$$

2.4.8 Methods for Frequency and Max Peak Detection

Transient frequency and maximum peak amplitude were calculated using a custom written MATLAB code incorporating open-source code[500]

(https://github.com/katemartian/Photometry_data_processing). The pipeline utilized an adaptive iteratively reweighted Penalized Least Square (airPLS) approach[501] to correct for baseline noise or signal drift and allow for uniform detection of transients and comparison between mice. The signal was then standardized using a Z score transformation and fit to the reference signal (405 nm, GCaMP only). Data points with a Z score ≥ 2.91 are considered statistical outliers from the baseline (i.e., transient activity above baseline)[502]. A single transient was measured from when a data point ≥ 2.91 Z scores was detected until a data point < 2.91 Z scores was detected. Maximum peak amplitude was calculated as the maximum Z score detecting during the transient. Transient frequency was calculated as the number of transients per second (Hz).

2.4.9 Brain clearing

SHIELD (Stabilization under Harsh conditions via Intramolecular Epoxide Linkages to prevent Degradation)[503]: Mouse brain tissue was prepared according to the LifeCanvas SHIELD protocol adapted from Park et al.[503,504] Briefly, mice were anesthetized with isoflurane and transcardially perfused with ice-cold PBS followed by 20 mL of ice-cold SHIELD Perfusion solution. Brains were then dissected out and shaken in the remaining 20 mL of SHIELD-Perfusion solution at 4°C for 48 hours. Brains were switched to fresh 20 mL of SHIELD-OFF solution and shaken for 24 hours at 4°C. Brains were then shaken in SHIELD-ON for 24 hours at 37°C.

SHIELD Perfusion Solution was prepared fresh before all perfusions. For each mouse, a total of 40 mL was made by mixing 5 mL DI water, 10 mL SHIELD-Buffer, 5 mL of 32% PFA, and 20 mL SHIELD-Epoxy (added in 10 mL increments). Solutions were kept on ice and vortexed after each new reagent was added.

SHIELD-OFF solution was prepared fresh before use. For each mouse, a total of 20 mL was made by mixing 5 mL DI water, 50 mL SHIELD-Buffer, and 10 mL SHIELD-Epoxy.

Active clearing: Brains were cleared using the SmartClear II Pro (LifeCanvas) following the SmartClear II Pro User's Manual[505], in beginner mode (limit = 85 V, Current = 1500 mA, buffer A temp. = 42°C, buffer B temp. = 30-40°C). This method uses stochastic electrotransport to remove electromobile molecules, such as phospholipids, from the sample[503,506]. A maximum of four brains were cleared until evenly transparent throughout (4 - 6 days).

Passive clearing: Brains were transferred to passive SDS clearing solution and shaken at 37°C until fully transparent (3-4 weeks). The passive clearing solution was changed once per week. The passive SDS clearing solution was prepared as a 2 L batch prior to clearing. 173 g of SDS (300 mM), 1.24g of sodium borate (10mM), and 25.2g sodium sulfate (100 mM) were mixed in Milli-Q filtered water (final volume = 2L, pH = 9).

Mounting for imaging: After clearing, brains were shaken in PBS at 37°C for 12 hours. The samples were then shaken in EasyIndex (LifeCanvas) refractive index (RI) matching solution overnight at 37°C. Custom sample holders were rinsed with DI H_2O, followed by 70% ethanol, and allowed to evaporatively dry. The sample holder (LifeCanvas) was filled with refractive index-matched agarose (SigmaAldrich). The brains were then placed in a sample holder, which was then quickly transferred to a 4°C cold room to congeal for ~15 minutes. Brains were shaken

in 50 mL conical tubes with 25 mL of EasyIndex for ~4hours at 37°C and then allowed to equilibrate in the imaging.

2.4.10 Light sheet microscopy

Imaging: Whole-brain light sheet images were captured with a selective plane illumination microscope (SmartSpim, LifeCanvas Technologies) incorporating axially swept light sheet generation[507,508]and a 3.6x objective (NA=0.2). Samples were illuminated with up to three excitation wavelengths: 488 nm, 561 nm, and 642 nm. Respective emission detection filters were 525/50, 600/52, 680/42. Laser power was set to 30-55% for each channel, and the step size was set to 2 µm (Nyquist sampling for the ~4µm axial point spread function for the 3.6x objective). Following acquisition, images were transferred to a Dell Precision 7920 Tower with (2) Intel Xeon Gold 6134 CPU at 3.2 GHz and 384 GB of RAM running Windows 10 Pro for Workstations. Images were stitched to generate composite TIFF images by using a modified version of Terastitcher[509]. Stitched TIFF images were converted to Imaris files using Imaris File Converter 9.2.1for visualization using Imaris 9.5.1.

2.4.11 Brain registration and cell quantification

The distribution of virally transduced neurons was registered to the Allen Coordinate Reference Framework[477] and regional densities of labeled cells quantified using NeUroGlancer Ground Truth (NUGGT)[510] (Supplementary Fig. c), with custom modifications provided by LifeCanvas Technologies. A minimum of 200 cells per brain were trained in the NUGGT pipeline.

2.4.12 Electrophysiology

We used whole-cell patch-clamp electrophysiological techniques as described in Centanni et al.[385] and Harris et al.[511] to interrogate the circuit. In brief, mice were deeply anesthetized using isoflurane, transcardially perfused with ice-cold sucrose-based artificial cerebrospinal fluid (ACSF; in mM: 194 sucrose, 20 NaCl, 4.4 KCl, 2 $CaCl_2$, $MgCl_2$, 1.2 NaH_2PO_4, 10 glucose, 26 $NaHCO_3$). Mice were decapitated, and the brains were removed and immediately placed in a holding chamber containing ice-cold sucrose ACSF. Acute coronal slices (300 µM) containing the insula were cut on a Leica vibratome. Slices were transferred to a holding chamber and incubated for 1 hour at 28°C in normal oxygenated ACSF (in mM: 124 NaCl, 4.4 KCl, 2.5 CaCl2, 1.3 MgSO4, 1 NaH2PO4, 10 glucose, 26 NaHCO3). In the recording chamber, slices were continuously perfused with oxygenated and heated (28°C) ACSF at a rate of 1-2 mL/min. Whole-cell voltage-clamp recordings were performed as previously described[334,349]. In brief, electrodes (2.5-5.0 MΩ) were filled with internal ACSF (in mM: 135 K+-gluconate, 5 NaCl, 10 HEPES, 0.6 EGTA, 4 Na_2GTP (pH 7.2-7.4, osmolarity 290-295). Fluorescently labeled (via AAVrg.DIO.tdTomato injection into the BNST and AAV1.Cre injection into the motor cortex) insula cells were held at -70mV throughout the recording, and all recordings were done in the presence of picrotoxin to block GABA signaling (25 µM; MilliporeSigma; St. Louis, MO). Postsynaptic parameters were monitored continuously during the experiments, and cells were excluded if the access resistance (R_a) changed by >20% in either direction.

2.4.13 RNA fluorescent *in situ* hybridization

Fluorescent *in situ* hybridization assays were performed as described in Fetterly et al. (2019).[159] Briefly, RNA- Scope Fluorescent Multiplex Reagent Kit (Advanced Cell Diagnostics) to visualize RNA transcripts in BNST coronal sections. Isoflurane was used to anesthetize mice immediately prior to brain extraction. Brains were then quickly submerged in oxygenated (95% O_2, 5% CO_2), ice-cold artificial cerebral spinal fluid (ACSF). ACSF contained 124 mM NaCl, 4.4 mM KCl, 2.5 mM CaCl2, 1.3 mM MgSO4, 1 mM NaH2PO4, 10 mM glucose, and 26 mM NaHCO3 in Milli-Q filtered H_2O. Brains were immediately flash-frozen in Optimal Cutting Temperature (OCT) Solution (VWR) using Super Friendly Freeze-It Spray (Fisher Scientific). OCT-embedded brains were kept at -80°C until they were sliced on a cryostat (Leica). 16 µm slices were stuck to charged slides (Denville Scientific), frozen on dry ice, and stored at -80°C until staining. Fixation, dehydration, hybridization, and staining protocols for fresh frozen tissue were performed according to ACD's online specifications. Z-stack BNST images were obtained with a 63×/1.4 NA oil lens on a Zeiss 710 scanning confocal microscope. Three images were taken to visualize the medial, lateral, and dorsal BNST (bregma –0.14). The negative control probe, DapB, was used to determine the parameters for brightness and contrast for experimental images. Images were processed as max intensity projections with Fiji software (NIH)[512]. Counts from the medial, lateral, and dorsal images were combined for each animal. Cells were identified using DAPI-labeled nuclei, and transcripts were identified as individual dots within a cell. A blinded reviewer classified cells as positive (at least one dot in the cell) or negative (zero dots in the cell). Probes used include Mm-Crh-C1 and Mm-Fos-C2. Negative control images were used to determine thresholding parameters that excluded nonspecific fluorescence.

2.4.14 Statistical analysis

Analyses were performed with R (version 3.6.1), Python (version 3.6.6), GraphPad Prism (GraphPad Software, version 8), or MATLAB (Mathworks; version 2019a). Animal numbers were selected to establish sufficient statistical power while using ethical guidelines for minimizing subject numbers and based on previous publications' ability to reliably measure variables from experiments with similar design. When manual scoring was performed, the scorer was blinded to the treatment. When automated behavior tracking was performed, a custom R script was used to determine bout onset in an unbiased manner. Fiberoptic implants and viral placements were histologically verified, and animals were removed if either did not work. Data is visualized as mean ± s.e.m., with individual data points. The number of mice in each experiment and the specific statistical tests are identified in the corresponding figure legends. Statistical significance was determined if $p \leq 0.05$.

Table 2.1: Resources Table.

REAGENT or RESOURCE	**SOURCE**	**IDENTIFIER**
Viruses		
AAV5.Syn.GCaMP6f.WPRE.SV40	Addgene	RRID:Addgene_100837
AAV9-syn-jGCaMP7f-WPRE	Addgene	RRID:Addgene_104488
AAV9-syn-FLEX-jGCaMP7f-WPRE	Addgene	RRID:Addgene_104492
AAV1.hSynapsin.SF-iGluSnFR.A184S	Addgene	RRID:Addgene_106183
AAV1.hSyn.FLEX.GABASnFR.N260A.F145W	Addgene	RRID:Addgene_112159
AAV5-AAV-CMV- GFP	UNC Vector Core	https://www.med.unc.edu/genetherapy/vectorcore/in-

		stock-aav-vectors/reporter-vectors/
pENN.AAV1.CamKII 0.4.Cre.SV40	Addgene	RRID:Addgene_105558
AAV5-hSyn-hM4D(Gi)-mCherry	Addgene	RRID:Addgene_44362
AAV5-hSyn-DIO-hM3D(Gq)-mCherry	Addgene	RRID:Addgene_44361
AAVrg-FLEX-tdTomato	Addgene	RRID:Addgene_28306
AAVrg-CAG-tdTomato	Addgene	RRID:Addgene_59462
pENN.AAVrg.hSyn.Cre.WPRE.hGH	Addgene	RRID:Addgene_105553
AAV5-hSyn-hChR2(H134R)-EYFP	Addgene	RRID:Addgene_26973
AAV1-syn-FLEX-splitTVA-EGFP-tTA	Addgene	RRID:Addgene_100798
AAV1-TREtight-mTagBFP2-B19G	Addgene	RRID:Addgene_100799
EnvA G-deleted Rabies-mCherry	Salk	RRID:Addgene_32636
Experimental Models: Organisms/Strains		
Mouse: C57BL/6J	The Jackson Laboratory	RRID:IMSR_JAX:000664
Mouse: B6(Cg)-*Crh*$^{tm1(cre)Zjh}$/J	The Jackson Laboratory	RRID:IMSR_JAX: 012704
Mouse: Tg(Prkcd-glc-1/CFP,-cre)EH124Gsat	Mutant Mouse Resource & Research Center	RRID:MMRRC_011559-UCD
Mouse: B6;129S6-*Gt(ROSA)26Sor*$^{tm14(CAG-tdTomato)Hze}$/J	The Jackson Laboratory	RRID:IMSR_JAX: 007908
Critical Commercial Assays		
EasyIndex	LifeCanvas	https://lifecanvastech.com/products/reagents/
SHIELD Kit	LifeCanvas	https://lifecanvastech.com/shield/
SmartClear II Pro System Buffers	LifeCanvas	https://lifecanvastech.com/products/reagents/
Chemicals		
Agarose, Type I, low EEO	SigmaAldrich	CAS Number: 9012-36-6
Tissue-Tek optimum cutting temperature compound	VWR	25608-930
Software and Algorithms		
Deeplabcut 2.1.5	DeepLabCut	https://github.com/AlexEMG/DeepLabCut
MATLAB 2019a	Mathworks	https://www.mathworks.com/products/matlab.html RRID:SCR_001622
Synapse Suite	Tucker-Davis Technologies	https://www.tdt.com/component/synapse-software/
RStudio	RStudio, Inc.	https://rstudio.com

		RRID:SCR_000432
R	R Foundation	https://www.r-project.org RRID:SCR_001905
ANVIL	Anvil: the video annotation research tool	ANVIL version 6.0 https://www.anvil-software.org
NeUroGlancer Ground Truth (NUGGT)	GitHub chunglabmit/nuggt	https://github.com/chunglabmit/nuggt
Fiji	NIH	https://fiji.sc
Other		
SmartClear II Pro	LifeCanvas	https://lifecanvastech.com/products/smartclear-ii-pro/
SmartSPIM	LifeCanvas	https://lifecanvastech.com/smartspim/
SPIM sample holder	LifeCanvas	
VWR Disposable Transfer Pipets with Reference Lines	VWR	414004-036
RZ5P Fiber Photometry Processor	Tucker-Davis Technologies	https://www.tdt.com/component/fiber-photometry-rz5p/
Fluorescence Mini Cube with 6 ports & Built-in Detector Head – Two-fluorophore and Lock-in Autofluorescence Detection	Doric Lenses	iFMC6_AE(405)_E1(460-490)_F1(500-540)_E2(555-570)_F2(580-680)_S
Low Autofluorescence Mono Fiber-optic Patch Cords (Metal Ferrule, Core = 400 µm, Outside diameter = 2.5 mm, NA=0.57)	Doric Lenses	MFP_400/430/1100-0.57_3m_FCM-MF2.5_LAF
Mono Fiber-optic Cannulas	Doric Lenses	MFC_400/430-0.57_4mm_MF2.5_FLT
Ceramic Split Sleeve 2.5mm ID 11.40mm length (for fiber implant)	Precision Fiber Products	SM-CS1140S
Four-Channel LED Driver, Four Modulation Input Channels	Thorlabs	DC4104
405 nm, 19.3 mW (Min) Fiber-Coupled LED, 1400 mA, SMA	Thorlabs	M405FP1
470 nm, 17.2 mW (Min) Fiber-Coupled LED, 1000 mA, SMA	Thorlabs	M470F3
ChiSquared Photometry System	ChiSquared Bioimaging	ChiSquared-202 System
ChiSquare Hybrid Fiber Assembly	ChiSquared Bioimaging	ChiF300-HYBRID-FC-LS-LC
473-nm Picosecond-Pulsed Laser	Becker & Hickl	BDL-473-MC
GFP Dichroic Filter	Thorlabs	MD498
FC/PC fiber coupler	Lasos	PM480
Fiber Coupler	Thorlabs	PAF-SMA-11-A

0.22 N.A., 105/125 µm Diameter core/cladding multimode fiber patch cord	Thorlabs	FG105UCA
Anti-reflection-coated multimode fiber (for collection)	Thorlabs	M200L02S-A
Polychromator	Becker and Hickl	PML-SPEC
Time-correlated single photon counting (TCSPC) module	Becker and Hickl	SPC-830
Optic Cannulae	Machine shop	NA
Logitech C920 Webcam	Logitech	C920
Ideal DualScribe Wedge Tip Carbide Scribe	Ideal Industries	45-359
FC/PC and SC/PC Ferrule Polishing Disc	Thorlabs	D50-F
Glass Polishing Plate	Thorlabs	CTG913
Polishing Pad for PC Finishes	Thorlabs	NRS913A
Aluminum Oxide Lapping Sheets-0.3 – 5.0 µm	Thorlabs	LF03p, LF01p, LF3p, LF5p
Leica Angle Two Small Animal Stereotaxic Instrument	Leica	https://www.leicabiosystems.com/research/neuroscience/products/leica-angle-two/
Micro4 MycroSyringe Pump Controller	World Precision Instruments	UMP3-4
Nanofil Syringe	World Precision Instruments	NANOFIL
Nanofil 33G Blunt Needle	World Precision Instruments	NF33BL-2
Gel Etchant	Kerr Dental	31297
Optibond FL Primer	Kerr Dental	35266
Optibond FL Adhesive	Kerr Dental	35265
XRV Herculite Unidose A3.5 Enamel	Kerr Dental	29838
Stainless-Steel Mounting Screws (cut length = 2.4mm)	PlasticsOne	00-96 X 3/32
Cordless 5W LED Light Cure Lamp	LY	LY-A180
Diet Gel 76A with Casein	Clear H2O	72-07-5022
Precision 7920 Tower with (2) Intel Xeon Gold 6134 CPU at 3.2 GHz and 384 GB of RAM	Dell	
Inateck USB-C RAID Dual Bay for 2x 2.5” SATA SSD/HDD Hard Drive Enclosure	Inateck	FE2101
4 TB Samsung 860 QVO SSD 4TB – 2.5 Inch SATA 3 Internal Solid State Drive with V-NAND Technology	Samsung	MZ-76Q4T0B/AM

Clear Acrylic	McMaster-Carr	8560K951
Low profile mouse running wheel	Med Associates	ENV-044-02
RNAscope Fluorescent Multiplex Reagent Kit	Advanced Cell Diagnostics	320850
Mm-Crh-C1Probe	Advanced Cell Diagnostics	316091
Mm-Fos-C2 Probe	Advanced Cell Diagnostics	316921-C2
Super Friendly Freeze-It Spray	Fisher Scientific	23-022524
Research Cryostat	Leica	CM3050 S
Microscope Slides, Diamond White Glass, 25 X 75Mm, Charged, 90° Ground Edges, White Frosted, 72/Box	Denville Scientific	M1021

Chapter 3

Discussion and Future Directions

3.1 Contributions to and future directions for the insula$^{\rightarrow BNST}$ circuit

In this work, we used in vivo fiber photometry, machine learning-based behavioral tracking, light sheet microscopy, fluorescent in situ hybridization, and transsynaptic viral tracing to explore the insula$^{\rightarrow BNST}$ circuitry involvement in active struggling behavior. Previous work

implicated this pathway in affective state[385]. Past studies also showed that insular Gi-DREADD decreased excitatory drive onto BNST cells and demonstrated that Gq-DREADD activation of BNST cells that receive insular input caused increased latency to feed in the NSFT[159,385]. One of those studies also implemented CRACM to explore inputs onto $BNST^{CRF}$ cells[159]. It found that a large portion of $BNST^{CRF}$ cells received insular input. This input also appears to be sensitive to pharmacologic manipulation of the endocannabinoid system[385].

Our work expands on these findings. At the BNST node in this pathway, we explored overall BNST, $BNST^{CRF}$, and $BNST^{PKC\delta}$ cell signaling. While all of these populations increased calcium signal at the onset of struggling, CRF transients were larger. Notably, displacing the behavioral timeclock by +10 seconds as a control did not entirely abolish the CRF signal like it did in other groups. The remaining signal indicates that some transients were present outside of struggle bout onset.

Given that $BNST^{CRF}$ cells appear to be involved in aversive signaling[366], it may be that there are other components of the restraint stress paradigm that these cells are communicating. Another cell group worth investigating in this context is CCK. $BNST^{CCK}$ cell activity has been shown to be oppositely valanced compared to that of $BNST^{CRF}$ cells[366]. Thus, we hypothesize that calcium activity would likely differ in the same restraint stress paradigm.

One alteration to our current protocol that would be worth employing to examine both $BNST^{CRF}$ and $BNST^{CCK}$ cells would be to add an eventual successful escape. In the current protocol, animals remain inescapably restrained for the duration of the trial. No form of relief accompanies the restraint stressor or the subsequent escape behavior. While

difficult to predict, it is not unreasonable to imagine a decrease in $BNST^{CRF}$ transient amplitude (or frequency) and the opposite in $BNST^{CCK}$ cells.

Successful escape could readily be incorporated by adding a triggerable release mechanism to the current restraint device. The design could either fully release the stopper so the animal is free to back out of the chamber unobstructed or to only loosen the back stopper so the animal still must work to push it out. Perhaps both would be useful as signaling could differ based on the volitional participation (or lack thereof) in successful escape effort, much like drug administration protocols can elicit different responses based on if they are contingent or not. Finally, it may also be worth creating a modified restraint device that quickly splits in half to examine instantaneous escape signaling. If designed, any of these procedures would also be worth testing on other nodes in the circuit.

To better understand the inputs to the dorsal BNST, we retrogradely labeled cells projecting to the BNST, creating an extensive map via light sheet microscopy, and validated the insula as a key input. The insula is densely interconnected internally and heavily connected externally to regions involved in emotional regulation, corporal awareness, autonomic regulation, and sensory integration. Based on human and primate studies, Evrard and Craig postulated that representations in the insula increase in complexity (from objective representations to subjective representations) along the posterior (granular) to mid (dysgranular) to anterior (agranular) insula axis[513,514]. Cells from across the insula sent efferents to the BNST with the highest density originating around the region directly lateral to the BNST (near Bregma: AP=0.0 or slightly posterior to the middle cerebral artery, which divides the insula into anterior-posterior divisions). This region of the middle insula sends significant excitatory projections to the amygdala, striatum, and thalamus.

We focused on the portion of the insula with the densest projections to the BNST, yet other work has shown that different regions of the insula have different downstream targets[416,438,515,516]. Gerlach et al. focused more caudally and recently demonstrated that stimulation of the posterior insula (pIC)$^{\rightarrow CeA}$ pathway increased the probability of anxiety-related behaviors[438]. Interestingly, behavior that they classified as "back escape" was more prevalent when optogenetically stimulating the pIC locally (i.e., not pathway-specific), while "stopping" and "freezing" dominated when the pIC$^{\rightarrow CeA}$ pathway was activated. This, combined with our work, provides evidence that separate insular outputs are differentially engaged in active stress responses. The varying regional output from insula could also hold for subregions of the BNST, i.e., afferents from the anterior, middle, and posterior insula could connect with divergent cell populations, a finding that would be congruent with the efferent macrocircuitry differences mentioned above[429].

After assessing the insula$^{\rightarrow BNST}$ cells' distribution, we anterogradely labeled (from the insula) cells in the BNST to better understand the distribution of neurons that receive insula inputs. We found the densest cell labeling in the region of the anterolateral, juxtacapsular, and oval subnuclei. An important consideration when interpreting our AAV1.Cre results is that labeling may be activity dependent[485]. Based on anatomical distributions (Fig. 1.4) in these areas, other cell-types that may receive significant insular input include somatostatin, AVP, dynorphin, enkephalin, and PKCδ. These cell types are associated with different behaviors; thus, other candidate roles for insula$^{\rightarrow BNST}$ could be in aggression[345–347], anxiety[371], stress[376–378], feeding[304], and fear memory consolidation[350].

Because Cre-driver lines exist for many of these cell-types, it is only a matter of time before monosynaptic tracing studies define their respective upstream networks. Afferent maps

will help delineate common and divergent circuit structures and provide valuable targets for further research.

Because the insula$^{\rightarrow BNST}$ pathway seems to be a functional structure[159,385], it may prove useful to more precisely characterize the cells in the BNST that receive input ($^{insula\rightarrow}$BNST cells). Expanded characterization may also be helpful for insular cells that receive motor input ($^{1°Motor\rightarrow}$insula). In both cases, combining AAV1-Cre anterograde tracing with fluorescent in situ hybridization (FISH) for various cell markers would be helpful. However, because only a small portion of virus crosses the synapse, best results will likely be achieved by using a transgenic strain that expresses ample fluorescent protein Cre-dependently (Fig. 2.18a). We can then use modern FISH probes for the fluorescent protein and various cell-types to combinatorically identify overlapping markers. Of note, AAV1.Cre viral labeling is known to have some retrograde properties, which, when used in a bidirectional circuit, can complicate its interpretation[484,485].

Our work used fiber photometry which necessarily assesses population dynamics. We know the brain is quite efficient in allocating resources, and no two cells perform exactly the same function. Therefore, photometry, when used with a calcium sensor in non-genetically restricted cells, produces transients from overlapping populations that blend together. This was apparent when we compared GCaMP to glutamate and GABA signaling in the insula. The average GCaMP transient appeared to comprise both the excitatory and inhibitory signals, though this assertion needs to be verified. Unpublished *ex vivo* data from slice GGCaMP recordings show differential pharmacologic modulation of individual neurons in the insula. Therefore, it may also be helpful to incorporate specific Cre-driver lines (i.e., for excitatory and inhibitory populations) with other *in vivo* techniques that provide single-cell resolution. Two-

photon microscopy or implantable miniscopes could shine a light on the individual cellular activity and the network dynamics that underly these bulk changes.

Single-cell activity may also help us understand the collapse of the relationship between struggling bout duration and transient size. We hypothesize this habituation to a homotypic stressor occurs post-synoptic to the incoming excitatory afferents in the insula because the GCaMP, but not glutamate, signal changes over repeated exposures.

3.2 Beyond the insula$^{\rightarrow BNST}$ circuit

Our work provides digestible input maps for brain regions critical to health and disease. We also illustrated functional engagement of cells in these areas during active coping and demonstrated a role for the insula$^{\rightarrow BNST}$ circuit in post-stress avoidance behavior. Future work will aim to exploit this new information to elucidate the complex signaling upstream and downstream of the insula$^{\rightarrow BNST}$ pathway.

Because the insula$^{\rightarrow BNST}$ pathway only encompasses two nodes in a broader network, delineating the downstream efferents from the BNST is a reasonable next step. As a reminder, the insula innervates many of the BNST^{CRF} cells[159], and BNST^{CRF} cells project to the hypothalamus[366]. Thus it seems plausible that some $^{insula\rightarrow}$BNST cells project to the lateral hypothalamus and possibly engage hypocretin-containing neurons[366], which could be part of how the insula$^{\rightarrow BNST}$ promotes avoidance behavior.

It would be valuable to know the percentage of BNST^{CCK} neurons that receive input from the insula and if those inputs are the same cells that project to the BNST^{CRF} cells. This could shed light on the possibility of multiple distinct afferent populations from the insula with alternate functions. Based on the lateral distribution of insular inputs to the BNST and the medial

distribution of BNST^{CCK} [366], it seems more likely that this pathway is biased away from CCK neurons and their respective downstream efferents. In either case, AAV1 anterograde tracing combined with recombinase-dependent axonal or synaptic tags could be used to identify the regional efferent distribution from $^{insula\rightarrow}$BNST cells[484,485].

Monosynaptic rabies tracing in our work labeled various regions connected to the insula$^{\rightarrow BNST}$ pathway, one of which was the motor cortex. After validating this connectivity, we then demonstrated calcium transients in 1°Motor$^{\rightarrow insula}$ neurons preceding movement onset. We hypothesize that this may at least in part be indicative of a motor efference copy that informs affective circuitry of motor commands[441,442]. While motor efference copy has been postulated to functionally cancel self-generated sensory stimuli [453–455,517], the function of motor efference copy in affective circuitry is largely unexplored.

Evidence exists that efference copy communicates motor command intent[518]. Thus, it could be an avenue to compare intended movement in response to a stressor and the resultant outcome on affective state. It is also conceivable that efference copy information suppresses emotionally charged signals during motor commands in certain circumstances. Much like eye saccades reduce concurrent visual signals[491–493], suppressing affective information during critical actions could help the organism successfully complete those actions, thus enhancing survival probability rather than being derailed by affective processing.

One challenge in manipulating this circuit is the fact that it includes the motor cortex. The very nature of conventional methods (e.g., chemo and optogenetics) would change neuronal activity in the motor cortex and presumably motor actions, thus complicating any behavioral scoring based on animal movement. However, there are paths by which future work could escape these confounds. First, and most simply, studies could temporally disconnect the circuit

manipulation and affective state testing. By changing motor efferent signaling during a stressor and then testing affective state later, researchers could partially address the issue of altering motor behavior (at least during scoring). Still, because coping style can modify affective state[239,240], researchers must consider the potential confound that changing the coping strategy could change behavior and physiology at later timepoints.

Second, inhibitory opsins could disengage regional efferents from the motor cortex while leaving the rest of the system largely undisturbed. One caveat here is the possibility of backpropagating action potentials following light stimulation. They are less of a problem than when using excitatory opsins, but they can occur and have the capacity to fire upstream neurons and their respective collaterals. Finally, if synthetic neurotransmitter systems (non-naturally occurring neurotransmitters that are packaged in typical vesicles but only activate designer receptors) can be produced, it would allow us to tune the gain of that pathway up or down with minimal impact on other parts of the circuit.

Of the many inputs to the insula$^{\rightarrow BNST}$ pathway that we identified, we only explored the motor afferents. Other regions likely warrant further interrogation. If we carry on with the theme of efference copy, we know much of the research in this area involves somatosensory processing[456]. In our study, bilateral somatosensory cortices send projections to insula$^{\rightarrow BNST}$ cells. The sensory and motor cortices are also reciprocally connected, raising the prospect of polysynaptic connections through the somatosensory cortex that could modulate this circuit[477,519–522]. Regardless of a polysynaptic circuit, investigation into somatosensory processing would be worthy in its own right given the input's scale. Other regions with particularly high-density retrograde labeling (e.g., piriform area, BLA, anterior insula, and posterior insula) could also make appealing candidates given their role in affective processing.

Finally, further exploration of the impact of the motor cortex, and perhaps even exercise, on insula and BNST function is another promising area of future research. Past work implicates exercise in stress alleviation; much of that literature focuses on peripheral signals and metabolites that carry information back to the CNS. Our work denotes another potential avenue by which the motor system can intervene in affective circuitry. We show that wheel-running initiation can induce insular calcium transients, yet much more detail would be required to make any assertions about function in a non-stressed paradigm. We generated whole-brain anterograde AAV1 efferent maps from 1°Motor cortex (Fig. X), and this would be another starting point to investigate other nodes in affective circuits. For instance, even though the virus did not label the BNST, it did label a significant number of cells in the amygdala. This divergence in connectivity may be related to differences in the fear processing roles held by the amygdala (phasic) and BNST (sustained)[294]. One could reasonably infer that the phasic fear and cue-based fear responses that engage the amygdala would be better served by direct motor command information.

Because of the 1°Motor cortex connection to the affective circuitry (insula$^{\rightarrow BNST}$) that we previously demonstrated to be involved in negative affect[385], we also suspect that it may prove a productive area of study and perhaps, one day, a candidate for the treatment of clinical illness. There has already been some success for motor stimulation in the treatment of chronic pain[523–525]. If evidence develops for the therapeutic efficacy of motor cortex activation, the region is well situated for non-invasive manipulation through techniques such as transcranial magnetic stimulation (TMS). Ultimately, much more work will be needed to fully elucidate the relationship between the motor cortex, affective circuitry, and exercise. We believe this is a worthy pursuit.

3.3 Genetically encoded tools, a way forward

The tools community deserves much credit in the current neuroscience renaissance. Many of these researchers also deserve accolades as exemplars of what science should be, that is, sharing discoveries openly and rapidly with the community. Hopefully, this culture permeates the rest of neuroscience and science in general. Advances span the breadth of cellular manipulation to novel and reimagined imaging techniques. The synergistic confluence of advances in a wide variety of fields, often only tangentially related to neuroscience, has empowered us to dissect the brain with scale and precision heretofore unimaginable.

The explosion of recombinase-driver lines (e.g., the recombinase Cre, whose name stands for "**C**auses **RE**combination.") and combined with Cre-dependent viruses provide innumerable combinations for spatial and cell-type-specific manipulation. One link in a series of inventions that made this possible was the FLEx (**FL**ip **EX**cision) or DIO (**D**ouble-floxed **I**nverse **O**rientation) systems. These systems provide high signal to noise by holding the gene of interest in the reversed orientation until a recombinase reorients them, locking them in the "on" state. There remains some confusion about this nomenclature, or the difference between DIO and FLEx. In short, there is none. They both use two loxP sites and two lox2272 sites (see below) - their sequences are the same.

Name	Left Recognition Site	Spacer	Right Recognition Site
loxP	ATAACTTCGTATA	ATGTATGC	TATACGAAGTTAT
lox2272	ATAACTTCGTATA	AAGTATCC	TATACGAAGTTAT

As the number of non-overlapping recombinases continues to expand, so too will our capacity to investigate increasingly specific cells[526]. Initial combinatorial strategies allowed restriction to two anatomical or genetic parameters and used channelrhodopsin and eYFP[526,527]. Recently, Fenno et al. expanded this tool kit to three potential parameters (called "Triplesect") and incorporated many more payload varients[528]. The group has also published protocols so other labs can develop their own multiplexed recombinase-dependent tools, allowing others to contribute to this expanding library[527]. These tools could have high utility as we dissect the insula$^{\rightarrow BNST}$ circuit in greater detail.

In addition to controlling the expression of existing payloads (e.g., opsins, DREADDs, sensors, and tags) more specifically, the payloads are also improving. One area that still requires improvement is the spectral overlap between sensors and opsins (i.e., the excitation wavelength of one can excite the other.) Variants like Chrismson[529] moved the field forward in this regard, yet the "blue shoulder" or sensitivity to blue light remains a problem. The opsin field has matured significantly in the past decade, and the promise of greater spectral selectivity will continue to increase the utility of this revolutionary field.

The Allen Brain Institute recently published a study highlighting another necessary advance, action potential detection using calcium sensors[530]. Under typical population imaging conditions, they found that <10% of single action potentials and between ~20%-30% of action potential pairs produce enough signal to be detected reliably. Therefore, population recordings are likely skewed towards bursts of multi-action potential activity. They did show that under optimal conditions (in which a neuron's soma fills almost the entire field of view), most single action potentials could be detected, which is promising as sensor sensitivity continues to

increase. Notably, this study used GCaMP6 variants. jGCaMP8 variants, which will be widely available soon, appear to be a step-change in kinetics and brightness compared to the already improved jGCaMP7. Once new sensors can reliably detect single action potentials (while maintaining enough dynamic range to capture action potential trains), our capacity for nuanced population-level single-cell analysis will be within reach.

The long-awaited gold standard for optically measuring neuronal activity is the invention of a genetically-encoded voltage sensor that could easily conform to current and readily available microscopy systems. Sensors do exist now, but the signal produced is too low for broad adoption[531]. The discrepancy for voltage sensors is primarily driven by the prerequisite that they are membrane-bound, decreasing the number of proteins by up to 1000-fold compared to cytosolic proteins. One clever design, Voltron[532], takes advantage of genetically encoded proteins and their interaction with chemical dyes, which are brighter and more photostable than fluorescent proteins. Still, Voltron remains relatively niche. Once researchers solve this puzzle, it will eliminate many calcium imaging issues, namely calcium's slow dynamics and compartmentalization.

3.4 More data. Less time. Less bias.

Just as population recordings via optical sensors are increasing throughput for *in vivo* and *ex vivo* physiology, the rate and nature of how we collect data in other neuroscience arenas are evolving as well. One shining example of enthusiastic adoption has been light sheet microscopy. Siedentopf and Zsigmondy originally developed light sheet microscopy in 1902 to examine colloidal particles in gold ruby glass[533]. Not until near the turn of the century did Voie et al. develop the first modern light sheet[534]. The sheet was a relatively course 20 um by today's

standards, but it set the technology on pace to reach where it is today. Today's use of light sheet microscopy to image whole and intact brain samples increases throughput and decreases bias introduced by "looking under the lamppost," or only searching where changes are expected. The full 3D reconstruction provides an easily digestible format that is amenable to whole-brain quantification.

Light sheet imaging generates a lot of data - one brain can exceed a terabyte in size. Thus, a critical issue to solve is data processing, storage, and sharing. We expect hardware solutions to continue to decrease in cost[535], but at least in the near term, if labs image more than a handful of brains, they are likely to struggle with these files' weight. Sharing datasets is problematic for the same reasons and has left groups resorting to shipping physical hard drives through the mail. These problems are likely to be transient, so looking forward, exciting potential remains.

Because each whole-brain experiment encompasses too many brain regions for one group to investigate, each dataset could be used by many across the neuroscience community. The included "negative" regions alone could be a boon for research efficiency as they often go unreported, and experiments may be repeated unnecessarily. At a time when federal spending and animal use have been under added scrutiny, the potential cost and animal savings make this particularly attractive. Universal sharing of whole-brain light sheet data would require infrastructure for a massive centralized database. If the raw data proved to be too large (at least initially), the locations of identified objects (e.g., cell bodies or terminal fields) could be mapped to a common coordinate framework and stored as such[536]. However, this strategy would likely decrease both long-term and creative use compared to making raw data available. We believe it is in the global interest to create such a resource. It would, however, require nation-state-level

funding. Accordingly, we feel it warrants consideration for centralized investment by the National Institute of Health.

Light sheet is well suited for mapping connected networks of neurons. We remain convinced that technology exists today, or will exist soon, to devise a tracing method capable of mapping polysynaptic connections between neurons while maintaining ordinal information. Polysynaptic connectivity labeling will provide far more extensive circuit maps about the brain and give far more information about circuit organization and feedback systems. While we have designed several theoretical frameworks to accomplish this, none of them are streamlined enough to be widely adopted, and thus we will not include them here.

Automated behavior analysis is a burgeoning field, aided by advances in computer vision and deep learning[537,538], that is currently revolutionizing behavioral neuroscience. Unstructured behavioral data can be reproducibly labeled and dissected with a speed, accuracy, and detail never before possible[539–544]. Until this advance, tracking body parts often required restricted experimental conditions or attaching markers to the subject[545–548]. Because these new tools do not require markers, they do not interfere with the animals' behavior, making it far more naturalistic. They can be used on virtually anything that a camera can capture[464]. Tracking gives positional data for each tracked point, which can, in turn, be used to reconstruct 3D models and score behavior[539,549]. Advances in transfer learning allow pre-trained networks to be used on new objects that the network has never seen[550]. These pre-trained models either dramatically speed training or require no training at all.

Many labs are working to automate behavioral quantification so it can handle complex behaviors[551–554]. The behaviors even include social interaction between multiple animals[555]. Fortunately, reliable multi-animal tracking has become a reality very quickly[539]. The next

frontier, which is likely to be crossed in the next few years, is unstructured behavioral classification[553,555]. When this comes to fruition, researchers will be able to run vast yet intricate studies, with the capacity to pull out nuanced behavioral responses that would otherwise be imperceptible to the human eye[556].

By alleviating time-consuming and soul-crushing manual scoring associated with large behavioral and histological studies, these tools are set to give neuroscientists back their most valuable resource, time to ponder the brain. We are at the precipice of a new neuroscience era, bigger, faster, and freer than those that came before. We also believe that this new era will spawn much-needed novel therapeutics. Finally, we hope it will provide a deeper understanding of ourselves so that we may better appreciate and care for each other.

3.5 Three pounds of flesh

No object in the known universe is more complex than the human brain. It can at once contemplate the far reaches of the cosmos, compose Ave Maria, and hold fast to memories of those who left this world before us. But, like life itself, it is fragile. Physical and emotional damage can be irrevocable. Though neurons persist throughout life as some of the longest-lived cells in our bodies, to study them takes tremendous care. Even the most meticulous scientists find their chatter to fade in a dish. They cannot go one without their neighbors. Like you and me, the connections to those around us make life possible.

If you were to stand inside the brain and look up, your gaze would fall on neurons shaped like stars, bursting into trees, branching to reach out and touch one another. In a time where physical contact has become scary, may it serve as a reminder that our connections give meaning

to the time we have on earth. They shape our perceptions and experiences. The brain is who we are, everything we believe, and the capacity for everything we will ever become.

References

1. Selye, H. Stress and the general adaptation syndrome. *Br. Med. J.* (1950). doi:10.1136/bmj.1.4667.1383

2. Bernard, C., Bert, P., Dastre, A. & Vulpian, A. *Leçons sur les phénomènes de la vie communs aux animaux et aux végétaux*. (J.-B. Baillière, 1878). doi:10.5962/bhl.title.44802

3. Bernard. *Introduction à l'étude de la médecine expérimentale*. *Introduction à l'étude de la médecine expérimentale* (1865). doi:10.14375/np.9782081307582

4. Cannon, W. B. Physiological Regulation of Normal States: Some Tentative Postulates Concerning Biological Homeostasis. in *Jubilee Volume to Charles Richet* (1926).

5. Cannon, W. B. *The Wisdom of the Body*. (1932).

6. Hartman, F. A. Cortin, vital hormone of the adrenal cortex. *Endocrinology* (1930). doi:10.1210/endo-14-4-229

7. Hartman, F. A. & Brownell, K. A. The hormone of the adrenal cortex. *Science* (1930). doi:10.1126/science.72.1855.76

8. Hartman, F. A., Brownell, K. A., Hartman, W. E., Dean, G. A. & MacArthur, C. G. THE HORMONE OF THE ADRENAL CORTEX. *Am. J. Physiol. Content* **86**, 353–359 (1928).

9. Dustin, A. P. *Les poisons caryoclasiques : moyens d'analyse cytophysiologique*. (Masson et Cie, 1929).

10. Selye, H. Confusion and controversy in the stress field. *J. Human Stress* (1975). doi:10.1080/0097840X.1975.9940406

11. Haubrich, W. S. *Medical meanings: A glossary of word origins. American College of Physicians* (2004).

12. Selye, H. A syndrome produced by diverse nocuous agents [13]. *Nature* (1936). doi:10.1038/138032a0

13. Sterling, P. & Eyer, J. Allostasis: A New Paradigm to Explain Arousal Pathology. in *Handbook of Life Stress, Cognition and Health* (1988).

14. McEwen, B. S. Protective and Damaging Effects of Stress Mediators. *N. Engl. J. Med.* (1998). doi:10.1056/nejm199801153380307

15. McEwen, B. S. *et al.* Mechanisms of stress in the brain. *Nat. Neurosci.* (2015). doi:10.1038/nn.4086

16. James, W. The Principles Of Psychology Volume I By William James (1890). *Princ. Psychol.* (1890).

17. Colegrove, F. W. Individual Memories. *Am. J. Psychol.* (1899). doi:10.2307/1412480

18. Stratton, G. M. Retroactive hyperamnesia and other emotional effects on memory. *Psychol. Rev.* (1919). doi:10.1037/h0074902

19. Brown, R. & Kulik, J. Flashbulb memories. *Cognition* (1977). doi:10.1016/0010-0277(77)90018-X

20. Curci, A. & Luminet, O. Follow-up of a cross-national comparison on flashbulb and event memory for the September 11th attacks. *Memory* (2006). doi:10.1080/09658210500340816

21. Terr, L. C. *et al.* Children's memories in the wake of Challenger. *Am. J. Psychiatry* (1996). doi:10.1176/ajp.153.5.618

22. Kvavilashvili, L., Mirani, J., Schlagman, S. & Kornbrot, D. E. Comparing flashbulb memories of September 11 and the death of Princess Diana: Effects of time delays and nationality. *Appl. Cogn. Psychol.* (2003). doi:10.1002/acp.983

23. *Proceedings of the United States Senate in the Impeachment Trial of Donald John Trump*. S. Doc.117-2 I-III (Senate, 2021).

24. Dodson, J. D. The relation of strength of stimulus to rapidity of habit-formation in the kitten. *J. Anim. Behav.* (1915). doi:10.1037/h0073415

25. Yerkes, R. M. & Dodson, J. D. The relation of strength of stimulus to rapidity of habit-formation. *J. Comp. Neurol. Psychol.* (1908). doi:10.1002/cne.920180503

26. McEwen, B. S. & Wingfield, J. C. The concept of allostasis in biology and biomedicine. *Hormones and Behavior* (2003). doi:10.1016/S0018-506X(02)00024-7

27. McEwen, B. S. & Wingfield, J. C. What is in a name? Integrating homeostasis, allostasis and stress. *Hormones and Behavior* (2010). doi:10.1016/j.yhbeh.2009.09.011

28. McEWEN, B. S. Stress, Adaptation, and Disease: Allostasis and Allostatic Load. *Ann. N. Y. Acad. Sci.* **840**, 33–44 (1998).

29. Arnsten, A. F. T. Stress weakens prefrontal networks: Molecular insults to higher cognition. *Nature Neuroscience* (2015). doi:10.1038/nn.4087

30. McEwen, B. S. Neurobiological and Systemic Effects of Chronic Stress. *Chronic Stress* (2017). doi:10.1177/2470547017692328

31. Shonkoff, J. P., Boyce, W. T. & McEwen, B. S. Neuroscience, molecular biology, and the childhood roots of health disparities: Building a new framework for health promotion and disease prevention. *JAMA - Journal of the American Medical Association* (2009). doi:10.1001/jama.2009.754

32. Felitti, V. J. *et al.* Relationship of Childhood Abuse and Household Dysfunction to Many of the Leading Causes of Death in Adults: The Adverse Childhood Experiences (ACE)Study. *Am. J. Prev. Med.* (2019). doi:10.1016/j.amepre.2019.04.001

33. Halfon, N., Larson, K., Lu, M., Tullis, E. & Russ, S. Lifecourse health development: Past, present and future. *Matern. Child Health J.* (2014). doi:10.1007/s10995-013-1346-2

34. McEwen, B. S. Brain on stress: How the social environment gets under the skin. *Proc. Natl. Acad. Sci. U. S. A.* (2012). doi:10.1073/pnas.1121254109

35. Faravelli, C. Life events preceding the onset of panic disorder. *J. Affect. Disord.* (1985). doi:10.1016/0165-0327(85)90016-3

36. Kendler, K. S., Karkowski, L. M. & Prescott, C. A. Causal relationship between stressful life events and the onset of major depression. *Am. J. Psychiatry* (1999). doi:10.1176/ajp.156.6.837

37. Collip, J. B., Anderson, E. M. & Thomson, D. L. THE ADRENOTROPIC HORMONE OF THE ANTERIOR PITUITARY LOBE. *Lancet* (1933). doi:10.1016/S0140-6736(00)44463-6

38. Johnstone, R. A sixty-year evolution of biochemistry at McGill University. *Sci. Can.* (2003). doi:10.7202/800458ar

39. Li, C. H., Simpson, M. E. & Evans, H. M. Isolation of adrenocorticotropic hormone from sheep pituitaries. *Science (80-.).* (1942). doi:10.1126/science.96.2498.450

40. Li, C. H. *et al.* Amino-acid sequence of alpha-corticotropin. *Nature* (1955). doi:10.1038/176687a0

41. Turecki, G. & Meaney, M. J. Effects of the Social Environment and Stress on Glucocorticoid Receptor Gene Methylation: A Systematic Review. *Biological Psychiatry* (2016). doi:10.1016/j.biopsych.2014.11.022

42. Mains, R. E., Eipper, B. A. & Ling, N. Common precursor to corticotropins and endorphins. *Proc. Natl. Acad. Sci. U. S. A.* (1977). doi:10.1073/pnas.74.7.3014

43. Roberts, J. L. & Herbert, E. Characterization of a common precursor to corticotropin and β-lipotropin: Cell-free synthesis of the precursor and identification of corticotropin peptides in the molecule. *Proc. Natl. Acad. Sci. U. S. A.* (1977). doi:10.1073/pnas.74.11.4826

44. Nakanishi, S. *et al.* Nucleotide sequence of cloned cDNA for bovine corticotropin-β-lipotropin precursor. *Nature* (1979). doi:10.1038/278423a0

45. Zakarian, S. & Smyth, D. G. β-endorphin is processed differently in specific regions of rat pituitary and brain. *Nature* (1982). doi:10.1038/296250a0

46. Eipper, B. A. & Mains, R. E. Existence of a common precursor to ACTH and endorphin in the anterior and intermediate lobes of the rat pituitary. *J. Supramol. Cell. Biochem.* (1978). doi:10.1002/jss.400080304

47. Watson, S. J., Akil, H., Richard, C. W. & Barchas, J. D. Evidence for two separate opiate peptide neuronal systems [22]. *Nature* (1978). doi:10.1038/275226a0

48. Civelli, O., Birnberg, N. & Herbert, E. Detection and quantitation of pro-opiomelanocortin mRNA in pituitary and brain tissues from different species. *J. Biol. Chem.* (1982). doi:10.1016/s0021-9258(18)34498-3

49. Gee, C. E., Chen, C. L. C., Roberts, J. L., Thompson, R. & Watson, S. J. Identification of proopiomelanocortin neurones in rat hypothalamus by in situ cDNA-mRNA hybridization. *Nature* (1983). doi:10.1038/306374a0

50. Harris, G. W. Electrical stimulation of the hypothalamus and the mechanism of neural control of the adenohypophysis. *J. Physiol.* (1948). doi:10.1113/jphysiol.1948.sp004286

51. Schally, A. V., Andersen, R. N., Lipscomb, H. S., Long, J. M. & Guillemin, R. Evidence for the existence of two corticotrophin-releasing factors, α and ß. *Nature* (1960). doi:10.1038/1881192a0

52. Vale, W., Spiess, J., Rivier, C. & Rivier, J. Characterization of a 41-residue ovine hypothalamic peptide that stimulates secretion of corticotropin and β-endorphin. *Science (80-.).* (1981). doi:10.1126/science.6267699

53. King, R. J. B. & Mainwaring, W. I. P. *Steroid-cell Interactions*. (Butterworth-Heinemann, 1974).

54. Wrange, O., Okret, S. & Radojcic, M. Characterization of the purified activated glucocorticoid receptor from rat liver cytosol. *J. Biol. Chem.* (1984). doi:10.1016/s0021-9258(17)43079-1

55. Wrange, O., Carlstedt-Duke, J. & Gustafsson, J. A. Purification of the glucocorticoid receptor from rat liver cytosol. *J. Biol. Chem.* (1979). doi:10.1016/s0021-9258(19)86842-4

56. Miesfeld, R. *et al.* Characterization of a steroid hormone receptor gene and mRNA in wild-type and mutant cells. *Nature* (1984). doi:10.1038/312779a0

57. Hollenberg, S. M. *et al.* Primary structure and expression of a functional human glucocorticoid receptor cDNA. *Nature* (1985). doi:10.1038/318635a0

58. Kagan, J. An Overly Permissive Extension. *Perspect. Psychol. Sci.* (2016). doi:10.1177/1745691616635593

59. McEwen, B. S. & McEwen, C. A. Response to Jerome Kagan's Essay on Stress (2016). *Perspect. Psychol. Sci.* (2016). doi:10.1177/1745691616646635

60. Selye, H. Thymus and Adrenals in the Response of the Organism to Injuries and Intoxications. *Br. J. Exp. Pathol.* (1936).

61. Sorrells, S. F., Caso, J. R., Munhoz, C. D. & Sapolsky, R. M. The Stressed CNS: When Glucocorticoids Aggravate Inflammation. *Neuron* (2009). doi:10.1016/j.neuron.2009.09.032

62. Abo, T., Kawate, T., Itoh, K. & Kumagai, K. Studies on the bioperiodicity of the immune response. I. Circadian rhythms of human T, B, and K cell traffic in the peripheral blood. *J. Immunol.* (1981).

63. Bartter, F. C., Delea, C. S. & Halberg, F. A MAP OF BLOOD AND URINARY CHANGES RELATED TO CIRCADIAN VARIATIONS IN ADRENAL CORTICAL FUNCTION IN NORMAL SUBJECTS. *Ann. N. Y. Acad. Sci.* (1962). doi:10.1111/j.1749-6632.1962.tb30612.x

64. Tavadia, H. B., Fleming, K. A., Hume, P. D. & Simpson, H. W. Circadian rhythmicity of human plasma cortisol and PHA induced lymphocyte transformation. *Clin. Exp. Immunol.* (1975).

65. Morrow-Tesch, J. L., McGlone, J. J. & Norman, R. L. Consequences of restraint stress on natural killer cell activity, behavior, and hormone levels in rhesus macaques (Macaca mulatta). *Psychoneuroendocrinology* (1993). doi:10.1016/0306-4530(93)90013-B

66. Kawate, T., Abo, T., Hinuma, S. & Kumagai, K. Studies on the bioperiodicity of the immune response. II. Co-variations of murine T and B cells and a role of corticosteroid. *J. Immunol.* (1981).

67. Griffin, A. C. & Whitacre, C. C. Sex and strain differences in the circadian rhythm fluctuation of endocrine and immune function in the rat: implications for rodent models of autoimmune disease. *J. Neuroimmunol.* (1991). doi:10.1016/0165-5728(91)90161-Y

68. Cox, J. H. & Ford, W. L. The migration of lymphocytes across specialized vascular endothelium. IV. Prednisolone acts at several points on the recirculation pathways of lymphocytes. *Cell. Immunol.* (1982). doi:10.1016/0008-8749(82)90190-3

69. Chung, H. T., Samlowski, W. E. & Daynes, R. A. Modification of the murine immune system by glucocorticosteroids: Alterations of the tissue localization properties of circulating lymphocytes. *Cell. Immunol.* (1986). doi:10.1016/0008-8749(86)90167-X

70. Beer, D. J. & Center, D. M. In vitro corticosteroid modulation of lymphocyte migration. *Clin. Res.* (1979).

71. Eguchi, K. *et al.* Interferon-alpha and dexamethasone inhibit adhesion of T cells to endothelial cells and synovial cells. *Clin. Exp. Immunol.* (1992). doi:10.1111/j.1365-2249.1992.tb06470.x

72. Sternberg, E. M. *et al.* A central nervous system defect in biosynthesis of corticotropin-releasing hormone is associated with susceptibility to streptococcal cell wall-induced arthritis in Lewis rats. *Proc. Natl. Acad. Sci. U. S. A.* (1989). doi:10.1073/pnas.86.12.4771

73. Crofford, L. J. *et al.* Hypothalamic–pituitary–adrenal axis perturbations in patients with fibromyalgia. *Arthritis Rheum.* (1994). doi:10.1002/art.1780371105

74. Tanriverdi, F., Karaca, Z., Unluhizarci, K. & Kelestimur, F. The hypothalamo-pituitary-

adrenal axis in chronic fatigue syndrome and fibromyalgia syndrome. *Stress* (2007). doi:10.1080/10253890601130823

75. Poteliakhoff, A. Adrenocortical activity and some clinical findings in acute and chronic fatigue. *J. Psychosom. Res.* (1981). doi:10.1016/0022-3999(81)90095-7

76. Ur, E., White, P. D. & Grossman, A. Hypothesis: Cytokines may be activated to cause depressive illness and chronic fatigue syndrome. *Eur. Arch. Psychiatry Clin. Neurosci.* (1992). doi:10.1007/BF02195983

77. Buske-Kirschbaum, A. *et al.* Attenuated free cortisol response to psychosocial stress in children with atopic dermatitis. *Psychosom. Med.* (1997). doi:10.1097/00006842-199707000-00012

78. Danese, A., Pariante, C. M., Caspi, A., Taylor, A. & Poulton, R. Childhood maltreatment predicts adult inflammation in a life-course study. *Proc. Natl. Acad. Sci. U. S. A.* (2007). doi:10.1073/pnas.0610362104

79. Johnson, J. D. *et al.* Catecholamines mediate stress-induced increases in peripheral and central inflammatory cytokines. *Neuroscience* (2005). doi:10.1016/j.neuroscience.2005.06.090

80. Besedovsky, H. & Sorkin, E. Network of immune-neuroendocrine interactions. *Clin. Exp. Immunol.* (1977).

81. Jain, R. *et al.* Corticotropin-releasing factor modulates the immune response to stress in the rat. *Endocrinology* (1991). doi:10.1210/endo-128-3-1329

82. McEwen, B. S. *et al.* The role of adrenocorticoids as modulators of immune function in health and disease: Neural, endocrine and immune interactions. *Brain Research Reviews* (1997). doi:10.1016/S0165-0173(96)00012-4

83. Bellinger, D. L. *et al.* Sympathetic modulation of immunity: Relevance to disease. *Cellular Immunology* (2008). doi:10.1016/j.cellimm.2007.09.005

84. Wurtman, R. J. & Axelrod, J. Control of enzymatic synthesis of adrenaline in the adrenal medulla by adrenal cortical steroids. *J. Biol. Chem.* (1966). doi:10.1016/s0021-9258(18)96620-2

85. Dhabhar, F. S., Miller, A. H., McEwen, B. S. & Spencer, R. L. Stress-induced changes in blood leukocyte distribution. Role of adrenal steroid hormones. *J. Immunol.* (1996).

86. Tarcic, N., Ovadia, H., Weiss, D. W. & Weidenfeld, J. Restraint stress-induced thymic involution and cell apoptosis are dependent on endogenous glucocorticoids. *J. Neuroimmunol.* (1998). doi:10.1016/S0165-5728(97)00186-0

87. Leu, S. J. C. & Singh, V. K. Modulation of natural killer cell-mediated lysis by corticotropin-releasing neurohormone. *J. Neuroimmunol.* (1991). doi:10.1016/0165-5728(91)90113-L

88. Irwin, M. R., Vale, W. & Britton, K. T. Central corticotropin-releasing factor suppresses natural killer cytotoxicity. *Brain Behav. Immun.* (1987). doi:10.1016/0889-1591(87)90009-2

89. Tsagarakis, S. & Grossman, A. Corticotropin-releasing hormone: interactions with the immune system. *Neuroimmunomodulation* (1994). doi:10.1159/000097184

90. De Bosscher, K., Vanden Berghe, W. & Haegeman, G. The interplay between the glucocorticoid receptor and nuclear factor-κB or activator protein-1: Molecular mechanisms for gene repression. *Endocrine Reviews* (2003). doi:10.1210/er.2002-0006

91. Leu, S. J. C. & Singh, V. K. Stimulation of interleukin-6 production by corticotropin-releasing factor. *Cell. Immunol.* (1992). doi:10.1016/0008-8749(92)90018-K

92. Reichardt, H. M. *et al.* Repression of inflammatory responses in the absence of DNA binding by the glucocorticoid receptor. *EMBO J.* (2001). doi:10.1093/emboj/20.24.7168

93. Dhabhar, F. S. & McEwen, B. S. Acute stress enhances while chronic stress suppresses cell-mediated immunity in vivo: A potential role for leukocyte trafficking. *Brain. Behav. Immun.* (1997). doi:10.1006/brbi.1997.0508

94. Bowers, S. L., Bilbo, S. D., Dhabhar, F. S. & Nelson, R. J. Stressor-specific alterations in corticosterone and immune responses in mice. *Brain. Behav. Immun.* (2008). doi:10.1016/j.bbi.2007.07.012

95. McKittrick, C. R., Caroline Blanchard, D., Blanchard, R. J., McEwen, B. S. & Sakai, R. R. Serotonin receptor binding in a colony model of chronic social stress. *Biol. Psychiatry* (1995). doi:10.1016/0006-3223(94)00152-S

96. Blanchard, D. C., Sakai, R. R., McEwen, B., Weiss, S. M. & Blanchard, R. J. Subordination stress: Behavioral, brain, and neuroendocrine correlates. *Behav. Brain Res.* (1993). doi:10.1016/0166-4328(93)90096-9

97. Albeck, D. S. *et al.* Chronic social stress alters levels of corticotropin-releasing factor and arginine vasopressin mRNA in rat brain. *J. Neurosci.* (1997). doi:10.1523/jneurosci.17-12-04895.1997

98. Mangold, D., Wand, G., Javors, M. & Mintz, J. Acculturation, childhood trauma and the cortisol awakening response in Mexican-American adults. *Horm. Behav.* (2010). doi:10.1016/j.yhbeh.2010.06.010

99. Kuhlman, K. R., Geiss, E. G., Vargas, I. & Lopez-Duran, N. L. Differential associations between childhood trauma subtypes and adolescent HPA-axis functioning. *Psychoneuroendocrinology* (2015). doi:10.1016/j.psyneuen.2015.01.020

100. Charlton, B. G., Leake, A., Wright, C., Griffiths, H. W. & Ferrier, I. N. A combined study of cortisol, ACTH and dexamethasone concentrations in major depression: Multiple time-point sampling. *Br. J. Psychiatry* (1987). doi:10.1192/bjp.150.6.791

101. Ribeiro, S. C. M., Tandon, R., Grunhaus, L. & Greden, J. F. The DST as a predictor of outcome in depression: A meta-analysis. *Am. J. Psychiatry* (1993). doi:10.1176/ajp.150.11.1618

102. Harvey, W., Guyton, A. C. & Willis, R. *The Works of William Harvey. The Works of William Harvey* (2014). doi:10.9783/9780812208627

103. Bosma, H. *et al.* Low job control and risk of coronary heart disease in Whitehall II (prospective cohort) study. *Br. Med. J.* (1997). doi:10.1136/bmj.314.7080.558

104. Räikkönen, K., Lassila, R., Keltikangas-Järvinen, L. & Hautanen, A. Association of chronic stress with plasminogen activator inhibitor-1 in healthy middle-aged men. *Arterioscler. Thromb. Vasc. Biol.* (1996). doi:10.1161/01.ATV.16.3.363

105. Ridker, P. M. From C-Reactive Protein to Interleukin-6 to Interleukin-1: Moving Upstream to Identify Novel Targets for Atheroprotection. *Circulation Research* (2016). doi:10.1161/CIRCRESAHA.115.306656

106. Kuper, H. & Marmot, M. Job strain, job demands, decision latitude, and risk of coronary heart disease within the Whitehall II study. *J. Epidemiol. Community Health* (2003). doi:10.1136/jech.57.2.147

107. North, F. M., Syme, S. L., Feeney, A., Shipley, M. & Marmot, M. Psychosocial work environment and sickness absence among British civil servants: The Whitehall II study. *Am. J. Public Health* (1996). doi:10.2105/AJPH.86.3.332

108. Vahtera, J., Kivimäki, M., Pentti, J. & Theorell, T. Effect of change in the psychosocial work environment on sickness absence: A seven year follow up of initially healthy employees. *J. Epidemiol. Community Health* (2000). doi:10.1136/jech.54.7.484

109. Schnall, P. L., Schwartz, J. E., Landsbergis, P. A., Warren, K. & Pickering, T. G. Relation between job strain, alcohol, and ambulatory blood pressure. *Hypertension* (1992). doi:10.1161/01.HYP.19.5.488

110. Everson, S. A. *et al.* Interaction of workplace demands and cardiovascular reactivity in progression of carotid atherosclerosis: Population based study. *Br. Med. J.* (1997). doi:10.1136/bmj.314.7080.553

111. Johnson, J. V. & Hall, E. M. Job strain, work place social support, and cardiovascular disease: A cross-sectional study of random sample of the Swedish Working Population. *Am. J. Public Health* (1988). doi:10.2105/AJPH.78.10.1336

112. Falk, A., Hanson, B. S., Isacsson, S. O. & Ostergren, P. O. Job strain and mortality in elderly men: Social network, support, and influence as buffers. *Am. J. Public Health* (1992). doi:10.2105/AJPH.82.8.1136

113. Turner, J. H., Neylan, T. C., Schiller, N. B., Li, Y. & Cohen, B. E. Objective evidence of myocardial ischemia in patients with posttraumatic stress disorder. *Biol. Psychiatry* (2013). doi:10.1016/j.biopsych.2013.07.012

114. Batten, S. V., Aslan, M., Maciejewski, P. K. & Mazure, C. M. Childhood maltreatment as a risk factor for adult cardiovascular disease and depression. *J. Clin. Psychiatry* (2004). doi:10.4088/JCP.v65n0217

115. Dong, M. *et al.* Insights into causal pathways for ischemic heart disease: Adverse childhood experiences study. *Circulation* (2004). doi:10.1161/01.CIR.0000143074.54995.7F

116. Bremner, J. D. *et al.* Brain Correlates of Mental Stress-Induced Myocardial Ischemia. *Psychosom. Med.* (2018). doi:10.1097/PSY.0000000000000597

117. Del Gaizo, A. L., Elhai, J. D. & Weaver, T. L. Posttraumatic stress disorder, poor physical health and substance use behaviors in a national trauma-exposed sample. *Psychiatry Res.* (2011). doi:10.1016/j.psychres.2011.03.016

118. Härter, M. C., Conway, K. P. & Merikangas, K. R. Associations between anxiety disorders and physical illness. *Eur. Arch. Psychiatry Clin. Neurosci.* (2003). doi:10.1007/s00406-003-0449-y

119. Frasure-Smith, N. & Lespérance, F. Depression and anxiety as predictors of 2-year cardiac events in patients with stable coronary artery disease. *Arch. Gen. Psychiatry* (2008). doi:10.1001/archgenpsychiatry.2007.4

120. Fleet, R., Lavoie, K. & Beitman, B. D. Is panic disorder associated with coronary artery disease? A critical review of the literature. *Journal of Psychosomatic Research* (2000). doi:10.1016/S0022-3999(99)00101-4

121. Smoller, J. W. *et al.* Panic attacks and risk of incident cardiovascular events among postmenopausal women in the women's health initiative observational study. *Arch. Gen. Psychiatry* (2007). doi:10.1001/archpsyc.64.10.1153

122. Barger, S. D. & Sydeman, S. J. Does generalized anxiety disorder predict coronary heart disease risk factors independently of major depressive disorder? *J. Affect. Disord.* (2005). doi:10.1016/j.jad.2005.05.012

123. Kawachi, I. *et al.* Prospective study of phobic anxiety and risk of coronary heart disease in men. *Circulation* (1994). doi:10.1161/01.CIR.89.5.1992

124. Watkins, L. L. *et al.* Phobic anxiety, depression, and risk of ventricular arrhythmias in patients with coronary heart disease. *Psychosom. Med.* (2006). doi:10.1097/01.psy.0000228342.53606.b3

125. Manuck, S. B., Kaplan, J. R., Adams, M. R. & Clarkson, T. B. Studies of psychosocial influences on coronary artery atherogenesis in cynomolgus monkeys. *Health Psychol.* (1988). doi:10.1037/0278-6133.7.2.113

126. Shively, C. A. & Clarkson, T. B. Social status and coronary artery atherosclerosis in female monkeys. *Arterioscler. Thromb.* (1994). doi:10.1161/01.atv.14.5.721

127. Joëls, M. Corticosteroid effects in the brain: U-shape it. *Trends Pharmacol. Sci.* (2006). doi:10.1016/j.tips.2006.03.007

128. Popoli, M., Yan, Z., McEwen, B. S. & Sanacora, G. The stressed synapse: The impact of stress and glucocorticoids on glutamate transmission. *Nature Reviews Neuroscience* (2012). doi:10.1038/nrn3138

129. Revollo, J. R. & Cidlowski, J. A. Mechanisms generating diversity in glucocorticoid receptor signaling. in *Annals of the New York Academy of Sciences* (2009). doi:10.1111/j.1749-6632.2009.04986.x

130. Venero, C. & Borrell, J. Rapid glucocorticoid effects on excitatory amino acid levels in the hippocampus: A microdialysis study in freely moving rats. *Eur. J. Neurosci.* (1999).

doi:10.1046/j.1460-9568.1999.00668.x

131. Lowy, M. T., Gault, L. & Yamamoto, B. K. Rapid Communication: Adrenalectomy Attenuates Stress-Induced Elevations in Extracellular Glutamate Concentrations in the Hippocampus. *J. Neurochem.* (1993). doi:10.1111/j.1471-4159.1993.tb09839.x

132. Di, S., Maxson, M. M., Franco, A. & Tasker, J. G. Glucocorticoids regulate glutamate and GABA synapse-specific retrograde transmission via divergent nongenomic signaling pathways. *J. Neurosci.* (2009). doi:10.1523/JNEUROSCI.4546-08.2009

133. Haller, J., Mikics, É. & Makara, G. B. The effects of non-genomic glucocorticoid mechanisms on bodily functions and the central neural system. A critical evaluation of findings. *Frontiers in Neuroendocrinology* (2008). doi:10.1016/j.yfrne.2007.10.004

134. Tasker, J. G., Di, S. & Malcher-Lopes, R. Minireview: Rapid glucocorticoid signaling via membrane-associated receptors. *Endocrinology* (2006). doi:10.1210/en.2006-0981

135. Di, S., Malcher-Lopes, R., Halmos, K. C. & Tasker, J. G. Nongenomic glucocorticoid inhibition via endocannabinoid release in the hypothalamus: A fast feedback mechanism. *J. Neurosci.* (2003). doi:10.1523/jneurosci.23-12-04850.2003

136. Karst, H. *et al.* Mineralocorticoid receptors are indispensable for nongenomic modulation of hippocampal glutamate transmission by corticosterone. *Proc. Natl. Acad. Sci. U. S. A.* (2005). doi:10.1073/pnas.0507572102

137. Treccani, G. *et al.* Stress and corticosterone increase the readily releasable pool of glutamate vesicles in synaptic terminals of prefrontal and frontal cortex. *Mol. Psychiatry* (2014). doi:10.1038/mp.2014.5

138. Magariños, A. M. & McEwen, B. S. Stress-induced atrophy of apical dendrites of hippocampal CA3c neurons: Involvement of glucocorticoid secretion and excitatory amino acid receptors. *Neuroscience* (1995). doi:10.1016/0306-4522(95)00259-L

139. Watanabe, Y., Gould, E. & McEwen, B. S. Stress induces atrophy of apical dendrites of hippocampal CA3 pyramidal neurons. *Brain Res.* (1992). doi:10.1016/0006-

8993(92)91597-8

140. McEwen, B. S. & Magarinos, A. M. Stress and hippocampal plasticity: Implications for the pathophysiology of affective disorders. *Hum. Psychopharmacol.* (2001). doi:10.1002/hup.266

141. Morimoto, M., Morita, N., Ozawa, H., Yokoyama, K. & Kawata, M. Distribution of glucocorticoid receptor immunoreactivity and mRNA in the rat brain: An immunohistochemical and in situ hybridization study. *Neurosci. Res.* (1996). doi:10.1016/S0168-0102(96)01105-4

142. Chattarji, S., Tomar, A., Suvrathan, A., Ghosh, S. & Rahman, M. M. Neighborhood matters: Divergent patterns of stress-induced plasticity across the brain. *Nature Neuroscience* (2015). doi:10.1038/nn.4115

143. McEwen, B. S., Weiss, J. M. & Schwartz, L. S. Selective retention of corticosterone by limbic structures in rat brain [18]. *Nature* (1968). doi:10.1038/220911a0

144. Reul, J. M. H. M. & De Kloet, E. R. Two receptor systems for corticosterone in rat brain: Microdistribution and differential occupation. *Endocrinology* (1985). doi:10.1210/endo-117-6-2505

145. Herman, J. P. & Cullinan, W. E. Neurocircuitry of stress: Central control of the hypothalamo-pituitary-adrenocortical axis. *Trends Neurosci.* (1997). doi:10.1016/S0166-2236(96)10069-2

146. Jacobson, L. & Sapolsky, R. The role of the hippocampus in feedback regulation of the hypothalamic-pituitary-adrenocortical axis. *Endocr. Rev.* (1991). doi:10.1210/edrv-12-2-118

147. Liu, D. *et al.* Maternal care, hippocampal glucocorticoid receptors, and hypothalamic-pituitary-adrenal responses to stress. *Science (80-.).* (1997). doi:10.1126/science.277.5332.1659

148. Sapolsky, R. M., Zola-Morgan, S. & Squire, L. R. Inhibition of glucocorticoid secretion

by the hippocampal formation in the primate. *J. Neurosci.* (1991). doi:10.1523/jneurosci.11-12-03695.1991

149. Diamond, D. M., Bennett, M. C., Fleshner, M. & Rose, G. M. Inverted-U relationship between the level of peripheral corticosterone and the magnitude of hippocampal primed burst potentiation. *Hippocampus* (1992). doi:10.1002/hipo.450020409

150. Pavlides, C., Watanabe, Y., Magarin˜os, A. M. & McEwen, B. S. Opposing roles of type I and type II adrenal steroid receptors in hippocampal long-term potentiation. *Neuroscience* (1995). doi:10.1016/0306-4522(95)00151-8

151. Kim, J. J. & Diamond, D. M. The stressed hippocampus, synaptic plasticity and lost memories. *Nat. Rev. Neurosci.* (2002). doi:10.1038/nrn849

152. Kim, J. J., Foy, M. R. & Thompson, R. F. Behavioral stress modifies hippocampal plasticity through N-methyl-D-aspartate receptor activation. *Proc. Natl. Acad. Sci. U. S. A.* (1996). doi:10.1073/pnas.93.10.4750

153. Xu, L., Anwyl, R. & Rowan, M. J. Behavioural stress facilitates the induction of long-term depression in the hippocampus. *Nature* (1997). doi:10.1038/387497a0

154. Nibuya, M., Morinobu, S. & Duman, R. S. Regulation of BDNF and trkB mRNA in rat brain by chronic electroconvulsive seizure and antidepressant drug treatments. *J. Neurosci.* (1995). doi:10.1523/jneurosci.15-11-07539.1995

155. Smith, M. A., Makino, S., Kvetnansky, R. & Post, R. M. Stress and glucocorticoids affect the expression of brain-derived neurotrophic factor and neurotrophin-3 mRNAs in the hippocampus. *J. Neurosci.* (1995). doi:10.1523/jneurosci.15-03-01768.1995

156. Vyas, A., Mitra, R., Shankaranarayana Rao, B. S. & Chattarji, S. Chronic stress induces contrasting patterns of dendritic remodeling in hippocampal and amygdaloid neurons. *J. Neurosci.* (2002). doi:10.1523/jneurosci.22-15-06810.2002

157. Krishnan, V. *et al.* Molecular Adaptations Underlying Susceptibility and Resistance to Social Defeat in Brain Reward Regions. *Cell* (2007). doi:10.1016/j.cell.2007.09.018

158. Bechtholt, A. J., Valentino, R. J. & Lucki, I. Overlapping and distinct brain regions associated with the anxiolytic effects of chlordiazepoxide and chronic fluoxetine. *Neuropsychopharmacology* (2008). doi:10.1038/sj.npp.1301616

159. Fetterly, T. L. *et al.* α 2A -adrenergic receptor activation decreases parabrachial nucleus excitatory drive onto BNST CRF neurons and reduces their activity in Vivo. *J. Neurosci.* (2019). doi:10.1523/JNEUROSCI.1035-18.2018

160. Pêgo, J. M. *et al.* Dissociation of the morphological correlates of stress-induced anxiety and fear. *Eur. J. Neurosci.* (2008). doi:10.1111/j.1460-9568.2008.06112.x

161. Vyas, A., Bernal, S. & Chattarji, S. Effects of chronic stress on dendritic arborization in the central and extended amygdala. *Brain Res.* (2003). doi:10.1016/S0006-8993(02)04162-8

162. Bennur, S. *et al.* Stress-induced spine loss in the medial amygdala is mediated by tissue-plasminogen activator. *Neuroscience* (2007). doi:10.1016/j.neuroscience.2006.08.075

163. Radley, J. J. *et al.* Chronic behavioral stress induces apical dendritic reorganization in pyramidal neurons of the medial prefrontal cortex. *Neuroscience* (2004). doi:10.1016/j.neuroscience.2004.01.006

164. Wellman, C. L. Dendritic reorganization in pyramidal neurons in medial prefrontal cortex after chronic corticosterone administration. *J. Neurobiol.* (2001). doi:10.1002/neu.1079

165. Radley, J. J. *et al.* Repeated stress induces dendritic spine loss in the rat medial prefrontal cortex. *Cereb. Cortex* (2006). doi:10.1093/cercor/bhi104

166. Radley, J. J. *et al.* Repeated stress alters dendritic spine morphology in the rat medial prefrontal cortex. *J. Comp. Neurol.* (2008). doi:10.1002/cne.21588

167. Liston, C. *et al.* Stress-induced alterations in prefrontal cortical dendritic morphology predict selective impairments in perceptual attentional set-shifting. *J. Neurosci.* (2006). doi:10.1523/JNEUROSCI.1184-06.2006

168. Starkman, M. N., Gebarski, S. S., Berent, S. & Schteingart, D. E. Hippocampal formation volume, memory dysfunction, and cortisol levels in patients with Cushing's syndrome. *Biol. Psychiatry* (1992). doi:10.1016/0006-3223(92)90079-F

169. Starkman, M. N. *et al.* Decrease in cortisol reverses human hippocampal atrophy following treatment of Cushing's disease. *Biol. Psychiatry* (1999). doi:10.1016/S0006-3223(99)00203-6

170. Bourdeau, I. *et al.* Loss of brain volume in endogenous Cushing's syndrome and its reversibility after correction of hypercortisolism. *J. Clin. Endocrinol. Metab.* (2002). doi:10.1210/jc.87.5.1949

171. Heinz, E. R., Martinez, J. & Haenggeli, A. Reversibility of cerebral atrophy in anorexia nervosa and cushing's syndrome. *J. Comput. Assist. Tomogr.* (1977). doi:10.1097/00004728-197710000-00006

172. Forget, H., Lacroix, A., Somma, M. & Cohen, H. Cognitive decline in patients with Cushing's syndrome. *J. Int. Neuropsychol. Soc.* (2000). doi:10.1017/S1355617700611037

173. Mauri, M. *et al.* Memory impairment in Cushing's disease. *Acta Neurol. Scand.* (1993). doi:10.1111/j.1600-0404.1993.tb04075.x

174. Brzozowska, M. M., Kepreotis, S., Tsang, F. & Fuentes-Patarroyo, S. X. Improvement in cognitive impairment following the successful treatment of endogenous Cushing's syndrome-a case report and literature review. *BMC Endocr. Disord.* (2019). doi:10.1186/s12902-019-0401-4

175. Bremner, J. D. *et al.* Magnetic resonance imaging-based measurement of hippocampal volume in posttraumatic stress disorder related to childhood physical and sexual abuse - A preliminary report. *Biol. Psychiatry* (1997). doi:10.1016/S0006-3223(96)00162-X

176. Bremner, J. D. *et al.* MRI-based measurement of hippocampal volume in patients with combat- related posttraumatic stress disorder. *Am. J. Psychiatry* (1995). doi:10.1176/ajp.152.7.973

177. Rauch, S. L. *et al.* Exaggerated amygdala response to masked facial stimuli in posttraumatic stress disorder: A functional MRI study. *Biol. Psychiatry* (2000). doi:10.1016/S0006-3223(00)00828-3

178. Shin, L. M. *et al.* A functional magnetic resonance imaging study of amygdala and medial prefrontal cortex responses to overtly presented fearful faces in posttraumatic stress disorder. *Arch. Gen. Psychiatry* (2005). doi:10.1001/archpsyc.62.3.273

179. Armony, J. L., Corbo, V., Clément, M. H. & Brunet, A. Amygdala response in patients with acute PTSD to masked and unmasked emotional facial expressions. *Am. J. Psychiatry* (2005). doi:10.1176/appi.ajp.162.10.1961

180. Whalen, P. J. *et al.* A Functional MRI Study of Human Amygdala Responses to Facial Expressions of Fear Versus Anger. *Emotion* (2001). doi:10.1037/1528-3542.1.1.70

181. Shin, L. M., Rauch, S. L. & Pitman, R. K. Amygdala, medial prefrontal cortex, and hippocampal function in PTSD. in *Annals of the New York Academy of Sciences* (2006). doi:10.1196/annals.1364.007

182. Britton, J. C., Phan, K. L., Taylor, S. F., Fig, L. M. & Liberzon, I. Corticolimbic blood flow in posttraumatic stress disorder during script-driven imagery. *Biol. Psychiatry* (2005). doi:10.1016/j.biopsych.2004.12.025

183. Admon, R. *et al.* Human vulnerability to stress depends on amygdala's predisposition and hippocampal plasticity. *Proc. Natl. Acad. Sci. U. S. A.* (2009). doi:10.1073/pnas.0903183106

184. Van Wingen, G. A., Geuze, E., Vermetten, E. & Fernández, G. Perceived threat predicts the neural sequelae of combat stress. *Mol. Psychiatry* (2011). doi:10.1038/mp.2010.132

185. Lorenzetti, V., Allen, N. B., Fornito, A. & Yücel, M. Structural brain abnormalities in major depressive disorder: A selective review of recent MRI studies. *Journal of Affective Disorders* (2009). doi:10.1016/j.jad.2008.11.021

186. De Asis, J. M. *et al.* Hippocampal and anterior cingulate activation deficits in patients

with geriatric depression. *Am. J. Psychiatry* (2001). doi:10.1176/appi.ajp.158.8.1321

187. Roberson-Nay, R. *et al.* Increased Amygdala Activity During Successful Memory Encoding in Adolescent Major Depressive Disorder: An fMRI Study. *Biol. Psychiatry* (2006). doi:10.1016/j.biopsych.2006.02.018

188. Esler, M. *et al.* The Peripheral Kinetics of Norepinephrine in Depressive Illness. *Arch. Gen. Psychiatry* (1982). doi:10.1001/archpsyc.1982.04290030035006

189. Walker, E. F., Bonsall, R. & Walder, D. J. Plasma hormones and catecholamine metabolites in monozygotic twins discordant for psychosis. *Neuropsychiatry, Neuropsychol. Behav. Neurol.* (2002).

190. Roy, A., Pickar, D., Jong, J., Karoum, F. & Linnoila, M. Norepinephrine and Its Metabolites in Cerebrospinal Fluid, Plasma, and Urine: Relationship to Hypothalamic-Pituitary-Adrenal Axis Function in Depression. *Arch. Gen. Psychiatry* (1988). doi:10.1001/archpsyc.1988.01800330081010

191. Siever, L. J. & Davis, K. L. Overview: Toward a dysregulation hypothesis of depression. *American Journal of Psychiatry* (1985). doi:10.1176/ajp.142.9.1017

192. Veith, R. C. *et al.* Sympathetic Nervous System Activity in Major Depression: Basal and Desipramine-Induced Alterations in Plasma Norepinephrine Kinetics. *Arch. Gen. Psychiatry* (1994). doi:10.1001/archpsyc.1994.03950050071008

193. Kassam-Adams, N. & Winston, F. K. Predicting child PTSD: The relationship between acute stress disorder and PTSD in injured children. *J. Am. Acad. Child Adolesc. Psychiatry* (2004). doi:10.1097/00004583-200404000-00006

194. Brodsky, B. S., Malone, K. M., Ellis, S. P., Dulit, R. A. & Mann, J. J. Characteristics of borderline personality disorder associated with suicidal behavior. *Am. J. Psychiatry* (1997). doi:10.1176/ajp.154.12.1715

195. Kaslow, N. *et al.* Risk factors for suicide attempts among African American women. *Depress. Anxiety* (2000). doi:10.1002/1520-6394(2000)12:1<13::AID-DA2>3.0.CO;2-Y

196. Kingree, J. B., Thompson, M. P. & Kaslow, N. J. Risk factors for suicide attempts among low-income women with a history of alcohol problems. *Addict. Behav.* (1999). doi:10.1016/S0306-4603(98)00109-9

197. Van der Kolk, B. A., Perry, J. C. & Herman, J. L. Childhood origins of self-destructive behavior. *Am. J. Psychiatry* (1991). doi:10.1176/ajp.148.12.1665

198. Kendall-Tackett, K. A., Williams, L. M. & Finkelhor, D. Impact of Sexual Abuse on Children: A Review and Synthesis of Recent Empirical Studies. *Psychol. Bull.* (1993). doi:10.1037/0033-2909.113.1.164

199. Kendler, K. S. *et al.* Childhood sexual abuse and adult psychiatric and substance use disorders in women: An epidemiological and cotwin control analysis. *Arch. Gen. Psychiatry* (2000). doi:10.1001/archpsyc.57.10.953

200. Putnam, F. W. Ten-year research update review: Child sexual abuse. *Journal of the American Academy of Child and Adolescent Psychiatry* (2003). doi:10.1097/00004583-200303000-00006

201. Osofsky, J. D. The impact of violence on children. *Future of Children* (1999). doi:10.2307/1602780

202. Anda, R. F. *et al.* The enduring effects of abuse and related adverse experiences in childhood: A convergence of evidence from neurobiology and epidemiology. *Eur. Arch. Psychiatry Clin. Neurosci.* (2006). doi:10.1007/s00406-005-0624-4

203. Horwitz, A. V., Widom, C. S., McLaughlin, J. & White, H. R. The impact of childhood abuse and neglect on adult mental health: A prospective study. *J. Health Soc. Behav.* (2001). doi:10.2307/3090177

204. Schilling, E. A., Aseltine, R. H. & Gore, S. Adverse childhood experiences and mental health in young adults: A longitudinal survey. *BMC Public Health* (2007). doi:10.1186/1471-2458-7-30

205. Rutter, M., Kim-Cohen, J. & Maughan, B. Continuities and discontinuities in

psychopathology between childhood and adult life. *J. Child Psychol. Psychiatry Allied Discip.* (2006). doi:10.1111/j.1469-7610.2006.01614.x

206. Danese, A. *et al.* Elevated inflammation levels in depressed adults with a history of childhood maltreatment. *Arch. Gen. Psychiatry* (2008). doi:10.1001/archpsyc.65.4.409

207. Nomura, Y. *et al.* Low birth weight and risk of affective disorders and selected medical illness in offspring at high and low risk for depression. *Compr. Psychiatry* (2007). doi:10.1016/j.comppsych.2007.04.005

208. Willner, P., Scheel-Krüger, J. & Belzung, C. The neurobiology of depression and antidepressant action. *Neuroscience and Biobehavioral Reviews* (2013). doi:10.1016/j.neubiorev.2012.12.007

209. Domenighetti, G., D'Avanzo, B. & Bisig, B. Health effects of job insecurity among employees in the Swiss general population. *International Journal of Health Services* (2000). doi:10.2190/B1KM-VGN7-50GF-8XJ4

210. McDonough, P. Job insecurity and health. *Int. J. Heal. Serv.* (2000). doi:10.2190/BPFG-X3ME-LHTA-6RPV

211. Cheng, Y., Chen, C. W., Chen, C. J. & Chiang, T. L. Job insecurity and its association with health among employees in the Taiwanese general population. *Soc. Sci. Med.* (2005). doi:10.1016/j.socscimed.2004.11.039

212. Bourbonnais, R., Comeau, M., Vézina, M. & Dion, G. Job strain, psychological distress, and burnout in nurses. *Am. J. Ind. Med.* (1998). doi:10.1002/(SICI)1097-0274(199807)34:1<20::AID-AJIM4>3.0.CO;2-U

213. Kawachi, I. & Berkman, L. F. Social ties and mental health. *J. Urban Heal.* (2001). doi:10.1093/jurban/78.3.458

214. Amick, B. C. *et al.* Relationship of job strain and iso-strain to health status in a cohort of women in the United States. *Scand. J. Work. Environ. Heal.* (1998). doi:10.5271/sjweh.278

215. Grzywacz, J. G. & Dooley, D. ‘Good jobs’ to ‘bad jobs’: Replicated evidence of an employment continuum from two large surveys. *Soc. Sci. Med.* (2003). doi:10.1016/S0277-9536(02)00170-3

216. Arnetz, B. B. *et al.* Neuroendocrine and immunologic effects of unemployment and job insecurity. *Psychother. Psychosom.* (1991). doi:10.1159/000288412

217. Macdonald, A., Murray, J. & Strathdee, G. Minor Psychiatric Morbidity and the Threat of Redundancy in a Professional Group. *Psychol. Med.* (1982). doi:10.1017/S0033291700049102

218. Ferrie, J. E., Shipley, M. J., Marmot, M. G., Stansfeld, S. & Smith, G. D. Health effects of anticipation of job change and non-employment: Longitudinal data from the Whitehall II study. *BMJ* (1995). doi:10.1136/bmj.311.7015.1264

219. Ferrie, J. E., Shipley, M. J., Marmot, M. G., Stansfeld, S. A. & Smith, G. D. An uncertain future: The health effects of threats to employment security in white-collar men and women. *Am. J. Public Health* (1998). doi:10.2105/AJPH.88.7.1030

220. Mattiasson, I., Lindgarde, F., Nilsson, J. A. & Theorell, T. Threat of unemployment and cardiovascular risk factors: Longitudinal study of quality of sleep and serum cholesterol concentrations in men threatened with redundancy. *Br. Med. J.* (1990). doi:10.1136/bmj.301.6750.461

221. Condren, R. M. & Thakore, J. H. Cushing’s disease and melancholia. *Stress* (2001). doi:10.3109/10253890109115725

222. Cushing, H. The Basophil Adenomas of the Pituitary Body and Their Clinical Manifestations (Pituitary Basophilism). *Bull. Johns Hopkins Hosp.* **50**, 137–195 (1932).

223. Sonino, N., Fava, G. A., Raffi, A. R., Boscaro, M. & Fallo, F. Clinical correlates of major depression in Cushing’s disease. *Psychopathology* (1998). doi:10.1159/000029054

224. Hudson, J. I., Hudson, M. S., Griffing, G. T., Melby, J. C. & Pope, H. G. Phenomenology and family history of affective disorder in Cushing’s disease. *Am. J. Psychiatry* (1987).

doi:10.1176/ajp.144.7.951

225. Loosen, P. T., Chambliss, B., DeBold, C. R., Shelton, R. & Orth, D. N. Psychiatric phenomenology in Cushings's disease. *Pharmacopsychiatry* (1992). doi:10.1055/s-2007-1014405

226. Starkman, M. N., Schteingart, D. E. & Schork, M. A. Depressed mood and other psychiatric manifestations of Cushing's syndrome: Relationship to hormone levels. *Psychosom. Med.* (1981). doi:10.1097/00006842-198102000-00002

227. Veenema, A. H., Meijer, O. C., de Kloet, E. R. & Koolhaas, J. M. Genetic selection for coping style predicts stressor susceptibility. *Journal of Neuroendocrinology* (2003). doi:10.1046/j.1365-2826.2003.00986.x

228. Gruene, T. M., Flick, K., Stefano, A., Shea, S. D. & Shansky, R. M. Sexually divergent expression of active and passive conditioned fear responses in rats. *Elife* (2015). doi:10.7554/elife.11352

229. Marcinkiewcz, C. A. *et al.* Sex-dependent modulation of anxiety and fear by 5-HT1A receptors in the bed nucleus of the stria terminalis. *ACS Chem. Neurosci.* (2019). doi:10.1021/acschemneuro.8b00594

230. Engel, G. L. & Schmale, A. H. Conservation-withdrawal: a primary regulatory process for organismic homeostasis. *Ciba Found. Symp.* (1972). doi:10.1002/9780470719916.ch5

231. Koolhaas, J. M. *et al.* Coping styles in animals: Current status in behavior and stress-physiology. *Neurosci. Biobehav. Rev.* (1999). doi:10.1016/S0149-7634(99)00026-3

232. Southwick, S. M., Vythilingam, M. & Charney, D. S. The psychobiology of depression and resilience to stress: Implications for prevention and treatment. *Annual Review of Clinical Psychology* (2005). doi:10.1146/annurev.clinpsy.1.102803.143948

233. Wood, S. K. & Bhatnagar, S. Resilience to the effects of social stress: Evidence from clinical and preclinical studies on the role of coping strategies. *Neurobiology of Stress* (2015). doi:10.1016/j.ynstr.2014.11.002

234. Grafe, L. A. *et al.* Passive Coping Strategies During Repeated Social Defeat Are Associated With Long-Lasting Changes in Sleep in Rats. *Front. Syst. Neurosci.* (2020). doi:10.3389/fnsys.2020.00006

235. Miczek, K. A. A new test for aggression in rats without aversive stimulation: Differential effects of d-amphetamine and cocaine. *Psychopharmacology (Berl).* (1979). doi:10.1007/BF00426664

236. Wood, S. K., Walker, H. E., Valentino, R. J. & Bhatnagar, S. Individual differences in reactivity to social stress predict susceptibility and resilience to a depressive phenotype: Role of corticotropin-releasing factor. *Endocrinology* (2010). doi:10.1210/en.2009-1026

237. Parsons, L. H. & Hurd, Y. L. Endocannabinoid signalling in reward and addiction. *Nat. Rev. Neurosci.* **16**, 579–594 (2015).

238. Finnell, J. E. *et al.* Physical versus psychological social stress in male rats reveals distinct cardiovascular, inflammatory and behavioral consequences. *PLoS One* (2017). doi:10.1371/journal.pone.0172868

239. Pearson-Leary, J. *et al.* Inflammation and vascular remodeling in the ventral hippocampus contributes to vulnerability to stress. *Transl. Psychiatry* (2017). doi:10.1038/tp.2017.122

240. Pearson-Leary, J. *et al.* The gut microbiome regulates the increases in depressive-type behaviors and in inflammatory processes in the ventral hippocampus of stress vulnerable rats. *Mol. Psychiatry* (2020). doi:10.1038/s41380-019-0380-x

241. Fucich, E. & Morilak, D. Shock-probe Defensive Burying Test to Measure Active versus Passive Coping Style in Response to an Aversive Stimulus in Rats. *BIO-PROTOCOL* (2018). doi:10.21769/bioprotoc.2998

242. Folkman, S. & Lazarus, R. S. An analysis of coping in a middle-aged community sample. *J. Health Soc. Behav.* (1980). doi:10.2307/2136617

243. Billings, A. G. & Moos, R. H. Coping, stress, and social resources among adults with unipolar depression. *J. Pers. Soc. Psychol.* (1984). doi:10.1037//0022-3514.46.4.877

244. Montgomery, K. C. The relation between fear induced by novel stimulation and exploratory drive. *J. Comp. Physiol. Psychol.* (1955). doi:10.1037/h0043788

245. Handley, S. L. & Mithani, S. Effects of alpha-adrenoceptor agonists and antagonists in a maze-exploration model of 'fear'-motivated behaviour. *Naunyn. Schmiedebergs. Arch. Pharmacol.* (1984). doi:10.1007/BF00504983

246. Pellow, S. & File, S. E. Anxiolytic and anxiogenic drug effects on exploratory activity in an elevated plus-maze: A novel test of anxiety in the rat. *Pharmacol. Biochem. Behav.* (1986). doi:10.1016/0091-3057(86)90552-6

247. Shepherd, J. K., Grewal, S. S., Fletcher, A., Bill, D. J. & Dourish, C. T. Behavioural and pharmacological characterisation of the elevated 'zero-maze' as an animal model of anxiety. *Psychopharmacology (Berl).* (1994). doi:10.1007/BF02244871

248. Viana, M. B., Tomaz, C. & Graeff, F. G. The elevated T-maze: A new animal model of anxiety and memory. *Pharmacol. Biochem. Behav.* (1994). doi:10.1016/0091-3057(94)90067-1

249. Hall, C. S. Emotional behavior in the rat. I. Defecation and urination as measures of individual differences in emotionality. *J. Comp. Psychol.* (1934). doi:10.1037/h0071444

250. David, D. J. *et al.* Neurogenesis-Dependent and -Independent Effects of Fluoxetine in an Animal Model of Anxiety/Depression. *Neuron* (2009). doi:10.1016/j.neuron.2009.04.017

251. Reardon, S. Depression researchers rethink popular mouse swim tests. *Nature* (2019). doi:10.1038/d41586-019-02133-2

252. Porsolt, R. D., Bertin, A. & Jalfre, M. Behavioral despair in mice: A primary screening test for antidepressants. *Arch. Int. Pharmacodyn. Ther.* (1977).

253. Porsolt, R. D., Le Pichon, M. & Jalfre, M. Depression: A new animal model sensitive to antidepressant treatments [27]. *Nature* (1977). doi:10.1038/266730a0

254. Veenema, A. H., Blume, A., Niederle, D., Buwalda, B. & Neumann, I. D. Effects of early

life stress on adult male aggression and hypothalamic vasopressin and serotonin. *Eur. J. Neurosci.* (2006). doi:10.1111/j.1460-9568.2006.05045.x

255. Kalynchuk, L. E., Gregus, A., Boudreau, D. & Perrot-Sinal, T. S. Corticosterone increases depression-like behavior, with some effects on predator odor-induced defensive behavior, in male and female rats. *Behav. Neurosci.* (2004). doi:10.1037/0735-7044.118.6.1365

256. Johnson, S. A., Fournier, N. M. & Kalynchuk, L. E. Effect of different doses of corticosterone on depression-like behavior and HPA axis responses to a novel stressor. *Behav. Brain Res.* (2006). doi:10.1016/j.bbr.2005.11.019

257. Commons, K. G., Cholanians, A. B., Babb, J. A. & Ehlinger, D. G. The Rodent Forced Swim Test Measures Stress-Coping Strategy, Not Depression-like Behavior. *ACS Chemical Neuroscience* (2017). doi:10.1021/acschemneuro.7b00042

258. Castagné, V., Moser, P., Roux, S. & Porsolt, R. D. Rodent models of depression: Forced swim and tail suspension behavioral despair tests in rats and mice. *Curr. Protoc. Neurosci.* (2011). doi:10.1002/0471142301.ns0810as55

259. Lucki, I. The forced swimming test as a model for core and component behavioral effects of antidepressant drugs. *Behavioural Pharmacology* (1997). doi:10.1097/00008877-199711000-00010

260. Overstreet, D. H. Modeling depression in animal models. *Methods in Molecular Biology* (2012). doi:10.1007/978-1-61779-458-2_7

261. Dalla, C., Pitychoutis, P. M., Kokras, N. & Papadopoulou-Daifoti, Z. Sex differences in response to stress and expression of depressive-like behaviours in the rat. *Current Topics in Behavioral Neurosciences* (2011). doi:10.1007/7854_2010_94

262. Blanchard, R. J. & Blanchard, D. C. Attack and defense in rodents as ethoexperimental models for the study of emotion. *Prog. Neuropsychopharmacol. Biol. Psychiatry* (1989). doi:10.1016/0278-5846(89)90105-X

263. Hendrie, C. A., Weiss, S. M. & Eilam, D. Exploration and predation models of anxiety:

Evidence from laboratory and wild species. in *Pharmacology Biochemistry and Behavior* (1996). doi:10.1016/0091-3057(95)02176-0

264. Blanchard, D. C., Griebel, G. & Blanchard, R. J. Conditioning and residual emotionality effects of predator stimuli: Some reflections on stress and emotion. in *Progress in Neuro-Psychopharmacology and Biological Psychiatry* (2003). doi:10.1016/j.pnpbp.2003.09.012

265. Apfelbach, R., Blanchard, C. D., Blanchard, R. J., Hayes, R. A. & McGregor, I. S. The effects of predator odors in mammalian prey species: A review of field and laboratory studies. in *Neuroscience and Biobehavioral Reviews* (2005). doi:10.1016/j.neubiorev.2005.05.005

266. Kavaliers, M., Choleris, E. & Colwell, D. D. Brief exposure to female odors 'emboldens' male mice by reducing predator-induced behavioral and hormonal responses. *Horm. Behav.* (2001). doi:10.1006/hbeh.2001.1714

267. Masini, C. V., Sauer, S. & Campeau, S. Ferret odor as a processive stress model in rats: Neurochemical, behavioral, and endocrine evidence. *Behav. Neurosci.* (2005). doi:10.1037/0735-7044.119.1.280

268. Day, H. E. W., Masini, C. V. & Campeau, S. The pattern of brain c-fos mRNA induced by a component of fox odor, 2,5-dihydro-2,4,5-Trimethylthiazoline (TMT), in rats, suggests both systemic and processive stress characteristics. *Brain Res.* (2004). doi:10.1016/j.brainres.2004.07.079

269. Dias Soares, D. *et al.* Fox odour affects corticosterone release but not hippocampal serotonin reuptake and open field behaviour in rats. *Brain Res.* (2003). doi:10.1016/S0006-8993(02)03944-6

270. Morrow, B. A., Elsworth, J. D. & Roth, R. H. Fear-like biochemical and behavioral responses in rats to the predator odor, TMT, are dependent on the exposure environment. *Synapse* (2002). doi:10.1002/syn.10109

271. Cohen, H., Benjamin, J., Kaplan, Z. & Kotler, M. Administration of high-dose ketoconazole, an inhibitor of steroid synthesis, prevents posttraumatic anxiety in an

animal model. *Eur. Neuropsychopharmacol.* (2000). doi:10.1016/S0924-977X(00)00105-X

272. Adamec, R., Kent, P., Anisman, H., Shallow, T. & Merali, Z. Neural plasticity, neuropeptides and anxiety in animals - Implications for understanding and treating affective disorder following traumatic stress in humans. in *Neuroscience and Biobehavioral Reviews* (1998). doi:10.1016/S0149-7634(98)00032-3

273. Dielenberg, R. A. & McGregor, I. S. Habituation of the hiding response to cat odor in rats (Rattus norvegicus). *J. Comp. Psychol.* (1999). doi:10.1037/0735-7036.113.4.376

274. Kvetňanský, R. & Mikulaj, L. Adrenal and Urinary catecholamines in rats during adaptation to repeated immobilization stress. *Endocrinology* (1970). doi:10.1210/endo-87-4-738

275. Gameiro, G. H. *et al.* Nociception- and anxiety-like behavior in rats submitted to different periods of restraint stress. *Physiol. Behav.* (2006). doi:10.1016/j.physbeh.2005.12.007

276. Patel, S., Roelke, C. T., Rademacher, D. J. & Hillard, C. J. Inhibition of restraint stress-induced neural and behavioural activation by endogenous cannabinoid signalling. *Eur. J. Neurosci.* (2005). doi:10.1111/j.1460-9568.2005.03916.x

277. McLaughlin, R. J. *et al.* Prefrontal cortical anandamide signaling coordinates coping responses to stress through a serotonergic pathway. *Eur. Neuropsychopharmacol.* (2012). doi:10.1016/j.euroneuro.2012.01.004

278. Campos, A. C., Ferreira, F. R., Guimarães, F. S. & Lemos, J. I. Facilitation of endocannabinoid effects in the ventral hippocampus modulates anxiety-like behaviors depending on previous stress experience. *Neuroscience* (2010). doi:10.1016/j.neuroscience.2010.01.062

279. Zhang, J. Y. *et al.* Chronic Stress Remodels Synapses in an Amygdala Circuit–Specific Manner. *Biol. Psychiatry* (2019). doi:10.1016/j.biopsych.2018.06.019

280. Holmes, A. & Wellman, C. L. Stress-induced prefrontal reorganization and executive

dysfunction in rodents. *Neuroscience and Biobehavioral Reviews* (2009). doi:10.1016/j.neubiorev.2008.11.005

281. Mitra, R., Jadhav, S., McEwen, B. S., Vyas, A. & Chattarji, S. Stress duration modulates the spatiotemporal patterns of spine formation in the basolateral amygdala. *Proc. Natl. Acad. Sci. U. S. A.* (2005). doi:10.1073/pnas.0504011102

282. Vyas, A., Jadhav, S. & Chattarji, S. Prolonged behavioral stress enhances synaptic connectivity in the basolateral amygdala. *Neuroscience* (2006). doi:10.1016/j.neuroscience.2006.08.003

283. Michelsen, K. A. *et al.* Prenatal stress and subsequent exposure to chronic mild stress influence dendritic spine density and morphology in the rat medial prefrontal cortex. *BMC Neurosci.* (2007). doi:10.1186/1471-2202-8-107

284. Ramón y Cajal, S. *Histologie du Systeme Nerveux de l'Homme et des Vertebres. Vol 2*. (1911).

285. Johnston, J. B. Further contributions to the study of the evolution of the forebrain. *J. Comp. Neurol.* (1923). doi:10.1002/cne.900350502

286. Ju, G. & Swanson, L. W. Studies on the cellular architecture of the bed nuclei of the stria terminalis in the rat: I. cytoarchitecture. *J. Comp. Neurol.* (1989). doi:10.1002/cne.902800409

287. Lebow, M. A. & Chen, A. Overshadowed by the amygdala: The bed nucleus of the stria terminalis emerges as key to psychiatric disorders. *Molecular Psychiatry* (2016). doi:10.1038/mp.2016.1

288. Dong, H. W. & Swanson, L. W. Projections from Bed Nuclei of the Stria Terminalis, Posterior Division: Implications for Cerebral Hemisphere Regulation of Defensive and Reproductive Behaviors. *J. Comp. Neurol.* (2004). doi:10.1002/cne.20002

289. Dong, H. W., Petrovich, G. D., Watts, A. G. & Swanson, L. W. Basic organization of projections from the oval and fusiform nuclei of the bed nuclei of the stria terminalis in

adult rat brain. *J. Comp. Neurol.* (2001). doi:10.1002/cne.1079

290. Alheid, G. F. *et al.* The neuronal organization of the supracapsular part of the stria terminalis in the rat: The dorsal component of the extended amygdala. *Neuroscience* (1998). doi:10.1016/S0306-4522(97)00560-5

291. Ju, G., Swanson, L. W. & Simerly, R. B. Studies on the cellular architecture of the bed nuclei of the stria terminalis in the rat: II. chemoarchitecture. *J. Comp. Neurol.* (1989). doi:10.1002/cne.902800410

292. Moga, M. M., Saper, C. B. & Gray, T. S. Bed nucleus of the stria terminalis: Cytoarchitecture, immunohistochemistry, and projection to the parabrachial nucleus in the rat. *J. Comp. Neurol.* (1989). doi:10.1002/cne.902830302

293. Mahan, A. L. & Ressler, K. J. Fear conditioning, synaptic plasticity and the amygdala: Implications for posttraumatic stress disorder. *Trends in Neurosciences* (2012). doi:10.1016/j.tins.2011.06.007

294. Davis, M., Walker, D. L., Miles, L. & Grillon, C. Phasic vs Sustained Fear in Rats and Humans: Role of the Extended Amygdala in Fear vs Anxiety. *Neuropsychopharmacology* **35**, 105–135 (2010).

295. Alheid, G. F. & Heimer, L. New perspectives in basal forebrain organization of special relevance for neuropsychiatric disorders: The striatopallidal, amygdaloid, and corticopetal components of substantia innominata. *Neuroscience* (1988). doi:10.1016/0306-4522(88)90217-5

296. Malenka, R. C., Nestler, E. J. & Hayman, S. E. Chapter 15: Reinforcement and Addictive Disorders. in *Molecular Neuropharmacology: A Foundation for Clinical Neuroscience* 376

297. Swanson, L. W. & Petrovich, G. D. What is the amygdala? *Trends Neurosci.* (1998). doi:10.1016/S0166-2236(98)01265-X

298. Alvarez-Bolado, G. & Swanson, L. W. *Developmental Brain Maps: Structure of the*

Embryonic Rat Brain. (Elsevier, 1996).

299. Canteras, N. S., Simerly, R. B. & Swanson, L. W. Organization of projections from the medial nucleus of the amygdala: A PHAL study in the rat. *J. Comp. Neurol.* (1995). doi:10.1002/cne.903600203

300. Dong, H. W., Petrovich, G. D. & Swanson, L. W. Topography of projections from amygdala to bed nuclei of the stria terminalis. *Brain Research Reviews* (2001). doi:10.1016/S0165-0173(01)00079-0

301. Choi, D. C. *et al.* Bed nucleus of the stria terminalis subregions differentially regulate hypothalamic-pituitary-adrenal axis activity: Implications for the integration of limbic inputs. *J. Neurosci.* (2007). doi:10.1523/JNEUROSCI.4301-06.2007

302. Choi, D. C. *et al.* The role of the posterior medial bed nucleus of the stria terminalis in modulating hypothalamic-pituitary-adrenocortical axis responsiveness to acute and chronic stress. *Psychoneuroendocrinology* (2008). doi:10.1016/j.psyneuen.2008.02.006

303. Silberman, Y. & Winder, D. G. Emerging Role for Corticotropin Releasing Factor Signaling in the Bed Nucleus of the Stria Terminalis at the Intersection of Stress and Reward. *Front. Psychiatry* (2013). doi:10.3389/fpsyt.2013.00042

304. Wang, Y. *et al.* A bed nucleus of stria terminalis microcircuit regulating inflammation-associated modulation of feeding. *Nat. Commun.* (2019). doi:10.1038/s41467-019-10715-x

305. Dumais, K. M., Alonso, A. G., Immormino, M. A., Bredewold, R. & Veenema, A. H. Involvement of the oxytocin system in the bed nucleus of the stria terminalis in the sex-specific regulation of social recognition. *Psychoneuroendocrinology* (2016). doi:10.1016/j.psyneuen.2015.11.007

306. Duque-Wilckens, N. *et al.* Oxytocin Receptors in the Anteromedial Bed Nucleus of the Stria Terminalis Promote Stress-Induced Social Avoidance in Female California Mice. *Biol. Psychiatry* (2018). doi:10.1016/j.biopsych.2017.08.024

307. Trainor, B. Activation of oxytocin receptors induces defeatinduced social withdrawal in female california mice. *Neuropsychopharmacology* (2016).

308. Duque-Wilckens, N. *et al.* Extrahypothalamic oxytocin neurons drive stress-induced social vigilance and avoidance. *Proc. Natl. Acad. Sci. U. S. A.* (2020). doi:10.1073/pnas.2011890117

309. Klampfl, S. M., Brunton, P. J., Bayerl, D. S. & Bosch, O. J. CRF-R1 activation in the anterior-dorsal BNST induces maternal neglect in lactating rats via an HPA axis-independent central mechanism. *Psychoneuroendocrinology* (2016). doi:10.1016/j.psyneuen.2015.11.015

310. Forray, M. I. & Gysling, K. Role of noradrenergic projections to the bed nucleus of the stria terminalis in the regulation of the hypothalamic-pituitary-adrenal axis. in *Brain Research Reviews* (2004). doi:10.1016/j.brainresrev.2004.07.011

311. Bienkowski, M. S. & Rinaman, L. Common and distinct neural inputs to the medial central nucleus of the amygdala and anterior ventrolateral bed nucleus of stria terminalis in rats. *Brain Struct. Funct.* (2013). doi:10.1007/s00429-012-0393-6

312. Bruijnzeel, A. W. *et al.* Long-term sensitization of Fos-responsivity in the rat central nervous system after a single stressful experience. *Brain Res.* (1999). doi:10.1016/S0006-8993(98)01350-X

313. Dong, H. W. & Swanson, L. W. Projections from bed nuclei of the stria terminalis, anteromedial area: Cerebral hemisphere integration of neuroendocrine, autonomic, and behavioral aspects of energy balance. *J. Comp. Neurol.* (2006). doi:10.1002/cne.20788

314. Dong, H. W. & Swanson, L. W. Projections from bed nuclei of the stria terminalis, dorsomedial nucleus: Implications for cerebral hemisphere integration of neuroendocrine, autonomic, and drinking responses. *J. Comp. Neurol.* (2006). doi:10.1002/cne.20790

315. Lange, M. D. *et al.* Cannabinoid {CB1} receptors in distinct circuits of the extended amygdala determine fear responsiveness to unpredictable threat. *Mol Psychiatr* (2016). doi:10.1038/mp.2016.156

316. Park, J. *et al.* Catecholamines in the bed nucleus of the stria terminalis reciprocally respond to reward and aversion. *Biol. Psychiatry* (2012). doi:10.1016/j.biopsych.2011.10.017

317. Kim, S. Y. *et al.* Diverging neural pathways assemble a behavioural state from separable features in anxiety. *Nature* (2013). doi:10.1038/nature12018

318. Kilts, C. D. & Anderson, C. M. The simultaneous quantification of dopamine, norepinephrine and epinephrine in micropunched rat brain nuclei by on-line trace enrichment HPLC with electrochemical detection: Distribution of catecholamines in the limbic system. *Neurochem. Int.* (1986). doi:10.1016/0197-0186(86)90086-0

319. Phelix, C. F., Liposits, Z. & Paull, W. K. Monoamine innervation of bed nucleus of stria terminalis: An electron microscopic investigation. *Brain Res. Bull.* (1992). doi:10.1016/0361-9230(92)90218-M

320. Daniel, S. E. & Rainnie, D. G. Stress Modulation of Opposing Circuits in the Bed Nucleus of the Stria Terminalis. *Neuropsychopharmacology* (2016). doi:10.1038/npp.2015.178

321. Park, J. *et al.* Opposing catecholamine changes in the bed nucleus of the stria terminalis during intracranial self-stimulation and its extinction. *Biol. Psychiatry* (2013). doi:10.1016/j.biopsych.2012.11.008

322. Radley, J. J. & Johnson, S. B. Anteroventral bed nuclei of the stria terminalis neurocircuitry: Towards an integration of HPA axis modulation with coping behaviors - Curt Richter Award Paper 2017. *Psychoneuroendocrinology* (2018). doi:10.1016/j.psyneuen.2017.12.005

323. Ventura-Silva, A. P. *et al.* Stress shifts the response of the bed nucleus of the stria terminalis to an anxiogenic mode. *Eur. J. Neurosci.* (2012). doi:10.1111/j.1460-9568.2012.08262.x

324. Laflamme, N., Nappi, R. E., Drolet, G., Labrie, C. & Rivest, S. Expression and neuropeptidergic characterization of estrogen receptors (ERα and ERβ) throughout the rat brain: Anatomical evidence of distinct roles of each subtype. *J. Neurobiol.* (1998).

doi:10.1002/(SICI)1097-4695(19980905)36:3<357::AID-NEU5>3.0.CO;2-V

325. Toufexis, D. J., Myers, K. M., Bowser, M. E. & Davis, M. Estrogen disrupts the inhibition of fear in female rats, possibly through the antagonistic effects of estrogen receptor α (ERα) and ERβ. *J. Neurosci.* (2007). doi:10.1523/JNEUROSCI.2529-07.2007

326. Wood, R. I. & Newman, S. W. The medial amygdaloid nucleus and medial preoptic area mediate steroidal control of sexual behavior in the male Syrian hamster. *Horm. Behav.* (1995). doi:10.1006/hbeh.1995.1024

327. Lesur, A., Gaspar, P., Alvarez, C. & Berger, B. Chemoanatomic compartments in the human bed nucleus of the stria terminalis. *Neuroscience* (1989). doi:10.1016/0306-4522(89)90117-6

328. Kash, T. L. *et al.* Neuropeptide regulation of signaling and behavior in the BNST. *Molecules and Cells* (2015). doi:10.14348/molcells.2015.2261

329. Walter, A., Mai, J. K., Lanta, L. & Görcs, T. Differential distribution of immunohistochemical markers in the bed nucleus of the stria terminalis in the human brain. *J. Chem. Neuroanat.* (1991). doi:10.1016/0891-0618(91)90019-9

330. Haubensak, W. *et al.* Genetic dissection of an amygdala microcircuit that gates conditioned fear. *Nature* (2010). doi:10.1038/nature09553

331. Ye, J. & Veinante, P. Cell-type specific parallel circuits in the bed nucleus of the stria terminalis and the central nucleus of the amygdala of the mouse. *Brain Struct. Funct.* (2019). doi:10.1007/s00429-018-01825-1

332. Flanigan, M. E. & Kash, T. L. Coordination of social behaviors by the bed nucleus of the stria terminalis. *European Journal of Neuroscience* (2020). doi:10.1111/ejn.14991

333. Rodriguez-Romaguera, J. *et al.* Prepronociceptin-Expressing Neurons in the Extended Amygdala Encode and Promote Rapid Arousal Responses to Motivationally Salient Stimuli. *Cell Rep.* (2020). doi:10.1016/j.celrep.2020.108362

334. Kash, T. L. & Winder, D. G. Neuropeptide Y and corticotropin-releasing factor bi-directionally modulate inhibitory synaptic transmission in the bed nucleus of the stria terminalis. *Neuropharmacology* (2006). doi:10.1016/j.neuropharm.2006.06.011

335. Nässel, D. R. Neuropeptide signaling near and far: How localized and timed is the action of neuropeptides in brain circuits? *Invertebrate Neuroscience* (2009). doi:10.1007/s10158-009-0090-1

336. Ludwig, M. & Leng, G. Dendritic peptide release and peptide-dependent behaviours. *Nature Reviews Neuroscience* (2006). doi:10.1038/nrn1845

337. Herkenham, M. Mismatches between neurotransmitter and receptor localizations in brain: observations and implications. *Neuroscience* (1987). doi:10.1016/0306-4522(87)90268-5

338. van den Pol, A. N. Neuropeptide Transmission in Brain Circuits. *Neuron* (2012). doi:10.1016/j.neuron.2012.09.014

339. Fink, G., Sumner, B. E. H., Rosie, R., Grace, O. & Quinn, J. P. Estrogen control of central neurotransmission: Effect on mood, mental state, and memory. *Cell. Mol. Neurobiol.* (1996). doi:10.1007/BF02088099

340. Dumais, K. M. & Veenema, A. H. Vasopressin and oxytocin receptor systems in the brain: Sex differences and sex-specific regulation of social behavior. *Frontiers in Neuroendocrinology* (2016). doi:10.1016/j.yfrne.2015.04.003

341. van Leeuwen, F. & Caffé, R. Vasopressin-immunoreactive cell bodies in the bed nucleus of the stria terminalis of the rat. *Cell Tissue Res.* (1983). doi:10.1007/BF00211473

342. Rood, B. D. & De Vries, G. J. Vasopressin innervation of the mouse (Mus musculus) brain and spinal cord. *J. Comp. Neurol.* (2011). doi:10.1002/cne.22635

343. Otero-Garcia, M. *et al.* Extending the socio-sexual brain: Arginine-vasopressin immunoreactive circuits in the telencephalon of mice. *Brain Struct. Funct.* (2014). doi:10.1007/s00429-013-0553-3

344. Rood, B. D. *et al.* Site of origin of and sex differences in the vasopressin innervation of the mouse (Mus musculus) brain. *J. Comp. Neurol.* (2013). doi:10.1002/cne.23288

345. Veenema, A. H., Beiderbeck, D. I., Lukas, M. & Neumann, I. D. Distinct correlations of vasopressin release within the lateral septum and the bed nucleus of the stria terminalis with the display of intermale aggression. *Horm. Behav.* (2010). doi:10.1016/j.yhbeh.2010.03.006

346. Bosch, O. J., Pförtsch, J., Beiderbeck, D. I., Landgraf, R. & Neumann, I. D. Maternal behaviour is associated with vasopressin release in the medial preoptic area and bed nucleus of the stria terminalis in the rat. *J. Neuroendocrinol.* (2010). doi:10.1111/j.1365-2826.2010.01984.x

347. Steinman, M. Q. *et al.* Hypothalamic vasopressin systems are more sensitive to the long term effects of social defeat in males versus females. *Psychoneuroendocrinology* (2015). doi:10.1016/j.psyneuen.2014.09.009

348. Cummings, S., Elde, R., Ells, J. & Lindall, A. Corticotropin-releasing factor immunoreactivity is widely distributed within the central nervous system of the rat: An immunohistochemical study. *J. Neurosci.* (1983). doi:10.1523/jneurosci.03-07-01355.1983

349. Silberman, Y., Matthews, R. T. & Winder, D. G. A corticotropin releasing factor pathway for ethanol regulation of the ventral tegmental area in the bed nucleus of the stria terminalis. *J. Neurosci.* **33**, 950–960 (2013).

350. Bruzsik, B. *et al.* Somatostatin neurons of the bed nucleus of stria terminalis enhance associative fear memory consolidation in mice. *J. Neurosci.* (2021). doi:10.1101/2020.05.22.103481

351. Wang, L. *et al.* Comparison of CRF-immunoreactive neurons distribution in mouse and rat brains and selective induction of Fos in rat hypothalamic CRF neurons by abdominal surgery. *Brain Res.* (2011). doi:10.1016/j.brainres.2011.07.024

352. Uchida, K. *et al.* Female-biased sexual dimorphism of corticotropin-releasing factor

neurons in the bed nucleus of the stria terminalis. *Biol. Sex Differ.* (2019). doi:10.1186/s13293-019-0221-2

353. Heisler, L. K., Zhou, L., Bajwa, P., Hsu, J. & Tecott, L. H. Serotonin 5-HT2C receptors regulate anxiety-like behavior. *Genes, Brain Behav.* (2007). doi:10.1111/j.1601-183X.2007.00316.x

354. Funk, D., Li, Z. & Lê, A. D. Effects of environmental and pharmacological stressors on c-fos and corticotropin-releasing factor mRNA in rat brain: Relationship to the reinstatement of alcohol seeking. *Neuroscience* (2006). doi:10.1016/j.neuroscience.2005.10.062

355. Lee, Y. & Davis, M. Role of the hippocampus, the bed nucleus of the stria terminalis, and the amygdala in the excitatory effect of corticotropin-releasing hormone on the acoustic startle reflex. *J. Neurosci.* (1997). doi:10.1523/jneurosci.17-16-06434.1997

356. Makino, S., Gold, P. W. & Schulkin, J. Effects of corticosterone on CRH mRNA and content in the bed nucleus of the stria terminalis; comparison with the effects in the central nucleus of the amygdala and the paraventricular nucleus of the hypothalamus. *Brain Res.* (1994). doi:10.1016/0006-8993(94)90961-X

357. Gafford, G. M. *et al.* Cell-type specific deletion of GABA(A) α1 in corticotropin-releasing factor-containing neurons enhances anxiety and disrupts fear extinction. *Proc. Natl. Acad. Sci. U. S. A.* (2012). doi:10.1073/pnas.1119261109

358. Sahuque, L. L. *et al.* Anxiogenic and aversive effects of corticotropin-releasing factor (CRF) in the bed nucleus of the stria terminalis in the rat: Role of CRF receptor subtypes. *Psychopharmacology (Berl).* (2006). doi:10.1007/s00213-006-0362-y

359. Sink, K. S. *et al.* Effects of continuously enhanced corticotropin releasing factor expression within the bed nucleus of the stria terminalis on conditioned and unconditioned anxiety. *Mol. Psychiatry* (2013). doi:10.1038/mp.2011.188

360. Erb, S. & Stewart, J. A role for the bed nucleus of the stria terminalis, but not the amygdala, in the effects of corticotropin-releasing factor on stress-induced reinstatement

of cocaine seeking. *J Neurosci Off. J Soc Neurosci* **19**, RC35 (1999).

361. Lee, Y., Fitz, S., Johnson, P. L. & Shekhar, A. Repeated stimulation of CRF receptors in the BNST of rats selectively induces social but not panic-like anxiety. *Neuropsychopharmacology* (2008). doi:10.1038/sj.npp.1301674

362. Walker, D. *et al.* Differential effects of the CRF-R1 antagonist GSK876008 on fear-potentiated, light- and CRF-enhanced startle suggest preferential involvement in sustained vs phasic threat responses. *Neuropsychopharmacology* (2009). doi:10.1038/npp.2008.210

363. Tran, L., Schulkin, J. & Greenwood-Van Meerveld, B. Importance of CRF receptor-mediated mechanisms of the bed nucleus of the stria terminalis in the processing of anxiety and pain. *Neuropsychopharmacology* (2014). doi:10.1038/npp.2014.117

364. Huang, M. M. *et al.* Corticotropin-releasing factor (CRF) sensitization of ethanol withdrawal-induced anxiety-like behavior is brain site specific and mediated by CRF-1 receptors: Relation to stress-induced sensitization. *J. Pharmacol. Exp. Ther.* (2010). doi:10.1124/jpet.109.159186

365. Overstreet, D. H., Knapp, D. J., Moy, S. S. & Breese, G. R. A 5-HT1A agonist and a 5-HT2C antagonist reduce social interaction deficit induced by multiple ethanol withdrawals in rats. *Psychopharmacology (Berl).* (2003). doi:10.1007/s00213-003-1425-y

366. Giardino, W. J. *et al.* Parallel circuits from the bed nuclei of stria terminalis to the lateral hypothalamus drive opposing emotional states. *Nat. Neurosci.* (2018). doi:10.1038/s41593-018-0198-x

367. Paul, E. D. & Chen, A. Neural Circuitry of Stress, Fear, and Anxiety. in *Stress: Neuroendocrinology and Neurobiology* 83–96 (Elsevier, 2017). doi:10.1016/B978-0-12-802175-0.00008-5

368. Desai, S. J., Borkar, C. D., Nakhate, K. T., Subhedar, N. K. & Kokare, D. M. Neuropeptide Y attenuates anxiety- and depression-like effects of cholecystokinin-4 in mice. *Neuroscience* (2014). doi:10.1016/j.neuroscience.2014.07.062

369. Poulin, J. F., Arbour, D., Laforest, S. & Drolet, G. Neuroanatomical characterization of endogenous opioids in the bed nucleus of the stria terminalis. *Prog. Neuro-Psychopharmacology Biol. Psychiatry* (2009). doi:10.1016/j.pnpbp.2009.06.021

370. Crowley, N. A. *et al.* Dynorphin Controls the Gain of an Amygdalar Anxiety Circuit. *Cell Rep.* (2016). doi:10.1016/j.celrep.2016.02.069

371. Koob, G. F. & Le Moal, M. Neurobiological mechanisms for opponent motivational processes in addiction. in *Philosophical Transactions of the Royal Society B: Biological Sciences* (2008). doi:10.1098/rstb.2008.0094

372. Chung, S. *et al.* Desipramine and citalopram attenuate pretest swim-induced increases in prodynorphin immunoreactivity in the dorsal bed nucleus of the stria terminalis and the lateral division of the central nucleus of the amygdala in the forced swimming test. *Neuropeptides* (2014). doi:10.1016/j.npep.2014.07.001

373. Day, H. E. W., Curran, E. J., Watson, S. J. & Akil, H. Distinct neurochemical populations in the rat central nucleus of the amygdala and bed nucleus of the stria terminalis: Evidence for their selective activation by interleukin-1β. *J. Comp. Neurol.* (1999). doi:10.1002/(SICI)1096-9861(19991011)413:1<113::AID-CNE8>3.0.CO;2-B

374. Pleil, K. E. *et al.* Chronic stress alters neuropeptide y signaling in the bed nucleus of the stria terminalis in DBA/2J but not C57BL/6J mice. *Neuropharmacology* (2012). doi:10.1016/j.neuropharm.2011.12.002

375. Chronwall, B. M. *et al.* The anatomy of neuropeptide-y-containing neurons in rat brain. *Neuroscience* (1985). doi:10.1016/0306-4522(85)90260-X

376. Cippitelli, A. *et al.* Neuropeptide y (NPY) suppresses yohimbine-induced reinstatement of alcohol seeking. *Psychopharmacology (Berl).* (2010). doi:10.1007/s00213-009-1741-y

377. Heilig, M. The NPY system in stress, anxiety and depression. *Neuropeptides* (2004). doi:10.1016/j.npep.2004.05.002

378. Heilig, M. & Thorsell, A. Brain neuropeptide Y (NPY) in stress and alcohol dependence.

Reviews in the Neurosciences (2002). doi:10.1515/revneuro.2002.13.1.85

379. Dale, H. H. On some physiological actions of ergot. *J. Physiol.* (1906). doi:10.1113/jphysiol.1906.sp001148

380. Steinman, M. Q. *et al.* Sex-Specific Effects of Stress on Oxytocin Neurons Correspond With Responses to Intranasal Oxytocin. *Biol. Psychiatry* (2016). doi:10.1016/j.biopsych.2015.10.007

381. De Bundel, D. *et al.* Dopamine D2 receptors gate generalization of conditioned threat responses through mTORC1 signaling in the extended amygdala. *Mol. Psychiatry* (2016). doi:10.1038/mp.2015.210

382. Jaramillo, A. A., Williford, K. M., Marshall, C., Winder, D. G. & Centanni, S. W. BNST transient activity associates with approach behavior in a stressful environment and is modulated by the parabrachial nucleus. *Neurobiol. Stress* (2020). doi:10.1016/j.ynstr.2020.100247

383. Shimada, S. *et al.* Coexistence of peptides (corticotropin releasing factor/neurotensin and substance P/somatostatin) in the bed nucleus of the stria terminalis and central amygdaloid nucleus of the rat. *Neuroscience* (1989). doi:10.1016/0306-4522(89)90259-5

384. Xiao, Q. *et al.* A new GABAergic somatostatin projection from the BNST onto accumbal parvalbumin neurons controls anxiety. *Mol. Psychiatry* (2020). doi:10.1038/s41380-020-0816-3

385. Centanni, S. W. S. W. *et al.* Endocannabinoid control of the insular-bed nucleus of the stria terminalis circuit regulates negative affective behavior associated with alcohol abstinence. *Neuropsychopharmacology* **44**, (2019).

386. Ch'ng, S., Fu, J., Brown, R. M., McDougall, S. J. & Lawrence, A. J. The intersection of stress and reward: BNST modulation of aversive and appetitive states. *Progress in Neuro-Psychopharmacology and Biological Psychiatry* (2018). doi:10.1016/j.pnpbp.2018.01.005

387. Vertes, R. P. Differential Projections of the Infralimbic and Prelimbic Cortex in the Rat.

Synapse (2004). doi:10.1002/syn.10279

388. AJ, M. Cortical pathways to the mammalian amygdala. *Prog. Neurobiol.* (1998).

389. Canteras, N. S. & Swanson, L. W. Projections of the ventral subiculum to the amygdala, septum, and hypothalamus: A PHAL anterograde tract-tracing study in the rat. *J. Comp. Neurol.* (1992). doi:10.1002/cne.903240204

390. Cullinan, W. E., Herman, J. P. & Watson, S. J. Ventral subicular interaction with the hypothalamic paraventricular nucleus: Evidence for a relay in the bed nucleus of the stria terminalis. *J. Comp. Neurol.* (1993). doi:10.1002/cne.903320102

391. Myers, B., Mark Dolgas, C., Kasckow, J., Cullinan, W. E. & Herman, J. P. Central stress-integrative circuits: Forebrain glutamatergic and GABAergic projections to the dorsomedial hypothalamus, medial preoptic area, and bed nucleus of the stria terminalis. *Brain Struct. Funct.* (2014). doi:10.1007/s00429-013-0566-y

392. Vranjkovic, O., Pina, M., Kash, T. L. & Winder, D. G. The bed nucleus of the stria terminalis in drug-associated behavior and affect: A circuit-based perspective. *Neuropharmacology* (2017). doi:10.1016/j.neuropharm.2017.03.028

393. Sakanaka, M., Shibasaki, T. & Lederis, K. Distribution and efferent projections of corticotropin-releasing factor-like immunoreactivity in the rat amygdaloid complex. *Brain Res.* (1986). doi:10.1016/0006-8993(86)91332-6

394. Marchant, N. J., Densmore, V. S. & Osborne, P. B. Coexpression of prodynorphin and corticotrophin-releasing hormone in the rat central amygdala: Evidence of two distinct endogenous opioid systems in the lateral division. *J. Comp. Neurol.* (2007). doi:10.1002/cne.21464

395. Betley, J. N., Cao, Z. F. H., Ritola, K. D. & Sternson, S. M. Parallel, redundant circuit organization for homeostatic control of feeding behavior. *Cell* (2013). doi:10.1016/j.cell.2013.11.002

396. Nilsson, I., Johansen, J. E., Schalling, M., Hökfelt, T. & Fetissov, S. O. Maturation of the

hypothalamic arcuate agouti-related protein system during postnatal development in the mouse. *Dev. Brain Res.* (2005). doi:10.1016/j.devbrainres.2005.01.009

397. Freedman, L. J. & Cassell, M. D. Distribution of dopaminergic fibers in the central division of the extended amygdala of the rat. *Brain Res.* (1994). doi:10.1016/0006-8993(94)91545-8

398. Meloni, E. G., Gerety, L. P., Knoll, A. T., Cohen, B. M. & Carlezon, W. A. Behavioral and anatomical interactions between dopamine and corticotropin-releasing factor in the rat. *J. Neurosci.* (2006). doi:10.1523/JNEUROSCI.4957-05.2006

399. Krawczyk, M. *et al.* Double-dissociation of the catecholaminergic modulation of synaptic transmission in the oval bed nucleus of the stria terminalis. *J. Neurophysiol.* (2011). doi:10.1152/jn.00710.2010

400. Egli, R. E. *et al.* Norepinephrine modulates glutamatergic transmission in the bed nucleus of the stria terminalis. *Neuropsychopharmacology* (2005). doi:10.1038/sj.npp.1300639

401. F. Phelix, C., Liposits, Z. & Willis, K. P. Catecholamine-CRF synaptic interaction in a septal bed nucleus: Afferents of neurons in the bed nucleus of the stria terminalis. *Brain Res. Bull.* (1994). doi:10.1016/0361-9230(94)90056-6

402. Park, J., Kile, B. M. & Wightman, M. R. In vivo voltammetric monitoring of norepinephrine release in the rat ventral bed nucleus of the stria terminalis and anteroventral thalamic nucleus. *Eur. J. Neurosci.* (2009). doi:10.1111/j.1460-9568.2009.07005.x

403. Forray, M. I., Gysling, K., Andrés, M. E., Bustos, G. & Araneda, S. Medullary noradrenergic neurons projecting to the bed nucleus of the stria terminalis express mRNA for the NMDA-NR1 receptor. *Brain Res. Bull.* (2000). doi:10.1016/S0361-9230(00)00229-X

404. Roder, S. & Ciriello, J. Collateral axonal projections to limbic structures from ventrolateral medullary A1 noradrenergic neurons. *Brain Res.* (1994). doi:10.1016/0006-8993(94)90648-3

405. Woulfe, J. M., Flumerfelt, B. A. & Hrycyshyn, A. W. Efferent connections of the A1 noradrenergic cell group: A DBH immunohistochemical and PHA-L anterograde tracing study. *Exp. Neurol.* (1990). doi:10.1016/S0014-4886(05)80022-6

406. Banihashemi, L. & Rinaman, L. Noradrenergic inputs to the bed nucleus of the stria terminalis and paraventricular nucleus of the hypothalamus underlie hypothalamic-pituitary- adrenal axis but not hypophagic or conditioned avoidance responses to systemic yohimbine. *J. Neurosci.* (2006). doi:10.1523/JNEUROSCI.3561-06.2006

407. Commons, K. G., Connolley, K. R. & Valentino, R. J. A neurochemically distinct dorsal raphe-limbic circuit with a potential role in affective disorders. *Neuropsychopharmacology* (2003). doi:10.1038/sj.npp.1300045

408. Radley, J. J., Gosselink, K. L. & Sawchenko, P. E. A discrete GABAergic relay mediates medial prefrontal cortical inhibition of the neuroendocrine stress response. *J. Neurosci.* (2009). doi:10.1523/JNEUROSCI.5924-08.2009

409. Sawchenko, P. E. & Swanson, L. W. The organization of forebrain afferents to the paraventricular and supraoptic nuclei of the rat. *J. Comp. Neurol.* (1983). doi:10.1002/cne.902180202

410. Moga, M. M. & Saper, C. B. Neuropeptide-immunoreactive neurons projecting to the paraventricular hypothalamic nucleus in the rat. *J. Comp. Neurol.* (1994). doi:10.1002/cne.903460110

411. Hosoya, Y. & Matsushita, M. Cells of origin of the descending afferents to the lateral hypothalamic area in the rat, studied with the horseradish peroxidase method. *Neurosci. Lett.* (1980). doi:10.1016/0304-3940(80)90290-6

412. Mahler, S. V. & Aston-Jones, G. S. Fos activation of selective afferents to ventral tegmental area during cue-induced reinstatement of cocaine seeking in rats. *J. Neurosci.* (2012). doi:10.1523/JNEUROSCI.2277-12.2012

413. Jennings, J. H. *et al.* Distinct extended amygdala circuits for divergent motivational states. *Nature* (2013). doi:10.1038/nature12041

414. Companion, M. A. & Thiele, T. E. Assessment of ventral tegmental area-projecting GABAergic neurons from the bed nucleus of the stria terminalis in modulating binge-like ethanol intake. *Eur. J. Neurosci.* (2018). doi:10.1111/ejn.14222

415. Rodaros, D., Caruana, D. A., Amir, S. & Stewart, J. Corticotropin-releasing factor projections from limbic forebrain and paraventricular nucleus of the hypothalamus to the region of the ventral tegmental area. *Neuroscience* (2007). doi:10.1016/j.neuroscience.2007.09.043

416. Reynolds, S. M. & Zahm, D. S. Specificity in the projections of prefrontal and insular cortex to ventral striatopallidum and the extended amygdala. *J. Neurosci.* (2005). doi:10.1523/JNEUROSCI.3432-05.2005

417. Reil, J. Exercitationum anatomicarum fasciculus primus. *Struct. nervorum. Venalis, Halle* (1796).

418. Gray, H. *Anatomy: descriptive and surgical*. ({J.W.} Parker and Son, 1858).

419. Semendeferi, K. & Damasio, H. The brain and its main anatomical subdivisions in living hominoids using magnetic resonance imaging. *J. Hum. Evol.* (2000).

420. Kaas, J. H. The evolution of brains from early mammals to humans. *Wiley Interdiscip. Rev. Cogn. Sci.* (2013). doi:10.1002/wcs.1206

421. Gallay, D. S., Gallay, M. N. & Jeanmonod, D. The insula of Reil revisited: multiarchitectonic organization in macaque monkeys. *Cereb. …* (2011).

422. Gogolla, N. The insular cortex. *Current Biology* (2017). doi:10.1016/j.cub.2017.05.010

423. Shi, C. J. & Cassell, M. D. Cascade projections from somatosensory cortex to the rat basolateral amygdala via the parietal insular cortex. *J. Comp. Neurol.* (1998). doi:10.1002/(SICI)1096-9861(19981005)399:4<469::AID-CNE3>3.0.CO;2-#

424. Craig, (Bud) A D. The sentient self. *Brain Struct. Funct.* **214**, 563–577 (2010).

425. Augustine, J. R. Circuitry and functional aspects of the insular lobe in primates including

humans. *Brain Res. Rev.* **22**, 229–244 (1996).

426. Nieuwenhuys, R. The insular cortex: a review. *Prog. Brain Res.* (2011).

427. Ghaziri, J., Tucholka, A., Girard, G. & Houde, J. C. The corticocortical structural connectivity of the human insula. *Cereb. …* (2015). doi:10.1093/cercor/bhv308

428. Mesulam, M. & Mufson, E. J. Insula of the old world monkey. {III:} Efferent cortical output and comments on function. *J. Comp. Neurol.* (1982). doi:10.1002/cne.902120104

429. Gehrlach, D. A. *et al.* A whole-brain connectivity map of mouse insular cortex. *Elife* (2020). doi:10.7554/ELIFE.55585

430. Kurth, F., Zilles, K., Fox, P. T. & Laird, A. R. A link between the systems: functional differentiation and integration within the human insula revealed by meta-analysis. *Brain Struct. …* (2010).

431. Etkin, A., Büchel, C. & Gross, J. J. The neural bases of emotion regulation. *Nature Reviews Neuroscience* (2015). doi:10.1038/nrn4044

432. Craig, A. D. How do you feel—now? the anterior insula and human awareness. *Nat. Rev. Neurosci.* (2009).

433. Craig, A. D. Significance of the insula for the evolution of human awareness of feelings from the body. *Ann. N. Y. Acad. Sci.* (2011).

434. Bermudez-Rattoni, F., Okuda, S., Roozendaal, B. & McGaugh, J. L. Insular cortex is involved in consolidation of object recognition memory. *Learn. Mem.* (2005). doi:10.1101/lm.97605

435. Lavi, K., Jacobson, G. A., Rosenblum, K. & Lüthi, A. Encoding of Conditioned Taste Aversion in Cortico-Amygdala Circuits. *Cell Rep.* (2018). doi:10.1016/j.celrep.2018.06.053

436. Rogers-Carter, M. M. *et al.* Insular cortex mediates approach and avoidance responses to social affective stimuli. *Nat. Neurosci.* (2018). doi:10.1038/s41593-018-0071-y

437. Contreras, M., Ceric, F. & Torrealba, F. Inactivation of the interoceptive insula disrupts drug craving and malaise induced by lithium. *Science (80-.).* (2007).

438. Gehrlach, D. A. *et al.* Aversive state processing in the posterior insular cortex. *Nat. Neurosci.* (2019). doi:10.1038/s41593-019-0469-1

439. Livneh, Y. *et al.* Estimation of Current and Future Physiological States in Insular Cortex. *Neuron* (2020). doi:10.1016/j.neuron.2019.12.027

440. Wang, L. *et al.* The coding of valence and identity in the mammalian taste system. *Nature* (2018). doi:10.1038/s41586-018-0165-4

441. Sperry, R. W. Neural basis of the spontaneous optokinetic response produced by visual inversion. *J. Comp. Physiol. Psychol.* (1950). doi:10.1037/h0055479

442. von Holst, E. & Mittelstaedt, H. Das Reafferenzprinzip. *Naturwissenschaften* **37**, 464–476 (1950).

443. Creutzfeldt, O., Ojemann, G. & Lettich, E. Neuronal activity in the human lateral temporal lobe - II. Responses to the subjects own voice. *Exp. Brain Res.* (1989). doi:10.1007/BF00249601

444. Curio, G., Neuloh, G., Numminen, J., Jousmäki, V. & Hari, R. Speaking modifies voice-evoked activity in the human auditory cortex. *Hum. Brain Mapp.* (2000). doi:10.1002/(SICI)1097-0193(200004)9:4<183::AID-HBM1>3.0.CO;2-Z

445. Flinker, A. *et al.* Single-trial speech suppression of auditory cortex activity in humans. *J. Neurosci.* (2010). doi:10.1523/JNEUROSCI.1809-10.2010

446. Greenlee, J. D. W. *et al.* Human auditory cortical activation during self-vocalization. *PLoS One* (2011). doi:10.1371/journal.pone.0014744

447. Bastian, J. The Generation and Subtraction of Sensory Expectations within Cerebellum-Like Structures. *Brain. Behav. Evol.* (1997). doi:10.1159/000113352

448. Poulet, J. F. A. & Hedwig, B. A corollary discharge mechanism modulates central

auditory processing in singing crickets. *J. Neurophysiol.* (2003). doi:10.1152/jn.0846.2002

449. Poulet, J. F. A. & Hedwig, B. The cellular basis of a corollary discharge. *Science (80-.).* (2006). doi:10.1126/science.1120847

450. Houde, J. F., Nagarajan, S. S., Sekihara, K. & Merzenich, M. M. Modulation of the auditory cortex during speech: An MEG study. *J. Cogn. Neurosci.* (2002). doi:10.1162/089892902760807140

451. Eliades, S. J. & Wang, X. Neural substrates of vocalization feedback monitoring in primate auditory cortex. *Nature* (2008). doi:10.1038/nature06910

452. Chang, E. F., Niziolek, C. A., Knight, R. T., Nagarajan, S. S. & Houde, J. F. Human cortical sensorimotor network underlying feedback control of vocal pitch. *Proc. Natl. Acad. Sci. U. S. A.* (2013). doi:10.1073/pnas.1216827110

453. Zaretsky, M. & Rowell, C. H. F. Saccadic suppression by corollary discharge in the locust [10]. *Nature* (1979). doi:10.1038/280583a0

454. Blakemore, S. J., Wolpert, D. M. & Frith, C. D. Central cancellation of self-produced tickle sensation. *Nat. Neurosci.* (1998). doi:10.1038/2870

455. Crapse, T. B. & Sommer, M. A. Corollary discharge across the animal kingdom. *Nature Reviews Neuroscience* (2008). doi:10.1038/nrn2457

456. Wolpert, D. M. & Flanagan, J. R. Motor prediction. *Current biology : CB* (2001). doi:10.1016/s0960-9822(01)00432-8

457. Johnson, S. B. *et al.* Prefrontal–bed nucleus circuit modulation of a passive coping response set. *J. Neurosci.* (2019). doi:10.1523/JNEUROSCI.1421-18.2018

458. Carroll, L. Active Coping. in *Encyclopedia of Behavioral Medicine* (eds. Turner, J. R. & Gellman, M. D.) (2013). doi:10.1007/978-1-4419-1005-9_1085

459. Kim, J. S., Han, S. Y. & Iremonger, K. J. Stress experience and hormone feedback tune distinct components of hypothalamic CRH neuron activity. *Nat. Commun.* (2019).

doi:10.1038/s41467-019-13639-8

460. Daviu, N. *et al.* Paraventricular nucleus CRH neurons encode stress controllability and regulate defensive behavior selection. *Nat. Neurosci.* (2020). doi:10.1038/s41593-020-0591-0

461. Van Praag, H., Christie, B. R., Sejnowski, T. J. & Gage, F. H. Running enhances neurogenesis, learning, and long-term potentiation in mice. *Proc. Natl. Acad. Sci. U. S. A.* (1999). doi:10.1073/pnas.96.23.13427

462. Miles, O. W. & Maren, S. Role of the bed nucleus of the stria terminalis in PTSD: Insights from preclinical models. *Frontiers in Behavioral Neuroscience* (2019). doi:10.3389/fnbeh.2019.00068

463. Grissom, N., Kerr, W. & Bhatnagar, S. Struggling behavior during restraint is regulated by stress experience. *Behav. Brain Res.* (2008). doi:10.1016/j.bbr.2008.03.030

464. Mathis, A. *et al.* DeepLabCut: markerless pose estimation of user-defined body parts with deep learning. *Nat. Neurosci.* (2018). doi:10.1038/s41593-018-0209-y

465. Nath, T. *et al.* Using DeepLabCut for 3D markerless pose estimation across species and behaviors. *Nat. Protoc.* (2019). doi:10.1038/s41596-019-0176-0

466. Moreira, F. A., Grieb, M. & Lutz, B. Central side-effects of therapies based on CB1 cannabinoid receptor agonists and antagonists: focus on anxiety and depression. *Best Practice and Research: Clinical Endocrinology and Metabolism* (2009). doi:10.1016/j.beem.2008.09.003

467. Blasio, A. *et al.* Rimonabant precipitates anxiety in rats withdrawn from palatable food: Role of the central Amygdala. *Neuropsychopharmacology* (2013). doi:10.1038/npp.2013.153

468. Gamble-George, J. C. *et al.* Dissociable effects of CB1 receptor blockade on anxiety-like and consummatory behaviors in the novelty-induced hypophagia test in mice. *Psychopharmacology (Berl).* (2013). doi:10.1007/s00213-013-3042-8

469. Marcinkiewcz, C. A. *et al.* Serotonin engages an anxiety and fear-promoting circuit in the extended amygdala. *Nature* **537**, 97–101 (2016).

470. Olive, M. F., Koenig, H. N., Nannini, M. A. & Hodge, C. W. Elevated extracellular CRF levels in the bed nucleus of the stria terminalis during ethanol withdrawal and reduction by subsequent ethanol intake. *Pharmacol. Biochem. Behav.* (2002). doi:10.1016/S0091-3057(01)00748-1

471. Snyder, A. E., Salimando, G. J., Winder, D. G. & Silberman, Y. Chronic Intermittent Ethanol and Acute Stress Similarly Modulate BNST CRF Neuron Activity via Noradrenergic Signaling. *Alcohol. Clin. Exp. Res.* (2019). doi:10.1111/acer.14118

472. Marvin, J. S. *et al.* Stability, affinity, and chromatic variants of the glutamate sensor iGluSnFR. *Nat. Methods* (2018). doi:10.1038/s41592-018-0171-3

473. Marvin, J. S. *et al.* A genetically encoded fluorescent sensor for in vivo imaging of GABA. *Nat. Methods* (2019). doi:10.1038/s41592-019-0471-2

474. Patel, S., Kingsley, P. J., MacKie, K., Marnett, L. J. & Winder, D. G. Repeated homotypic stress elevates 2-arachidonoylglycerol levels and enhances short-term endocannabinoid signaling at inhibitory synapses in basolateral amygdala. *Neuropsychopharmacology* (2009). doi:10.1038/npp.2009.101

475. Morgan, A. *et al.* Cyclooxygenase-2 inhibition reduces anxiety-like behavior and normalizes enhanced amygdala glutamatergic transmission following chronic oral corticosterone treatment. *Neurobiol. Stress* (2019). doi:10.1016/j.ynstr.2019.100190

476. Schwarz, L. A. *et al.* Viral-genetic tracing of the input-output organization of a central noradrenaline circuit. *Nature* **524**, 88–92 (2015).

477. Oh, S. W. *et al.* A mesoscale connectome of the mouse brain. *Nature* (2014). doi:10.1038/nature13186

478. Petreanu, L., Huber, D., Sobczyk, A. & Svoboda, K. Channelrhodopsin-2-assisted circuit mapping of long-range callosal projections. *Nat. Neurosci.* (2007). doi:10.1038/nn1891

479. Davis, M., Walker, D. L., Miles, L. & Grillon, C. Phasic vs sustained fear in rats and humans: role of the extended amygdala in fear vs anxiety. **35**, 105–135 (2010).

480. Di Bonaventura, M. V. M. *et al.* Role of bed nucleus of the stria terminalis Corticotrophin-Releasing factor receptors in frustration stress-induced binge-like palatable food consumption in female rats with a history of food restriction. *J. Neurosci.* (2014). doi:10.1523/JNEUROSCI.1854-14.2014

481. Kayyal, H. *et al.* Activity of Insula to Basolateral Amygdala Projecting Neurons is Necessary and Sufficient for Taste Valence Representation. *J. Neurosci.* (2019). doi:10.1523/JNEUROSCI.0752-19.2019

482. Flook, E. A. *et al.* BNST-insula structural connectivity in humans. *Neuroimage* (2020). doi:10.1016/j.neuroimage.2020.116555

483. Gerfen, C. R. & Clavier, R. M. Neural inputs to the prefrontal agranular insular cortex in the rat: Horseradish peroxidase study. *Brain Res. Bull.* (1979). doi:10.1016/S0361-9230(79)80012-X

484. Zingg, B. *et al.* AAV-Mediated Anterograde Transsynaptic Tagging: Mapping Corticocollicular Input-Defined Neural Pathways for Defense Behaviors. *Neuron* **93**, 33–47 (2017).

485. Zingg, B., Peng, B., Huang, J., Tao, H. W. & Zhang, L. I. Synaptic specificity and application of anterograde transsynaptic AAV for probing neural circuitry. *J. Neurosci.* (2020). doi:10.1523/JNEUROSCI.2158-19.2020

486. Zschucke, E., Renneberg, B., Dimeo, F., Wüstenberg, T. & Ströhle, A. The stress-buffering effect of acute exercise: Evidence for HPA axis negative feedback. *Psychoneuroendocrinology* (2015). doi:10.1016/j.psyneuen.2014.10.019

487. Chen, C. *et al.* The exercise-glucocorticoid paradox: How exercise is beneficial to cognition, mood, and the brain while increasing glucocorticoid levels. *Frontiers in Neuroendocrinology* (2017). doi:10.1016/j.yfrne.2016.12.001

488. Moylan, S. *et al.* Exercising the worry away: How inflammation, oxidative and nitrogen stress mediates the beneficial effect of physical activity on anxiety disorder symptoms and behaviours. *Neuroscience and Biobehavioral Reviews* (2013). doi:10.1016/j.neubiorev.2013.02.003

489. Eyre, H. & Baune, B. T. Neuroimmunological effects of physical exercise in depression. *Brain, Behavior, and Immunity* (2012). doi:10.1016/j.bbi.2011.09.015

490. Wolpert, D. M. & Miall, R. C. Forward Models for Physiological Motor Control. *Neural Networks* (1996).

491. Blakemore, S. J., Wolpert, D. & Frith, C. Why can't you tickle yourself? *NeuroReport* (2000). doi:10.1097/00001756-200008030-00002

492. Whitford, T. J. *et al.* Neurophysiological evidence of efference copies to inner speech. *Elife* (2017). doi:10.7554/eLife.28197

493. Blakemore, S. J., Smith, J., Steel, R., Johnstone, E. C. & Frith, C. D. The perception of self-produced sensory stimuli in patients with auditory hallucinations and passivity experiences: Evidence for a breakdown in self-monitoring. *Psychol. Med.* (2000). doi:10.1017/S0033291799002676

494. Taniguchi, H. *et al.* A Resource of Cre Driver Lines for Genetic Targeting of GABAergic Neurons in Cerebral Cortex. *Neuron* **71**, 995–1013 (2011).

495. Madisen, L. *et al.* A robust and high-throughput Cre reporting and characterization system for the whole mouse brain. *Nat. Neurosci.* (2010). doi:10.1038/nn.2467

496. R Core Team. R: A language and environment for statistical computing. (2019).

497. Wickham, H. *et al.* Welcome to the Tidyverse. *J. Open Source Softw.* (2019). doi:10.21105/joss.01686

498. Kolde, R. pheatmap: Pretty Heatmaps. (2019).

499. Wickham, H. *ggplot2: Elegant Graphics for Data Analysis*. (Springer-Verlag, 2016).

500. Martianova, E., Aronson, S. & Proulx, C. D. Multi-fiber photometry to record neural activity in freely-moving animals. *J. Vis. Exp.* (2019). doi:10.3791/60278

501. Zhang, Z. M., Chen, S. & Liang, Y. Z. Baseline correction using adaptive iteratively reweighted penalized least squares. *Analyst* (2010). doi:10.1039/b922045c

502. Calipari, E. S. *et al.* In vivo imaging identifies temporal signature of D1 and D2 medium spiny neurons in cocaine reward. *Proc. Natl. Acad. Sci. U. S. A.* (2016). doi:10.1073/pnas.1521238113

503. Park, Y. G. *et al.* Protection of tissue physicochemical properties using polyfunctional crosslinkers. *Nat. Biotechnol.* (2019). doi:10.1038/nbt.4281

504. LifeCanvas. SHIELD Protocol with LifeCanvas Devices. https://lifecanvastech.com/wp-content/uploads/2019 (2019).

505. LifeCanvas. SmartClear II Pro User's Manual. https://lifecanvastech.com/wp-content/uploads/2019 (2019).

506. Kim, S. Y. *et al.* Stochastic electrotransport selectively enhances the transport of highly electromobile molecules. *Proc. Natl. Acad. Sci. U. S. A.* (2015). doi:10.1073/pnas.1510133112

507. Hedde, P. N. & Gratton, E. Selective Plane Illumination Microscopy with a Light Sheet of Uniform Thickness Formed by an Electrically Tunable Lens. *Microsc Res Tech.* 924–928 (2016).

508. Dean, K. M., Roudot, P., Welf, E. S., Danuser, G. & Fiolka, R. Deconvolution-free Subcellular Imaging with Axially Swept Light Sheet Microscopy. *Biophys. J.* (2015). doi:10.1016/j.bpj.2015.05.013

509. Bria, A., Bernaschi, M., Guarrasi, M. & Iannello, G. Exploiting Multi-Level Parallelism for Stitching Very Large Microscopy Images. *Front. Neuroinform.* **13**, 41 (2019).

510. Swaney, J. *et al.* Scalable image processing techniques for quantitative analysis of

volumetric biological images from light-sheet microscopy. *bioRxiv* (2019). doi:10.1101/576595

511. Harris, N. A. *et al.* Dorsal BNST α2a-adrenergic receptors produce HCN-dependent excitatory actions that initiate anxiogenic behaviors. *J. Neurosci.* (2018). doi:10.1523/JNEUROSCI.0963-18.2018

512. Schindelin, J. *et al.* Fiji: An open-source platform for biological-image analysis. *Nature Methods* (2012). doi:10.1038/nmeth.2019

513. Evrard, H. C. The organization of the primate insular cortex. *Frontiers in Neuroanatomy* (2019). doi:10.3389/fnana.2019.00043

514. Evrard, H. C. & (Bud) Craig, A. D. Insular Cortex. in *Brain Mapping: An Encyclopedic Reference* (2015). doi:10.1016/B978-0-12-397025-1.00237-2

515. Berret, E. *et al.* Insular cortex processes aversive somatosensory information and is crucial for threat learning. *Science* (2019). doi:10.1126/science.aaw0474

516. Gehrlach, D. A. *et al.* A whole-brain connectivity map of mouse insular cortex. *bioRxiv* (2020). doi:10.1101/2020.02.10.941518

517. Umeda, T., Isa, T. & Nishimura, Y. The somatosensory cortex receives information about motor output. *Sci. Adv.* (2019). doi:10.1126/sciadv.aaw5388

518. Niziolek, C. A., Nagarajan, S. S. & Houde, J. F. What does motor efference copy represent? evidence from speech production. *J. Neurosci.* (2013). doi:10.1523/JNEUROSCI.2137-13.2013

519. Arce-McShane, F. I., Ross, C. F., Takahashi, K., Sessle, B. J. & Hatsopoulos, N. G. Primary motor and sensory cortical areas communicate via spatiotemporally coordinated networks at multiple frequencies. *Proc. Natl. Acad. Sci. U. S. A.* (2016). doi:10.1073/pnas.1600788113

520. Ghosh, S., Brinkman, C. & Porter, R. A quantitative study of the distribution of neurons

projecting to the precentral motor cortex in the monkey (M. fascicularis). *J. Comp. Neurol.* (1987). doi:10.1002/cne.902590309

521. Jones, E. G., Coulter, J. D. & Hendry, S. H. C. Intracortical connectivity of architectonic fields in the somatic sensory, motor and parietal cortex of monkeys. *J. Comp. Neurol.* (1978). doi:10.1002/cne.901810206

522. Pons, T. P. & Kaas, J. H. Corticocortical connections of area 2 of somatosensory cortex in macaque monkeys: A correlative anatomical and electrophysiological study. *J. Comp. Neurol.* (1986). doi:10.1002/cne.902480303

523. Johnson, S., Summers, J. & Pridmore, S. Changes to somatosensory detection and pain thresholds following high frequency repetitive TMS of the motor cortex in individuals suffering from chronic pain. *Pain* (2006). doi:10.1016/j.pain.2006.02.030

524. Lefaucheur, J. P., Drouot, X. & Nguyen, J. P. Interventional neurophysiology for pain control: Duration of pain relief following repetitive transcranial magnetic stimulation of the motor cortex. *Neurophysiol. Clin.* (2001). doi:10.1016/S0987-7053(01)00260-X

525. Treister, R., Lang, M., Klein, M. M. & Oaklander, A. L. Non-invasive Transcranial Magnetic Stimulation (TMS) of the Motor Cortex for Neuropathic Pain—At the Tipping Point? *Rambam Maimonides Med. J.* (2013). doi:10.5041/rmmj.10130

526. Fenno, L. E. *et al.* Targeting cells with single vectors using multiple-feature Boolean logic. *Nat. Methods* (2014). doi:10.1038/nmeth.2996

527. Fenno, L. E., Mattis, J., Ramakrishnan, C. & Deisseroth, K. A guide to creating and testing new INTRSECT constructs. *Curr. Protoc. Neurosci.* (2017). doi:10.1002/cpns.30

528. Fenno, L. E. *et al.* Comprehensive Dual- and Triple-Feature Intersectional Single-Vector Delivery of Diverse Functional Payloads to Cells of Behaving Mammals. *Neuron* (2020). doi:10.1016/j.neuron.2020.06.003

529. Klapoetke, N. C. *et al.* Independent optical excitation of distinct neural populations. *Nat. Methods* (2014). doi:10.1038/nmeth.2836

530. Huang, L. *et al.* Relationship between simultaneously recorded spiking activity and fluorescence signal in GCaMP6 transgenic mice. *Elife* **10**, (2021).

531. Piatkevich, K. D. *et al.* A robotic multidimensional directed evolution approach applied to fluorescent voltage reporters article. *Nat. Chem. Biol.* (2018). doi:10.1038/s41589-018-0004-9

532. Abdelfattah, A. S. *et al.* Bright and photostable chemigenetic indicators for extended in vivo voltage imaging. *Science (80-.).* (2019). doi:10.1126/science.aav6416

533. Siedentopf, H. & Zsigmondy, R. Uber Sichtbarmachung und Größenbestimmung ultramikoskopischer Teilchen, mit besonderer Anwendung auf Goldrubingläser. *Ann. Phys.* (1902). doi:10.1002/andp.19023150102

534. VOIE, A. H., BURNS, D. H. & SPELMAN, F. A. Orthogonal-plane fluorescence optical sectioning: Three-dimensional imaging of macroscopic biological specimens. *Journal of Microscopy* (1993). doi:10.1111/j.1365-2818.1993.tb03346.x

535. Moore, G. E. Cramming more components onto integrated circuits. In: Electronics. *Electronics* (1965).

536. Fürth, D. *et al.* An interactive framework for whole-brain maps at cellular resolution. *Nat. Neurosci.* (2018). doi:10.1038/s41593-017-0027-7

537. Mathis, M. W. & Mathis, A. Deep learning tools for the measurement of animal behavior in neuroscience. *Current Opinion in Neurobiology* (2020). doi:10.1016/j.conb.2019.10.008

538. Datta, S. R., Anderson, D. J., Branson, K., Perona, P. & Leifer, A. Computational Neuroethology: A Call to Action. *Neuron* (2019). doi:10.1016/j.neuron.2019.09.038

539. Mathis, A., Schneider, S., Lauer, J. & Mathis, M. W. A Primer on Motion Capture with Deep Learning: Principles, Pitfalls, and Perspectives. *Neuron* (2020). doi:10.1016/j.neuron.2020.09.017

540. Forys, B., Xiao, D., Gupta, P., Boyd, J. D. & Murphy, T. H. Real-time markerless video tracking of body parts in mice using deep neural networks. *bioRxiv* (2018). doi:10.1101/482349

541. Mathis, A. & Warren, R. On the inference speed and video-compression robustness of DeepLabCut. *bioRxiv* (2018). doi:10.1101/457242

542. Newell, A., Yang, K. & Deng, J. Stacked hourglass networks for human pose estimation. in *Lecture Notes in Computer Science (including subseries Lecture Notes in Artificial Intelligence and Lecture Notes in Bioinformatics)* (2016). doi:10.1007/978-3-319-46484-8_29

543. Badrinarayanan, V., Kendall, A. & Cipolla, R. SegNet: A Deep Convolutional Encoder-Decoder Architecture for Image Segmentation. *IEEE Trans. Pattern Anal. Mach. Intell.* (2017). doi:10.1109/TPAMI.2016.2644615

544. Graving, J. M. *et al.* Deepposekit, a software toolkit for fast and robust animal pose estimation using deep learning. *Elife* (2019). doi:10.7554/eLife.47994

545. Johansson, G. Visual perception of biological motion and a model for its analysis. *Percept. Psychophys.* (1973). doi:10.3758/BF03212378

546. Winter, D. A. *Biomechanics and Motor Control of Human Movement: Fourth Edition*. *Biomechanics and Motor Control of Human Movement: Fourth Edition* (2009). doi:10.1002/9780470549148

547. Vargas-Irwin, C. E. *et al.* Decoding complete reach and grasp actions from local primary motor cortex populations. *J. Neurosci.* (2010). doi:10.1523/JNEUROSCI.5443-09.2010

548. Wenger, N. *et al.* Closed-loop neuromodulation of spinal sensorimotor circuits controls refined locomotion after complete spinal cord injury. *Sci. Transl. Med.* (2014). doi:10.1126/scitranslmed.3008325

549. Karashchuk, P. *et al.* Anipose: A toolkit for robust markerless 3D pose estimation. *bioRxiv* (2020). doi:10.1101/2020.05.26.117325

550. Mathis, A., Yüksekgönül, M., Rogers, B., Bethge, M. & Mathis, M. W. Pretraining boosts out-of-domain robustness for pose estimation. *arXiv* (2019).

551. Bohnslav, J. P. *et al.* DeepEthogram: A machine learning pipeline for supervised behavior classification from raw pixels. *bioRxiv* (2020). doi:10.1101/2020.09.24.312504

552. Berman, G. J., Choi, D. M., Bialek, W. & Shaevitz, J. W. Mapping the stereotyped behaviour of freely moving fruit flies. *J. R. Soc. Interface* (2014). doi:10.1098/rsif.2014.0672

553. Hsu, A. I. & Yttri, E. A. B-SOiD: An Open Source Unsupervised Algorithm for Discovery of Spontaneous Behaviors. *bioRxiv* (2019). doi:10.1101/770271

554. Sturman, O. *et al.* Deep learning-based behavioral analysis reaches human accuracy and is capable of outperforming commercial solutions. *Neuropsychopharmacology* (2020). doi:10.1038/s41386-020-0776-y

555. Nilsson, S. R. O. *et al.* Simple Behavioral Analysis (SimBA) – an open source toolkit for computer classification of complex social behaviors in experimental animals. *bioRxiv* (2020). doi:10.1101/2020.04.19.049452

556. Dolensek, N., Gehrlach, D. A., Klein, A. S. & Gogolla, N. Facial expressions of emotion states and their neuronal correlates in mice. *Science (80-.).* (2020). doi:10.1126/science.aaz9468